MECHANISMS OF INFRARED NERVE INHIBITION:

COMPUTATIONAL MODELING AND EXPERIMENTAL VALIDATION

By

Mohit Ganguly

Dissertation

Submitted to the Faculty of the

Graduate School of Vanderbilt University

In partial fulfillment of the requirements

of the degree of

DOCTOR OF PHILOSOPHY

in

Biomedical Engineering

June 30, 2019

Nashville, Tennessee

Approved:

E. Duco Jansen, PhD, Committee Chair

Anita Mahadevan-Jansen, PhD

Hillel J. Chiel, PhD

John P. Wikswo, PhD

Marc A. Huntoon, MD

ACKNOWLEDGEMENTS

Although, this PhD is awarded to me exclusively, but it involves the effort of multiple people over numerous years. I would like to start by thanking Dr. E. Duco Jansen for taking me under his wing as a student and serving as a mentor all these years. He always pushed me to put forward my best work, and his unbounded optimism served as a guiding light during tough times. I also thank Dr. Anita Mahadevan-Jansen for her support as my grant PI and always providing me opportunities to showcase my work in front of peers and experts in the field. I hope I can count on the Jansen's counsel and friendship as I embark on the next phase of my life after graduation. I would like to thank Dr. Hillel Chiel for being tough and always asking pertinent questions, which helped me become a critical thinker and honed my analytical skills. I would also like to thank my other committee members Dr. John Wikswo and Dr. Marc Huntoon. Dr. Wikswo provided valuable critiques to my work which refined the dissertation, and Dr. Huntoon provided his inputs that helped me understand the clinical perspectives and challenges of my work.

Other than the committee members, I cannot underscore the valuable contribution of my friends in Nashville and elsewhere around the world. I cannot name them all, but I would like to especially acknowledge almost doctor Jeremy Ford. His support was valuable from the beginning and was especially useful when I was performing my experiments towards the latter half of my PhD. His out-of-lab suggestions were valuable as well in making in stay in Nashville a memorable one. Our conference trips together are some of the fond memories I will cherish for a long time. I would also like to thank the alumni of the lab (Jonathan Wells, Austin Duke, Jonathan Cayce,

Chetan Patil, Christine O'Brien, Amy Shah, Isaac Pence, Melanie McWade, and others) who helped in whenever I asked them for advice and help.

Finally, I would like to thank my parents for their unconditional love and support all through my graduate career. This PhD is the culmination of the numerous sacrifices they have made along the way and its completion wouldn't have been possible without them. I would like to dedicate this dissertation to them.

TABLE OF CONTENTS

Page

LIST OF FIGURES

Figure   Page

LIST OF TABLES

LIST OF COMMON SYMBOLS

Symbol	Parameter Name	S.I. Units
Optical thermal model		
L	Radiance	$W/m^2.sr$
μ_a	Absorption coefficient	$1/m$
μ_s	Scattering coefficient	$1/m$
g	Anisotropy factor	-
n_r	Index of refraction	-
f	Laser pulse repetition rate	$1/s$ (Hz)
τ_p	Laser pulse duration	s
r	Laser beam radius	m
λ	Laser wavelength	m
H	Fluence rate/ Radiant exposure	J/m^2
T	Temperature	K
k	Thermal conductivity	W/m.K
C	Specific heat capacity	J/(kg.K)
h	Convection coefficient	W/m^2K
ρ	Density	kg/m^3
Q_{met}	Metabolic heat generation rate	W/m^3
ω	Blood perfusion rate	$m^3/(s.kg)$
E_a	Activation energy	J/mol
A	Frequency factor	$1/s$
λ	Wavelength	m

P	Power (coming out of optical fiber)	W
Ω	Thermal damage parameter	-
S	Source term	W/m^3 sr
p	Phase scattering function	1/sr

Hodgkin Huxley Model (NEURON)

g_x	Ionic conductance to ion x (x can be Na, K)	S/m^2
$\overline{g_x}$	Maximum ionic conductance to ion x	S/m^2
r_a	Intracellular axonal resistivity	$\Omega.cm$
C_m	Membrane capacitance	F/m^2
α_x	Activation term of gate x (x can be m, n or h)	1/s
β_x	Inactivation term of gate x (x can be m, n or h)	1/s
τ_x	Time constant of gate x (x can be m, n or h)	s
E_x	Nernst potential of ion x	V
V or V_m	Membrane potential	V
Q_{10}	Ratio of rate of biological processes between T and T+10 ^oC	-
κ_x	Thermic coefficient of ion x	-
I_x	Current due to ion x	A
m,n,h	Gating variables	-

Note: Some parameters may have identical symbols, but their meanings are clarified when used in contex

1   INTRODUCTION

1.1   Motivation

There is a need to find an inexpensive pain management technique that is free of the side-effects listed above. Chronic pain is a large public health problem that affects about 100 million people annually (US) leading to loss in quality of life and productivity. Apart from that, chronic pain also affects economically and drains $ 600 billion (2010) dollars from the U.S. economy. The long-term aim of this research is to inhibit transmission of pain signals in humans in a way that is free of the side effects of the conventional analgesics and other electrical stimulation methods. Currently, there are several types of techniques that are used to treat and manage various types of pain. Some of them include Acetaminophen (Tylenol) for muscle, joint or bone pain, corticosteroids, NSAIDs (Nonsteroidal anti-inflammatory drugs), anticonvulsants, and opiate pain relievers. Apart from the chemical drugs, there are electrical methods also available like the use of high frequency currents (Bhadra 2006). Almost all of the pain management techniques involve side effects which may include nausea, rash, liver damage, constipation, addiction and subsequent withdrawal.

The inhibition of nerve signals using infrared laser light offers an alternative to the conventional pain management techniques. It is reversible, non-contact and free of onset responses. In order to devise a strategy towards the development of this pain management modality using infrared lasers in the form of a nerve cuff, we need to understand the physiology of pain transmission in humans. This will provide us with the limitations and the constraints that

we need to keep in mind when designing and developing effective approaches that utilize infrared neural inhibition.

1.2   Specific Aims

One of the newer neuromodulation techniques uses pulsed infrared laser light for the activation or inhibition of nerves. This method has been shown to be free of electrical artifacts, is spatially specific and the light source doesn't require direct contact with the nerve (Duke 2013, Wells 2005). Infrared inhibition has the potential to replace or augment electrical stimulation as the preferred method for neuromodulation in humans. One possible clinical application of this technique would be the inhibition of pain signals through the development of nerve cuffs that selectively inhibit C fibers. These unmyelinated fibers in mammals are responsible for the transmission of slow pain signals that lead to chronic pain. To realize this vision, the mechanism behind the interaction of infrared laser with excitable unmyelinated nerves has to be understood so that an optimum block can be achieved using the cuff. Experiments and computational models (Hodgkin 1949, Mou 2012) have suggested that an increase in temperature of water in tissue due to infrared laser absorption affects the dynamics of ion channels in the neuron . However, a clear mechanism has not yet been described.

The primary objective of this dissertation is to understand the mechanism behind the infrared inhibition of action potentials in unmyelinated nerves. Most unmyelinated nerves in invertebrates have relatively simple anatomical features due to the absence of complicated secondary channels, TRPV (Transient receptor potential) channels, and lack a thick myelin sheath. This makes the unmyelinated nerve axon an attractive model to simulate and perform experiments to identify the mechanism and to optimize the thermal modulation technique. The conclusions

derived from the unmyelinated nerve experiments can then be translated to the unmyelinated C fiber setting. The following specific aims have been proposed to the understanding of infrared neural inhibition.

Specific Aim 1: Develop a computational model to simulate effect of elevated temperature on neural propagation: A modeling approach was used to explore the mechanism by which infrared light inhibits neural activity. The Hodgkin Huxley (HH) model was modified by incorporating temperature dependent features (sodium/potassium pump, peak sodium and potassium conductances and axial resistances). These features are either not present or assumed to be temperature independent in the original HH model. These changes were based on the experimentally published results on the squid giant axon. Faster activation of voltage dependent potassium ion channels was found to be the major contributor responsible for causing thermal block observed at elevated temperatures. The results provided a testable hypothesis for IR-induced block which are validated in Specific Aim 2.

Specific Aim 2: Validate hypothesis generated as a result of Aim 1 results: Hypotheses derived from the modeling studies were tested in a tractable system of the marine mollusk *Aplysia californica*, where all nerves are unmyelinated. Using isolated nerves (pleural abdominal) from *Aplysia*, it was determined that the ability of infrared light to cause nerve block is compromised by inhibiting the activity of voltage-dependent potassium ion channels and is relatively unaffected if the activity of voltage-dependent sodium ion channels is blocked. A custom-made 3D printed chamber was designed that allowed the administration of selective ion channel blocking agents on a specific length of the nerve while the nerve is irradiated with IR light at that specific region of the nerve. Results show that selectively inhibiting voltage-dependent potassium ion channels

compromises IR-induced thermal block, whereas selectively inhibiting voltage-dependent sodium ion channels does not affect IR block. These conclusions were consistent with the modeling predictions in Specific Aim 1.

Specific Aim 3: Develop an integrated multiphysics model computational model to perform parametric analysis of infrared inhibition in unmyelinated nerves: A multiphysics computational model was developed that integrates optical-thermal simulations with neural simulations. The model combines an optical-thermal computational model with a neurophysiological computational model, which is used to devise design inputs to optimize infrared light delivery to nerves in a safe way.

The content in this dissertation has been organized into the following chapters.

1.3   Outline

Chapter 1 provides an introduction to the problem tackled in the dissertation and mentions the introductory justification and the specific aims used to guide the research.

Chapter 2 of this dissertation provides a historical background of the development of the technology of infrared neuromodulation. It mentions the efforts undertaken for the development of the technology since its invention. A brief explanation of the various scientific principles that aid in the understanding behind the phenomenon is also provided. This chapter also provides a detailed (but not necessarily exhaustive) review of the current efforts both in the understanding of the mechanisms as well as the clinical translation of the technology of infrared neuromodulation.

Chapter 3 discusses the development of a computational model to understand the mechanism of infrared inhibition in unmyelinated nerves. The computational model developed in this chapter was based on the widely accepted Hodgkin Huxley (HH) model with multiple changes. The model results suggest that voltage-gated potassium ion channels play a critical role during thermal inhibition in unmyelinated axons.

Chapter 4 of the dissertation discusses the experiments performed to test the main finding from Chapter 3 of the dissertation. The results shown in this chapter appeared to validate the predictions derived from the computational model that potassium channels were critical (necessary and sufficient) to produce action potential conduction block in unmyelinated nerves such as those found in *Aplysia californica*.

Chapter 5 discusses the development of a multiphysics model that combines an optical-thermal computational model with a neurophysiological computational model, to devise design inputs to optimize infrared light delivery to nerves in a safe way.

Chapter 6 provides the conclusions of the research work undertaken as a part of the dissertation. The chapter also discusses future steps that can be undertaken to make further progress in the research.

Appendix A is the final report submitted as a part of the class MGT 6499 (Innovation Realization). This report details a commercialization plan and lays out a strategy to commercialize the technology of infrared nerve blocks in this dissertation in the future as an alternative chronic pain management modality.

Appendix B is a SPIE proceedings chapter discussing the initials steps taken in the development of the model shown in Chapter 3.

Appendix C details the work done in collaboration with Eric C. Yeats (BE 2019) that focuses on simulating the response of a multi axon nerve in response to a time and space varying temperature distribution, as is observed during infrared irradiation.

A version of Chapter 3 is published as Ganguly, M., Jenkins, M. W., Jansen, E. D., & Chiel, H. J. (2019). Thermal block of action potentials is primarily due to voltage-dependent potassium currents: A modeling study. *J. Neural Eng.*

A version of Chapter 4 has been submitted to *Neurophotonics Letters* as 'Voltage-gated Potassium Channels are Critical for Infrared Inhibition of Action Potential: An Experimental Study'.

A version of Chapter 5 is currently in preparation to be submitted to Neurophotonics Technical Reports for peer review.

Appendix B is published in SPIE proceedings as Ganguly, M., Jenkins, M. W., Chiel, H. J., & Jansen, E. D. (2016, March). Modeling the effects of elevated temperatures on action potential propagation in unmyelinated axons. In Clinical and Translational Neurophotonics; Neural Imaging and Sensing; and Optogenetics and Optical Manipulation (Vol. 9690, p. 96901O). International Society for Optics and Photonics.

Appendix C was submitted as an abstract for a poster presentation by Eric Yeats (EECS 2019) at

the Biomedical Engineering Society (BMES) Annual Meeting in Atlanta on October 18, 2019.

2 BACKGROUND

Action potentials, which are the signals units in the nervous system are a result of the complex interplay of sodium and potassium channels across the cell membrane. The movement of these ions are driven by the electrochemical gradient established between the extracellular and intracellular environment of the neuron (nerve cell). These movements are facilitated by special ion selective channels located in the cell membrane (ion channels). These channels only allow the unidirectional movement of specific ions (sodium, potassium, calcium etc). These channels remain closed when the neuron is in its resting potential. When the membrane potential rises due to the influence of a stimulus, the voltage gated sodium ion channels open rapidly and allow the movement of sodium ions inside the cells, which leads to depolarization of the neuron. As this movement proceeds, the voltage gated potassium ion channels open, and as a result, the potassium ions are moved outside of the cell causing repolarization of the cell. Rapid influx of sodium ions causes the polarity of the plasma membrane to reverse, and the ion channels then rapidly inactivate. As the sodium channels close, sodium ions can no longer enter the neuron, and they are then actively transported back out of the plasma membrane. Potassium channels are then activated, and there is an outward current of potassium ions, returning the electrochemical gradient to the resting state. After an action potential has occurred, there is a transient negative shift, called the refractory period (Fig. 2-1).
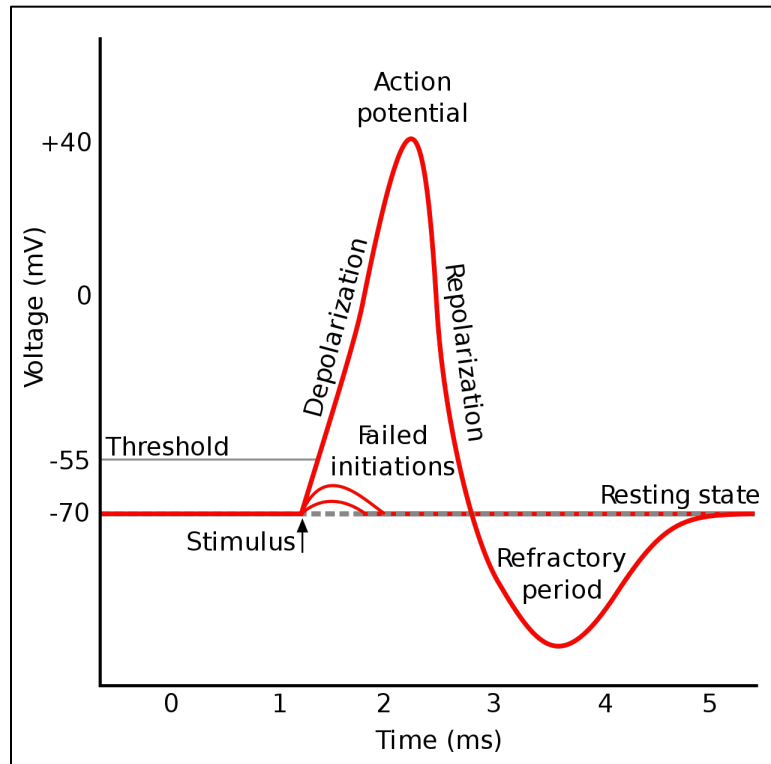
Figure 2-1: Phases of an action potential (Source: Kenneth Casey, Wikipedia)

In humans, the nervous system is responsible for the transmission of important sensory and motor signals in our body to and from the control centers, the brain and the spinal cord. The major component of the nervous system, the nerve cell or neuron, consists of the cell body (soma), the axon which contains the nerve terminals and acts as the point of release of neurotransmitters that interface with the next nerve cell to transmit the nerve signal over a distance, and the dendrites. In mammalian peripheral nervous systems, the axon is covered with a myelin sheath which consists of Schwann cells (Fig. 2-2). This layer speeds up conduction across the length of the axon which may be useful when fast responses are required, for example, when moving our hand while touching a hot object. As with other organs, nerves also malfunction and are prone to diseases. For example, in the case of Alzheimer's disease, the nerve cells in the brain start to lose their myelination which disables their ability to transmit information efficiently. Sometimes nerve

damage may result from injury which may result in paralysis. In this case, it is important to restore function to the affected part of the body that the damaged nerve innervates. In other cases, pain arising from damage to the sensory neurons (neuropathic pain), it is desirable to inhibit in order to reduce the pain sensation and provide comfort to the patient. Hence, artificial control of nerve behavior is vital in clinical applications.
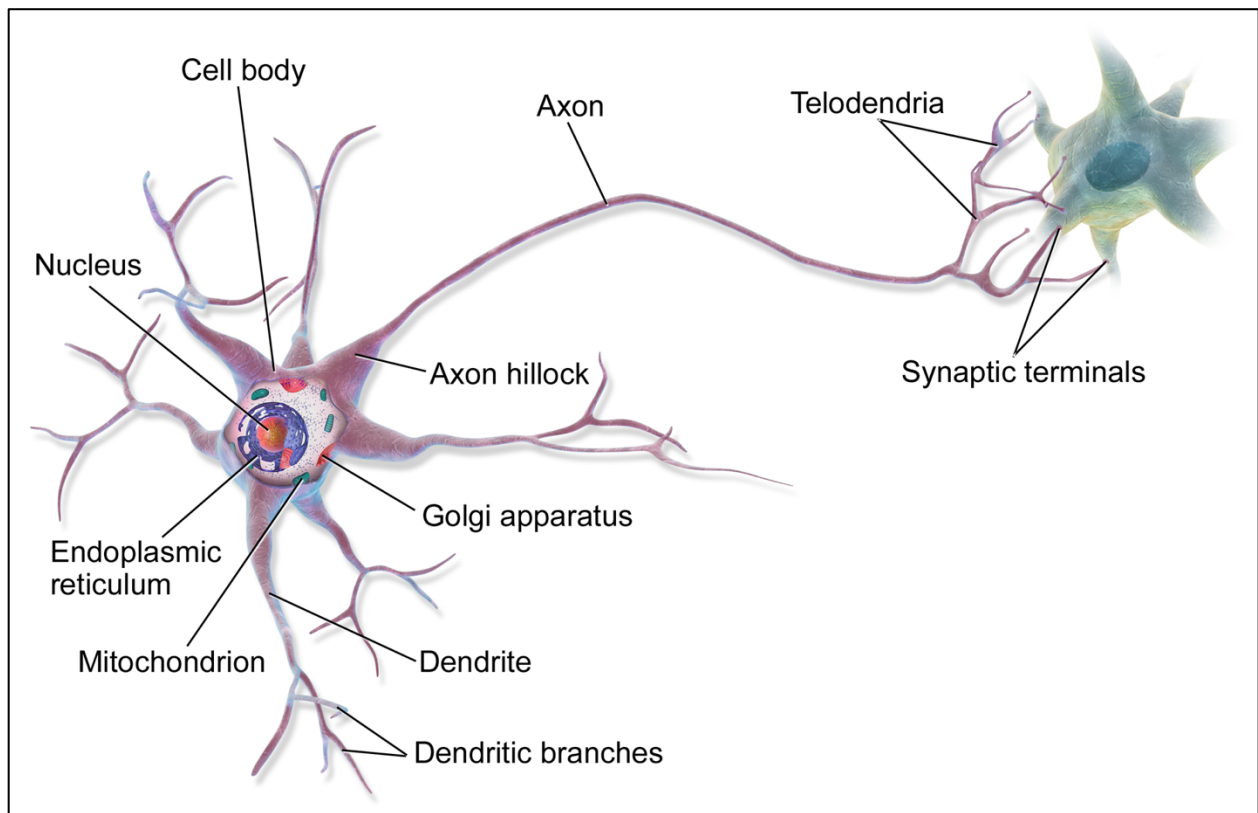
Figure 2-2: Anatomy of mammalian nerve cell (Source: BruceBlaus, Wikipedia)

Electrical stimulation has been the gold standard for the control of nerve behavior. Some of the applications of electrical nerve stimulation include the treatment of foot drop (Kottink 2007), deep brain stimulation (DBS) (Kern 2007), for disorders such as Parkinson's disease, auditory

implants for the profoundly deaf (Shannon 2012), and vagus nerve stimulation for epilepsy and depression (Groves 2005).

Currently, there are several types of techniques that are used to treat and manage various types of pain. Some of them include Acetaminophen (Tylenol) for muscle, joint or bone pain, corticosteroids for pain caused by inflammation, NSAIDs (Nonsteroidal anti-inflammatory drugs), Anticonvulsants for nerve pain, and opiate pain relievers. Apart from the chemical drugs, there are electrical methods also available for the control of pain that includes the stimulation of high frequency electrical currents (or in combination with direct currents) to block nerve conduction. This technique, called KHFAC (kilo-hertz frequency AC) block is plagued with the problem of the occurrence of the 'onset response' which is highly undesirable. 'Onset response' is defined as prolonged period of strong activity (lasts for a few seconds) that is produced when KHFAC is turned on (Ackermann 2011). Some of the non-conventional methods of pain management include hypnotic analgesia and placebo analgesia. Almost all of these pain management techniques involve side effects indicating nausea, rash, liver damage, constipation, addiction and subsequent withdrawal. There is a need to find an inexpensive pain management technique that is free of all the side-effects in the listed above.

Recently, optical methods of neural inhibition have also been explored and their applications in the control of pain is an area of active research. Researchers have used infrared pulsed lasers to invoke action potentials in frogs, rats, *Aplysia* and other organisms (Cayce 2008, Duke 2009, Tozburun 2012, Wells 2005). It has been shown to be free of recording artifacts, is non-contact, and non-damaging to the nerve tissue. Though a clear mechanism for this phenomenon has not been identified, it remains an area of active research (Beier 2014, Plaksin

2018, Shapiro, Homma 2012, Thompson 2013, Wells 2005). Some of the studies have shown that it is a photothermal effect where the temporal and spatial gradient of temperature rise plays an active role in the activation of nerves (Wells 2007). Another study has shown the change in membrane capacitance due to temperature rise is an important factor that governs the change in transmembrane voltage (Plaksin 2018, Shapiro 2012) . Studies on the activation of TRPV channels (thermosensitive channels) (Albert 2012) and formation of membrane pores (Beier 2014) during infrared neural stimulation have also been studied.

An alternative observation using pulsed infrared lasers was the observation of inhibition of nerve signals in the rat sciatic nerve and in *Aplysia* alike (Duke 2013). The successful use of infrared laser light in inhibition of unmyelinated nerves may lead to the development of nerve cuffs that can inhibit pain signals carried by unmyelinated C fibers. This requires proper characterization of the laser parameters required to observe conduction block in the specific nerve without exceeding the thermal damage threshold. A clear understanding of the mechanism behind the observation of block is required so that we can make targeted adjustments to the clinical applications to make it suitable for patients suffering from chronic pain. In the case of infrared nerve inhibition, the primary mechanism of heat generation is through the photothermal interaction of laser light by nerve and the surrounding tissues. This includes the distribution of laser light in the tissue medium and conversion of the absorbed light into thermal energy (heat), the dissipation of heat leading to temperature rise in the vicinity of the laser irradiated zone of the tissue medium. The resultant temperature rise then affects the behavior of temperature sensitive voltage-gated ion channels (Hodgkin 1949). In the following subsections, principles behind these phenomena and the equations governing them are discussed.

2.1   Computational models

As mentioned in the section above, the relationship between light distribution inside tissues, resultant temperature rise, and the effect of temperature rise on the ion-channel kinetics are studied. This section contains an explanation of each of these processes and the tools and strategies to model them.

2.1.1   Hodgkin and Huxley model

Hodgkin and Huxley (HH) model has been used by neuroscientists since the 1950's and resulted in Nobel prizes for the original authors. Based on the series of experiments performed by Hodgkin, Huxley and their associates (Hodgkin 1952, Hodgkin 1952) on the squid giant axon, the electric behavior of the squid giant axon membrane was qualitatively and quantitatively defined. For the brief treatment of the Hodgkin Huxley (HH) equations, we assume that the axon is modeled as a cylinder with radius of r_i and negligible membrane thickness. The extracellular space is assumed to be a good conductor and grounded. The membrane has a capacitance of C_m (F/cm^2) and three parallel membrane conductances, g_{Na}, g_K and g_{leak} (S/cm^2). g_{Na} and g_k are considered to be voltage and time dependent. A voltage source is connected in series with each of the conductances (or resistances) that represents the Nernst potential (equilibrium potential) of the particular ion species. In this case, we have only considered sodium and potassium ions.
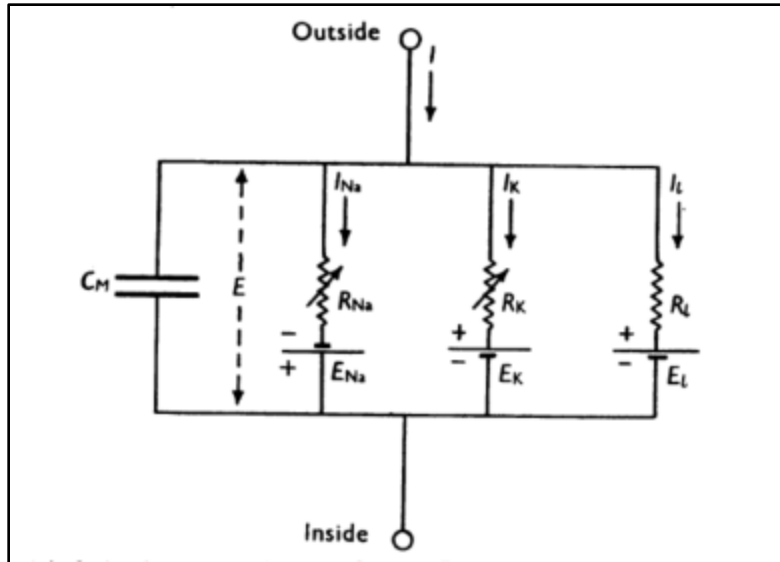
Figure 2-3: Electrical equivalent of a HH cell membrane (Hodgkin 1952)

The total membrane current consists of the capacitive current and the ionic current. In the HH model, the ionic currents are simplified by assuming linear relationships between ionic currents and their Nernst potentials. The total membrane ionic current I_{ionic} is the sum of the individual ionic currents and the leak current (I_L).

$$I_{ionic} = I_L + I_{K^+} + I_{Na^+} \qquad (2\text{-}1)$$

and each ionic current (I_{ionic}) can be written as the product of its conductance g_{ion} and the driving force.

$$I_{ion} = g_{ion}(V_m - E_{ion}) \qquad (2\text{-}2)$$

where V_m is the membrane voltage and the E_{ion} is the equilibrium potential (Nernst potential) for the ion.

Hodgkin and Huxley predicted that the potassium current depended on the simultaneous activation of four gating elements, whose probability of moving into a conducting state is

14

represented by the symbol n. Hodgkin and Huxley found the best fit for the potassium conductance data by assuming that there were four of these gates. Since they were assumed to act independently of one another, the overall probability of a potassium channel opening was the probability that all four of the gates had switched into a conducting state, or $n \times n \times n \times n = n^4$. Thus, if the maximum possible conductance for the potassium channels was $\overline{g_{K+}}$, the overall conductance for the potassium channels was

$$g_{K+} = \overline{(g_{K+})}n^4 \tag{2-3}$$

Similarly, the sodium current is dependent on the simultaneous activation of three gating elements, whose probability of moving into a conducting state is represented by m and another gating element, which was initially open at rest, but then closes with a probability h. The overall conductance of the sodium channel is represented by

$$g_{Na+} = \overline{(g_{Na+})}m^3 h \tag{2-4}$$

Hodgkin and Huxley assumed that there would be some rate (α_n) at which a gate that is currently not conducting would become conducting and some rate (β_n) at which a gate that is currently conducting would move into a non-conducting configuration. The total rate of change in the probability of gates conducting would be the probability that some gates became conducting, minus the probability that same became non-conducting.

$$\frac{dn}{dt} = \alpha_n(1 - n) - \beta_n n \tag{2-5}$$

where α_n and β_n are complex functions of the membrane voltage V_m.

This equation is often written in the following mathematically equivalent form

$$\frac{dn}{dt} = \frac{(n_\infty - n)}{\tau_n} \tag{2-6}$$

The voltage dependence of the rate constants α and β are as follows, based on measurements on a squid giant axon at 6.3 °, where n_∞ represents the value of n attained after a long time and τ_n represents the time constant of the rise of the variable n.

$$\alpha_n(V) = \frac{-(V+55)}{100\left(e^{\frac{-(V+55)}{10}} - 1\right)} \tag{2-7}$$

$$\beta_n(V) = 0.125\left(e^{\frac{-(V+65)}{80}}\right) \tag{2-8}$$

$$\alpha_m(V) = \frac{-(V+40)}{10\left(e^{\frac{-(V+40)}{10}} - 1\right)} \tag{2-9}$$

$$\beta_m(V) = 4\left(e^{\frac{-(V+65)}{18}}\right) \tag{2-10}$$

$$\alpha_h(V) = 0.07\left(e^{\frac{-(V+65)}{20}}\right) \tag{2-11}$$

$$\beta_m(V) = \frac{1}{\left(e^{\frac{-(V+35)}{10}} + 1\right)} \tag{2-12}$$

Where V is the transmembrane potential (mV). The resting potential is considered at -65 mV. However, Hodgkin and Huxley had considered their resting potentials at 0 mV for simplicity. A detailed derivation of these equations is outside the scope of this proposal and can be found in (Hodgkin 1952).

A summary of the various HH electrophysiological parameters is shown in Fig. 2-4. An action potential is generated in a squid giant axon at 6.3 °C (diameter 0.5 mm). Fig. 2-4 shows the

membrane voltage (V_m, A), gating variables (m, n, h, B), membrane ionic currents densities (J_K, J_{Na}, J_{leak}, C), and the total membrane current densities (J_{total}, D).
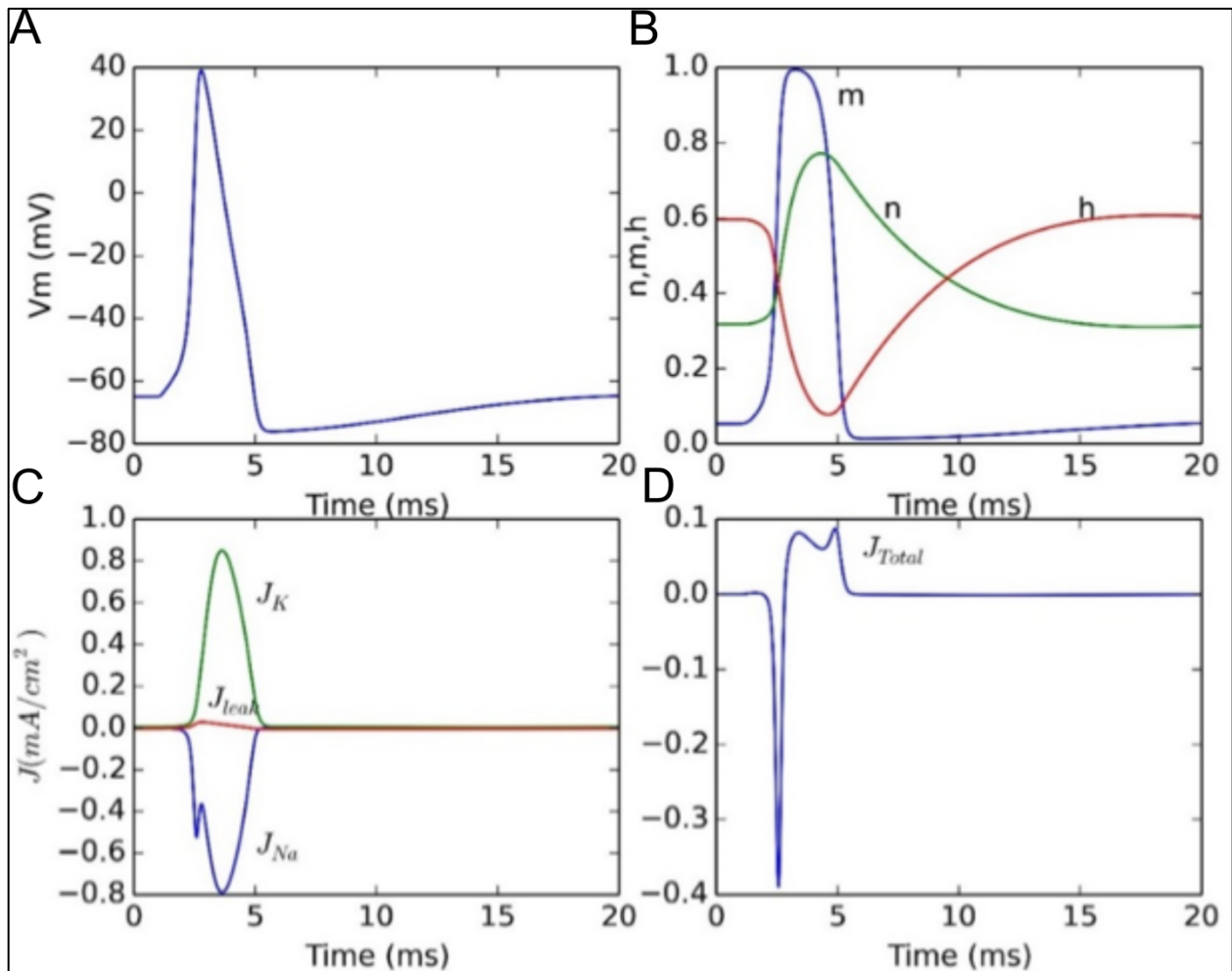
Figure 2-4: Summary of electrophysiological parameters for an action potential

(**A**) Membrane voltage versus time. (**B**) Change in gating variables versus time. (**C**) Ionic membrane current densities. (**D**) Total membrane current density. (Own work)

2.1.2 Temperature dependence of action potentials

The temperature dependence of nerves have been studied since the early 1900's. Bernstein first studied the effect of temperature on the electrical activity of nerves and muscles (Bernstein, 1902). Lucas measured the velocity ratios in temperature differences of 10 $^{\circ}$C (Lucas 1908). This led to the definition of Q_{10} for nerves. Q_{10} is defined as the rate by which biological processes are accelerated when their temperatures are increased by 10 $^{\circ}$C. Lucas measured the Q_{10} of about 1.8 for an amphibian nerve conduction velocity that closely matched with that of muscles and hence surmised that conduction process in mammalian nerves and muscles are probably of a similar nature. Further improvements were made to our understanding of the temperature dependence of ion channel kinetics through the works of Verzar, Gasser, and Tasaki and Fujita (Graham 1931, Tasaki 1948, Verzar 1912). Hodgkin and Katz published their results (Hodgkin 1952) of the comprehensive work performed on the stellar nerve of *Loligo forbesi* (squid giant axon). They concluded that the resting membrane potential is minimally affected by temperatures up to ~20 $^{\circ}$C, but then decreases (become more negative) rapidly beyond that. They measured the derivatives of the action potentials at various temperatures and observed the change in the maximum rates of rise and fall of the action potentials. They observed that as temperature rises, the rates of fall of action potentials accelerate faster than their rates of rise at those temperatures. Tasaki performed the same experiments in 1948 on the single motor nerve fibers (myelinated) in toad and observed that rheobase (minimum stimulation current amplitude) is not affected by temperature, whereas the recovery of the nerve after spike is affected by temperature (Tasaki 1948). Hodgkin and Huxley (Hodgkin 1952) in their landmark paper established the Q_{10} value of 3 for squid giant axon ion channel kinetics which is still considered a standard in many temperature dependent nerve models. Huxley commented that, based on these observations, at higher temperatures, sodium permeability is gradually overtaken by potassium permeability that leads to a block of the onset or propagation

of an action potential leading to a heat block (Huxley 1959). Computer simulations by Chapman (Chapman 1967) showed that there was a good agreement between the calculated and the experimentally measured conduction velocities of squid giant axons. Studies of temperature effects in conduction in myelinated nerves in various animals were studied by Paintal, Moore, Rasminsky, Schauf, and Chiu (Chiu 1979, Frankenhaeuser 1963, Paintal 1965, Rasminsky 1973, Schauf 1987). Rattay and Aberham (Rattay 1993) commented on the efficacy of Hodgkin Huxley model at different temperatures and suggested that the HH model may not be adequate to predict behavior or mammalian axons at elevated temperatures.. Rosenthal and Bezanilla (Rosenthal 2000) studied seasonal acclimation of giant axons in squid caught in warm and cold waters and measured various neurokinetic parameters at different temperatures. They found that the squid giant axons adapt seasonally to keep their conduction velocities constant with changing external temperatures. They measured the rates of fall and rise of action potentials, conduction velocities, action potential half-widths and the normalized conduction velocities (raw conduction velocities divided by the square root of axon diameter). Rosenthal and Bezanilla also studied temperature dependence in four different species of squid giant axons and found that conduction velocities followed the same trend across species at various temperatures (Rosenthal 2002). Mou et al. presented a detailed computational modeling study of the temperature dependence of myelinated nerve axon model and the effect of axon diameters on the block temperature (Mou 2012). A detailed discussion of this chapter can be found in section 2.1.3 where the modeling tool-NEURON is discussed.

2.1.3   NEURON

To predict the behavior of ion channels with temperature, in this dissertation, we have used NEURON (Hines 1997). NEURON is a simulation environment for modeling individual neurons and networks of neurons. It provides computationally efficient tools for conveniently building,

managing, and using models. NEURON has in-built functions that are tailored for conveniently controlling simulations and presenting the results of real neurophysiological problems graphically in ways that are quickly and intuitively grasped. NEURON is designed to let users deal directly with familiar neuroscience concepts. NEURON offers several different, user-selectable numerical integration methods.

- The default integration method is implicit Euler, which provides robust stability and first order accuracy in time (sufficient for most applications).
- Crank-Nicholson method that provides second order accuracy at little additional computational cost.
- Increased accuracy, faster run times, and sometimes both, may be achieved by choosing adaptive integration, which adjusts integration order and time step as necessary to satisfy a local error criterion.

User-defined mechanisms such as voltage- and ligand-gated ion channels, diffusion, buffering, active transport, etc., can be added by writing model descriptions in NMODL, a high-level programming language that has a simple syntax for expressing kinetic schemes and sets of simultaneous algebraic and/or differential equations. NMODL can also be used to write model descriptions for new classes of artificial spiking cells. These model descriptions are compiled so that membrane voltage and states can be computed efficiently using integration methods that have been optimized for branched structures.

NEURON has traditionally used the Hoc (higher order compiler) interpreter for the setup and control of neural simulations. Hoc is an interpreted programming language. NEURON has also been developed to be used with Python. Python is a modern programing language and provides

convenient syntax, powerful debugging capabilities and support for developing complex programs. Python also makes available to NEURON users, powerful scientific computing (SciPy, Numpy) and plotting tools (Matplotlib). Because of the benefits of combining NEURON with Python, it has been used for neural modeling work in this dissertation. A manual on the use of NEURON with Python for beginners can be found in (Hines 2009).

NEURON has been used for modeling various applications in neuroscience and there have been at least 1600 publications in various fields of computational neuroscience as of the end of 2018. More specifically, and more relevant to our work, Mou et al. showed the dependence of threshold block temperature (temperature at which thermal block occurs) with the diameter of nerve axon (Mou 2012). They simulated high temperatures at specific nodes in a frog (myelinated) sciatic nerve model at varying lengths along the axon. They showed that the threshold temperature required for achieving a propagation block is greater than the threshold temperature required to produce a generation block. While the results of Mou et al. were substantial and offered new insights on conduction blocks, they were unable to provide a clear mechanism of the heat block (generation or propagation) observed in nerve due to axonal temperature rise. The heat block simulated in the model was confined to specific length of the axon. This spatial distribution of temperature is not practical in either electrophysiological setups or in clinical settings. There was also little quantitative or qualitative representation of the change in the gating variables or the ion channels due to increasing temperatures over time.

2.1.4 Laser irradiation modeling in nerve tissues

Use of MC methods to study light propagation in tissues during photodynamic theory (PDT) was first introduced by Wilson and Adam (Wilson 1983). Their simple model consisting of a homogenous medium was extended by (Prahl 1989) to include anisotropy in the tissues and better handle the boundary conditions. (Wang 1995) further extended the existing MC models to allow light transport in multi-layered tissue (MCML). A review of the applications of MC model for various light distribution applications can be found here (Jacques 2010). Recently, both analytical and numerical approaches have been developed to understand the rise in temperature in nerve tissues during infrared neural stimulation (INS) (Norton 2013). Thompson et al. predicted the distribution of light and the temperature increase from a single pulse , pulse train and multiple emitters(Thompson 2013). They also compared their modeled temperature rises to experimental measurements of temperature rise as observed during INS in cochlea. Liljemalm et al. (Liljemalm 2014) developed a numerical multiphysics model to predict the temperature rise during infrared neural stimulation (INS). In all cases, the temperature rise was observed in the range of $1 - 10$ ºC depending on the laser power and the laser pulse repetition rate. *To our knowledge, none of the existing models combine an optical thermal model with a temperature dependent Hodgkin and Huxley model that can predict the effect of the temperature rise on excitable nerves.*

2.1.5 Light distribution modeling

Light incident at a tissue surface can undergo either scattering or absorption. A small portion of the incident light undergoes reflection at the surface (governed by Snell's Law and Fresnel's equations, beyond the scope of this dissertation). The fate of the remaining light is decided by the optical properties of the tissue medium. The absorbed light is then either converted

to heat energy, mechanical energy, pressure change, or re-emitted as fluorescence or phosphorescence, or may drive a chemical reaction through the dissociation of chemical bonds. Scattered light from the laser beam undergoes multiple scattering events as it is propagated through the tissue. Ideally, this interaction of laser light can be rigorously described in terms of Maxwell's equations. That description is beyond the scope of this dissertation, nor is it a practical description of light propagation in a complex medium such as tissue. Instead, a heuristic approach based on the statistical approximation of photon transport in multiple scattering medium is used. This theory governed by the transport equation describes the transfer of energy through a scattering medium (it usually neglects polarization but can be included). The transport equation is of the form (Welch 2010):

$$\frac{dL(r,\hat{s})}{ds} = \mu_a L(r,\hat{s}) - \mu_s L(r,\hat{s}) + \int_0^{4\pi} p(\hat{s},\hat{s}')L(r,\hat{s}')d\omega' + S(r,\hat{s}) \qquad (2\text{-}13)$$

where L is the radiance [W/m^2.sr], μ_a is the absorption coefficient [1/m], μ_s is the scattering coefficient [1/m], p is the phase (scattering) function [1/sr] and S is the optical source of the power generated at r in direction $\hat{s}$ [W/m^3. sr]. This equation relates the gradient of radiance L at position r in direction $\hat{s}$ to losses owing to absorption and scattering and to a gain owing to light scattered from all other directions $\hat{s}'$ into direction $\hat{s}$. This theory treats light propagation as a transport of particles (photons). The equation can be derived from Maxwell's equations for special cases where each particle lies in the far-field of the other particles and there are no correlations between particle positions.

The radiative transport equation (RTE), though very rigorous in its approach, is not easy to handle and solve in the closed form. In fact, the RTE can be solved in the closed form in very few cases, one of them describing transport in one dimension. Hence the idea of stochastic solvers

23

(Monte Carlo simulations) to replicate the behavior of RTE in tissue medium was introduced (Prahl 1989, Wilson 1983).

In a general Monte Carlo (MC) simulation, photon packets are inserted into the medium (tissue) at the surface (in case of an external light source) or inside the tissue (in case of internal light source). All photons are assigned an initial probability 'weight' of 1 that refers to the size of the photon packet. The photon weight undergoes reduction every time the photon undergoes an absorption or a scattering event in its propagation pathway. The reduction of this weight ΔW is calculated as

$$\Delta W = \frac{\mu_a}{\mu_t} W \qquad (2\text{-}14)$$

where μ_a and μ_t are absorption and scattering coefficient of the tissue respectively, and W is the initial weight of the photon before the reduction. The absorbed weight is stored in the tissue voxel/pixel corresponding to the existing photon position.

The photon is moved a random distance (which depends on a random number between 0 and 1 and the absorption coefficient of the tissue in the vicinity) on a trajectory defined by the direction cosines. The remaining non-absorbed weight is then used to propagate the photon further. The step size s is defined as

$$s = \frac{-\ln(x)}{\mu_t} \qquad (2\text{-}15)$$

where x is a random number $[0,1]$ and μ_t is the total attenuation coefficient $[\text{m}^{-1}]$ and is the sum of the absorption and the scattering coefficients of the tissue medium. After encountering multiple scattering events, the photon's weight becomes progressively smaller ("Drop"). To terminate the photon's journey, a "Roulette Method" is used. In this method, a threshold value is

chosen (usually 10^{-4}), and when the photon's weight drops below this threshold value, the roulette is used. A random number x is generated and if this random number is less than a value called "chance" (usually 0.1), then the photon weight is increased by dividing the existing weight by the "chance" value. Otherwise the photon is terminated. For chance=0.1 the weight is increased 10 times. Consequently, 9 out of 10 times the photon is terminated, but 1 out of 10 times the photon's weight is increased 10-fold and the photon continues to propagate. The result is that photons are usually terminated, but energy is conserved by the occasional surviving photon being given extra weight. Since the number of photons run is large, the result is a statistically averaged result of absorbed photons which provides an accurate estimation of light distribution in the tissue (Welch 2011). A flow diagram for Monte Carlo calculation for light distribution is as shown in Fig. 2-6.

To calculate the trajectory (direction of propagation) of the propagating photon, two scattering angles are calculated: deflection scattering angle θ and azimuthal scattering angle φ. The commonly used function for the deflection angle is the Henyey-Greenstein (HG) function which was proposed for describing the scattering of light from distant galaxies by galactic dust. The Monte Carlo sampling for the HG function for calculating the deflection angle θ is dependent on the anisotropy factor g of the tissue and is defined as:

$$\cos(\theta) = \frac{1+g^2-\left(\frac{1-g^2}{(1-g+2gx)}\right)^2}{2g} \tag{2-16}$$

where x is a random number between 0 and 1. If g = 1 for a tissue, then cosθ is assumed 0 and the direction of photon propagation doesn't change. Usually the value of g for biological tissues range from 0.8 to 0.9 which denotes that the biological tissue is mostly a forward scattering material. The azimuthal angle is calculated as

$$\varphi = 2\pi x \tag{2-17}$$

where x is a random number between 0 and 1.
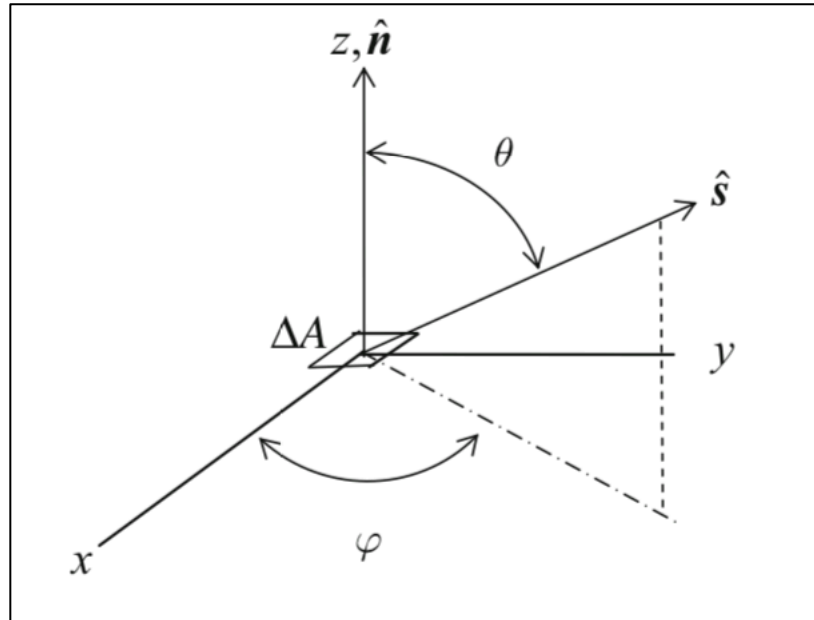
Figure 2-5: Typical scattering geometry

An element of solid angles showing the scattering (θ) and azimuthal angle (φ) is shown.

ΔA represents a different area in the *x-y* plane. Unit vector $\hat{s}$ represents the location of and direction

of radiance *L* (Welch 2011, Pg 31)

Boundary conditions

As the photon moves toward the front surface of the tissue and attempts to cross the boundary to escape the tissue, there is a possibility that the photon will be reflected by the surface boundary where the air/tissue interface (or external medium/tissue interface) presents a mismatch in refractive indices ($n_f = n$ or $n_r = n$, for front and rear boundaries, respectively). The method chosen for handling the boundary is to let a fraction of the photon weight escape the tissue as observable reflectance or transmission and let the remaining fraction of photon weight reflect back into the tissue and continue to propagate.

Figure 2-6: Algorithm to dictate the fate of a photon in a MC simulation

"Hop" refers to the propagation step taken by the photon, "Drop" refers to the reduction in weight by the photon after each event, and "Spin" refers to the change in direction of propagation of the photon after each event (Welch 2000, Pg 116)

Absorbed energy density

Once all the photons are terminated, the total weight A deposited in each pixel is evaluated. This weight is normalized by the volume of the pixel and the number of photons used to find the absorbed fraction for each pixel. The fractional transport $T_{fractional}$ is then calculated by dividing A by the absorption coefficient μ_a of the pixel. Fluence at each pixel is then incident energy Q times $T_{fractional}$.

Temperature rise

Laser light absorbed by the tissue as a result of irradiation results is converted to heat. This generated by the tissue results in local temperature rise. This temperature rise ΔT is dependent on the local thermal properties of the tissue density ρ, the specific heat c, and the radiant exposure H. For short durations (neglecting any heat transfer, for example, short pulse lasers), the temperature rise at a point z can be estimated as

$$\Delta T(z) = \frac{\mu_a H(z)}{\rho c} \qquad (2\text{-}18)$$

The transfer of heat energy in biological tissues occurs mainly via conduction. In the absence of phase change, some of the heat absorbed by the tissues gives rise to temperature rise in and around the laser irradiated zone. The temperature distribution in the tissue is obtained by solving the Pennes bio-heat transfer equation (BHTE)(Pennes 1948):

$$\rho_{tissue} c_{tissue} \frac{\partial T_{tissue}}{\partial t} = \nabla \cdot (k_{tissue} \nabla T_{tissue}) + Q_L + Q_{met} \qquad (2\text{-}19)$$

where k is the thermal conductivity [W m^{-1} K^{-1}], ρ is density [kg m^{-3}], c is specific heat [J kg^{-1} K^{-1}], Q_{met} is the volumetric metabolic heat generation [W m^{-3}], Q_L is the laser generated heat energy [W m^{-3}], and T_{tissue} is temperature of the tissue [K]. The thermal conductivity of a tissue region is dependent on the chemical composition of the tissue and the state of the system and can undergo changes with temperature and pressure. The boundary conditions at the surface of the tissue exposed to the ambient air is considered convective and the internal boundaries in contact with the surrounding tissue region are considered isothermal (at a constant temperature) typically maintained at the body-core temperature of 37 ºC.

2.1.6 Optical thermal modeling

Modeling of heat transfer in tissues as a result of laser irradiation have been done for the applications of photodynamic therapy (PDT) (Seteikin 2013), retinal applications (Sun 2011), skin treatments (Humphries 2013), hyperthermia applications and tumor ablation (Feng 2009). In all these applications, a version of the Pennes' bio-heat equation is used since conduction is the primary method by which heat travels through biological tissues. Other heat transfer models may also include heat transfer through convection, blood perfusion, radiation or evaporation. Efforts have been made to combine Monte Carlo light transport models with heat transfer models. Jaunich et al. (Jaunich 2008) modeled and experimentally validated temperature rise in human and mouse skin tissues as a result fo short pulse irradiation of two different infrared wavelengths (1064 nm, 1552 nm). Fanjul-Velez and Arce-Diego (Fanjul-Vélez 2008) monitored temperature rise in vocal cord tissue during endoscopic thermotherapy at 1064 nm. Gould et al. developed a three-dimensional, transient, optical thermal model for measuring temperature rise due to pulse laser trains at 800 and 1064 nm (Gould 2014). The list provided above is by no means an exhaustive list and provides a helpful direction for curious readers. An excellent review of various models and applications of bio-heat transfer equation can be found here (Diller 2010).

2.1.7 SESE model

We have used SESE (Scalable Effects Simulation Environment) developed at the Air Force Research Laboratory at San Antonio, TX (Bixler 2015, Walsh 2017) for calculating photon distribution and temperature rise due to laser irradiation. A time-independent Monte Carlo propagation technique is used, where 100,000 (or more) photons are randomly generated across the source plane are launched into the tissue underneath. Absorptive and isotropic scattering events are implemented to simulate the path of photons upon propagation into the tissue. To accomplish

the simulation, a finite-difference explicit/implicit RBSOR (Red-Black Series Over-Relaxation) method in SESE is used to solve the heat equation. First, the rays are propagated through the tissue and the resultant dose per voxel is set as the irradiation source term $S(r, \hat{s})$ (Eq. 2.13). Then a surface explicit heat solver method, incorporating a time-step bisection method, is used to calculate an initial surface voxel temperature profile. This is then used as a starting point for the subsequent body voxel temperature solver method, an implicit RBSOR method.

2.2 Experimental validation of modeling conclusions using *Aplysia californica*

While computational modeling studies can provide insights into the change in the macroscopic and microscopic parameters governing infrared nerve inhibition, experimental results are required to provide validity to the predictions derived by the modeling studies. For our studies, we have chosen *Aplysia californica* (sea slug) as our model organism to experiment upon. *Aplysia* serves as excellent model system in our studies because (a) since it consists solely of unmyelinated axons of different diameters, thereby enabling research on unmyelinated C fibers in humans; (b) we can selectively control large number axons of specific diameter due to large size of neurons; (c) different methods of light delivery can be tried relatively easily since the nerves can be exposed and isolated for long periods of time (Bedini 2011; Musio 1990). The *Aplysia* animal model system has been successful in efforts to reduce variability during optical neural stimulations (Duke 2012), demonstrate optical inhibition (Duke 2013, Lothet 2014). The results from these studies were subsequently used to design and perform experiments in higher level animals (Lothet 2017).
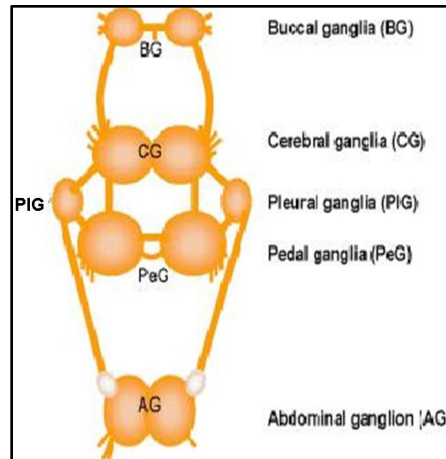
Figure 2-7: Diagram showing the simple and well characterized nervous system in _Aplysia californica_

Source: (Moroz 2011)

2.3   Clinical applications of infrared inhibition

As mentioned, the long-term goal of this research work is the translation of this technology into clinical applications. An important clinical application is inhibition of nerve fibers that transmit chronic pain signals in our body. The long-term goal of this research is to inhibit transmission of pain signals in humans in a way that is free of the side effects of the conventional analgesics and other electrical stimulation methods.

The inhibition of nerve signals using infrared laser light offers an alternative to the conventional pain management techniques. It is reversible, non-contact and free of onset responses. In order to devise a strategy towards the development of this pain management modality using infrared lasers in the form of a nerve cuff, we need to understand the physiology of pain transmission in humans. This will provide us with the limitations and the constraints that

we need to keep in mind when carrying out simulations and trials of our prototypes. This calls for a brief understanding of the physiology of pain in the human body.

Pain is a conspicuous sensory experience that warns of danger. In humans, pain is mediated by different classes of afferent nociceptive (pain sensing) fibers. These fibers respond to damaging stimuli by sending signals to the spinal cord and brain. Thermal or mechanical nociceptors have small diameter, thinly myelinated Aδ fibers that conduct at about 5-30 m/s (http://thebrain.mcgill.ca/flash/d/d_03/d_03_cl/d_03_cl_dou/d_03_cl_dou.html). These fibers provide the sensations of sharp, pricking pain. Polymodal nociceptors transmit sensations of high-intensity mechanical, chemical, and thermal shocks. They have smaller diameters, unmyelinated C fibers and conduct slowly at a speed of around 0.5-2 m/s (Dale 2001). This difference in conduction velocity between the fibers can explain why in the event of an injury, we feel a sharp and acute pain in the beginning followed by a more diffuse, dull pain. A comparison of the fiber sizes of A and C fibers and their conduction rates is shown in Fig. 2-8.
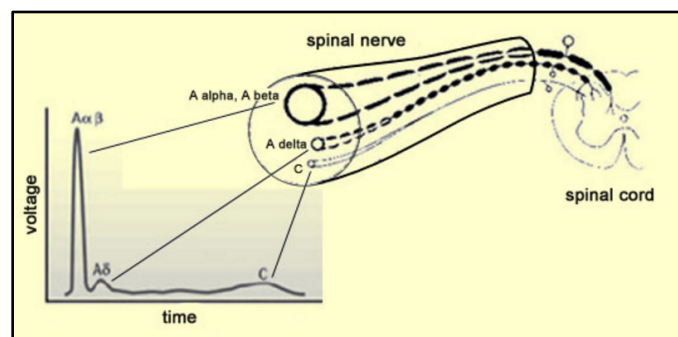
Figure 2-8: Arrangement of the A and C fibers and their rates of conduction

(Source: Bruno Dubuc, McGill University)

Conduction velocity of an action potential is dependent on the axon diameter and the axonal resistivity. Assuming identical membrane resistivities, the conduction velocities only depend on the axon diameter. Larger axons having higher axon diameters conduct action potentials faster than small-diameter axons. C fibers being smaller than A fibers, conduct action potential much slower than A fibers. When unmyelinated C fiber afferents are activated repetitively by electrical stimuli, their conduction latency increases gradually (the conduction velocity of the afferent decreases). In addition, with increasing stimulation frequency, the amount of this activity-dependent slowing increases. C fibers present an important target for nerve inhibition given where the expertise and research with infrared nerve inhibition in unmyelinated nerve stands at this time. A comparison of the different kinds of pain signals carried by Aδ and C fibers is shown in Fig. 2-9.
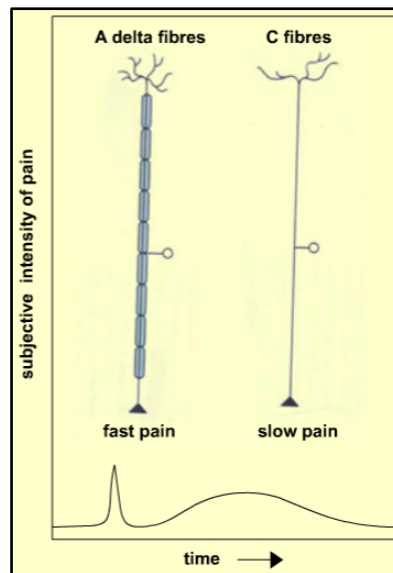
Figure 2-9: Comparison of the pain signals carried by Aδ and C fibers

(Source: Bruno Dubuc, McGill University)

3   THERMAL BLOCK OF ACTION POTENTIALS IS PRIMARILY DUE TO VOLTAGE-DEPENDENT POTASSIUM CURRENTS

3.1   Abstract

Objective: Thermal block of action potential conduction using infrared lasers is a new modality for manipulating neural activity. It could be used for analysis of the nervous system and for therapeutic applications. We sought to understand the mechanisms of thermal block.

Approach: To analyze the mechanisms of thermal block, we studied both the original Hodgkin/Huxley model, and a version modified to more accurately match experimental data on thermal responses in the squid giant axon.

Main results: Both the original and modified models suggested that thermal block, especially at higher temperatures, is primarily due to a *depolarization-activated hyperpolarization* as increased temperature leads to faster activation of voltage-gated potassium ion channels. The minimum length needed to block an axon scaled with the square root of the axon's diameter.

Significance: The results suggest that voltage-dependent potassium ion channels play a major role in thermal block, and that relatively short lengths of axon could be thermally manipulated to selectively block fine, unmyelinated axons, such as C fibers, that carry pain and other sensory information.

A version of this chapter is published as Ganguly, M., Jenkins, M. W., Jansen, E. D., & Chiel, H. J. (2019). Thermal block of action potentials is primarily due to voltage-dependent potassium currents: A modeling study. *J. Neural Eng.*

3.2   Introduction

Targeted optical manipulation of the nervous system has become an exciting new possibility in recent years. Using lasers, it is possible to deliver infrared light to tissue with high spatial and temporal specificity to control excitable tissues such as the sciatic nerve (Wells 2005) , visual cortex (Cayce 2014) cochlear neurons (Matic 2011), and both embryonic and adult hearts (Jenkins 2010, Jenkins 2013). The new field of infrared control of excitable tissue has been recently reviewed (Thompson 2014). Several possible mechanisms have been suggested for IR-induced excitation, including the induction of capacitive currents due to thermal gradients (Plaksin 2018, Shapiro 2012), activation of mitochondrial calcium currents (Dittami 2011), endoplasmic reticulum (Tolstykh 2017), and direct actions on ion channels (Albert 2012).

More recently, it has been shown that infrared laser light can be used to inhibit both action potentials traveling through axons and through cardiomyocytes(Duke 2013, Lothet 2014, 2017, Wang 2016). Rather than inducing a thermal gradient, it appears that the inhibitory mechanism is due to raising tissue temperature (Duke 2013). Thus, understanding the effects of temperature on axonal conduction could be very useful for more precisely designing ways of controlling neural activity.

A recent study demonstrated that IR could selectively block small-diameter axons prior to blocking large-diameter axons, both in an invertebrate (the marine mollusk *Aplysia californica*) and in a mammal (the vagus nerve of the musk shrew *Suncus murinus*) (Lothet 2017). Since electrical stimulation or inhibition generally affect large diameter axons before affecting small diameter axons (Rattay 1986), a modality such as IR that selectively controls small-diameter axons could be the basis for new ways of analyzing neuronal function and could lead to novel therapeutic interventions.

Since IR inhibition was demonstrated in both invertebrate and vertebrate axons, we sought to analyze the potential mechanism of thermal inhibition by using computational models of a well-studied invertebrate model, the squid giant axon (Hodgkin 1952). We chose to focus on the squid giant axon because, to our knowledge, it is the only experimental system in which there is both a detailed, biophysically-based model of action potential generation and propagation, and detailed experimental data about the effects of temperature on detailed characteristics of the action potential (i.e., rates of rise, rates of fall, changes in axial resistance) at the level of a single axon (Rosenthal 2000. Bezanilla 2002).

A mechanism of thermal inhibition had previously been proposed. Initial studies of the effects of temperature on the generation of the action potential (Hodgkin 1949) led Huxley to postulate that, at higher temperatures, potassium currents overwhelm sodium currents, leading to action potential failure (Huxley 1959). Other temperature-dependent changes, however, could account for thermal inhibition. Rosenthal and Bezanilla studied the responses of the giant axon in squid acclimated to seasonally warm or cold temperatures (Bezanilla 2000)and in squid living in temperate or tropical climates (Rosenthal 2002). Their studies suggested that in addition to changes

36

in the kinetics of the voltage-gated ion channels, there may be changes in axial resistance with temperature. Other studies suggested that the sodium/potassium pump (Carpenter 1968) and even the peak conductances of the voltage-gated channels could change with temperature (Cao 2005).

Thus, we sought to test Huxley's hypothesis that activation of voltage-dependent potassium ion channels was primarily responsible for thermal inhibition. In the original Hodgkin Huxley model, the only mechanism by which temperature affected the model was through the temperature-dependence of the gating variables – m and h for the voltage-dependent sodium ion channels, and n for the voltage-dependent potassium ion channels. Would the same mechanism that Huxley had proposed operate in a modified model that more accurately captured the actual experimentally measured responses to temperature, and that incorporated changes in peak ion channel conductances, axial resistance, and the sodium/potassium pump. By addressing this question, we could explore a much broader range of possible models than the original Hodgkin Huxley model. We therefore modified the original model to allow it to more accurately capture the experimental data, and tested whether the original mechanism proposed by Huxley primarily accounted for thermal block. We then sought to determine the effect of scaling of axon diameter to see the applicability of these results to small-diameter unmyelinated axons, such as vertebrate C fibers.

The results do support Huxley's hypothesis that thermally-induced block, especially at higher temperatures, is primarily due to increased activation of voltage-dependent potassium ion channels in response to depolarization. In response to the depolarizing currents from an advancing action potential, the membrane depolarizes. This activates the voltage-dependent potassium ion channels, allowing potassium ions to flow out of the neuron, which in turn hyperpolarizes the neuron. The hyperpolarizing current through these channels antagonizes the depolarizing current

that activated them. Thus, this mechanism effectively and rapidly blocks the propagation of the action potential. Note that a hyperpolarizing current is more effective than simply blocking all the ion channels, since a depolarizing current from an advancing action potential would propagate through the passive region of blocked ion channels, diminishing only as it leaked out through the passive components of the axonal membrane (i.e., the leak channels and the capacitance), rather than being actively antagonized.

3.3   Methods

3.3.1   Model axon geometry

The squid giant axon varies in size, but a standard length of 100 mm and diameter of 0.5 mm (500 µm) was chosen based on values reported in the literature (Rosenthal 2000). This geometry was implemented in the NEURON simulation environment (Carnevale 2005). In general, the differential equations for the model (see below) were numerically integrated using a time step of 0.01 ms, and the voltages and ionic currents were measured in each segment of the model neuron. For studies in which compensatory current was injected to maintain the resting potential (see below), the time step was reduced considerably (to 0.2 µs) to ensure high accuracy.

To ensure stability of all state neurokinetic variables (m,n,h) , the system was simulated for a total of 500 ms, and stimulating current was injected into the model after 250 ms. Depolarizing current (1 ms duration) was injected within the first segment of the first section of the model axons to initiate an action potential. For model axons of diameter greater than 10µm, 2000 nA of depolarizing current was used. For model axons of diameter less than 10µm, 100 nA of depolarizing current was used.

To explore how axon diameter affects its response to temperature, we varied axon diameters from 0.5 μm to 500 μm. The axon was divided into either two or three sections, each having different lengths and properties, i.e., temperature, resistivity, and ionic conductances (as described below). The number of segments within each section was chosen to allow for precise measurements of threshold block lengths over the entire length of the model axon. In the modified Hodgkin/Huxley model, the axial resistances varied with temperature. Thus, to construct regions of different temperature, we used the built-in NEURON function *connect* to ensure that each region had the appropriate axial resistance for its temperature.

Segmental currents over the j different segments (where j ranged from 1 to the total number of segments) were computed as

$$I_{segment}(j) = \frac{V_{j-1} - V_j}{r_{a,j-1,j}} - \frac{V_j - V_{j+1}}{r_{a,j,j+1}}, \tag{3-1}$$

where V_{j-1} corresponded to the voltage of the previous segment (if there was a previous segment), V_{j+1} corresponded to the voltage of the next segment (if there was a next segment), $r_{a,j-1,j}$ corresponded to the axial resistance between compartment $j-1$ and j, and $r_{a,j,j+1}$ corresponded to the axial resistance between compartment j and $j + 1$. Note that $r_a = \frac{R_a}{\pi d^2/4} * L$, where r_a is the axial resistance, R_a is the axial resistivity (in Ω cm), L is the length of the segment in μm, d is the axon diameter (in μm), and r_a's units of Ω-cm μm/μm^2 yield $10^4\Omega$. Multiplying this by 10^{-2} makes it possible to report the resistance in MΩ.

3.3.2 Simulating changing temperature in the model

Temperature changes were applied to the model neurons in two ways. First, to determine the changes in currents that occur as an action potential encounters a change in temperature, we maintained one half of a model axon at the base temperature of 6.3˚C while varying the temperature of the second half of the axon. For these studies, the model axon consisted of two sections. By increasing the temperature of half of the axon (the second section), we ensured that transient currents induced by the initiation of an action potential, which occur at the beginning of the first section, were minimized. In the NEURON simulation environment, temperature is a global variable that is uniformly applied to every segment. Temperature was changed to be a local variable so that it could be accessed and modified at each segment independently. Ordinarily, NEURON uses the TABLE command in the .mod file to access a look-up table for all segments; by commenting out this command in the .mod file, the NEURON program evaluated the differential equations at every segment, rather than using the default parameters in the lookup table to decrease run time. This usually increased the simulation duration by a factor of about five.

To approximate a continuously changing temperature profile that might be induced by a thermal source such as a laser, temperature profile *T(x)* was calculated, that interpolated smoothly between an initial temperature T_1 (6.3˚C) and a final temperature T_2 (25˚C) at all points *x* along the axon, such that the temperature began to change from its initial value T_1 at location *a* along the axon (10 mm before the midpoint, or 40 mm from the beginning of the axon) and reached temperature value T_2 at location *b* along the axon (10 mm after the midpoint, or 60 mm after the beginning of the axon). The temperature reached an intermediate temperature value of *(T_2 + T_1)/2* at the midpoint between points *a* and *b*, i.e., at *(a + b)/2*:

$$T(x) = T_1 + (T_2 - T_1)F(x, a, b),\tag{3-2}$$

$$F(x, a, b) = \begin{cases} 0, & x \leq a, \\ 2\left(\frac{x-a}{b-a}\right)^2, & a < x \leq \frac{(a+b)}{2}, \\ 1 - 2\left(\frac{x-b}{b-a}\right)^2, & \frac{(a+b)}{2} < x \leq b \\ 1, & x \geq b. \end{cases}\tag{3-3}$$

Second, temperature change was applied along the central region of a model axon to determine the minimum length of elevated temperature that could block action potential conduction. The axon was modeled using three sections, and the length of the central section that was subjected to elevated temperatures was systematically varied until the action potential no longer propagated beyond the region of block. We classified an action potential as blocked if the potential at the end of the axon never exceeded -60 mV, which is far below the threshold for initiating an action potential. Note that the resting potential of the model is -65 mV, so that this is a fairly conservative criterion.

3.3.3   Temperature-dependent parameters and functions

To capture the response of the neuron to changing temperatures, several features of the original Hodgkin/Huxley model became functions of temperature: (1) a temperature-varying Q_{10} factor for the gating variables of the Hodgkin/Huxley model based on the experimental measurements of Rosenthal and Bezanilla (2000), (2) the peak potassium and sodium conductances varied with temperature, (3) a temperature-dependent sodium/potassium pump, and (4) the axial resistance as a function of temperature (a schematic comparing the original and modified Hodgkin/Huxley model is shown in Fig. 3-2A). After describing the detailed

modifications that were made to the model, the entire set of equations is shown (below, Model Equations).

(1) The Q_{10} factor: In the standard Hodgkin and Huxley model (Hodgkin 1952), temperature dependence is captured by altering the rate constants for the three gates controlling the voltage gated ion channels. The m gate (sodium activation), the h gate (sodium inactivation) and the n gate (potassium activation) are modified to account for changes in temperature. The corresponding modified rate constants are α_m and β_m for the m gate, α_h and β_h for the h gate, and α_n and β_n for the n gate. The values are changed by using the Q_{10} relationship, which is

$$Q_{10} = \left(\frac{R_2}{R_1}\right)^{\frac{10}{(T_2 - T_1)}}. \qquad \text{(3-4)}$$

where temperature T_2 is greater than temperature T_1, rate R_2 is measured at T_2, and rate R_1 is measured at T_1. If both sides of the equation are raised to the power $\frac{T_2 - T_1}{10}$, it is possible to solve directly for R_2 at temperature T_2 as

$$R_2 = R_1 Q_{10}^{\frac{T_2 - T_1}{10}}. \qquad \text{(3-5)}$$

Thus, for example, to modify the differential equation for the n gate (see below, Model Equations), since rate constants α_n and β_n are multiplied by the same factor to adjust them for temperature, the right-hand side of the entire differential equation for n is multiplied by the Q_{10} term of equation (5). The same factor is used to modify the right-hand sides of the differential equations for the m and h gates. In the original Hodgkin and Huxley model, a fixed value of 3 was used for Q_{10} for all temperature ranges, and the base temperature (T_1) was set at 6.3°C (Hodgkin 1952). Thus, the

factor by which all the differential equations for gates *m*, *n* and *h* were multiplied simplified to

$$3^{\frac{T_2 - 6.3}{10}}.$$

An earlier study of the change in the shape of the action potential (Hodgkin 1949, their Table 2) showed that the Q_{10} for the rates of fall (illustrated in their Figure 1B), an approximate measure of the activity of the voltage-dependent potassium gates, changed in the temperature ranges 5˚C to 10˚C, 10˚C to 20˚C, and 20˚C to 30˚C. They also observed changes in the Q_{10} for the rate of rise with temperature, though these changes were smaller. These data suggested that the Q_{10} factors multiplying the differential equations for *m*, *n* and *h* were different and varied with temperature. We therefore used a systematic grid search to simultaneously find sets of Q_{10} values for all three gates, varying them from a value of 1.0 (temperature independent) to 3.0 (the original Hodgkin/Huxley model value) in increments of 0.1. Values that did not allow the model to generate an action potential were excluded. For those values that did generate an action potential, the total amplitude of the action potential (measured from the resting potential to the peak of the action potential) was determined, by comparing these values to the amplitudes actually determined experimentally at that temperature (Hodgkin 1949, their Table 1 [c], p. 243). Among those sets of Q_{10} values producing total amplitudes within 5% of those measured experimentally, errors for maximum rates of rise and fall of the resulting action potentials were evaluated (see below, equations (3-11) – (3-13)), choosing the Q_{10} values that led to the smallest errors (Fig. 3-9).

As a result of the systematic and exhaustive search, the multiplicative factor was found to be slightly different for each gate, and will be designated as $\phi_m(T)$, $\phi_h(T)$ and $\phi_n(T)$ for the *m*, *h* and *n* gates (respectively). Each of these are piecewise continuous functions:

$$\phi_m(T) = \begin{cases} 3^{\frac{T-6.3}{10}}, & 5°C \leq T \leq 10°C, \\ 3^{\frac{10-6.3}{10}} 3^{\frac{T-10}{10}}, & 10°C < T \leq 15°C, \\ 3^{\frac{10-6.3}{10}} 3^{\frac{15-10}{10}} 2.8^{\frac{T-15}{10}}, & 15°C < T \leq 20°C \\ 3^{\frac{10-6.3}{10}} 3^{\frac{15-10}{10}} 2.8^{\frac{20-15}{10}} 2.7^{\frac{T-20}{10}}, & 20°C < T \leq 25°C \end{cases} \tag{3-6a}$$

$$\phi_h(T) = \begin{cases} 3^{\frac{T-6.3}{10}}, & 5°C \leq T \leq 10°C, \\ 3^{\frac{10-6.3}{10}} 2.9^{\frac{T-10}{10}}, & 10°C < T \leq 15°C, \\ 3^{\frac{10-6.3}{10}} 2.9^{\frac{15-10}{10}} 3^{\frac{T-15}{10}}, & 15°C < T \leq 20°C \\ 3^{\frac{10-6.3}{10}} 2.9^{\frac{15-10}{10}} 3^{\frac{20-15}{10}} 3^{\frac{T-20}{10}}, & 20°C < T \leq 25°C \end{cases} \tag{3-6b}$$

$$\phi_n(T) = \begin{cases} 3^{\frac{T-6.3}{10}}, & 5°C \leq T \leq 10°C, \\ 3^{\frac{10-6.3}{10}} 2.8^{\frac{T-10}{10}}, & 10°C < T \leq 15°C, \\ 3^{\frac{10-6.3}{10}} 2.8^{\frac{15-10}{10}} 2.4^{\frac{T-15}{10}}, & 15°C < T \leq 20°C \\ 3^{\frac{10-6.3}{10}} 2.8^{\frac{15-10}{10}} 2.4^{\frac{20-15}{10}} 2.3^{\frac{T-20}{10}}, & 20°C < T \leq 25°C \end{cases} \tag{3-6c}$$

(2) <u>Sodium-potassium pump</u>: In the original Hodgkin and Huxley model, the sodium/potassium pump was not incorporated, because their initial studies suggested that the resting membrane potential was unchanged by temperature (Hodgkin 1952). In the studies of Rosenthal and Bezanilla (2000) in *Loglio pealei*, however, the resting potential varied with temperature and season, suggesting that components of the resting potential were temperature dependent. Studies in other molluscan species, such as *Aplysia californica* (Carpenter 1968) and *Anisodoris nobilis* (Gorman 1970), demonstrated that a temperature-dependent sodium-potassium pump significantly contributed to changes in the resting potential with temperature. (Rakowski 1989) characterized an electrogenic sodium-potassium pump in the squid giant axon that exchanged 3 sodium ions for 2 potassium ions. Equations of (Van Egeraat 1993) for the pump currents were used, based on the study of Rakowski et al. (Rakowski 1989), and incorporated

temperature-dependence based on the studies in *Anisodoris* (Gorman 1970). The Q_{10} for the pump conductance from its change in permeability ratio of P_{Na}/P_K from 0.028 at 4°C to 0.0068 at 18°C was used (Gorman 1970), yielding an estimated Q_{10} of 1.88 (using equation (3-1)), which was then used to scale the peak pump conductance, $g_{NaKinitial}$. Given that the pump exchanges three sodium ions for two potassium ions, the pump equations are:

$$g_{NaK}(T) = g_{NaKinitial}\ 1.88^{\frac{(T-6.3)}{10}},$$

$$I_{Na\_pump} = 3\ g_{NaK}(T)(V_m - E_{pump}),$$

$$I_{K\_pump} = -2\ g_{NaK}(T)(V_m - E_{pump}),\qquad\qquad(3\text{-}7)$$

where I_{Na_pump} and I_{K_pump} are the sodium and potassium currents due to the pump, respectively, V_m is the membrane potential, and E_{pump} is the reversal potential of the pump.

(3) <u>Peak sodium and potassium conductances</u>: In the original Hodgkin and Huxley model, the peak sodium and potassium conductances, $\bar{g}_{Na}$ and $\bar{g}_K$, were assumed to be constant and independent of temperature. As reviewed above, more recent work suggests that these values may vary with temperature.

To estimate the peak conductance values, rates of rise and rates of fall were extracted from Figure 3 of Rosenthal & Bezanilla (Rosenthal 2000) using the program DataThief (www.datathief.org). The center of the triangle indicating the mean data value was extracted as well as the values of the top and bottom error bars to provide a measure of the errors associated with each data point. In the model, the peak of the derivative of the rising phase was used as an

estimate of the peak rate of rise, and the peak of the derivative of the falling phase was used as an estimate of the peak rate of fall (Fig. 3-1B).

A systematic grid search was used to determine the peak sodium and potassium conductance values that minimized the difference between the rates of rise and fall observed experimentally (Rosenthal 2000) and those observed in the model (see below for details of how errors were minimized; Fig. 3-1C). The data at each of the temperatures reported by Rosenthal & Bezanilla were then fit by exponentials:

$$g_{Kmax}(T) = 1.60\, e^{-\left(\frac{T-27.88}{12.85}\right)^2},$$

$$g_{Namax}(T) = 0.42\, e^{-\left(\frac{T-31.83}{31.62}\right)^2}, \qquad\qquad (3\text{-}8)$$

where the maximum potassium and sodium conductances, g_{Kmax} and g_{Namax}, have units of S/cm^2 (Fig. 3-1D shows plots of these functions).

(4) <u>Axial resistance</u>: Earlier work showed that the product of the axial resistance and the membrane capacitance could be estimated by the time constant of the rise of the foot of the action potential and its conduction velocity (Brown 1976). In this study, the "foot" was defined as the region of the simulated action potential between the time points when the action potential begins (i.e., the time that the potential increased by 1% above the resting membrane potential; another 0.1 ms of data prior to this (100 points) was added to improve the exponential fit) and halfway between this point of onset and the point at which the derivative of the action potential reached its maximum value (Fig. 3-1B, region indicated by the blue line). The resulting data was fit to an exponential,

whose time constant, τ_{foot}, was then used for estimating the axial resistance (see below). The time constant of the model action potential shown in Fig. 3-1B was 179.9 µs.

Conduction velocity was calculated as a function of temperature by measuring the time it took the action potential to travel between two points along the axon separated by 8 mm on either side of the midpoint of the axon. For all conduction velocity studies, the model axon was brought to the same uniform temperature along its entire length. The time of arrival of the action potential was determined as the instant when the action potential reached half its maximum value at a specific point on the axon. Conduction velocity was then calculated by dividing the distance between the two points on the axon by the time it took the action potential to travel between the points.

Having measured the time constant, τ_{foot}, and the conduction velocity, θ, from the model, we then determined the product of the membrane capacitance per unit area (C_m, in µF/cm^2) and the axial resistivity (R_a, kΩ cm) from the equation

$$R_a C_m = \frac{r}{2\tau_{foot}\theta^2} \tag{3-9}$$

where r is the radius of the axon (Jack 1975, pp. 116 – 118). To derive this equation, it is assumed that the conduction velocity of the action potential is large relative to the electrotonic velocity, i.e., the passive propagation of signals along the axon; in addition, it is assumed that the extracellular resistance is negligible relative to the axial resistance.

To illustrate the computation for a specific example: at 5˚C, the time constant of the foot of the simulated action potential, τ_{foot}, was 179.9 µs (Fig. 3-1B); the conduction velocity of that action potential, θ, was 11.3 m/sec. The simulated axon diameter is 500 µm, so that its radius is 250 µm. The resultant value of $R_a C_m$ is $\frac{250\ 10^{-6} meters}{2(179.9\ 10^{-6}\ seconds)(11.3\ meters/second)^2}$, which equals 0.0054 s/m or 0.0054 Ω Farads/m. This value is similar to the value shown in Figure 5B of (Rosenthal 2000) for axons at 5˚C from squid acclimatized to the cooler temperature of May (Please note that the units shown in their figure 5, ΩFarads cm, do not appear to be correct, based on our email and Skype conversations with the authors). Rosenthal and Bezanilla also determined experimentally that the capacitance of the membrane did not vary significantly from 1 µF/cm^2 in both warm and cold seasons. Thus, the equation for the axial resistance, $R_a(T)$, in Ω cm, as a function of temperature (in ˚C; the coefficient of determination R^2 for the fit is 0.94) is

$$R_a(T) = 56.84\ e^{-0.03\ T} \qquad\qquad (3\text{-}10)$$

3.3.4   Error analysis for average model parameters

To fit parameters to the actual data, the squared deviations were minimized between model measurements for a given set of parameter values and the original data for the rates of rise and fall at each temperature. To capture changes both in the rate of rise and the rate of fall, a systematic grid search was used, varying the peak potassium and sodium conductances from their initial values in the Hodgkin/Huxley model in increments of 0.02 S/cm^2, and testing for two failure conditions: (1) spontaneous activity in the absence of any excitatory input, which indicated that the potassium conductance was too small to maintain a stable resting potential, and (2) failure to

generate an action potential in response to excitatory current, indicating that the potassium conductance was large enough to overwhelm the inward sodium current.

The peak rate of fall was determined in the model action potential by finding the maximum of the derivative of the falling phase (Fig. 3-1B). The error in the rate of fall was computed using equation (3-11):

$$E_{fall}\ (T_i) = \left| \frac{F_{exp}(T_i) - F_{est}(T_i)}{F_{exp}(T_i)} \right|, \qquad (3\text{-}11)$$

where $E_{fall}\ (T_i)$ is the error at temperature T_i during the falling phase of the action potential, $F_{exp}(T_i)$ is the rate of fall measured experimentally at temperature T_i, and $F_{est}(T_i)$ is the estimated rate of fall from the model at temperature T_i.

The error in the experimentally measured rate of rise and that produced by the model was also computed. The peak rate of rise was determined from the derivative of the rising phase of the model action potential (Fig. 3-1B). Errors in the rate of rise were computed using equation (3-12):

$$E_{rise}\ (T_i) = \left| \frac{R_{exp}(T_i) - R_{est}(T_i)}{R_{exp}(T_i)} \right|, \qquad (3\text{-}12)$$

where $E_{rise}\ (T_i)$ is the error at temperature T_i in the rising phase, $R_{exp}(T_i)$ is the rate of rise measured experimentally at temperature T_i, and $R_{est}(T_i)$ is the estimated rate of rise from the model at temperature T_i.

Total error was then computed by summing the squares of the errors at each temperature over the entire set of temperatures that were matched, which were 5˚C, 7.5˚C, 10˚C, 12.5˚C, 15˚C, 17.5˚C, 20˚C, and 25˚C (based on the measurements of Rosenthal and Bezanilla (Rosenthal 2000)). Thus, the final computed error was

$$E_{total} = \sum_{all\ T_i} \left(\frac{R_{exp}(T_i) - R_{est}(T_i)}{R_{exp}(T_i)} \right)^2 + \sum_{all\ T_i} \left(\frac{F_{exp}(T_i) - F_{est}(T_i)}{F_{exp}(T_i)} \right)^2. \qquad (3\text{-}13)$$

The total error is plotted on a logarithmic scale (Fig. 3-1E) for several variations of the model. The results demonstrate that if only the sodium/potassium pump is temperature dependent (Fig. 3-1E, second set of bars), or if only the peak sodium and potassium conductances are varied as a function of temperature (Fig. 3-1E, third set of bars), error is not reduced as much as if both features of the model vary with temperature (Fig. 3-1 E, fourth set of bars). Since Rosenthal and Bezanilla (Rosenthal 2002) observed that at 29.5˚C the action potential in *Loligo pealei* was blocked, this information was used to determine the value for g_{Kmax} at this temperature.

Similar optimization was performed for the temperature dependence of the axial resistivity. The simulations were initialized with the standard Hodgkin/Huxley model value of membrane resistivity of 35.4 Ω-cm and the conduction velocity at a given temperature T_i was evaluated as described above. The resultant conduction velocity was compared with the published results, and membrane resistivity was changed until the modeled conduction velocity was within 1% of the experimentally published values. No other parameters were varied to adjust the conduction velocity.

3.3.5 Accounting for experimental error

In the original experimental data (Rosenthal 2000), measurements of the rates of rise and fall had accompanying error bars. Not only the mean values shown in the data plots were measured, but also the values of the error bars were measured, and those values were propagated through the model. This provides some estimate of the errors of the parameters, which are the maximum sodium and potassium conductances, the axial resistivity, and the product of $R_a C_m$. Fig. 3-1F illustrates this for one parameter at one temperature (17.5˚C): the range of measured values for the rates of fall are shown along the x axis; the function relating the rate of fall to the peak potassium conductance is plotted, and the corresponding range in the peak potassium conductance parameter is indicated along the y axis. The arrow points to the measured mean value of the parameter.

3.3.6 Model equations

These are the model equations that were used in each segment of the NEURON model:

$$C_m \frac{dV_m}{dt} = -g_L(V_m - E_L) - g_{Kmax}(T)n^4(V_m - E_K) - g_{Namax}(T)m^3h(V_m - E_{Na}) - I_{Na_{pump}} - I_{K_{pump}} + I_{segment},$$

$$\frac{dm}{dt} = \phi_m(T)(\alpha_m(1 - m) - \beta_m m),$$

$$\frac{dh}{dt} = \phi_h(T)(\alpha_h(1 - h) - \beta_h h),$$

$$\frac{dn}{dt} = \phi_n(T)(\alpha_n(1 - n) - \beta_n n),$$

51

$$\alpha_n(V) = \frac{-0.01(V+55)}{\left(e^{\frac{-(V+55)}{10}}-1\right)}$$

$$\beta_n(V) = 0.125\left(e^{\frac{-(V+65)}{80}}\right)$$

$$\alpha_m(V) = \frac{-0.1\ (V+40)}{\left(e^{\frac{-(V+40)}{10}}-1\right)}$$

$$\beta_m(V) = 4\left(e^{\frac{-(V+65)}{18}}\right)$$

$$\alpha_h(V) = 0.07\left(e^{\frac{-(V+65)}{20}}\right)$$

$$\beta_m(V) = \frac{1}{\left(e^{\frac{-(V+35)}{10}}+1\right)}$$

$$g_{Kmax}(T) = 1.60\ e^{-\left(\frac{T-27.88}{12.85}\right)^2},$$

$$g_{Namax}(T) = 0.42\ e^{-\left(\frac{T-31.83}{31.62}\right)^2}$$

$$g_{NaK}(T) = g_{NaKinitial}\ 2^{\frac{(T-6.3)}{10}}$$

$$I_{Napump} = 3\, g_{NaK}(T)\big(V_m - E_{pump}\big)$$

$$I_{Kpump} = -2\, g_{NaK}(T)(V_m - E_{pump})$$

$$I_{segment} = \frac{V_{j-1} - V_j}{r_{a,j-1,j}} - \frac{V_j - V_{j+1}}{r_{a,j,j+1}}$$

$$\phi_m(T) = \begin{cases} 3^{\frac{T-6.3}{10}}, & 5°C \le T \le 10°C, \\ 3^{\frac{10-6.3}{10}}\, 3^{\frac{T-10}{10}}, & 10°C < T \le 15°C, \\ 3^{\frac{10-6.3}{10}}\, 3^{\frac{15-10}{10}}\, 2.8^{\frac{T-15}{10}}, & 15°C < T \le 20°C \\ 3^{\frac{10-6.3}{10}}\, 3^{\frac{15-10}{10}}\, 2.8^{\frac{20-15}{10}}\, 2.7^{\frac{T-20}{10}}, & 20°C < T \le 25°C \end{cases}$$

$$\phi_h(T) = \begin{cases} 3^{\frac{T-6.3}{10}}, & 5°C \le T \le 10°C, \\ 3^{\frac{10-6.3}{10}}\, 2.9^{\frac{T-10}{10}}, & 10°C < T \le 15°C, \\ 3^{\frac{10-6.3}{10}}\, 2.9^{\frac{15-10}{10}}\, 3^{\frac{T-15}{10}}, & 15°C < T \le 20°C \\ 3^{\frac{10-6.3}{10}}\, 2.9^{\frac{15-10}{10}}\, 3^{\frac{20-15}{10}}\, 3^{\frac{T-20}{10}}, & 20°C < T \le 25°C \end{cases}$$

$$\phi_n(T) = \begin{cases} 3^{\frac{T-6.3}{10}}, & 5°C \le T \le 10°C, \\ 3^{\frac{10-6.3}{10}}\, 2.8^{\frac{T-10}{10}}, & 10°C < T \le 15°C, \\ 3^{\frac{10-6.3}{10}}\, 2.8^{\frac{15-10}{10}}\, 2.4^{\frac{T-15}{10}}, & 15°C < T \le 20°C \\ 3^{\frac{10-6.3}{10}}\, 2.8^{\frac{15-10}{10}}\, 2.4^{\frac{20-15}{10}}\, 2.3^{\frac{T-20}{10}}, & 20°C < T \le 25°C \end{cases}$$

$$R_a(T) = 56.84\, e^{-0.03\,T}$$

$$r_a(T) = \frac{R_a(T)}{\pi r^2/4}$$

3.3.7 Fixed parameter values

Parameter	Symbol	Value (units)
Leak conductance	g_L	0.3 mS/cm^2
Membrane capacitance	C_m	1 µF/cm^2
Maximum pump conductance	g_{NaK}	7 µS/cm^2
Pump reversal potential	E_{pump}	-220 mV
Squid giant axon radius	r	0.25 mm
Leak reversal potential	E_L	-51 mV
Potassium ion Nernst potential	E_K	-74 mV
Sodium ion Nernst potential	E_{Na}	53 mV

3-1: Summary of constant parameters used in NEURON

3.3.8 Code availability

The simulation environment NEURON was scripted using Python to search for parameter values while minimizing errors, as described above. The Python package "numpy" was used for numerical analysis, and the package "matplotlib" was used for plotting data. Fits of data to curves were done using MATLAB's Curve Fitting toolbox. All code used in the modeling and optimization for this chapter are available for download under the appropriate licenses from the GitHub repository: (https://github.com/mohitganguly/IRBlock_Vanderbilt).

3.3.9 Compensatory current

To test the role of voltage-dependent ion channels on thermal block, the conductances of all or some of the channels were set to zero, similar to experimental manipulations such as applying the drug TTX to block voltage-dependent sodium ion channels, or the drug TEA to block voltage-dependent potassium ion channels (Prinz 2004). Doing so has a significant side effect: the resting membrane potential changes, as it depends in part on the currents through the voltage-dependent ion channels. Thus, to separate the effects of removing ion channels from the resulting changes in resting membrane potential, we used compensatory current, which is based on the concept of dynamic clamp to restore the membrane potential to its original resting potential. Conceptually, the idea is simple: one can computationally "remove" a particular ionic current by computing the value of current that should be generated through that ion channel, and then inject the opposite amount of current; a similar approach can be used to computationally "add" a particular ionic current.

To show a specific example of how this was done, in Fig. 3-6A, the schematic lower axon has a central section whose peak potassium conductance, g_{Kmax}, is set to zero (indicated by the orange rectangle). The schematic lower axon has its potassium channel conductances set to zero in the central region (indicated by the red rectangle). Into each segment of the central region in the lower axon, a compensatory current clamp is inserted (using a new NEURON function, specifically written for this purpose, kd.mod). For each of the segments in this central section, corresponding to the identical segment in the axon above it, the program determines the current of the upper axon, $I_K (x, t)$, at that location over time, and injects the negative of this current into that segment of the lower axon, I_{clamp}. The injected current negates the current change due to the absent

ion channels in the lower axon. Thus, the compensatory current clamp restores the lower axon to

its original resting potential despite the absence of the potassium ion channels.

To provide an objective measure of the discrepancy between the original values and those

in the axon receiving compensatory current, the mean square error was computed between the peak

voltage changes along the control axon as compared to the peak voltage changes along the axon

whose central region was subjected to compensatory current. Fig. 3-6B is a plot of the mean square

error as the step size for the compensatory current is varied, demonstrating the importance of using

a very small step size to keep the error low because of the high conduction velocity of the squid

giant axon.
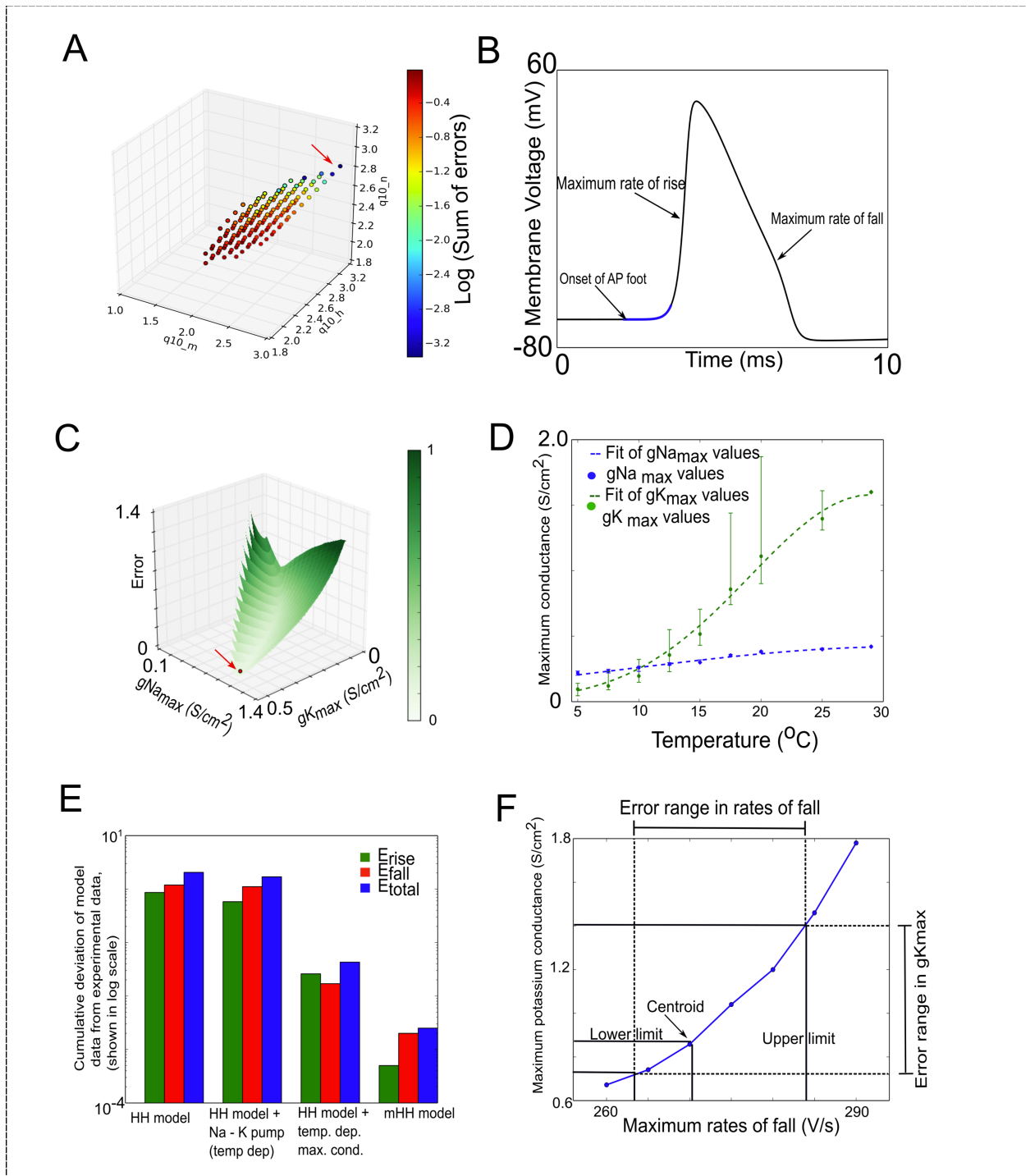
Figure 3-1: Temperature-dependent modifications of the original Hodgkin Huxley model

A. To find the valid set of Q_{10} values for all three gates (m, n, h), we performed an exhaustive three-dimensional grid search to arrive at the correct Q_{10} parameter. At a specific temperature, the Q_{10} values for each gate (m, n, and h) were systematically varied from 1.0 (gates not temperature dependent) to 3.0 (the value in the Hodgkin/Huxley model) in increments of 0.1, totaling 20*20*20 = 8,000 cases. In each of these cases, the total amplitude of the action potential was evaluated, if

57

an action potential was generated. We defined the total amplitude as the absolute difference between the resting potential and the peak of the action potential. These total amplitudes were then compared against the experimentally reported values obtained at that specific temperature (Hodgkin and Katz, 1949). We focused on the set of Q_{10} values that produced action potentials whose total amplitudes were within 5% of the reported values. Among the selected sets of values, we evaluated the errors for maximum rates of rise and fall, using equations (3-11) – (3-13). The combined errors for rates of rise and fall of action potentials are plotted. The Q_{10} values for each of the gates are shown along the three axes. Each dot in the figure represents a set of Q_{10} values that produce an action potential whose peak amplitude is within 5% of the experimentally reported values. The color of each dot represents the sum of the errors for the particular set of Q_{10} values. The range of error values are shown by the adjoining color bar (using a logarithmic scale). As the color of the dot changes from red to blue, the error decreases. The Q_{10} values associated with the least error (shown with a red arrow) were chosen for the particular temperatures. The figure shows the analysis for 5˚C. Similar analyses were done for 10˚C, 15˚C, 20˚C and 25˚C. **B**. Measurements from the model action potential that were compared to the data of Rosenthal & Bezanilla (2000). The model action potential shown here was generated by the modified Hodgkin/Huxley model at 5˚C. The maximum rate of rise, the maximum rate of fall, and the onset of the foot of the action potential are all indicated. See Methods section for how these were used for parameter estimation. **C**. To find the sodium and potassium maximum conductance that fit the maximum rates of rise and fall of action potential recorded experimentally, we performed an exhaustive grid search by varying the maximum sodium conductance from 0.12 S/cm^2 (original value in the Hodgkin/Huxley model) to 0.5 S/cm^2, and the potassium maximum conductance from 0.036 S/cm^2 (original value in the Hodgkin/Huxley model) to 1.5 S/cm^2, in increments of 0.02 S/cm^2. Errors were calculated at each point of these values. The expression used to calculate the errors between the experimentally reported maximum rates and the simulation-derived rates are described in equations (3-11) – (3-13) in the Methods. For a particular pair of maximum sodium and maximum potassium conductances, the sum of the errors observed for the maximum rates of rise and maximum rates of fall are plotted (plot shows the results obtained from searches at 25˚C). The sum of the errors smoothly decreases as the sodium and potassium conductance increase without any local minima or maxima. At points with low values of sodium maximum conductance and high values of potassium conductance, an action potential was not generated, and hence the errors for those value pairs are not shown in the plot. The red arrow shows the point where the sum of the errors reached the global minimum. We used the sodium and potassium conductance obtained at this point as the basis for the peak sodium and potassium conductances in the modified Hodgkin/Huxley model. This analysis was repeated for all the temperatures reported in the experimentally published work, which ranged from 5˚C to 25˚C. **D**. Variation of the peak sodium (blue) and potassium (green) conductances with temperature (equation (3-8)). The R^2 value for the Gaussian fits is > 0.99. See the text for details. **E**. Errors in rates of rise (E_{rise}, green), rates of fall (E_{fall}, red) and total error (E_{total}, blue) plotted on a logarithmic scale for three versions of the model (equations (3-11) - (3-13)). The errors associated with the unmodified Hodgkin/Huxley model are shown in the left-most group of bars; the errors associated with the Hodgkin/Huxley model to which a temperature-dependent Na/K pump were added are shown in the next group of bars; the errors associated with the Hodgkin/Huxley model and temperature-varying peak conductances are shown in the next group of bars, and the errors associated with the Hodgkin/Huxley model which has both a temperature-dependent sodium-potassium pump and the modified peak conductances are shown in the right-most bars (we refer to this as the modified Hodgkin/Huxley model, or the

mHH model). The mHH has the smallest errors. **F**. Translating errors in the original data (rate of fall at 17.5˚C) into error ranges for the estimated model parameters. See Methods for details.

3.3.10 Incorporating temperature dependence improves model accuracy

Incorporating temperature-dependence into the peak sodium and potassium conductances, the sodium/potassium pump, and the axial resistance led to model outputs that more closely matched experimental observations in squid giant axons (Rosenthal 2000) than those predicted by the original Hodgkin/Huxley model. Modified model predictions of the influence of temperature on rates of action potential rise and fall (Fig. 3-2B), axial resistance multiplied by membrane capacitance (Fig. 3-2C), and conduction velocity (Fig. 3-2D) better matched the experimental results than those predicted by the original Hodgkin/Huxley model.

A

Na$^+$ channel   K$^+$ channel   Na - K pump   Axial Resistivity

	gNa$_{max}$	Q$_{10}$ m,h	gK$_{max}$	Q$_{10}$ n	gpump	ρ
HH	Constant	Constant	Constant	Constant	Absent	Constant
mHH	Variable, temperature dependent	Variable, temperature dependent	Variable, temperature dependent	Variable, temperature dependent	Present, temperature dependent	Variable, temperature dependent

B

900

- Published ROR (rate of rise)
- Published ROF (rate of fall)
- HH model
- mHH model

mHH ROR

dV/dt (mV/ms)

HH ROR

600

mHH ROF

300

HH ROF

0

Temperature (^{O}C)
5   10   15   20   25

C

▼ Published R$_a$C$_m$ Values
● mHH R$_a$C$_m$ Values
- - - HH R$_a$C$_m$ Values

0.0055

R$_a$C$_m$ (ohm.F.cm)

0.0020

Temperature (^{O}C)
5   10   15   20   25

D

30

- Published conduction velocity
- HH model
- mHH model

Conduction velocity (m/s)

20

10

Temperature (^{O}C)
5   10   15   20   25

Figure 3-2: Comparison of HH and mHH models

60

A. Schematic indicating how the modified model incorporates more temperature-dependent features than the original Hodgkin/Huxley model. The symbol ρ represents axial resistivity. **B**. Comparisons of model outputs to experimental data measuring rates of rise or fall of squid action potentials (dots and error bars correspond to data from Rosenthal and Bezanilla (2000)). Red line labeled mHH ROR shows the modified Hodgkin/Huxley model fit to data for rate of rise, whereas the black line labeled HH ROR shows the predictions of the unmodified Hodgkin/Huxley model for the rate of rise. Red line labeled mHH ROF shows the modified Hodgkin/Huxley model fit to data for rate of fall, whereas the black line labeled HH ROF shows the predictions of the unmodified Hodgkin/Huxley model for rate of fall. **C**. Comparison of measured product of membrane capacitance and axial resistance (R_aC_m) to values predicted by the two models. Black line, triangles and error bars are values measured by Rosenthal and Bezanilla (2000) in squid giant axons. Red line, dots and error bars correspond to values predicted by the modified Hodgkin/Huxley model. The dashed line, which is temperature-independent, corresponds to the value used in the original Hodgkin/Huxley model. **D**. Comparisons of measured conduction velocity to model predictions. Note that the red line corresponding to the mHH model yields a better match to the experimental data (dots and error bars) than the black line corresponding to the original Hodgkin/Huxley model.

3.4   Results

3.4.1   Increasing temperature leads to a net increase in hyperpolarizing current

It was determined whether adding temperature-dependence to components of the original Hodgkin/Huxley led to qualitatively new behavior, or primarily altered the quantitative response of the modified model to temperature. Since most temperature manipulations generate a smooth change from an initial temperature to a final temperature, an action potential was generated along a model axon whose first half was at the control temperature of 6.3˚C, and then smoothly changed the temperature of the second half of the model axon to 25˚C (see equations (3-2) and (3-3), Methods; Figs. 3-3A, B). By generating the temperature change near the middle of the axon, it was ensured that initial currents at the point of action potential initiation were gone by the time the action potential encountered the change in temperature. The consequence of a gradual change in temperature was a clear increase in net hyperpolarizing (outward) current for both the original Hodgkin/Huxley model (Figs. 3-3C – F, position 2) and for the modified model (Fig. 3-3G – J, position 2) at the center of the region undergoing a change in temperature. In the region at the

61

control temperature, the relative ratio of outward to inward current was more similar for both models (Figs. 3-3C – F and 3-3G-J, position 1). In the region that was at the new, higher temperature in the modified model, the ratio of outward to inward current was also increased (Figs. 3-3G – J, position 3), although the currents were much smaller.
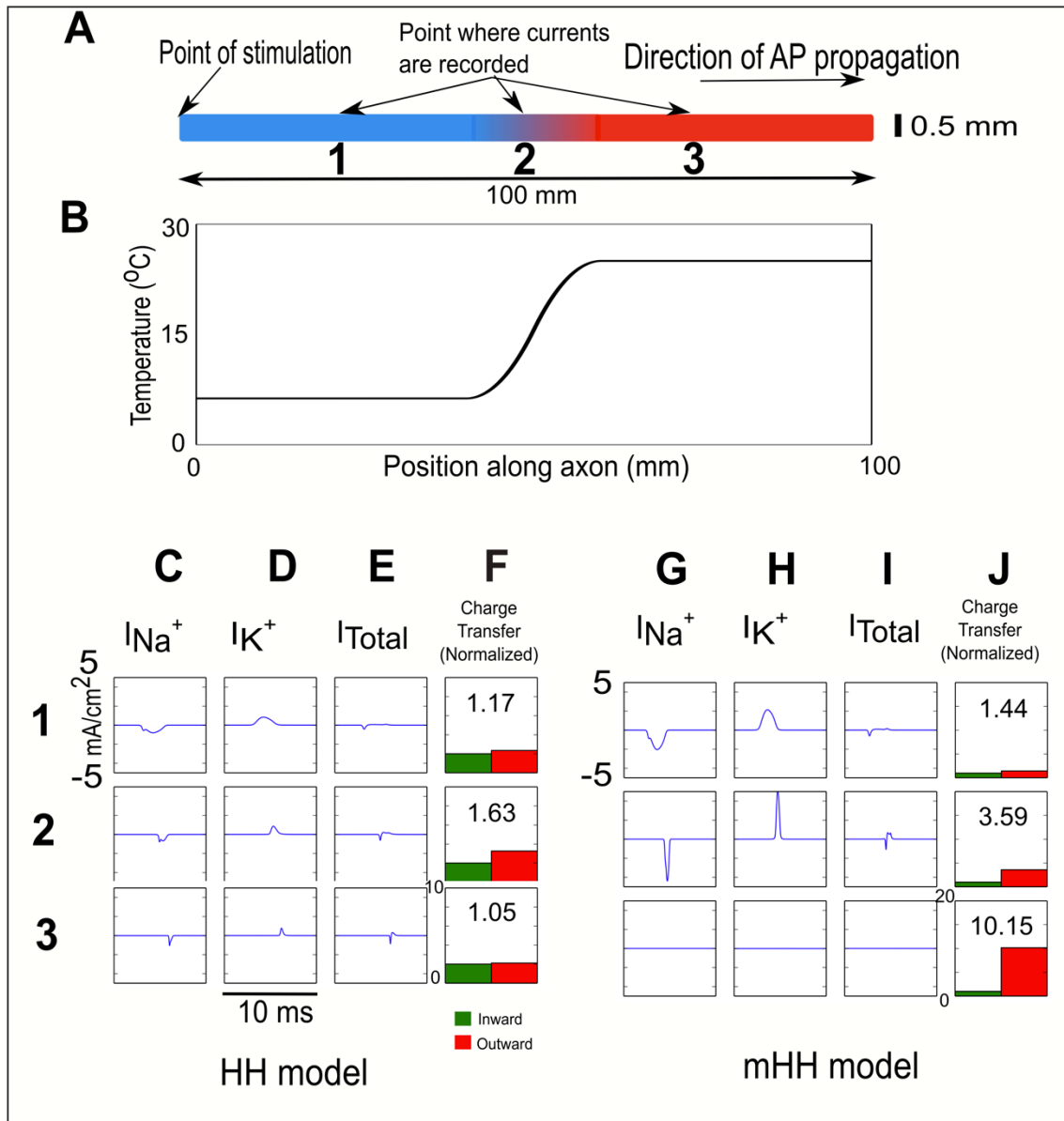
Figure 3-3: Effect of Gaussian temperature rise on AP propagation

Net increase in hyperpolarizing current in the central region of an axon in response to an action potential as the axon's temperature is smoothly increased from 6.3˚ to 25˚C around the center of the axon. **A**. Schematic of experiment. The left-hand side of the model axon (0.5 mm diameter) was held at 6.3˚C, and then, from 40 to 60 mm from its left-hand side, its temperature was smoothly increased to 25˚C (see Methods, Simulating temperature changes in the model, equations (2) and (3)). An action potential was initiated using a current pulse of 2000 nA (1 ms duration) injected into the left-hand side of the axon, and the sodium, potassium and net currents were measured at the center of the axon. Sodium current, potassium current, net current and charge transfer were measured at three positions: Position 1 – region of the axon at the control temperature (25% along its length). Position 2 – center of axon, region within which temperature is changing (50% along its length). Position 3 – region of the axon at the new, higher temperature (75% along its length). **B**. Temperature profile along the axon, ranging from 6.3˚C to 25˚C from 40 mm to 60 mm. **C – F**. Results for the Hodgkin/Huxley model. **C**. Inward sodium current. **D**. Outward potassium current. **E**. Net current. **F**. Inward versus outward charge transfer. The ratio was 5.76. **G – J**. Results for the modified Hodgkin/Huxley model. **G**. Inward sodium current. **H**. Outward potassium current. **I**. Net current. **J**. Inward versus outward charge transfer. Both models show a net increase in hyperpolarizing (outward) current in the central region as temperature increases in response to an action potential; in the modified model, the net outward current is also larger in the region of elevated temperature.

To better understand the development of the net hyperpolarizing current as a function of temperature, the temperature change was confined to a single step change (Fig. 3-4A), since in Fig. 3-3, it was observed that the changes in currents primarily occur where the axon shows significant changes in temperature. Both the original Hodgkin/Huxley model and the modified model qualitatively showed similar responses: as temperature increased from 5˚C to 25˚C, the sodium inward current became shorter (Figs. 3-4B and 3-4F, for Hodgkin/Huxley model and for modified model, respectively), due to the increased speed of sodium ion channel inactivation. Over the same temperature range, the potassium outward current became faster and larger (Figs. 3-4C and 3-4G, for Hodgkin/Huxley model and modified model, respectively), due to the increased speed of potassium ion channel activation. As a consequence, the net current (I_{total}) became increasingly outward (hyperpolarizing) with increasing temperature as the membrane was depolarized by the action potential (Figs. 3-4D and 3-4H for Hodgkin/Huxley model and modified

model, respectively). For both models, much more outward charge was transferred relative to inward charge (Fig. 3-4E and 3-4I).
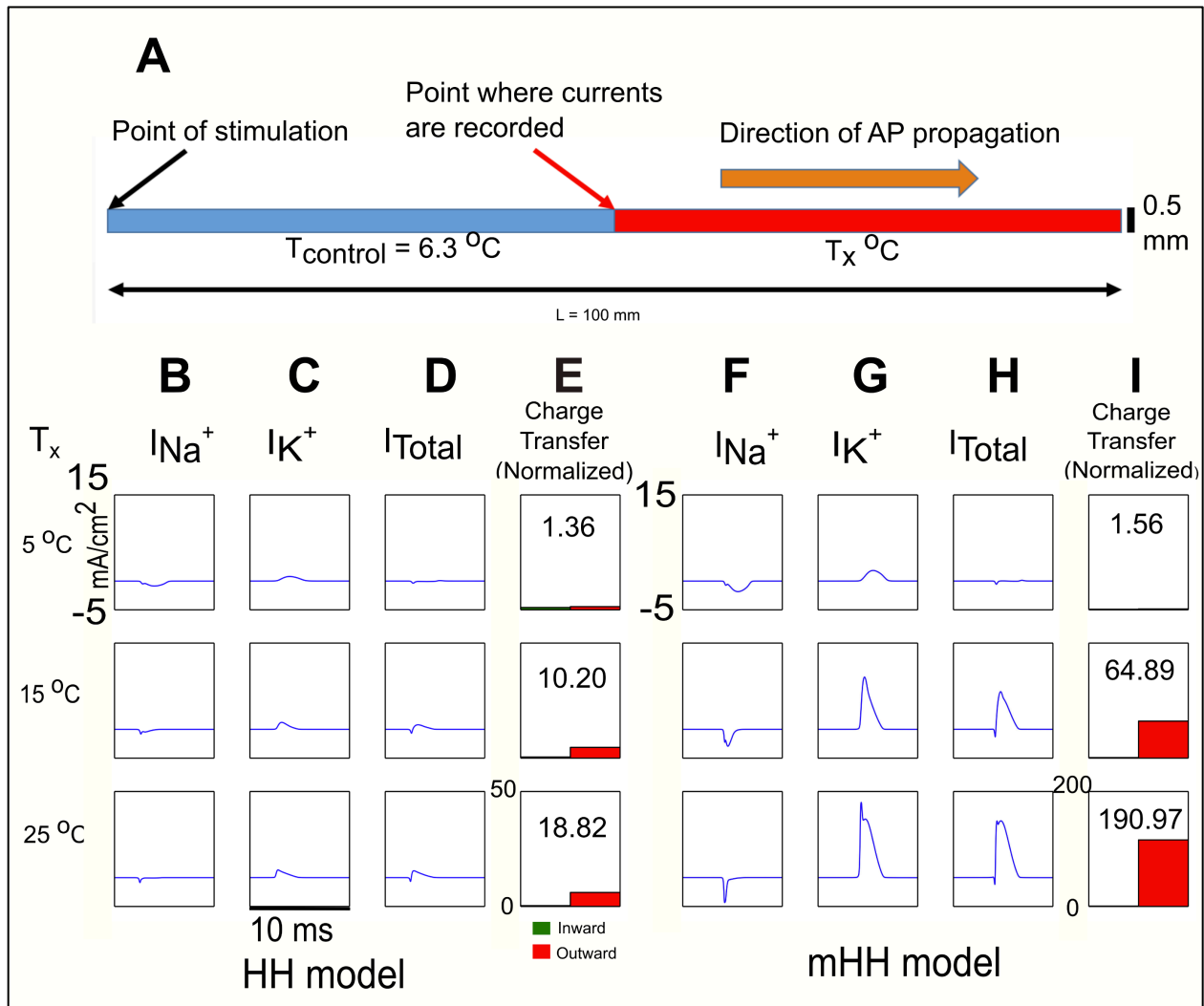
Figure 3-4: Effect of step temperarure rise on AP propagation

Sharply increasing temperature at the center of an axon leads to a net increase in hyperpolarizing current in response to an action potential. **A.** Schematic showing that the left half of the model axon (0.5 mm diameter) was kept at the control temperature of 6.3˚C, whereas the right-hand side was kept at temperatures of 5˚C, 15˚C or 25˚C. An action potential was initiated using a current pulse (2000 nA, 1 ms duration), and currents were measured at the middle of the axon, right at the transition between the control and the experimental temperatures. **B – E.** Measurements of sodium current (I_{Na}), potassium current (I_K), total current (I_{total}), and normalized charge transfer at 5˚K, 15˚C and 25˚C for the Hodgkin/Huxley model (respectively). Area under curves in parts **B** and **C** were computed (total sodium or potassium currents, respectively), and

then normalized to the inward sodium current predicted by the Hodgkin/Huxley model at 5˚C (currents are measured in units of mA/cm^2; when integrated over time, the resulting units are pC/cm^2). The actual sodium current at 5˚C used for normalization was 0.27 pC/cm^2). **F – I.** Results of the same measurements for the modified Hodgkin/Huxley model. Note that for both models, the ratio of outward to inward current (number at the top of the box in sections **E** and **I**) increases as temperature increases. Thus, with increasing temperature, a net hyperpolarizing current develops in response to the action potential. Note the larger y-axis scale for charge transfer in the modified Hodgkin/Huxley model.

3.4.2   Voltage-dependent ion channels are necessary for thermal block

In both models, increased temperature alters both the sodium and the potassium ion

channels, so both could contribute to thermal block. To determine the contributions of the voltage-

dependent ion channels to thermal block, we changed the temperature of a model neuron in its

center while selectively removing ion channels computationally from that central region, and then

initiating an action potential at one end of the axon. The voltage changes were recorded at the

beginning of the central region at which the temperature change occurred, and at the end of the

model axon (Figs. 3-5A and 3-5K, points marked 1 and 2). In both models, when all ion channels

were present, a minimum length was determined and temperature at which action potential

propagation was blocked (35˚C applied to a 5.6 mm length at the center of the axon for the

Hodgkin/Huxley model, 29.5˚C applied to an 0.9 mm length at the center of the axon for the

modified model, which were the minimum lengths at which the action potentials propagation were

blocked for the respective models).

As the action potential reached the region of changed temperature, its amplitude was

significantly reduced (red lines in Figs. 3-5B and 3-5L for the Hodgkin/Huxley and modified

Hodgkin/Huxley models, respectively; blue lines show the action potential when the central region

is at the control temperature of 6.3˚C). No action potential was recorded at the end of the model

axon (red lines in Figs. 3-5C and 3-5M for the Hodgkin/Huxley and modified Hodgkin/Huxley models, respectively; blue lines show the action potential when the central region is at the control temperature - the action potential propagates through the central region unchanged to the end of the axon).
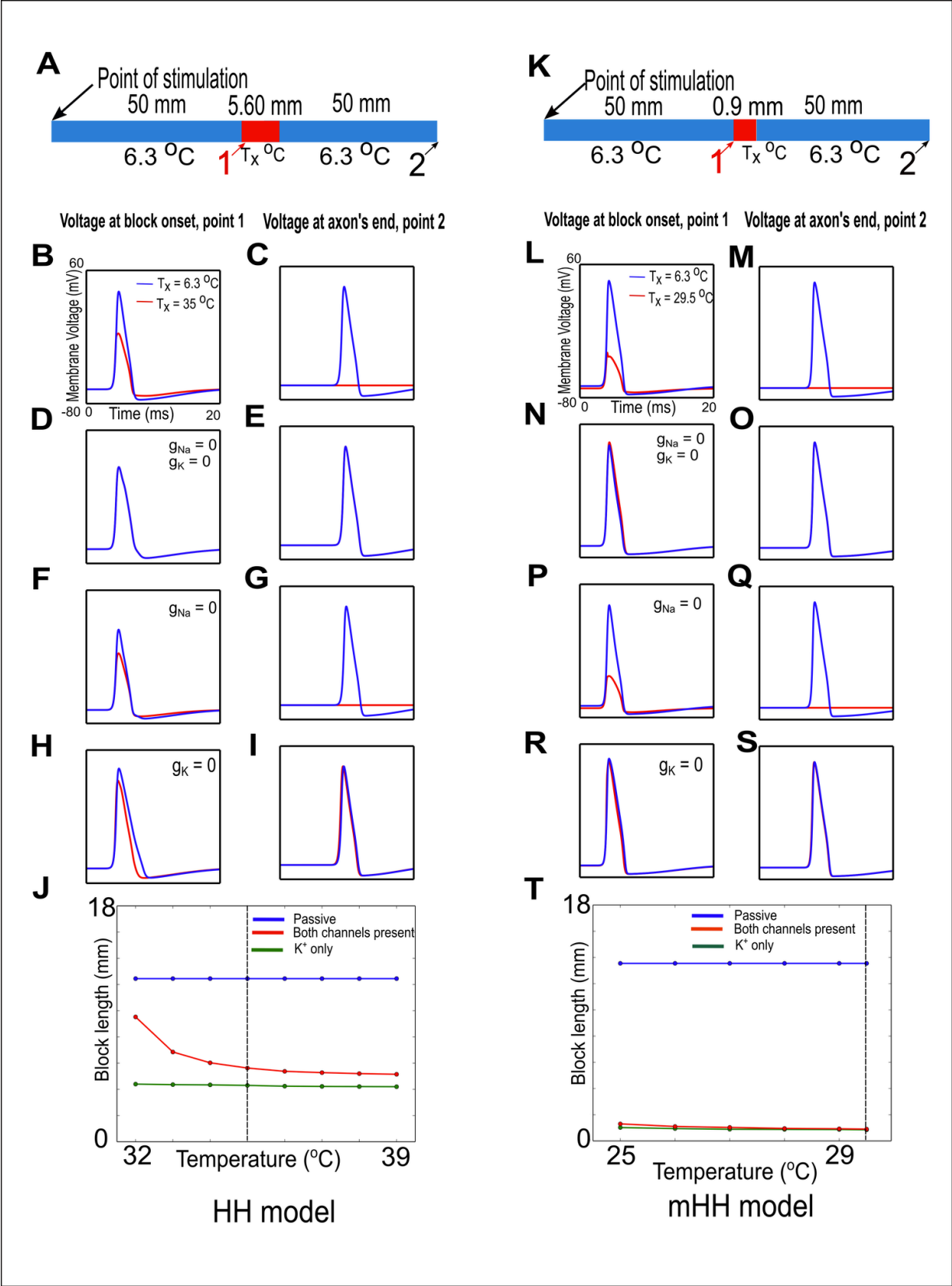
Figure 3-5: Role of ion channels in heat block

Voltage-gated ion channels are critical for thermal block, and voltage-dependent potassium channels dominate the block at higher temperatures. **A** and **K**. Schematic of the experiment. The central region of a model axon was changed to a temperature, T_x, that blocked action potential propagation for the original Hodgkin/Huxley model (**A**) and for the modified model (**K**). Regions of the axon before and after the central region were kept at the control temperature of 6.3˚C. An action potential was initiated at the left-hand side of the model axon with a current of 2000 nA (1 ms duration), and the propagating action potential was measured as it reached the region of changed temperature (point labeled 1) and at the end of the axon (point labeled 2). **B – C, L – M.** Control responses. When the central region remained at 6.3˚C, the action potential propagated normally through the region and reached the end of the axon (**B**, **C** and **L**, **M**, blue lines). As the action potential reached the central region subjected to a higher temperature, it was reduced in amplitude (**B**, **L**, red lines; compare to blue lines), and it was completely blocked at the end of the axon (**C**, **M**, red lines). **D-E, N-O.** The conductances of both the voltage-gated sodium ion and potassium ion channels were set to zero in the central region. When the temperature of the central region was not changed, the action potential shape changed slightly as it reached the region without ion channels (**D**, **N**, blue lines), but by the end of the axon, its shape was again similar to the control action potential (**E**, **O**, blue lines). When the central region is subjected to an increase in temperature, there is no change in the action potential in the Hodgkin/Huxley model (**D**, **E**; the red lines are completely covered by the blue lines). A slight widening of the action potential is visible in the modified Hodgkin/Huxley model as the action potential reaches the region at a higher temperature (**N**, red line), but the action potential at the end of the axon is identical to that generated when the central region is at its original temperature (**O**; red line is covered by blue line). **F – G, P – Q.** Voltage-dependent potassium channels are sufficient to induce thermal block. The conductance of the voltage-dependent sodium ion channels was set to zero in the central region. The peaks of the action potentials were slightly reduced when the central region was at its original temperature (**F**, **P**, blue lines), but the action potentials at the end of the axon were similar to control action potentials (**G**, **Q**, blue lines). In contrast, increasing the temperature of the central region blocked action potentials. The action potential was reduced as it reached the region of increased temperature (**F**, **P**, red lines), and was completely absent at the end of the axon (**G**, **Q**, red lines). **H – I, R – S.** Voltage-dependent potassium channels are necessary to induce thermal block. The conductance of the voltage-dependent potassium ion channels was set to zero in the central region. As the action potentials reached the central region, they were slightly wider than normal (**H**, **R**, blue lines), but were similar to control action potentials at the end of the axon (**I**, **S**, blue lines). Action potentials were not blocked by increased temperature; they narrowed as they reached the region of increased temperature (**H**, **R**, red lines), but were essentially similar to control action potentials at the end of the axon (**I**, **S**, red lines; in **S**, the blue line covers the red line). **J, T**. Minimum lengths required to block the action potential when all voltage-gated ion channels are intact (light green line) are similar to those needed to block when only voltage-gated potassium ion channels are present (red line), especially at higher temperatures. At low temperatures, the original Hodgkin/Huxley model is also affected by the effects of temperature on the voltage-gated sodium ion channels (dark green line). At high temperatures, the voltage-gated potassium ion channels clearly dominate the block length (**J**), and these channels dominate at all temperatures in the modified model (**T**). The dashed lines in **J** and **T** (at 35˚C and 29.5˚C, respectively), correspond to the results shown in parts **A – I** and **K – S** of this figure, respectively.

To demonstrate that all of the voltage-gated ion channels were necessary for thermal block, we set the conductances of both the sodium and potassium voltage-gated ion channels to zero within the central region. Removing ion channels can change the resting potential of the central region because the voltage-dependent ion channels contribute significantly to the resting potential. Since, at rest, the membrane is primarily permeable to potassium ions, removing all ion channels will tend to depolarize the membrane. In turn, a depolarized membrane will alter the states of voltage-dependent ion channels on either side of the central region. To eliminate this potentially confounding factor, a compensatory current was applied to the central region to ensure that it remained at the control resting potential after ion channels were removed computationally (see Methods, Compensatory Current, and Fig. 3-7).

When the action potential encountered the central region, its amplitude decreased and the waveform broadened (Figs. 3-5D and 3-5N, blue lines). By the time the action potential reached the end of the model axon, it was identical to the control action potential (Fig. 3-5E and 3-5O, blue lines). Removing all the voltage-dependent ion channels did not prevent passive currents from propagating through the region in which the ion channels were blocked, and these passive currents re-activated an action potential that propagated to the end of the model axon.

When the central region was subjected to an increased temperature, the Hodgkin/Huxley model showed no changes (Figs. 3-5D and 3-5E; the red lines corresponding to the increased temperature condition are completely covered by the blue lines). The lack of response is predictable, as all of the temperature-dependent aspects of the model have been removed. In the modified Hodgkin/Huxley model, both the axial resistance (Fig. 3-5D) and the sodium/potassium pump depend on temperature. When the central region was subjected to an increased temperature,

69

the action potential showed a small increase in width relative to the control (Fig. 3-5N, red line), but the action potential at the end of the axon was essentially unchanged (Fig. 3-5O; the red line is covered by the control blue line). Thus, both models clearly require the voltage-dependent ion channels to generate thermal block in response to increased temperature.

3.4.3   Voltage-gated potassium channels are necessary and sufficient for thermal block

To determine if voltage-gated sodium ion channels are necessary for thermal block, we set the conductance of the voltage-gated sodium ion channels to zero. We did not modify the conductance of the voltage-gated potassium ion channels. Again, compensatory current was used to ensure that the resting potential was unchanged by computationally removing the voltage-gated sodium ion channels. In both models, when the central region was kept at the control temperature of 6.3˚C, the action potential peak was reduced as it reached the central region (Figs. 3-5F and 3-5P for the Hodgkin/Huxley and modified models, respectively, blue lines). Passive currents were able to propagate through the region and re-activate an action potential, which arrived at the end of the axon essentially unchanged (Figs. 3-5G and 3-5Q, respectively, blue lines). When the central region was subjected to increased temperature, the peak of the action potential was significantly reduced in both models as it reached the region of increased temperature (Fig. 3-5F and 3-5P, respectively, red lines). The action potential was completely blocked by the end of the axon (Figs. 3-5G and 3-5Q, respectively, red lines). These results demonstrate that voltage-gated sodium ion channels are not necessary, whereas voltage-gated potassium ion channels are sufficient alone to induce thermal block.

To determine if voltage-gated potassium channels are necessary for thermal block, we set the conductance of these channels to zero, but did not modify the conductance of the voltage-gated

sodium ion channels. Again, we used compensatory current to ensure that the resting potential was unchanged despite the computational removal of the voltage-gated potassium ion channels. In both models, when the central region was kept at the control temperature of 6.3°C, the action potential broadened slightly as it reached the central region (Figs. 3-5H and 3-5R for the Hodgkin/Huxley and modified models, respectively, blue lines), but propagated normally to the end of the axon (Fig. 3-5I and 3-5S, respectively, blue lines). When the central region was subjected to increased temperature, the action potential narrowed slightly as it reached the central region (Figs. 3-5H and 3-5R, respectively, red lines), but propagated through and reached the end of the axon essentially unchanged (Figs. 3-5I and 3-5S, respectively, red lines). Under these conditions, voltage-gated potassium ion channels are necessary for thermal block, and voltage-gated sodium channels are not sufficient alone to induce thermal block.

To generalize these results, minimum block lengths for all four conditions (all voltage-gated ion channels intact, all voltage-gated ion channels blocked, voltage-gated sodium ion channels blocked, or voltage-gated potassium ion channels blocked) were measured in both models, with compensatory current applied to ensure no change from the resting potential after computational removal of ion channels. Since voltage-gated sodium ion channels contribute depolarizing current and voltage-gated potassium ion channels contribute hyperpolarizing current, the block lengths when all ion channels are intact should lie midway between the block lengths for either of the two voltage-gated ion channels alone. If one of the voltage-gated ion channels dominates, then the block lengths when all ion channels are intact should lie closer to the block lengths for that ion channel alone. The data suggest that, at the lowest temperature that can cause block in the Hodgkin/Huxley model, both voltage-gated sodium and potassium ion channels contribute to the block, but as the temperature is raised, the block length is dominated by the

71

voltage-gated potassium ion channels (Fig. 3-5J). In contrast, for the modified Hodgkin/Huxley model, at all temperatures capable of inducing block, the block length associated with the potassium channels dominates (Fig. 3-5T).

As another way of testing the role of the different voltage-dependent ion channels in thermal inhibition, we changed the temperature-dependence of the gating variables m, h and n in the modified Hodgkin Huxley model. By setting the Q_{10} of n to 1, we ensured that the voltage-dependent potassium ion channels would not open more rapidly as the axon temperature increased. After this modification, application of increased temperature did not induce block of the action potential (data not shown). In contrast, after setting the Q_{10} of m and h to 1, eliminating the temperature-dependence of the voltage-dependent sodium ion channels, increased temperature could still induce block (data not shown). Because it is not currently feasible to eliminate the temperature-dependence of ion channels, we did not pursue this approach further.

Applying compensatory current to an axon may be experimentally challenging, so we determined whether qualitatively similar results were observed if the central region's resting potential was allowed to change after computationally removing voltage-dependent ion channels in either the original Hodgkin/Huxley model or the modified model (Fig. 3-7A and F). As expected, in both models, computational removal of all voltage-dependent ion channels from the central region caused a small depolarization of the central region and regions around it (Fig. 3-7B and G); computational removal of all voltage-dependent potassium ion channels caused a larger depolarization (Figs. 3-7C and H); and computational removal of all voltage-dependent sodium ion channels caused a small hyperpolarization (Figs. 3-7D and I). Despite these changes in potential, the qualitative results we obtained for length of block needed as a function of temperature

were very similar to those obtained using compensatory current (Figs. 3-7E and J; compare Fig. 3-7J and T): at higher block temperatures, the length of the block was clearly dominated by the voltage-dependent potassium ion channels. In the Hodgkin/Huxley model, at lower block temperatures, the voltage-dependent sodium ion channels clearly played an important role in determining block length (Fig. 3-7E). In the absence of compensatory current, the central region of the axon depolarizes once the voltage-gated potassium ion channels are blocked. In turn, this depolarization reduces the inward current through the voltage-dependent sodium ion channels because they inactivate in response to depolarization. The depolarizing current is also partially shunted by the increased conductance when the voltage-dependent sodium ion channels are activated. The net result is the same: the block lengths when all ion channels are intact lie between block lengths for either of the two voltage-gated ion channels alone.
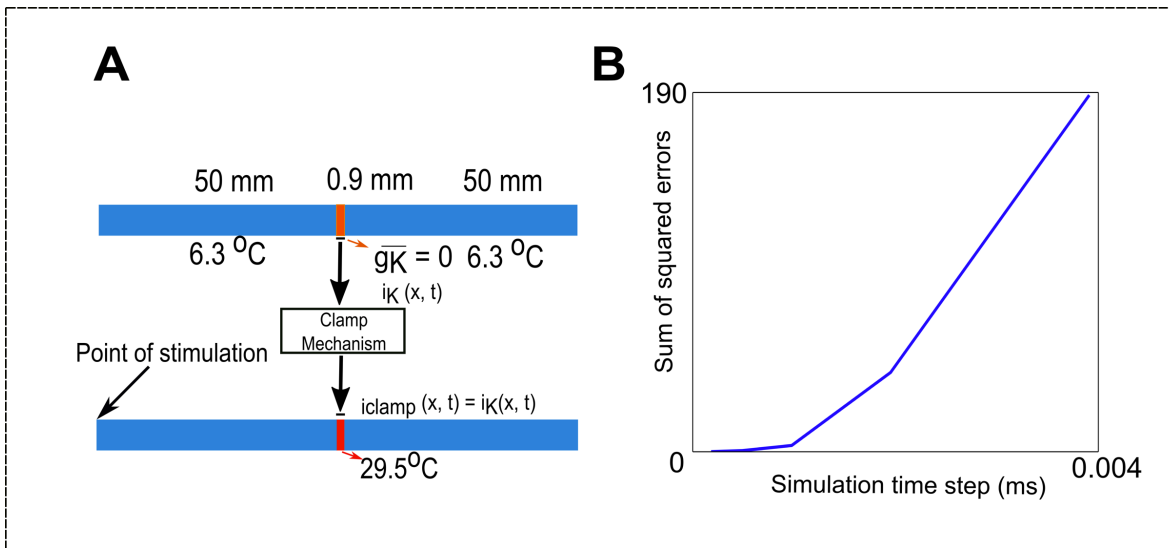
Figure 3-6: Effect of compensatory current

A. Schematic illustration of the compensatory current experiment. (Top schematic) The currents were measured from a model neuron whose voltage-dependent potassium ion channel conductances were maintained at their control values (indicated by orange rectangle), and whose temperature was at 6.3˚C throughout (see Fig. 3-7H for the potential change in the central region). (Bottom schematic) The opposite current was injected into each of the corresponding segments of the second axon whose peak potassium conductances were set to zero (indicated by the red rectangle) to ensure that the second axon maintained its original resting potential despite the

removal of the voltage-dependent potassium ion channels. **B**. Mean square error in change in voltage along the length of an axon in the presence of compensatory current compared to a control axon as a function of integration step size. See Methods.
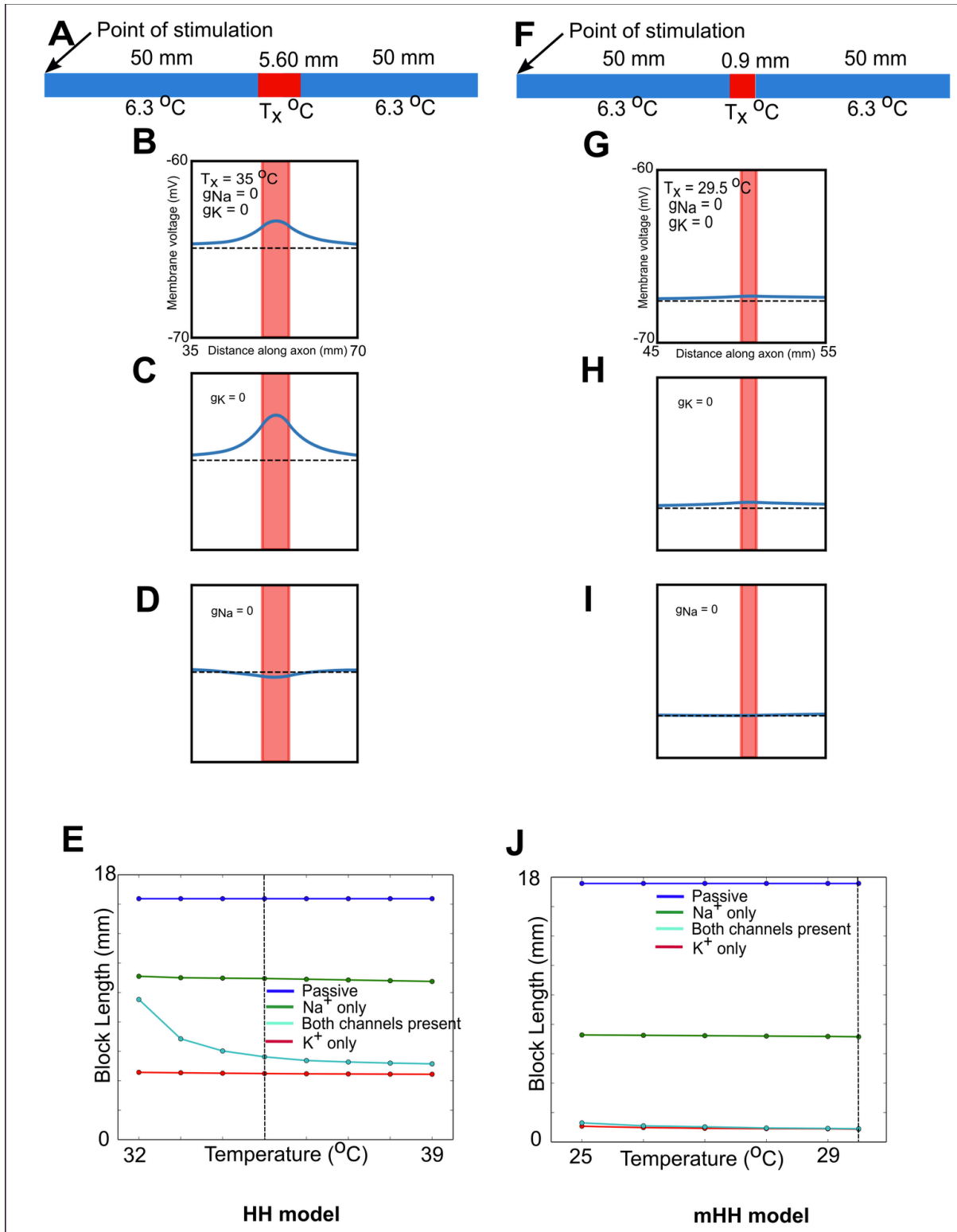
Figure 3-7: Role of ion channels in heat block (no compensatory current)

Small changes in membrane potential due to removal of ion channels do not significantly alter the minimal lengths necessary to block action potential propagation, and still demonstrate that voltage-gated ion channels, especially potassium ion channels, are critical for thermal block. In addition, thermal block for single action potentials is sufficient to block repetitive firing. **A**, **F**. Schematics of the experiments for the Hodgkin/Huxley model and the modified Hodgkin/Huxley model, respectively. An action potential was initiated at the left side with an injected current pulse (2000 nA, 1 ms). Ion channel conductances were altered, and the central region of the model axon was subjected to an increase in temperature. The minimum length needed to block the conduction of the action potential was determined. Unlike the data in Figure 6, compensatory current was not used to ensure that the resting potential was kept at its original value (-65 mV) after the ion channel conductances were manipulated. **B**, **G**. Setting the conductances of both the sodium and potassium voltage-gated ion channels to zero induces a depolarization of the membrane towards the leak conductance's equilibrium potential in both the Hodgkin/Huxley (**B**) and modified Hodgkin/Huxley (**G**) models. **C**, **H**. Setting the conductance of the voltage-gated potassium ion channels to zero induces a depolarization of the membrane in both the Hodgkin/Huxley (**C**) and modified Hodgkin/Huxley (**H**) models. **D**, **I**. Setting the conductance of the voltage-gated sodium ion channels to zero induces a hyperpolarization of the membrane in both the Hodgkin/Huxley (**D**) and modified Hodgkin/Huxley (**I**) models. **E**, **J**. Despite the small changes in potential when ion channel conductances are eliminated, the lengths necessary to block action potential conduction are dominated by the voltage-gated potassium ion channels for both models, especially at higher temperatures. At the lowest block temperatures, the Hodgkin/Huxley model (**E**) is also significantly affected by the block lengths of the voltage-gated sodium ion channels.

Since neurons generally fire repetitively in response to stimuli, we tested whether a thermal block that was sufficient to stop an action potential could also block repetitive firing (Fig. 3-8A). Thermal block sufficient to block a single action potential was able to block repetitive firing, whether induced by a steady depolarizing current (Fig. 3-8B), or by individual depolarizing current pulses (Fig. 3-8C).
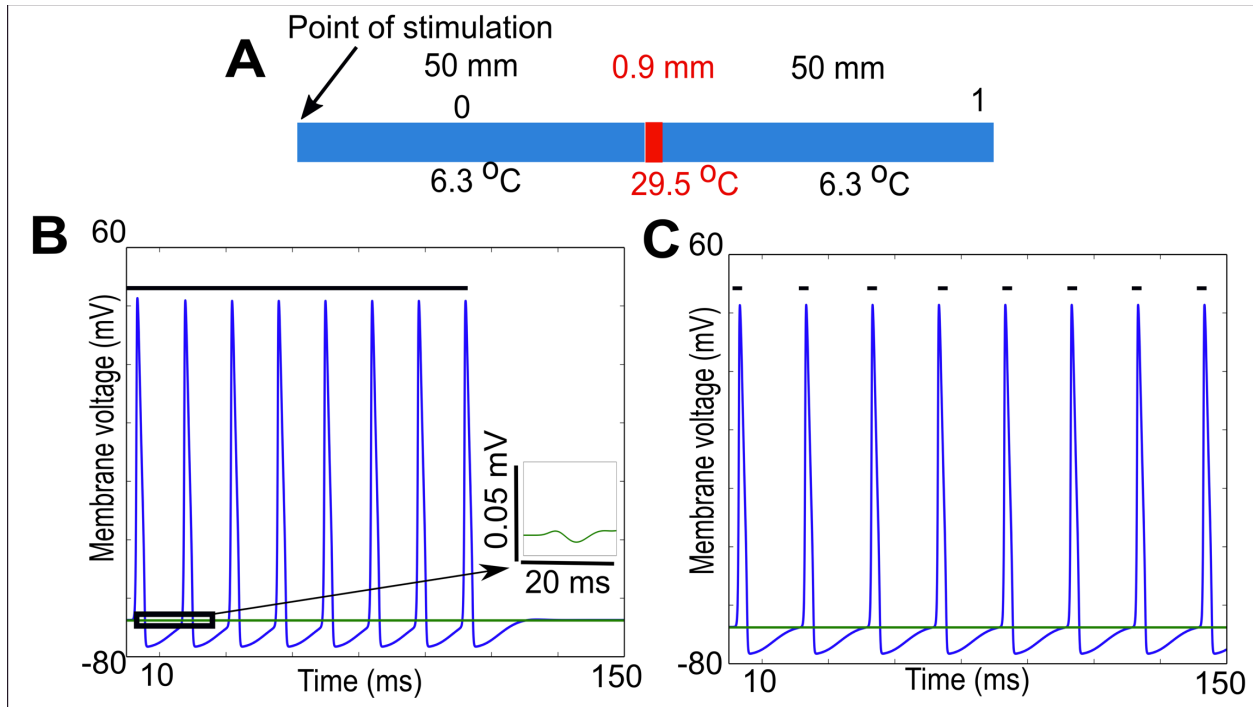
Figure 3-8: Heat block in repetitive firing

Block of single action potentials also blocks repetitive firing. **A.** Schematic of experiment: current was injected on the left-hand side, the axon was raised to a temperature sufficient to induce block of a single propagating action potential, and potentials were recorded at the points labeled 0 and 1. **B**. Repetitive firing (80 Hz) due to a steady depolarizing pulse (2000 nA; duration is indicated by the green line above the action potentials) is completely blocked by the same conditions that block a single action potential. Action potentials are measured prior to the block region (blue line, at 25% of the length of the axon; point labeled 0 on the schematic diagram), and membrane potential is measured at the end of the axon (green line, at 90% of the length of the axon, point labeled 1 on the schematic diagram). Small residual filtered versions of the original action potential appear at the end of the axon, but the action potential does not propagate past the block region (see inset, which shows an expanded view of the green line contained within the box; the potential measured at the end of the axon is a small passive response). **C**. Repetitive firing (66.67 Hz) due to individual current pulses (2000 nA, 1 ms duration, 15 ms period; small green lines above each action potential indicate time of current injection) is completely blocked by the same conditions that block a single action potential. Once again, the action potentials propagate normally until the block region (blue line, measured at the point labeled 0 in the schematic), and only small residual passive versions appear at the end of the axon (green line, measured at the point labeled 1 in the schematic), but the action potential does not propagate past the block region.

3.4.4 Thermal block length scales with the square root of axon diameter

Unmyelinated fibers range widely in size across phylogeny; some are as small as 0.2 µm (e.g., unmyelinated C fibers in a muscle nerve or a cutaneous nerve;(Gardner 2013)). We sought to determine the minimal thermal block lengths as a function of fiber diameter. A mathematical analysis of the cable equation predicted that modalities acting on the surface of axons would scale with the square root of the diameter of the axon (Lothet 2017, Supplemntary information). In the mathematical model, a generalized form of the cable equation was derived in which the dependence of membrane capacitance and resistance and axial resistance was made explicit. The equation was then rewritten to re-scale length by the square root of the axon diameter, and in this new coordinate system, the dependence of all the terms on axon diameter could be factored out, making the new equation independent of axon diameter. In turn, this immediately implied that if one axon has diameter d_1, and could be blocked by a high-temperature region whose minimum length was L, then an axon of diameter d_2 would be blocked by a high temperature region of minimum length $L\sqrt{\frac{d_2}{d_1}}$. These mathematical predictions have been confirmed by the experimental studies in Lothet et al. 2017, which demonstrated that thermal inhibition could selectively block small-diameter axons before large-diameter axons in both an invertebrate nerve (from *Aplysia californica*) and the vertebrate vagus (from the musk shrew *Suncus murinus*). The conduction velocity and length constant of an unmyelinated axon also scale with the square root of axon diameter (Debanne 2011, Hodgkin 1954). These observations suggest that the spread of current away from the region of increased temperature should also scale as the square root of the axon diameter. Thus, if voltage changes were plotted against the distance scaled by the length constant of the axon, which is proportional to the square root of the axon diameter, the resulting voltage changes should be independent of axon diameter.

The length constant of an unmyelinated axon is defined from the solution of the cable equation after time-dependent changes in voltage have died out while a steady current is injected into the cable, yielding

$$V_m(x) = V_0 e^{-x/\lambda},$$ (3-14)

where $V_m(x)$ is the membrane potential V_m at point x along the cable, V_0 is the voltage at the point of current injection, and λ is the length constant (Jack 1975). Note that when the original voltage V_0 has fallen by 1/e of its original value, x = λ. Thus, to determine the length constant of an axon with a region of increased temperature, we injected a steady hyperpolarizing current, and determined the distance at which the hyperpolarization had fallen to a value of 1/e of its value at the point of injection. For a 500 μm axon, this value was 3.96 mm. The length constant of the same axon at its original temperature was 3.93 mm (a difference of 1%). To determine how the current spread scaled with axon diameter, an action potential and its blocked version were also determined for a 10 μm diameter axon, and then rescaled by the length constant (the length constant was 0.56 mm; note that 3.96 is equal to 0.56 times the square root of the ratio of the diameters, i.e., 0.56 x $\sqrt{\frac{500}{10}}$ = 3.96, as predicted by the square root scaling law).

To determine the spatial extent of an action potential in the absence of block, an action potential was initiated in response to a stimulating current (2000 nA for 1 ms) in an axon at its original temperature. At the instant the peak of the action potential reached the middle of the axon, we recorded the voltage along the entire axon (Figure 3-9A, blue line). Note the large spatial extent

of the action potential. It is also worth noting the difference in shape from the action potentials shown in Fig. 3-5: in that figure, we record the change in voltage over time at the initial point of the block region and at the end of the axon, so we look at the time profile at a *single point in space*. In contrast, here we record the change in voltage over the entire length of the axon (i.e., over all space) at a *single instant in time*. To determine the effect of the spatial extent of the thermal block on the action potential, an action potential was initiated while the minimum length along the axon necessary for thermal block (1.12 mm) had its temperature increased to 29.5°C, starting at the middle of the axon. At the identical time after the stimulating current initiated the action potential, we recorded the voltage along the entire axon. Note the large spatial extent of the block (Fig. 3-9A, green line). We rescaled these results by the axonal length constant so they could be compared to results obtained in axons of different diameters (Fig. 3-9B). We then repeated the simulation using a 10 µm diameter axon (Fig. 3-9C); when the results were rescaled by the length constant, they were essentially identical to those observed in the 500 µm diameter axon (Fig. 3-9D; compare Fig. 3-9B).

The scaling of thermal block suggested that it would act first on smaller-diameter axons, rather than on larger-diameter axons. Once axons are scaled by the square root of their diameters, the spatial spread of voltage at a fixed point of time becomes identical. In turn, this implies that the voltage changes experienced by the voltage-dependent ion channels will also be identical, and thus the currents induced by these depolarizations will be identical. As a consequence, this numerically confirms the mathematical model of (Lothet 2017 – Supplemental Material), which demonstrated that the length of block would scale with the square root of axon diameter. In contrast, extracellular currents are known to act on larger-diameter axons before smaller-diameter axons, since these currents scale as the square of the axon diameter (Rattay 1986). To further test

the predictions of the mathematical analysis (Lothet 2017), we determined the minimum lengths of the central region that needed to be increased in temperature to induce thermal block as a function of axon diameter. As predicted by the mathematical model, the block lengths scaled linearly with the square root of the axon diameter (Fig. 3-10). The scaling effects were observed for the Hodgkin/Huxley model (Fig. 3-10A), as well as for the modified Hodgkin/Huxley model (Fig. 3-10B) even at diameters that are similar to those of unmyelinated C fibers in vertebrates (Fig. 3-10C). Furthermore, as temperatures were increased, the minimum block length decreased for both models (Fig. 3-10).
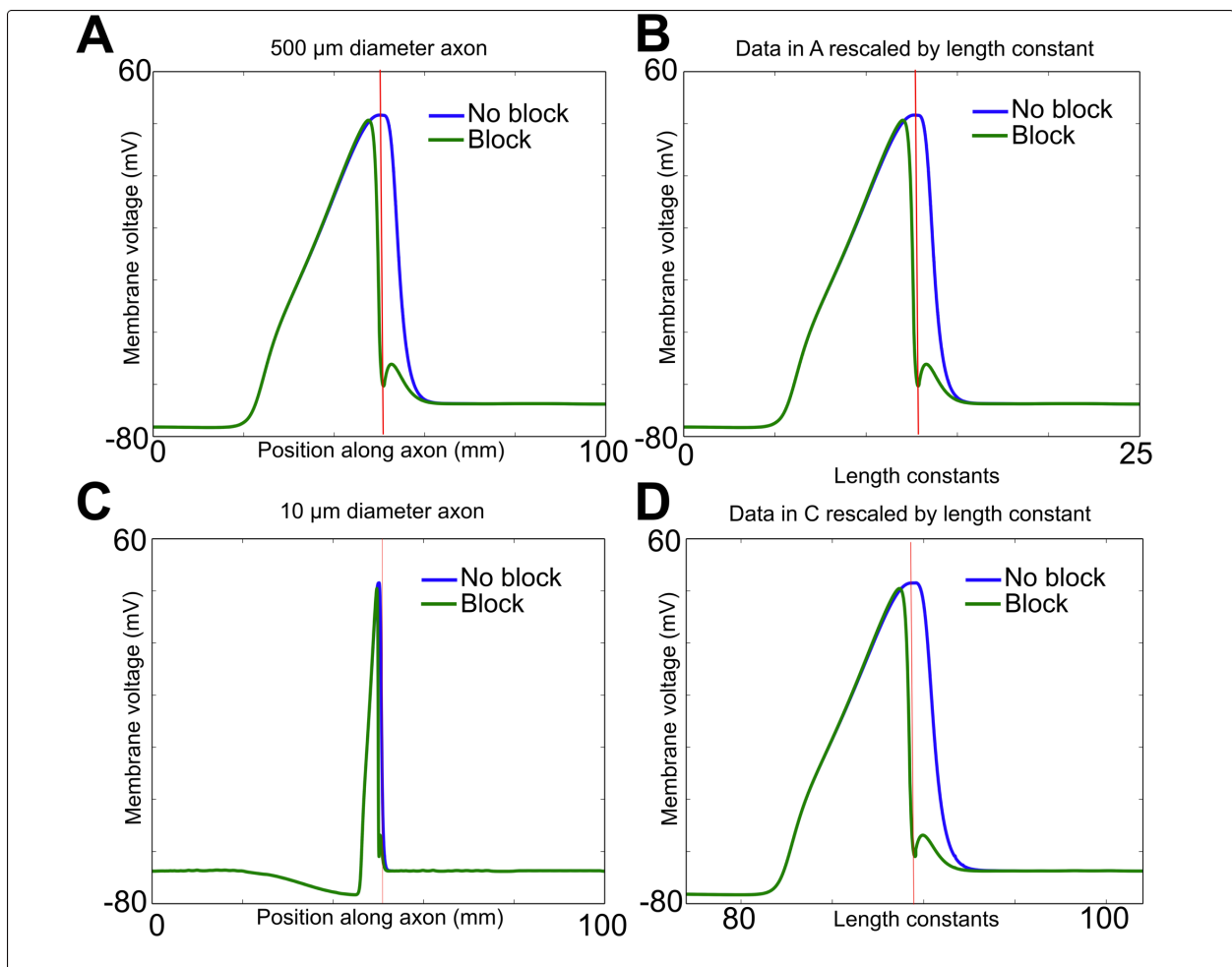
Figure 3-9: Spread of block currents during heat block

Spread of effects of block currents beyond the region of elevated temperature in the model squid giant axon scales with diameter. **A**. At the time that the peak of the action potential reached the middle of aa 500 μm diameter axon at its original temperature in response to a stimulating current (2000 nA for 1 ms), the voltage along the entire axon was plotted (blue line). The action potential occupies a large fraction of the entire length of the axon. The action potential was again induced as the temperature of the central region was increased to 29.5˚C, and at the identical time, the voltage along the entire axon was plotted (green line). Note that the voltage of the second action potential is identical to the first at the beginning and at the end of the axon. Anterior to the region of block, however, the voltage of the second action potential begins to significantly change relative to the voltage of the first action potential; these changes continue beyond the region of elevated temperature as well. The red line indicates the region of block. **B**. Effect of spread of block currents rescaled by the axonal length constant. Data in panel **A** were rescaled by the length constant of the original axon (see text). The red line indicates the region of block. **C**. Effect of spread of block currents beyond the region of elevated temperature in a smaller unmyelinated axon. The simulations done in panel **A** were repeated in a 10 μm diameter axon. The effect of the block currents clearly extends beyond the region of elevated temperature. Red line indicates region of block. **D**. Effect of spread of block currents rescaled by the length constant. Data in panel **C** were rescaled by the length constant of the original 10 μm axon (see text). After rescaling, results in the 10 μm diameter axon are essentially identical to those in the 500 μm diameter axon (compare panels **B** and **D**). Red line indicates region of block.
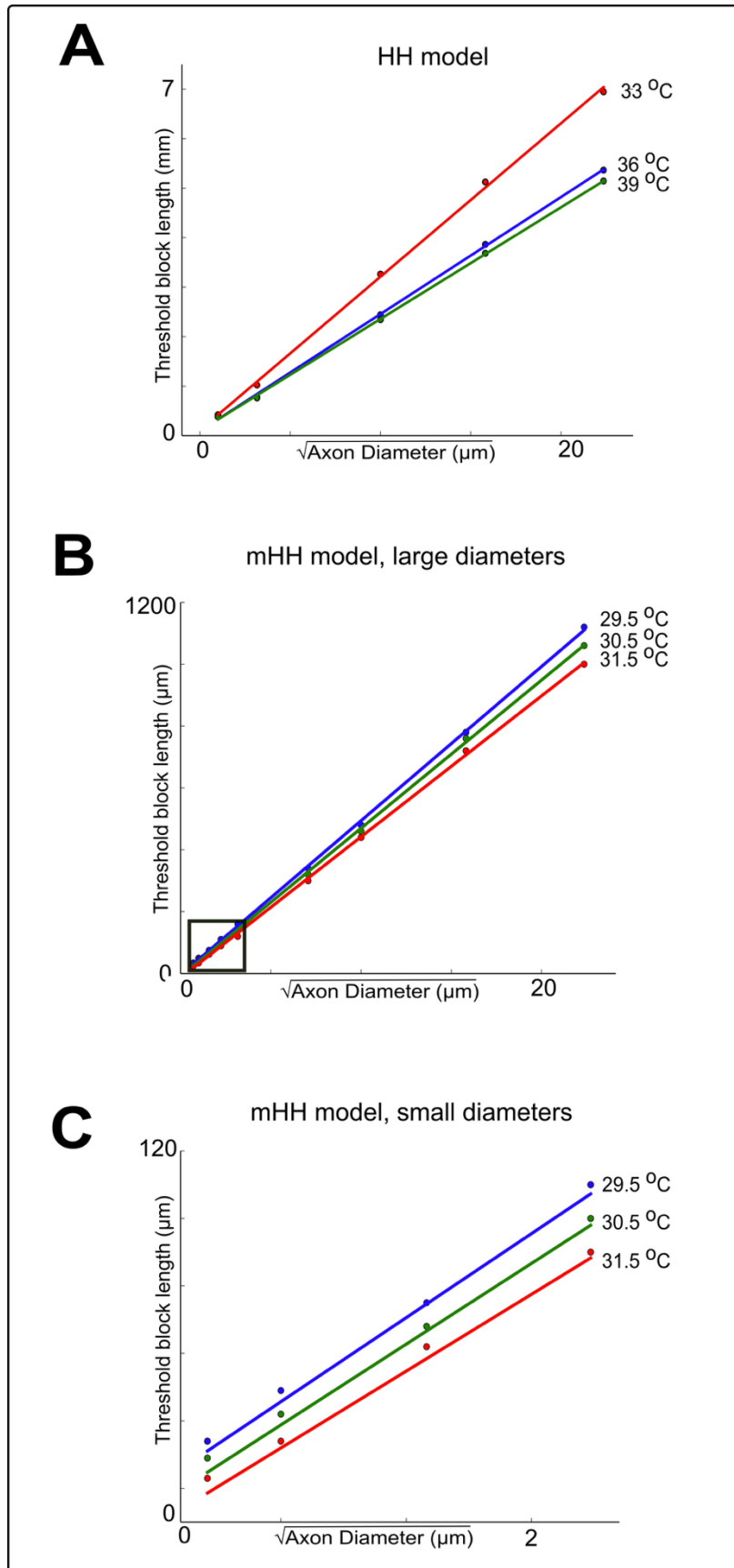
Figure 3-10: Scaling of block lengths with axon diameter

Thermal block length scales with the square root of axon diameter. **A**. Thermal block length scales linearly with the square root of axon diameter in the unmodified Hodgkin/Huxley model, and length decreases with increasing temperature. **B**. Thermal block length scales linearly with the square root of axon diameter in the modified Hodgkin/Huxley model, and the minimum length required for thermal block decreases with increasing temperature. **C**. Expanded view of region highlighted by a square in panel **B**. The linear relationship between the square root of axon diameter and threshold block length is observed for axon diameters similar to those of vertebrate unmyelinated C fibers.

3.4.5 Action potential initiation can be thermally blocked

When an action potential is initiated in the initial segment of the axon, the currents generated are larger than those generated by the propagating action potential (Kole 2008). Since the thermal blocks described above were applied to a propagating action potential, thermal block of action potential initiation might be different (schematics of experiment shown Fig. 3-11A and D, respectively). To determine how thermal block of initiation scales with axon diameter, we first determined the minimum current needed to initiate an action potential for a given diameter axon. Whenever an action potential is initiated using a very short current pulse, there is little time for activation of voltage-dependent ion channels, and thus the current needed to reach the voltage threshold is inversely proportional to the passive input resistance of the cable. In turn, this implies that the minimum current needed to initiate an action potential would scale as the square root of the axon diameter cubed (Jack 1975, p. 32). Indeed, the minimum currents needed to initiate an action potential scaled in this way for both the Hodgkin Huxley and the modified model (Fig. 3-11B and E, respectively). When thermal block was applied to either model after it was stimulated by the appropriate threshold current to initiate an action potential, the inhibition block temperature again scaled with the square root of axon diameter (Fig. 3-11C and F, respectively).

These results suggest that thermal block in unmyelinated axons, especially at higher temperatures, are primarily due to the activation of voltage-dependent potassium ion channels in response to depolarization, which induce a strong hyperpolarization and thus block action potential initiation and propagation, and can act preferentially to block smaller-diameter axons before larger-diameter axons.
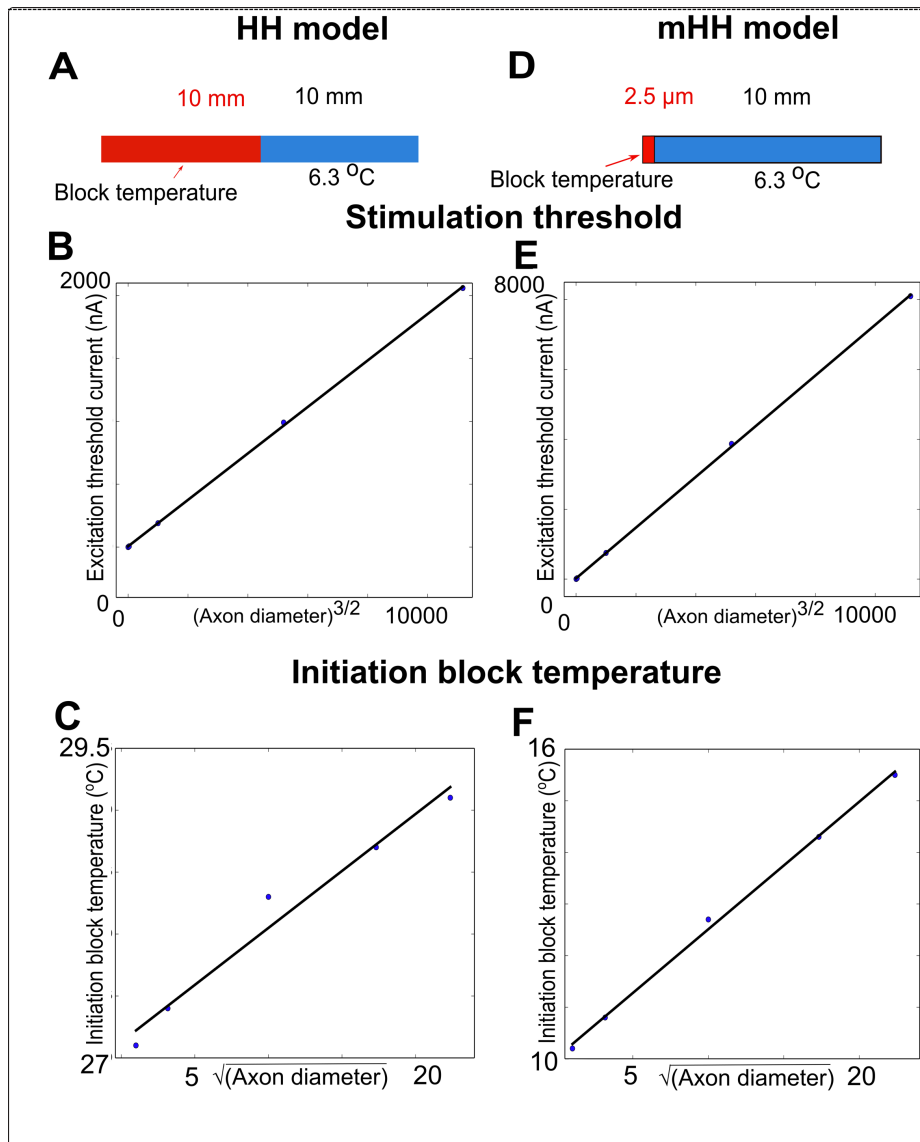
Figure 3-11: Scaling of thermal block of action potential initiation

A. Schematic of the model axon for the Hodgkin/Huxley model, indicating the initial region (10 mm) that was used to determine the minimum current needed to initiate an action potential at the control temperature (6.3˚C) and then subjected to an increase in temperature to determine the minimum temperature to block action potential initiation. **B**. Scaling of minimum current needed to initiate an action potential in the Hodgkin Huxley model. Minimum current (pulse length: 0.5 ms) was determined for axons whose diameter was 1μm, 10μm, 100 μm, 300 μm and 500 μm. The minimum current scales with the axon diameter raised to the 3/2 power. See text. $R^2 = 0.99$. **C**. The minimum temperature needed to block action potential initiation using the threshold current determined for each axon diameter in the Hodgkin/Huxley model scales linearly with the square root of the axon diameter. $R^2 = 0.97$. **D**. Schematic for initial increase in temperature of modified Hodgkin/Huxley model. Because the potassium currents generated by the model are much larger, a smaller region of the axon can be subjected to an increase in temperature (2.5 μm). **E**. Minimum current for inducing an action potential again scales with the axon diameter raised to the 3/2 power. $R^2 = 0.99$. **F**. Minimum temperature for block when action potentials are initiated by the appropriate threshold current scales linearly with the square root of axon diameter. $R^2 = 0.97$.

3.5   Discussion

To our knowledge, this is the first study to provide quantitative evidence for a mechanism of thermal block that was originally suggested by Huxley (Huxley 1959): thermal block at higher temperatures is due primarily to activation of voltage-dependent potassium ion channels (Fig. 3-4). Thermal block also appears to work for repetitive firing as well as for single action potentials (Fig. 3-5). In our previous study (Lothet 2017, Figures 2, 3 and Supplemental Figure 5), we demonstrated that thermal inhibition could block a repetitively stimulated compound action potential. The results shown in Fig. 3-5 suggest that the mechanism of this block is the same as the mechanism that blocks a single propagating action potential.

The data presented in this chapter also provide further support for the prediction of a mathematical model based on the cable equation (Lothet 2017 – Supplemental Materials) that treatments that act on surface ion channels (such as infrared light or drugs) will have effects that scale as the square root of the diameter of the axon (Figs. 3-6, 3-7 and 3-8). In turn, this implies that small-diameter axons will have lower thresholds for responding to such treatments than will

large-diameter axons. Since extracellular electrical currents, a major modality for affecting neural activity, preferentially affect large-diameter axons before affecting small-diameter axons (Rattay 1986), the results presented in this study open up a range of new approaches to analyzing nervous system function, and new ways to alter physiology or to treat diseases that selectively affect small-diameter unmyelinated axons (Dubin 2010, Duchesne 2016, Pekala 2016).

The modified Hodgkin/Huxley model presented in this chapter more accurately describes the response of squid giant axons to changes in temperature than does the original Hodgkin Huxley model (Fig. 3-2). The modified model still has significant limitations. It does not fully capture the complexities of the activation and inactivation of the sodium ion channel (e.g., (Clay 1998, Sangrey 2004)), which may be important for fully understanding the response of axons to increasing temperatures. It does not capture the sub-classes of voltage-dependent potassium ion channels that have been described in the squid giant axon (Rosenthal 2012), which could account for some aspects of temperature responses (Garrett 2012). Finally, if the modified model were to be applied to studies of unmyelinated C fibers in vertebrates, it would also need to capture the properties of other ion channels that are known to be present and sensitive to temperature, such as TRP channels (Cortright 2007, Patapoutian 2003, Voets 2014). Despite these limitations, both the original and the modified Hodgkin/Huxley model are in substantial qualitative agreement, and the results presented in this study are an important step towards developing a fuller understanding of a novel modality for modifying neural activity.

Previous studies of invertebrate axons have indicated that the operating temperatures of poikilotherms (such as fish, lizards, insects, or mollusks) range from above freezing to about 40˚C, and that animals can tolerate changes in temperature over this range both through changes in

behavior and in properties of their neurons (Galarza-Muñoz 2011, Janssen 1992, Prosser 1981, Robertson 2012). In contrast, the operating temperatures for homeotherms is about the top of the range for poikilotherms, and homeotherms can generally tolerate only a few degrees of change in temperature. Elevated temperatures can block unmyelinated fibers in the gray matter of mammalian cerebellum and hippocampus, which may contribute to many of the symptoms of fever (Pekala 2016). In the periphery, temperature can significantly affect the transmission of motor signals in patients suffering from de-myelinating diseases such as multiple sclerosis (Schauf 1974), as well as in normal subjects (Rutkove 1997). Thus, applying the results of these studies to vertebrate axons will require the development of models more suitable to vertebrate operating temperatures.

The model we have presented has implications for understanding thermal block in mammalian systems. Studies of individual *unmyelinated* C fibers in primates that are sensitive to both temperature and mechanical stimuli suggested that fatigue in response to high temperature stimuli, which increased strongly with temperature, might be due to prolonged hyperpolarization; the authors point out, however, that transduction of the signals and initiation of action potentials might also play an important role (Peng 2003). A recent study in *myelinated* peripheral human sensory and motor axons demonstrated that safety factors were reduced in response to hyperthermia, which could lead to thermal block, and modeling of the results suggested that a major factor underlying these changes was alterations in slow potassium ion channels. In addition, a hyperpolarizing activated cation current, I_h, was reduced, and this could also reduce recovery of axons from hyperpolarization due to activity (Howells 2013). As the investigators point out, the sensitivity of these myelinated fibers to temperature has significant implications for their responses to fever and to demyelinating diseases such as multiple sclerosis.

To generalize the conclusions shown in this chapter to vertebrate unmyelinated axons, it will also be critical to characterize the role of the other voltage-activated channels that have been found in these axons, such as TRP channels, many of which are thermally sensitive (Cortright 2007, Patapoutian 2003, Voets 2014). In very fine axons, in which there are many fewer ion channels, it may be necessary to modify the kinetics of ion channels, which differ across species (Krouchev 2015), as well as incorporate channel noise and the non-uniform distributions of ion channels along the axon (Neishabouri 2014). Capturing the changes in the resting potential, which could affect the voltage-activated channels, may require incorporating the temperature-dependence of the chloride channels (Pusch 1997). If the constricted extracellular space affects the external resistance, the model could also be modified to incorporate the effect of this resistance (Wu 1997).

Other investigators have begun to create models of the effects of infrared laser light on neural excitability. To model the excitatory effects of infrared light, a model modified the capacitance of the Hodgkin/Huxley model in response to increasing temperature. The resulting model generated action potentials in response to rapid temperature increases (Fribance 2016). The mechanisms, targets and progress in modeling thermal excitation has been recently reviewed in (Ford 2018, Thompson 2014, Zhao 2016). A modeling study of *Xenopus myelinated* fibers indicated that high temperatures from a continuous wave laser focused on single nodal regions could block action potential initiation or propagation, which they argued was consistent with faster sodium inactivation and stronger potassium channel activation. These investigators also showed, experimentally, that electrical stimulation thresholds to evoke an electrical response increased in response to laser heating (Mou 2012).

Developing better models of the effects of laser light, and other thermal modalities for affecting neural activity, may provide important insights into the relationship between the spatio-temporal dynamics of temperature and neuronal function during disease. In the periphery, temperature can significantly affect the transmission of motor signals in patients suffering from de-myelinating diseases such as multiple sclerosis (Schauf 1974), as well as in normal subjects (Rutkove 1997).

Finally, these results suggest that the predictions of the mathematical model (Lothet 2017 – Supplemental Materials) that smaller-diameter axons may have lower thresholds for response than larger-diameter axons to any modality that acts along their surface. Thus, cuff applications of ion channel blockers or agonists may selectively affect the sub-population of smaller-diameter axons, and this in turn could lead to new approaches to analyzing the nervous system, or to novel treatments of diseases that affect smaller-diameter axons.

3.6   Conclusion

In conclusion, a range of models of thermally-sensitive unmyelinated axons suggest that thermal inhibition, especially at higher temperatures, is due to the faster activation of voltage-dependent potassium ion channels. In turn, these channels generate a hyperpolarizing current that effectively blocks depolarizing currents. The minimum length needed to block action potential initiation, propagation, or repetitive firing scales with the square root of an axon's diameter. Manipulations of relatively short axonal regions containing voltage-dependent potassium ion channels could selectively block fine, unmyelinated axons, such as C fibers, that carry pain and other sensory information.

4 IMPORTANCE OF POTASSIUM CHANNELS DURING INFRARED INHIBITION IN *APLYSIA CALIFORNICA*

4.1 Abstract

Elevated temperatures induced by infrared laser irradiation have been shown experimentally to inhibit action potential (AP) generation and propagation in rats and in *Aplysia*. It is hypothesized that laser-induced water absorption locally increases temperature in the axon which leads to abnormal opening and closing rates for voltage-gated ion channels. Through modeling studies, we have shown that potassium channels are required to observe thermal block in squid giant axon model. In this work, experimental evidence for this modeling conclusion is shown. Pleural abdominal nerves from *Aplysia californica* were placed in a specially designed chamber. Suction electrodes were placed at both ends of the nerve. The nerve was subjected to infrared irradiation (1875 nm), and a thermal block was obtained. Thereafter, using the custom chamber the potassium channels in the nerve were blocked by applying a potassium channel blocker, tetraethylammonium (TEA) only at a spatially confined region (2.5- 3 mm), approximately at the center of the axon length, around the region of irradiation. The thermal nerve block that was seen when the nerve was irradiated was abolished in the presence of TEA. This effect was reversible as the thermal block was restored when TEA in the region was removed after multiple washouts. Control experiments using sodium current blockers (choline chloride and tetrodotoxin - TTX) failed to block the propagation of compound action potentials in the setup. These observations suggest that potassium channels are necessary and sufficient to cause thermal block in unmyelinated nerves, as predicted by our modeling studies.

A version of this chapter is currently submitted to *Neurophotonics Letters* as 'Voltage-gated Potassium Channels are Critical for Infrared Inhibition of Action Potential: An Experimental Study'

4.2   Introduction

Precise control of neural activity (neuromodulation) is a challenge that has major scientific and clinical applications for treating and managing symptoms and conditions which are neuropathic in origin (Mekhail 2010). Electrical methods of neuromodulation have been used for some time, primary applications being in chronic pain management, pacemakers, cochlear implants (Verrills 2016). These techniques suffer from disadvantages like surgical complications, lead migration, lead breakage, and tolerance buildup (Bendersky 2015). There is a need for an alternate modality of neuromodulation that can mitigate, if not completely eliminate these disadvantages (Chernov 2012). Use of infrared (IR) irradiation on nerves could be one such method. It has been previously shown that infrared light can be used for excitation (Duke 2009, Wells 2007, Wells 2005) and inhibition of nerves (Duke 2013, Lothet 2014, 2017, Wang 2016) . Duke et al (Duke 2013) were able to inhibit both the generation and propagation of compound action potentials in rats and sea slugs (*Aplysia californica*). Lothet et al. (Lothet 2014) were able to observe inhibition in *Aplysia* using a combination of high frequency electrical stimulation and infrared laser irradiation. Using this method , they were able to eliminate onset responses often associated with the nerve blocks during high frequency electrical conduction block (Ackermann 2010). Wang et al. (Wang 2016) were able to obtain spatially specific contraction blocks in quail embryo hearts. The technique of infrared inhibition of nerves is spatially precise and can be targeted to particular axons. It has also been shown that the IR inhibition can selectively target small diameter axons (Lothet 2017). In this study, they were able to selectively inhibit small

diameter axons in sea slugs (*Aplysia californica*) and musk shrew (*Suncus murinus*) by varying the levels of radiant exposure of the irradiated infrared light. The ability to target axons of small diameters helps motivate IR (infrared) inhibition as a modality that can target finer pain carrying fibers causing undesirable side effects on other larger axons.

Understanding the mechanism of action of IR on nerves is critical to exploit the potential of IR inhibition as a clinical or even experimental modality. It is believed that heating caused by IR absorption of nerves is responsible for observing inhibition (Ganguly 2016, Huxley 1959, Mou 2012). From prior simulations using a Hodgkin Huxley based computer model in NEURON (Ganguly 2016), we hypothesize *that the mechanism underlying infrared inhibition of action potentials is a thermally-driven enhancement of the activation of voltage-gated potassium ion channels*. When a depolarizing current travels through a region of heated axon, it is counteracted by hyperpolarizing currents through those ion channels (Ganguly 2016). The role of increased potassium channels in causing thermal block have also been mentioned in previous literature (Beam 1983, Lee 1990, Liu 2003). Using the NEURON model (chapter 3 in this dissertation), we have shown that removing voltage dependent potassium channels in a localized region of the axon eliminated the ability of elevated temperatures to induce propagation block of action potentials along the axon. As a control, using the same NEURON model, we have also shown that blocking voltage dependent sodium ion channels does not eliminate the ability of elevated temperatures to cause thermal block (Please refer to Figs. 3-5 and 3-7).

To experimentally test both these hypotheses derived from the modeling studies, we have used a tractable system of the marine mollusk *Aplysia californica*. *Aplysia* have unmyelinated axons that range from 1-10s of microns in diameter (Bedini 2000, Moroz 2011). Using excised

nerves (pleural abdominal) from *Aplysia*, we sought to determine whether the ability of infrared light to cause nerve block would be compromised by inhibiting the activity of voltage-dependent potassium ion channels and would be relatively unaffected when the activity of voltage-dependent sodium ion channels is blocked. Conduction blocks have been reported to disappear when potassium channel blocker is introduced. Multiple studies done by Eliasson et al. (Eliasson 1989, Eliasson 1991, Eliasson 1986) showed that conduction blocks, which were produced as a result of nerve heating (RF heating 45-50 °C) ,were abolished when using potassium channel blockers, 4-aminopyridine and tetraethylammonium (TEA). At that time, they couldn't provide a suitable explanation for their observation. Additional studies by Bostock et al. (Bostock 1981) and Wu et al. (Wu 2001) have confirmed that effects of nerve heating are reversed by the application of potassium channel blockers. To the best of our knowledge, our results provides the first instance of the effects of both potassium and sodium channel blockers in an unmyelinated nerve system, during infrared inhibition. These observations suggest that conduction blocks generated through thermal modalities appear to share a common underlying mechanism with other inhibition modalities, for example focused ultrasound inhibition (Prieto 2018).

In this study, we have designed and fabricated a 3D printed chamber (details in Methods section) that allowed us to administer selective ion channel blocking agents on a specific length of the nerve while simultaneously irradiating that region with IR light. This allows us to monitor the effect of selectively blocking ion channels on the effect of the infrared light to block propagation of nerve signals in *Aplysia californica.* Results appear to suggest that selectively inhibiting voltage-dependent potassium ion channels compromises IR-induced thermal block, whereas

selectively inhibiting voltage-dependent sodium ion channels does not affect IR block significantly. This conclusion is consistent with our modeling predictions.

4.3   Methods

4.3.1   *Aplysia* preparation and nerve dissection

Aplysia californica weighing 250–350 g (Marinus Scientific, Long Beach, CA) were maintained in an aerated aquarium containing circulating artificial seawater (ASW) kept at 16–17°C. The animals were fed dried seaweed every 1–3 days. *Aplysia* were anesthetized with an injection of 333 mM $MgCl_2$ (~50% of body weight) prior to dissection. Once they were anesthetized, they were dissected and the right pleural abdominal (PA) nerve was removed and placed in a custom chamber containing *Aplysia* saline (460 mM NaCl, 10 mM KCl, 22 mM $MgCl_2$, 33 mM $MgSO_4$, 10 mM $CaCl_2$, 10 mM glucose, 10 mM HEPES, pH 7.6). Because the nerve was removed from its associated ganglion, little or no spontaneous neural activity was observed.

4.3.2   *Aplysia* electrophysiology, electrodes, stimulation protocol

The pleural abdominal (PA) nerve was suctioned into nerve-recording electrodes to record their electrophysiological response. Nerve-recording electrodes were made by hand-pulling polyethylene tubing (1.27 mm outer diameter, 0.86 mm inner diameter) over a flame and cutting them to the desired diameter. Recording electrodes were suction-filled with *Aplysia* saline prior to suctioning of the nerve. Nerve signals were amplified (×10000) and band-pass filtered (300–500 Hz) using an AC-coupled differential amplifier (A-M Systems, Sequim, WA), digitized using an Axon Digidata 1440A digitizer (Molecular Devices, San Jose, CA) and recorded using Clampex computer software (Molecular Devices, San Jose, CA). Monophasic stimulation current was

supplied by a WPI A365 stimulus isolator (World Precision Instruments, Sarasota, FL) for all experiments (stimulation parameters 200 μA, τ_p = 2 ms, 1 Hz).
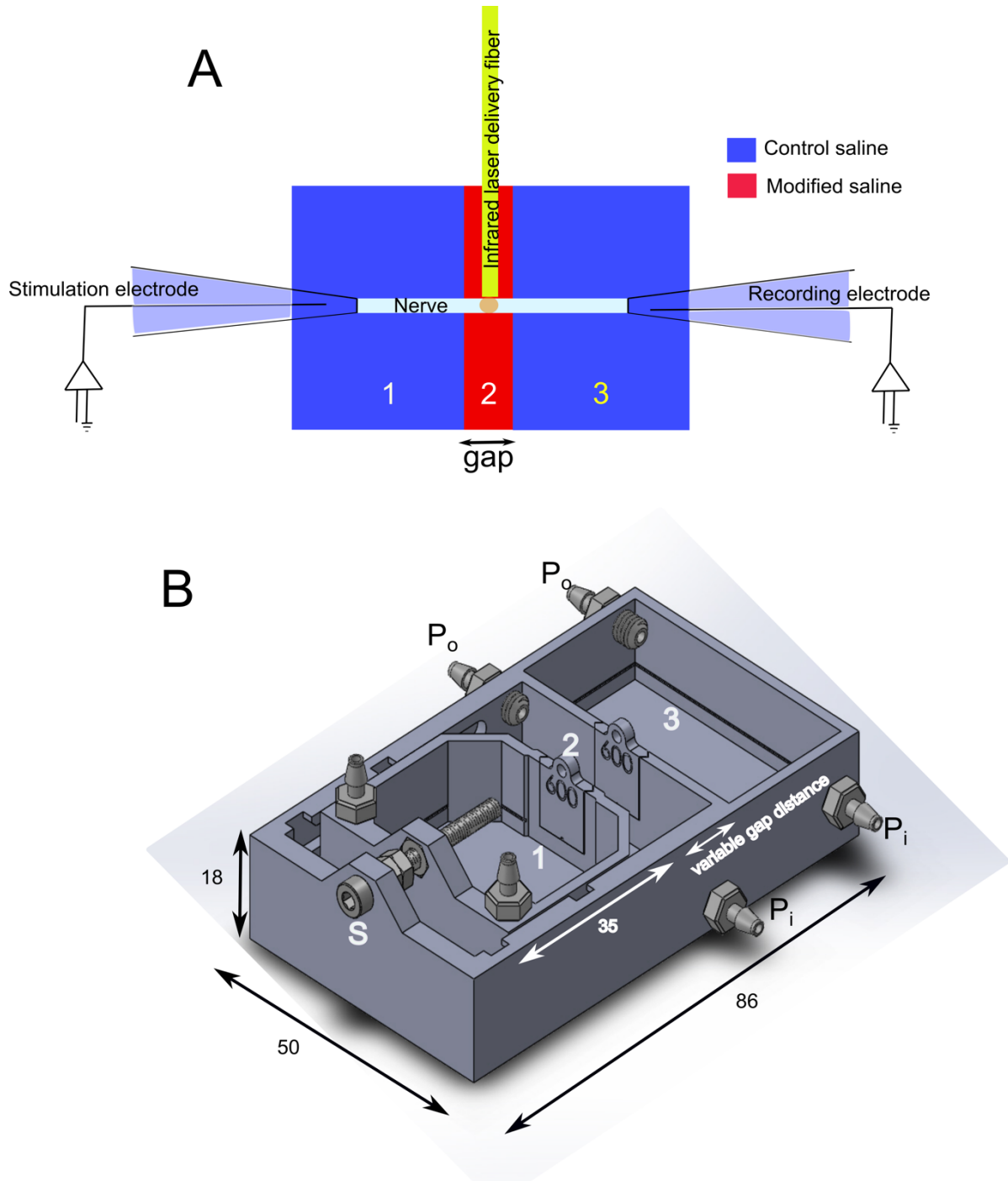
Figure 4-1: Schematic of experimental setup

(**A**) Schematic of experimental setup. The setup consists of a nerve in a three-dimensional chamber (shown in B) that consists of three sections (1,2,3). The sections at the ends (shown in blue) contain normal saline to allow for generation and recording of compound action potentials. The section in the middle (2, shown in red) contains saline solution with ion channel blockers. The nerve is irradiated with infrared laser in the middle section and suction electrodes are used at the ends allow for stimulation and recording for compound action potentials in the nerve. (**B**) Computer aided design of the nerve chamber used for our experiments. The screw (S) shown allows for change in the length of the gap of the middle section of the chamber, which exposes the nerve to the ion channels used in the experiments. Dimensions shown in mm. P_i and P_o are the inlet and outlet flow ports. The '*600*' on the chamber doors show that the doors have a 600 μm sized groove that allows for the nerve to lay under without any damage when the doors are slid down.

4.3.3   Light delivery to nerve

The laser system consisted of a tunable diode laser (Capella Neurostimulator; Lockheed-Martin-Aculight, Bothell, WA) with wavelength $\lambda = 1875$ nm coupled to a 400 μm diameter fiber optic (Ocean Optics, Dunedin, FL). The optical fiber (multimode) was secured in place using micromanipulators (Fig 1A). The laser was triggered at 200 Hz with 200 μs pulses for all experiments. Radiant exposures per pulse at the fiber output were calculated after measuring the power output using a power meter. The optical fiber was maintained in contact with the nerve surface for all irradiation experiments.

4.3.4   Chamber design and structure

A specially designed chamber was fabricated for the experiments. The chamber, as shown in Fig. 4-1B, consists of 3 sections. The chamber was 3D printed on a black Formlabs Standard Resin (https://formlabs.com/store/us/form-2/materials/black-resin/), 50 μm layer height, on a Form 2 printer (Formlabs Inc., Somerville, MA). The sections within the chamber were separated using 3D printed partitions using HP 3D High Reusability PA 12 to perfect the finer details of the doors. Resin was used for printing since it provided a good balance between quality and cost. An

SLA (stereolithography) printing method was used to fine print the small features. The chamber was printed in black to act as good contrast when working with *Aplysia californica* nerves, which are whitish in color. The Formlabs Standard Resin prints were compatible with black paint polishing. A fine screw is used to adjust the width of the middle section according to the experimental requirements. The screw has a 0.5 mm thread spacing which allows to move the chamber by 0.5 mm with each turn. For experiments described in this chapter, this width was maintained between 2.5-3 mm. This width is short enough to allow the transmission of nerve signals from the largest nerve units to pass through the section under the presence of voltage-gated sodium ion channel blockers. The width was also wide enough to allow reliable placement of the optical fiber in contact with the nerve. The partitions have tiny grooves (diameter 600 μm) to allow for the nerve to fit snugly when the partitions were gently placed down on the nerves. Any additional leaks were plugged by brushing the edges of the partitions with '*Vaseline*' (Unilever, London/Rotterdam) petroleum jelly. 'Vaseline' was used since it provides a good seal and is biocompatible with biological tissues.

4.3.5   Channel blockers and inhibitors

In order to test our hypotheses derived from computational modeling studies, as mentioned in the introduction, we used a voltage gated potassium ion channel blocker (Tetra-ethyl chloride, TEA), a sodium chloride substitute (choline chloride), and voltage gated sodium ion channel blocker (Tetrodotoxin). Tetra-ethyl ammonium chloride (50 mM) solution was prepared by adding tetraethylammonium chloride (Sigma Aldrich, St. Louis, MO) to a version of the *Aplysia* saline (410 mM NaCl, 50 mM TEA, 10 mM KCl, 22 mM $MgCl_2$, 33 mM $MgSO_4$, 10 mM $CaCl_2$, 10 mM glucose, 10 mM HEPES, pH 7.6). In this modified saline solution, an identical concentration (50 mM) of sodium chloride was replaced by tetraethylammonium chloride. This was done in

order to maintain the osmolarity of the TEA solution with that of the control *Aplysia* saline. The concentration and the saline recipe was consistent with past studies of TEA on *Aplysia* (Hermann & Gorman, 1981, 1979). The rationale for using TEA in our study is that since TEA blocks voltage dependent potassium channels, it tests the hypothesis that *activation of voltage dependent potassium channels is critical for observing IR blocks*.

Choline chloride solution was prepared by adding choline chloride (Sigma Aldrich, St. Louis, MO) to a control (normal) *Aplysia* saline, in which sodium chloride is replaced by an equal concentration of choline chloride (460 mM), to maintain osmolarity (460 mM ChCl, 10 mM KCl, 22 mM $MgCl_2$, 33 mM $MgSO_4$, 10 mM $CaCl_2$, 10 mM glucose, 10 mM HEPES, pH 7.6).

Tetrodotoxin (TTX, 1 mg) was purchased from Enzo Life Sciences (Farmingdale, NY). The toxin was diluted to 1 mM and then aliquoted to 300 μL tubes. To prepare a 60 μM TTX saline solution, contents from two of the 300 μL of 1 mM TTX are added to normal *Aplysia* saline solution to make the final volume of the solution 10 mL. The concentration of tetrodotoxin in saline is chosen to be consistent and in range of that observed in published experimental studies in *Aplysia* (Futamachi 1982, Geduldig 1970, Miller 2011). The effect of all ion channel blockers was reversible which was confirmed by performing recordings after washing off the ion channel blocker solutions through multiple washouts. The effect of TEA took 2-4 washouts over approximately 30 minutes to be washed out. The effect of TTX took 2-3 washouts over approximately 15 minutes to be washed out. The pH of all versions of saline solutions used were adjusted to 7.6, which is the same as that of the normal *Aplysia* saline. All solutions were brought to room temperature prior to infusion in the chamber. Use of choline chloride and TTX disrupts sodium currents by blocking sodium influx and voltage dependent sodium channels respectively.

Hence their use will help test the hypothesis that *voltage blocking dependent sodium channels don't significantly affect IR blocks*.

4.3.6   Methodology, Characterization of block

Our nerve recording protocol consisted of multiple recordings of 20 second intervals. The nerve was electrically stimulated at a frequency of 1 Hz. Each recording consisted of three phases, 1) the time when the laser is OFF (t = 0-5 secs), 2) the time when the laser is ON (t = 5-15 secs), and 3) the time when the laser is OFF (t = 15-20 seconds), as shown in Fig. 4-2. Phase 3 of the recording allows for the nerve to recover from the thermal block induced by the IR laser irradiation during the second phase of the recording. In each study, the power of the laser was adjusted to obtain a complete block of the compound action potential within the first five seconds of the laser turning on. The radiant exposure hence determined was kept constant for the entire duration of a study. Studies mentioned in the chapter consisted of three experimental conditions. First, normal saline solution was introduced in the middle section of the chamber for control recordings. In the other two experiments, the saline was replaced by the ion channel blocker solutions (TEA and Choline/TTX). The study was conducted in a series of experiments in A-B-A-C-A (Fig 4-3) or A-B-A-D-A (Fig 4-4) format. Experiment A refers to the observation of an IR block in the control saline solution, before any ion channel blocker is introduced (Fig. 4-3B, 4-4B). In the experimental condition involving the use of TEA, experiment B refers to the observation of IR block failure in the presence of IR (Fig. 4-3F), and experiment C refers to the observation of IR block in the presence of choline chloride in the chamber (Fig. 4-3J). In the experimental condition involving the use of TTX, experiment D refers to the observation of IR block in the presence of TTX in the chamber (Fig. 4-4J). In the experimental condition involving the use of TEA, experiment B refers to the failure to observe thermal blocks in the presence of IR (Fig. 4-3F) The height of fluid in the

middle was kept slightly higher than the surrounding sections to prevent fluid flow from the surrounding sections into the middle section. Once an observation was recorded (block or block failure), the ion channel blocker solution was washed off and replaced by fresh control saline solution, until the amplitude of the compound action potentials was restored to the level observed prior to the introduction of the ion channel blocker solution. Washouts and replacement of solution was done by first sucking off the ion channel blocker solution using a 2 mL disposable dropper and introducing the replacement solution (fresh saline) using another disposable dropper. During each of the experimental conditions with a nerve, the radiant exposure was kept constant throughout. Six nerves were used for the study that exposed the nerves to TEA and choline solutions. Three nerves were used for the study exposing nerves to TEA and TTX solution. The order of the TEA and choline application was varied, and it wasn't found to have any effect on the final outcome of the study.

4.3.7   Data acquisition and analysis

Compound nerve action potentials (CNAPs) were acquired at 50 kHz. Clampex (Molecular Devices, San Jose, CA) was used to record acquired data in the computer. After acquisition, data analysis was performed using a combination of AxoGraph X (Axograph Scientific, Berkeley, CA), Matlab (Mathworks, Natick, MA) and Microsoft Excel (Microsoft, Redmond, WA). Each recording was divided into three phases (laser off 0-5 sec, laser on 5-15 sec, laser off 15-20 sec, Fig. 4-2 top). The rectified area under the curve (rAUC) was evaluated for signals in each phase of the recording. The average of the areas under 'laser on' phase (phase 1, 3) were plotted and analyzed for significance. For the 'laser off' phase (phase 2), rAUC for the signals observed between t = 11-15 seconds of the recordings were considered. This was done to ascertain that IR blocks had been established for stimulations where rAUC was calculated. Using the truncated time

frame allows to calculate average rAUC over five events (stimulus), which is equal to the number of events in rAUC calculations in phase 1 and phase 2. The areas were normalized to the average area calculated for when the laser was off, during the first phase of the recording. Similar analysis have been used in the past for analyzing infrared inhibition in *Aplysia* (Lothet 2017).

4.4   Results

4.4.1   Control block (IR block in saline)

The effect of using IR irradiation is shown in Fig. 4-2. These recordings show a recording trace from a representative thermal block experiment. In the specific study shown in Fig. 4-2, the block was obtained within 2 seconds (Fig 4-2A shown in red). Activity returns when the laser is turned off, 10 seconds after it was switched on, demonstrating that the effect of the IR irradiation is reversible and doesn't compromise the functionality of the nerve. Higher temporal resolution views of signals from each phase are shown in Fig. 4-2B,C,D. This can be ascertained when the average of the normalized areas under the curve is analyzed. The areas of pre- and post-laser irradiation (phase 1 and phase 3 of the recording) do not differ significantly ($p > 0.05$). The normalized area under the curves for phase 2 are smaller than that of both phase 3 and phase 1 and is significantly different ($p < 0.05$). The comparison of areas is shown in Fig. 4-3 (D, H, L)
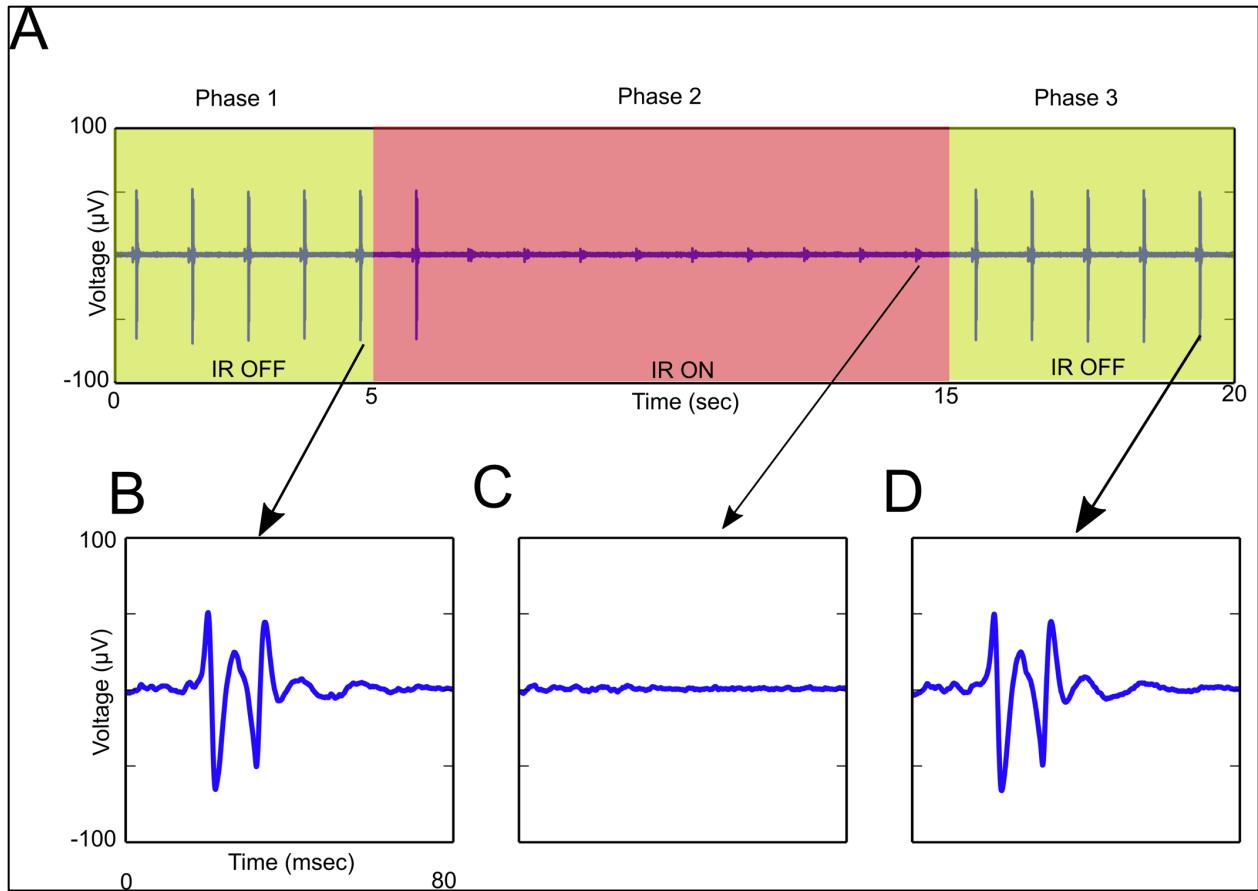
Figure 4-2: Recording obtained in normal *Aplysia* saline

(**A**) Recording showing a block obtained when the nerve is in normal *Aplysia* saline. The laser is switched off for the first 5 seconds (green), switched on the next 10 seconds (red), and switched off for the last 5 seconds (green) of each recording. In the recording shown, thermal block is observed within the first two seconds of the laser being switched on. The nerve returns to normal activity immediately after the laser switched off showing the reversibility of the block mechanism and indicating that the irradiation is non-damaging in nature. (**B, C, D**). Three signals from the recordings are shown at higher temporal resolution in each of the three phases of the recording (pre-irradiation (B), during irradiation (C), and post irradiation(D)). In each of the signals shown, the electric stimulation artefacts are removed. (Laser parameters $\lambda = 1875$nm, optical fiber size = 400 μm, f = 200Hz, $\tau_p = 200$ μs, $H_o = 183$ mJ/cm^2)

4.4.2   Effect of TEA

Once the control saline is washed off from the middle section of the chamber, and TEA (tetraethyl ammonium chloride) rich saline solution is added to the middle section of the chamber, the blocking effect of IR irradiation as observed during the control saline block disappeared (Fig.

4-3F). Signals observed during the 'laser on' (second) phase of the recordings were significantly similar (p>0.05) to the areas observed prior to the laser on phase (Fig. 4-3, D,H,L) The time taken for TEA to take effect was variable in different experiments (34 ± 12 mins). The effect of TEA was reversible and usually required three to four washouts with approximately 5 mL saline in each washout.

4.4.3 Effect of choline chloride

When choline chloride is added to the middle section of the chamber, the block effect of the IR irradiation appears to be unaffected. These results are shown in Fig. 4-3 I-L.
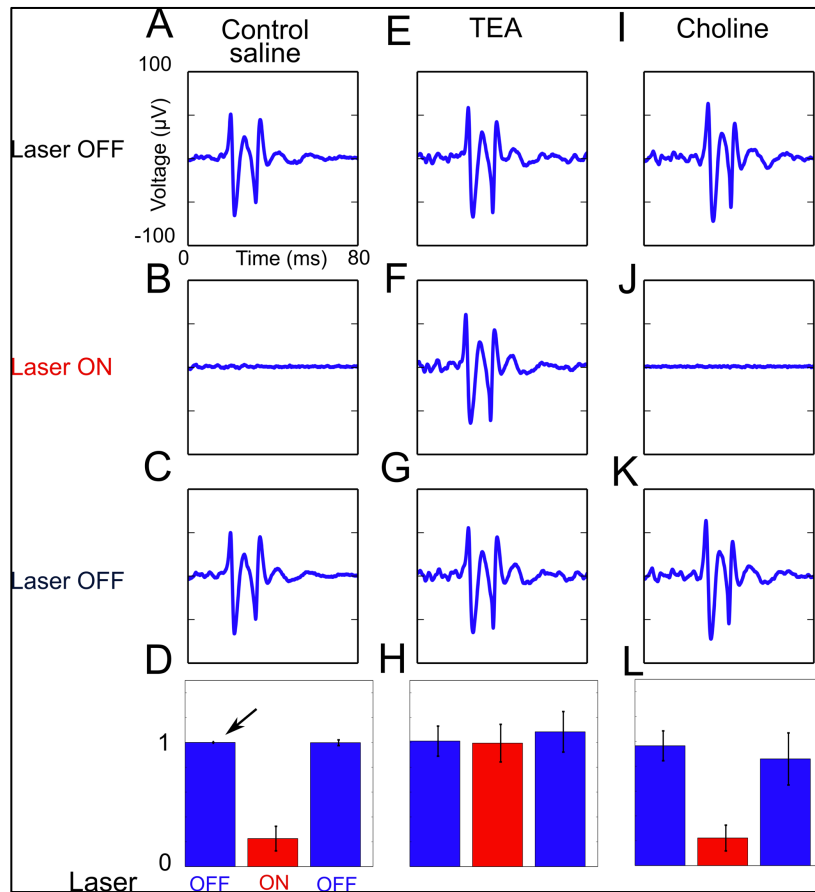
Figure 4-3: Representative signals from a nerve undergoing block (Choline)

High temporal resolution views of representative signals from a nerve undergoing block under the effect of various ion channel blockers. (Laser parameters $\lambda = 1875$nm, optical fiber size = 400 μm, f = 200Hz, $\tau_p = 200$ μs, $H_o = 183$ mJ/cm^2). Thermal inhibition is observed in control (normal) saline (**B**), and in choline chloride (**J**) when the IR laser is switched on. Thermal inhibition fails when the potassium channel blocker (tetraethylammonium chloride TEA) is used (**F**). These effects are quantified in the form of rectified areas under the curve (**D, H, L,** n = 6). All areas are normalized to the area under curve prior to laser irradiation (black arrow). Signals prior to, during, and after laser irradiation in control saline (**A-C**), in TEA (**E-G**), and in choline (**I-K**) are also shown.

4.4.4   Effect of TTX

The effect of the addition of TTX (Fig. 4-4) is similar to that observed to the effect of choline chloride. The nerve was monitored for two hours post introduction of TTX to allow TTX enough time to take effect. Under the influence of TTX, some smaller peaks of the compound action potential seemed to disappear (Fig. 4-4I). When the nerve was exposed to IR light in the presence of TTX, thermal block was observed (Fig. 4-4J). Similar to other channel blockers TEA and choline, the effect of TTX is also reversible. In these experiments, the effect of TTX was observed as the reduction of CAP amplitude and reduction in area under the compound action potential. Effects of TTX were reversible as TTX was washed out using 2-3 washouts with approximately 5 mL of saline in each washout. These effects are consistent with published experimental results and prior modeling results.
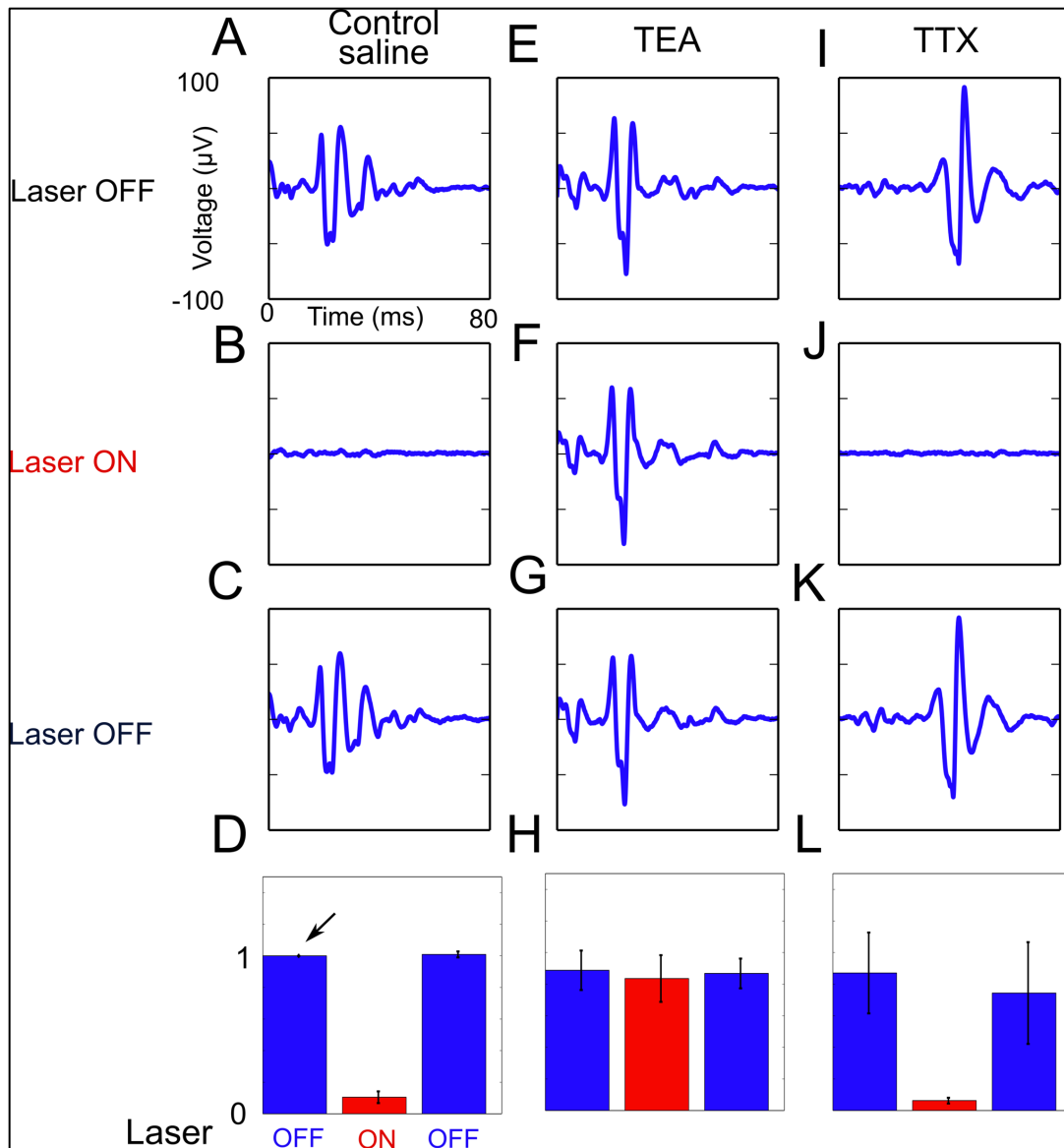
Figure 4-4: Representative signals from a nerve undergoing block (TTX)

High temporal resolution view of representative signals prior to, during, and after laser irradiation in control saline (**A-C**), in TEA (**E-G**), and in TTX (**I-K**) are also shown. Thermal inhibition is observed in control (normal) saline (**B**), and in TTX (**J**) when the IR laser is switched on. Thermal inhibition fails when the potassium channel blocker (tetraethylammonium chloride TEA) is used (**F**). These effects are quantified in the form of rectified areas under the curve (**D, H, L,** n = 3). All areas are normalized to the area under curve of the saline prior to laser irradiation (black arrow). Signals prior, during, and after laser irradiation in control saline (**A-C**), in TEA (**E-G**), and in TTX (**I-K**) are also shown.

106

4.5   Discussion

In this chapter, it was shown that blocking voltage gated potassium ion channels using TEA in a region of the pleural abdominal nerve of *Aplysia californica* disrupts the ability of infrared irradiation to cause thermal block. Additionally, it was also shown that weakening either sodium current influx (using choline chloride) or blocking voltage gated sodium ion channels (using TTX) doesn't have any significant effect ($p > 0.05$) on the thermal block observed. These observations suggest that the voltage gated potassium channels are critical to infrared mediated thermal blocks in unmyelinated nerves such as that of *Aplysia*. It also suggests that sodium channels do not play a significant role in establishing a thermal block. These observations are consistent with the results predicted using computational models (Ganguly 2016) (also refer to Chapter 3 of the dissertation).

Tetraethyl ammonium chloride (TEA), when added to the nerve was able to reverse the thermal blocks in the nerve. It took around 30-45 minutes to take effect. TEA is expected to work by the diffusion of tetraethyl ammonium ions into the nerve and binding with the potassium ion channels thereby undermining their effect to conduct potassium currents through them (Armstrong 2004, Hille 1967). The time for TEA to show this effect was required likely due to the need for TEA to properly diffuse through the nerve.

Choline chloride was substituted for sodium chloride in one of the solutions tested, which eliminated extracellular sodium around the middle region of the nerve. This removed the sodium currents influx in that region of the nerve (Baker 1969). When the laser is on, choline also appeared to get rid of the 'resistant' components of the CAPs which were visible when blocks were obtained in control saline solutions. (Fig. 4-3B versus Fig. 4-3I). These components are evident in the form of small 'fuzz' visible when observing thermal block in control saline (Fig. 4-3B). In control saline

experimental conditions, these 'resistant' signal components seem to disappear when the laser power was increased (result not shown). However, in our studies, it was not desirable to increase the power level to such extents in order to avoid thermal damage to the nerve. These seemingly thermally resistant signal components have been observed in past experiments with *Aplysia* when higher levels of stimulation currents are used (Lothet 2017). Adding tetrodotoxin in the chamber section had effects similar to that observed with choline. The concentration and time required for TTX was determined using whole bath experiments. These thermally resistant units may represent axons that have sodium ion channels that are resistant to higher temperatures, but conduct sodium ions, and thus are sensitive to choline substitution, and are blocked by TTX.

The three-dimensional printed nerve chamber suffers from some design challenges. The current design of the chamber doesn't allow for the fine movement of partitions and working with gap distances below 2 mm is fraught with issues of visibility and reliable placement of optical fibers on the nerve. This hinders the use of chamber when studying the differential effect of ion channel blockers on finer axon diameters. Future iterations for design improvements are currently under preparation. Due to imperfections and limited spatial precision of three-dimensional printing and the space occupied by the nerve itself, there is a possibility of small leaks between the sections in the center and the adjacent ones. Even though we tried to seal the openings with Vaseline, there might arise a possibility of some sodium ions from adjacent sections (section 1 and 3 as shown in Fig 4-1B) to be present in the middle section of the chamber, and potentially partially negate the use of choline for sodium current block. Maintaining the solution in the middle section to be higher than the adjacent sections also minimized any movement of solutions into the middle section through hydrostatic pressure. However, the use of sodium channel blocker TTX in the center section will negates the effect of any leakage from the adjacent sections, since TTX directly blocks

sodium ion channels, blocks any sodium current that may arise due to potential leakage of sodium ions into the center compartment of the chamber.

It has been shown that elevated temperatures also modulate potassium conductance in mammalian systems. Beam and Donaldson showed that in mammalian systems, potassium activation kinetics appear to change with rise in temperature (Beam 1983). Their results suggested that change in temperature leads to change in kinetic transition states in potassium channel gating. Work by Fleischmann et al. showed that outward currents in ferret muscle cells, which are dominated by voltage dependent potassium currents, increased markedly when the bath temperature rose from 22 to 35°C (Fleischmann 1993). They believed that this increase in current is due to the effect of temperature on maximum conductance of potassium ion channels, and the kinetics of these currents were likely similar to that exhibited by A-type potassium currents, which are the rapidly inactivating alpha subunits of the voltage-gated potassium channels. Peak potassium conductance has also been reported to increase progressively when human T lymphocytes were heated to above room temperatures (Pahapill 1990). It was suggested that the increase in conductance resulted from both the increase in unit conductance and the increase in the number of so called "sleepy" channels. While all of the above studies examined mammalian systems, we believe that our study is the first to highlight the role of potassium channels during thermal block in an unmyelinated axon system like *Aplysia* caused by infrared laser irradiation.

4.6   Conclusion

In this chapter, it is shown that blocking potassium channels using TEA disrupts the block of compound nerve action potential caused by IR irradiation on the pleural abdominal connective nerve in *Aplysia californica*. Disrupting sodium currents using choline chloride and TTX was

unable to significantly alter IR block. These observations suggest that potassium channels are critical for IR block. These observations align with the modeling predictions in NEURON. The conclusion about the role of potassium channels in IR block is consistent with observations in which block was obtained using alternative thermal block modalities.

5 AN INTEGRATED MODEL FOR OPTIMIZING LASER INDUCED THERMAL INHIBITION IN NERVES

5.1 Abstract

Infrared (IR) laser light (e.g. wavelengths 1.45 µm or 1.87 µm) can induce thermally mediated action potential (AP) block in *Aplysia* and rat nerves. This phenomenon of AP block is reversible and appears safe, but the relationship between the input laser parameters and the resulting laser-induced inhibition of APs is not clearly understood. This prevents optimization and adoption of this technology for clinical applications and limits its use in the research setting. We present a comprehensive computational model that integrates optical-thermal simulations, which consists of Monte-Carlo simulation, to determine light distribution and heat source which is fed into a finite difference thermal model which calculates the temperature distribution as function of space and time. The output from the optical-thermal model component is used by a neurophysiological model based on the NEURON simulation environment which calculates the effect of the temperature rise on the initiation or propagation of APs. An Arrhenius thermal damage parameter integrated into the model calculates which laser parameters are most likely to cause thermally induced changes in the nerve. We observe that the maximum temperature rise due to infrared irradiation at the nerve surface occurs when the optical fiber delivering laser energy is 150 µm from the nerve. At radiant exposures used in neural inhibition experiments, IR fiber diameters below 400 µm are prone to cause thermal damage during thermal inhibition in nerves. The model also predicts that expanding the spatial extent over which the laser light is delivered decreases the minimum temperature rise for thermal block in unmyelinated axons. The model provides a novel tool to explore parameter space of infrared nerve inhibition, and design devices to selectively and safely block AP propagation in nerve fibers.

A version of this chapter is being prepared to be submitted to Neurophotonics Technical Reports for peer review

5.2 Introduction

Pulsed infrared light irradiation alters the excitability of nerve tissues. It can either generate action potentials (Duke 2009, Izzo 2006, Wells 2005, Wells 2007, Wells 2005) , or it can inhibit action potentials generation and propagation in myelinated and in unmyelinated nerves (Duke 2013, Lothet 2014, 2017, Walsh 2016). Currently, a comprehensive mechanism to explain these observations is lacking. However, studies have pointed to different factors that could be responsible for the observation of action potential generation. These mechanistic factors include change in membrane capacitance with heat, activation of heat sensitive channel proteins, and change in membrane porosity. Infrared inhibition of action potentials, however is well established to be a photothermal driven process (Lothet 2017), in which the temperature rise caused due to laser irradiation influences ion channel activity in the nerve cells (Huxley 1959). It has been shown through experiments and computational modeling that elevated temperatures leads to reduction in amplitude of action potentials (Hodgkin 1949, Mou 2012, Rattay 1993). As the temperature of nerve is increased, eventually, there is no propagation of action potential beyond the region of elevated temperature. At this point, the hyperpolarizing potassium ion channel kinetics overwhelm depolarizing sodium channel ion kinetics.

While existing studies have uncovered mechanism for inhibition, they have not focused on the techniques to control infrared nerve inhibition. There is little understanding on the exact relationship between the rise in nerve temperature and the electrophysiological response of the nerve axon. This rise in temperature is governed by the infrared beam characteristics, which

include the irradiance, wavelength, pulse repetition rate, laser beam diameter, and the distance of the laser fiber from the nerve surface (Thompson 2013). The heat generated in the nerve tissue is also dependent on the number of laser delivery fibers present. A careful selection of laser parameters is required that can cause temperature rise high enough to result in neural inhibition, but not so large that it causes thermal damage during the irradiation process. Theoretically, the parameter space that needs to be optimized is infinite and hence, a careful and refining of parameters is required. A computational model will be a useful tool to study the relationship between the laser induced thermal transients and electrophysiological response of the nerve. Ideally, this model should be capable of accepting laser parameters as input and produce a neurophysiological response of the nerve as output. This output will allow us to determine if the temperature rise due to laser irradiation causes nerve inhibition or not. Apart from the inhibition response, the model should also alert us if the selected laser parameters have potential to cause thermal damage. The assembly, validation, and preliminary application of such a model is the purpose of this chapter.

In this chapter, a multiphysics model is developed that combines an optical-thermal computational model with a neurophysiological computational model. The optical-thermal model evaluates the temperature rise in the nerve tissue as a result of the infrared laser irradiation. This is done in two steps. The first step in this process is the distribution of light inside the tissue (Wang 1995), which is evaluated using Monte Carlo simulations. The deposition of light inside the tissue is then used a heat source to evaluate temperature rise inside the tissue, using Pennes' bioheat transfer equation (Pennes 1948). Once the temperature rise is evaluated, a temperature dependent neurophysiological model evaluates the behavior of nerve axon in response to that rise in temperature. These components and their governing equations are explained in detail in the

113

Methods section. Since infrared inhibition entails transient elevation of temperature in the nerve (Lothet 2017), the nerve is vulnerable to thermal damage in the form of thermal denaturation (or other mechanisms) of proteins in the nerves (Sapareto 1984). Infrared lasers allow us to deliver optical energy to a localized space and hence control the resultant temperature rise to prevent nerve damage. Hence there is a need to strike a balance between the inhibitive (potentially valuable) and damaging effects of infrared irradiation. Multiple damage models have been used to evaluate the safety of using the specific inhibition laser parameters.

There are multiple published models that study laser irradiation on nerves. However, none of these models account for all components of laser-nerve interactions (light distribution, heat transfer, and temperature dependent action potential generation and inhibition). Current models either analyze the temperature rise due to the infrared irradiation or use artificial temperature distributions to study neurophysiological responses to temperature rise. Thompson et al. predicted the distribution of light and the temperature rise from a single pulse (Thompson 2012), pulse train and multiple emitters (Thompson 2013). They also compared their modeled temperature rises to experimental measurements of temperature rise as observed during INS (infrared nerve stimulation) in cochlea. Liljemalm et al. (Liljemalm 2014) developed a numerical multiphysics model to predict the temperature rise during INS. In all cases, the temperature rise was observed in the range of $1 - 10\ ^{\circ}\text{C}$ depending on the spatial configurations, the laser power, and the pulse frequency of the laser beam. Mou et al. (Mou 2012) showed the dependence of threshold block temperature (temperature at which thermal block occurs) with the diameter of nerve axon. They simulated high temperatures at specific nodes in a frog (myelinated) sciatic nerve model at varying lengths along the axon. They showed that the threshold temperature required for achieving a propagation block is greater than the threshold temperature required to produce a generation block.

Using their results, they showed that axonal dynamics have a bigger role to play than the local ion channel dynamics in the arrest of a propagating action potential. These results were unable to provide a clear mechanism of the heat block (generation or propagation) observed in nerve due to axonal temperature rise. The heat block simulated in the model was confined to specific spatial nodes. This spatial confinement of temperature is not practical in either experimental electrophysiological setups or in clinical settings. There was little quantitative or qualitative discussion of the change in the gating variables or the ion channels due to increasing temperatures over time. You et al. (You 2017) published their study in which they used a combined electrical and infrared heating to study neural responses in mammalian nerves. In this chapter, they combined the results of a combined Monte Carlo light distribution followed by a temperature rise evaluation. They used the results to study the neurophysiological responses in a frog sciatic nerve computational model. This study shows that a multiphysics model produced by combining a light distribution, heat transfer and neurophysiological response is not only possible, but also useful to study nerve responses to infrared irradiation. You et al.'s specific study was limited to the application of a combined electrical infrared inhibition for selective stimulation of the sciatic nerve, previously shown experimentally by Duke et al. (Duke 2013). We can use a similar setup to establish a modeling platform to study infrared inhibition of unmyelinated nerves, perform parametric evaluation of laser parameters to minimize temperature rise, and explore the feasibility for using alternate modalities of temperature rise that can result in neural inhibition.

Once the model is developed, the efficacy of using various laser parameters for inhibition are studied. Efficacy of a set of laser parameters to produce infrared nerve inhibition is measured in terms of whether irradiation with these particular laser parameters is capable of producing a thermal block without causing thermal damage. The relevant laser parameters considered are laser fiber diameter, the separation of the fiber from the nerve surface, and the number of laser spots.

Other laser parameters such as repetition rate and irradiance were chosen in accordance to those used regularly during experimental work (Ford 2017). The conclusions derived through parametric calculations help develop mechanistic hypothesis and inputs for experimental design, and a path towards a future medical device development. An example is shown in this chapter. The hypothesis that use of adjacent optical fibers instead of one fiber reduces the threshold temperature rise required for inhibition is tested using the model. Lastly, in order to show that this computational model can be combined with sources of heat other than infrared laser irradiation, an example of neural inhibition using resistive heating is shown. A helical steel coil is envisioned that is placed around a model nerve axon and current is passed through it. The heat generated due to the resistance of the wire leads to rise in temperature in the nerve surface that then influences the action potential propagation in the nerve axon.

5.3   Model setup

The model used to study the electrophysiological behavior of nerve axons consists of three different model components (Fig. 5-1A) each governing their own physical phenomena (Eq. 2-1 to 2-13). When nerve tissue is irradiated with laser light, the distribution of infrared light inside the biological tissue (nerve tissue in this case) is governed by the radiative transport equation, and the wavelength dependent tissue optical properties (absorption coefficient and scattering coefficient, Eq. 5-1). In this chapter, we have used the Monte Carlo light distribution method to evaluate the spatial distribution of laser light in the tissue (L. Wang et al., 1995). Followed by the evaluation of light deposition inside the tissue, the deposited energy is converted into heat resulting in temperature rise inside the tissue. This relationship between the delivered energy and temperature rise is governed by the Pennes' bio-heat equation (Eq. 5-2). Laser induced temperature rise is evaluated in the nerve, and the resulting temperature distribution is extracted and used to

predict the change in the electrophysiological changes in the propagation of action potential. The relationship between temperature rise and action potential propagation is governed by the Hodgkin Huxley model equations (Eqs. 2-1 to 2-13). To calculate the light distribution and resultant temperature rise, SESE (Scalable Effects Simulation Environment) has been used (Beier 2014, Walsh 2016). Results from SESE have been used in NEURON to evaluate the electrophysiological response of the axon to spatio-temporal variation of temperature along the axon. In the following section, the tools and the equations used will be discussed in detail along with the assumptions in each of the modeling components.
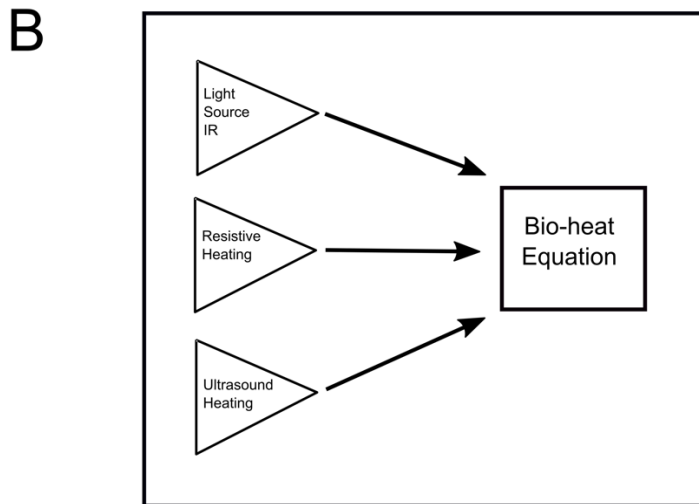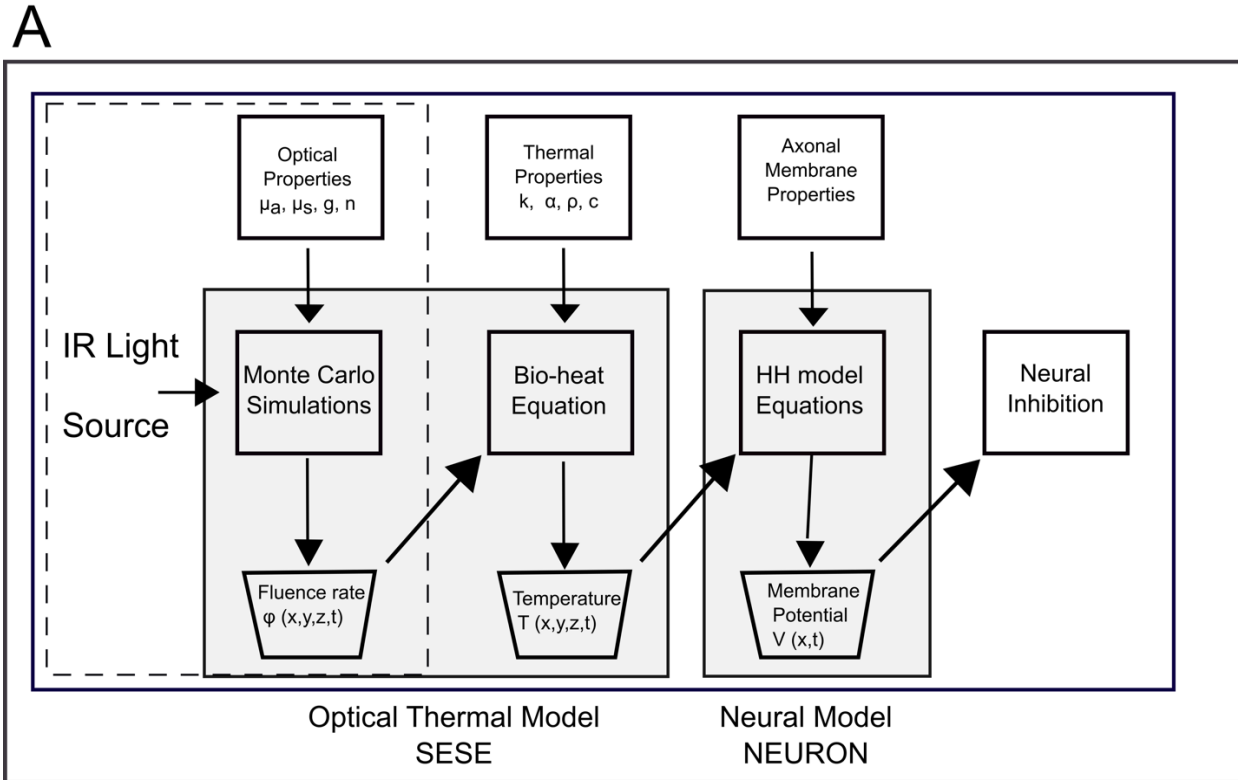
Figure 5-1: Schematic of the model components used in the computational model

 (A) Schematic of the model components used in the computational model. The optical-thermal model evaluates the temperature rise in the nerve tissue as a result of infrared laser irradiation. Once the temperature rise is evaluated, its subsequently used in a temperature dependent neurophysiological model that evaluates the behavior of nerve axon in response to rise in temperature. SESE (Scalable Effects Simulation Environment) is used for calculating light distribution and temperature rise in nerves. NEURON is used for evaluating the resultant neural response due to time and space varying temperature rise from the nerve surface. The components shown inside the dotted box represent the source of the temperature rise feeding into the NEURON

model. **(B)** This section can be replaced with a customizable heat source to study alternate kinds of neural thermal inhibition (eg. Focused ultrasound heating, RF heating).

5.4   Model tools

5.4.1   SESE (Scalable Effects Simulation Environment)

SESE enables the study of materials (tissues) and their response to incident laser irradiation (Beier 2014; Walsh 2016). It can perform transient simulations in three-dimensional space domains. Users can assign inhomogeneous properties to materials with user defined shapes, and physical properties. Laser light sources can be modulated in terms of time dependence of pulses, beam position, beam direction, beam shape, and power. SESE can perform calculations on four mechanism resulting from laser irradiation on the nerve tissue. These are: 1) Light energy distribution through tracing of light rays (photon), 2) diffusion of heat generated due to light absorption due to irradiation, 3) modification of materials structure and boundaries due to material ejection and 4) accounting for change in material's physical properties due to thermal and chemical changes associated with rise in temperature. In this chapter, SESE has been used only for the first two phenomena. It is assumed that there is no material removal due to the laser irradiation used for the modeling studies. It is also assumed that the thermal and optical properties remain constant over the range of temperatures observed.

5.4.2   Light distribution modeling

Light is distributed in biological tissues according to the radiative transport equation (Eq. 5-1) (Welch 2010).

$$\frac{dL(\boldsymbol{r},\hat{\boldsymbol{s}})}{ds} = \mu_a L(\boldsymbol{r},\hat{\boldsymbol{s}}) - \mu_s L(\boldsymbol{r},\hat{\boldsymbol{s}}) + \int_0^{4\pi} p(\hat{\boldsymbol{s}},\hat{\boldsymbol{s}}')L(\boldsymbol{r},\hat{\boldsymbol{s}}')d\omega' + S(\boldsymbol{r},\hat{\boldsymbol{s}}) \qquad (5\text{-}1)$$

where μ_a is the absorption coefficient [1/m], L is the radiance [W/m^2.sr], μ_s is the scattering coefficient [1/m], p is the phase (scattering) function [1/sr] and S is the source term at position $\boldsymbol{r}$ in direction $\hat{\boldsymbol{s}}$ [W/m^3. sr]. This equation considers light propagation as a transport of particles (photons). The equation can be derived from Maxwell's equations for special cases where each particle lies in the far-field of the other particles and there are no correlations between particle positions. The radiative transport equation (RTE), though very rigorous in its approach, is not easy to handle and solve in the closed form. RTE can be solved in the closed form in very few cases, one of them describing transport in one dimension. Hence the idea of stochastic solvers (Monte Carlo simulations) was introduced to replicate the behavior of RTE in tissue mediums. In SESE, laser radiation is modeled as a collection of small packets of energy called "rays (photons)" that can undergo absorption, scattering or reflection or refraction at a material surface. An initial ray position is set by sampling from a probability distribution corresponding to a planar source irradiance distribution. The ray is then propagated along a direction determined by radiance and the interaction at that point, propagation of rays continues until it reaches a boundary or experience a scattering event. As the ray travels, it loses "weight" associated with it exponentially, representative of absorbed photons. The "lost weight" is deposited at the voxel. Once the weight of the ray falls below a certain threshold, its propagation is terminated. Scattering angles at any point are governed by the Henyey Greenstein scattering function (Henyey 1941). At boundaries, the direction of propagation is governed by the Snell's law. The optical properties required to compute the distribution of light inside the tissue for the various geometry components used in the SESE model are listed in Table 5-1.

Optical Properties	Symbol (Units)	Water	Nerve	Optical fiber
Index of refraction	n_r	1.33	1.33	1.46
Absorption coefficient	μ_a (m^{-1})	2700	2130	0 (assumed negligible)
Scattering coefficient	μ_s (m^{-1})	0	0	0
Anisotropy factor	g	0.8	0.9	NA

Table 5-1: Optical properties of different components of the SESE model

(Hale 1973)

We want to study the three-dimensional temperature rise in the nerve and the surrounding tissue. In order to accomplish this, we had to employ a three-dimensional MC (Monte Carlo) model which allows us to 1) use irregular tissue structures, and 2) assign inhomogeneous tissue thermal and optical properties. Some past work in three dimensional Monte Carlo light distributions are included in the excellent review article by Zhu and Liu (Zhu 2013). Pfefer (Pfefer 1996) used a three dimensional modular adaptable grid numerical model (MAGNUM) to evaluate light propagation in a complex biological tissue, and used the model specifically to evaluate the outcome of PWS (port wine stain) treatment. Their results for transmission and diffuse reflectance were within 2% of both the classical (2D) Monte Carlo simulation method and the experimental observations. They also noted the increase in computational effort required to increase the

efficiency of the model in predicting the light distribution inside tissues. Other voxel based studies include tissue structures in an adult human head (Boas 2002) and skin lesions (Patwardhan 2005). Balbas (Margallo-Balbás 2007) and Ren (Ren 2010) developed triangular surface based MC models in order to model light transport in complex tissue structures, with improved approximation of interfaces between different domains, that are computationally less intensive than the voxel based approach. Triangular meshes aren't suitable for incorporating continuously varying optical properties and require scanning a large number of triangular surfaces leading to redundant calculations. As an improvement, Shen (Shen 2010) and Fang (Fang 2010) employed a tetrahedron mesh based inhomogeneous MC scheme. Since the mean free path of a photon is limited to inside the tetrahedron space, it leads to substantial improvement to the processing time when simulating light transport in complex tissue structures. SESE utilizes a three-dimensional voxel-based approach, with each voxel containing the optical and thermal properties of the tissue in that location. In cases of voxels containing boundaries, a piecewise planar approximation is used to specify the local shape in the geometry, details of which can be found in this report (Karch 2013). SESE is designed to be easily parallelized to calculate the light distribution in each voxel independently, using a hybrid of MPI (message passing interface) and OpenMP.

5.4.3 Thermal modeling

Once the absorbed light energy at each voxel is calculated, SESE uses the bioheat equation (Pennes 1948) to calculate the temperature rise at any point in the geometry. The heat equation (Eq. 5-2) is integrated over a control volume of tissue (voxel) through finite volume discrete approximation. When simulating pulsed laser irradiation, an adaptive time step method is used to

achieve computational efficiency. The thermal properties of the various geometry components are as listed in Table 5-2. The heat equation is as shown below:

$$\rho_{tissue} C_{tissue} \frac{\partial T_{tissue}}{\partial t} = \nabla \cdot (k_{tissue} \nabla T_{tissue}) + Q_L + Q_{met} \quad (5\text{-}2)$$

where k_{tissue} is the thermal conductivity [W m^{-1} K^{-1}], ρ is density [kg m^{-3}], C is specific heat [J kg^{-1} K^{-1}], Q_{met} is the volumetric metabolic heat generation [W m^{-3}], Q_L is the heat generated due to the laser irradiation (Wm^{-3}), and T_{tissue} is temperature of the tissue [K]. All the thermal properties are assumed to be independent of temperature.

Thermal Properties	Symbol (units)	Water	Nerve	Optical Fiber
Specific heat capacity	C (kJ/(K.kg))	4.18	3.74	1.54
Thermal conductivity	k (W/m.K)	0.58	0.49	1.46
Convective heat transfer coefficient	h (W/m^{2}K)	15	15	0

Table 5-2: Thermal properties for the different components of the SESE model

(Hasgall 2015)

5.4.4   SESE model geometry

The model geometry used for the SESE optical thermal model is as shown in Fig. 5-2A. The geometry constructed is a 4 mm x 4 mm x 4 mm block, generated with 100 x 100 x 100 voxels of 40 µm side length dimensions. The nerve (in the form of a cylinder) is constructed at the bottom half of the block, at 2 mm depth (0.5 mm diameter). A 400 µm diameter cylinder, representing the laser delivery fiber, is constructed orthogonal to the nerve, and terminated where contact with the nerve is ensured. The optical fiber is assumed to be made of fused silica. The entire setup is modeled to be surrounded by water to mimic a nerve tissue submerged in blood and body fluids. A simplified two-dimensional representation of the geometry is shown in Fig. 5-2B. Light scattering with the wavelength of interest (1875 nm) can be neglected since $\mu_a \gg \mu_s$' and in these simulations is assumed zero everywhere but could easily be incorporated if needed. Given the tie period of irradiation (5 seconds or lower) and the radiant exposures involved, effects like radiative, evaporative heat losses have been assumed to be negligible in this study. Change in geometry shape due to material removal and ablation can reasonably be ignored and hence are not considered in this study.

5.4.5   NEURON model

NEURON is a simulation environment for modeling individual neurons and networks of neurons (Hines 1997). It provides computationally efficient functions for building, managing, and using models easily. NEURON uses special algorithms to achieve high efficiency by exploiting the structure of the equations that describe neuronal properties. It has in-built functions that are tailored for conveniently controlling simulations, and presenting the results of real neurophysiological problems graphically in ways that are quickly and intuitively grasped. NEURON lets us deal with familiar neuroscience and electrophysiological concepts rather than

spend our resources on writing specialized functions to solve equations that govern action potential generation and propagation. NEURON offers several different, user-selectable numerical integration methods. The default solver method is implicit Euler, which provides robust stability and first order accuracy in time (sufficient for most applications). User-defined mechanisms such as voltage- and ligand-gated ion channels, diffusion, buffering, active transport, etc., can be added by writing model descriptions in NMODL, a high-level programming language.

5.4.5.1   One dimensional axon model

An unmyelinated nerve axon of length 4 mm is constructed in NEURON. The diameter of this axon varies from (5-25 µm) according to the simulation. The diameter is consistent with observations in *Aplysia* (Kreiner 1987). The length of the axon chosen is long enough to reduce dimensionality of the problem and make our simulated recordings free of end-effects encountered due to the finite length of the axon cable. These end-effects (closed end or sealed end effects) distort the voltage measurements of the nodes located at the ends of the axons. The axon is then divided into a number of computational segments, where the voltages and other parameters like ionic currents, gating variables (*m,n,h*) and ionic conductance are calculated. When integrating with an optical thermal model, the time varying temperatures are assigned to these nodes. The number of segments is chosen to make the model code computationally efficient without compromising on the quality of the results obtained. At present, the model geometries described in SESE and NEURON are different. SESE uses a 3D model geometry consisting of a nerve axon whereas the model geometry in NEURON uses a one-dimensional axon. This is a limitation of the model and we will address this point later in the discussion section. The output of SESE is a four dimensional temperature rise $\Delta T(x,y,z,t)$, and the NEURON model is designed to account for only a two dimensional temperature distribution ($\Delta T(x,t)$).

The axon sizes considered in this chapter for studying neural responses are relatively small (5-25 μm) as compared to the size of the nerve (500 μm). Hence, time and space varying temperature distribution from a one-dimensional line at the surface of the nerve are considered. While doing so, it is assumed that the temperature distribution is uniform across the depth of the axon (z direction as shown in Fig. 5-2B). Given the penetration depth (~ 600 μm) of the laser light at the wavelength used, and that the scope of the research is aimed towards blocking pain carrying C fibers which are mostly found at the surface of the nerve fiber, we believe that focusing our simulation efforts on a surface axon is a reasonable simplification. Development of a model is currently in process which considers multiple axons and depth dependence of a three-dimensional temperature distribution. The preliminary results from the model are shown in a later section of this chapter.

The default version of the Hodgkin Huxley model mechanism (HH) in NEURON (Hodgkin 1952) is used. This mechanism does not predict neuronal responses at elevated temperatures satisfactorily (Rattay 1993), but improving the classic HH model to correctly predict neural response at elevated temperature is beyond the scope of this chapter. This is addressed in detail in Chapter 3. The model used in this chapter only uses the HH model. The mHH model, though appears to predict response of unmyelinated axon at elevated temperature, can only be applied for very specific cases (range of temperature, squid giant axon). We will address this point later (Discussion section 5.6) as it represents another point of improvement for the model. The model equations that were used in each segment of the NEURON model:

$$C \frac{dV_m}{dt} = -g_L(V_m - E_L) - g_{Kmax}(T)n^4 - g_{Namax}(T)m^3h + I_{Na\_pump} + I_{K\_pump} \quad \text{(5-3)}$$

$$\frac{dm}{dt} = \kappa(T)\alpha_m(1 - m) - \beta_m m \quad \text{(5-4)}$$

$$\frac{dh}{dt} = \kappa(T)\alpha_h(1 - h) - \beta_h h \quad \text{(5-5)}$$

$$\frac{dn}{dt} = \kappa(T)\alpha_n(1 - n) - \beta_n n. \quad \text{(5-6)}$$

$$\kappa(T) = 3^{\frac{(T-6.3)}{10}} \quad \text{(5-7)}$$

$$\alpha_n(V) = \frac{-0.01(V+55)}{\left(e^{\frac{-(V+55)}{10}} - 1\right)} \quad \text{(5-8)}$$

$$\beta_n(V) = 0.125\left(e^{\frac{-(V+65)}{80}}\right) \quad \text{(5-9)}$$

$$\alpha_m(V) = \frac{-0.1\,(V+40)}{\left(e^{\frac{-(V+40)}{10}} - 1\right)} \quad \text{(5-10)}$$

$$\beta_m(V) = 4\left(e^{\frac{-(V+65)}{18}}\right) \quad \text{(5-11)}$$

$$\alpha_h(V) = 0.07\left(e^{\frac{-(V+65)}{20}}\right) \quad \text{(5-12)}$$

$$\beta_m(V) = \frac{1}{\left(e^{\frac{-(V+35)}{10}} + 1\right)} \quad \text{(5-13)}$$

Please refer to the description of these parameters in chapter 3, section 3.3 of the dissertation, and also the "list of common symbols" at the beginning of the dissertation.

The parameters with constant parameters are as shown in Table 5-3.

Parameter	Symbol	Value (units)
Leak conductance	g_L	0.3 mS/cm^2
Membrane capacitance	C_m	1 µF/cm^2

Table 5-3: Constant parameters used in the HH model
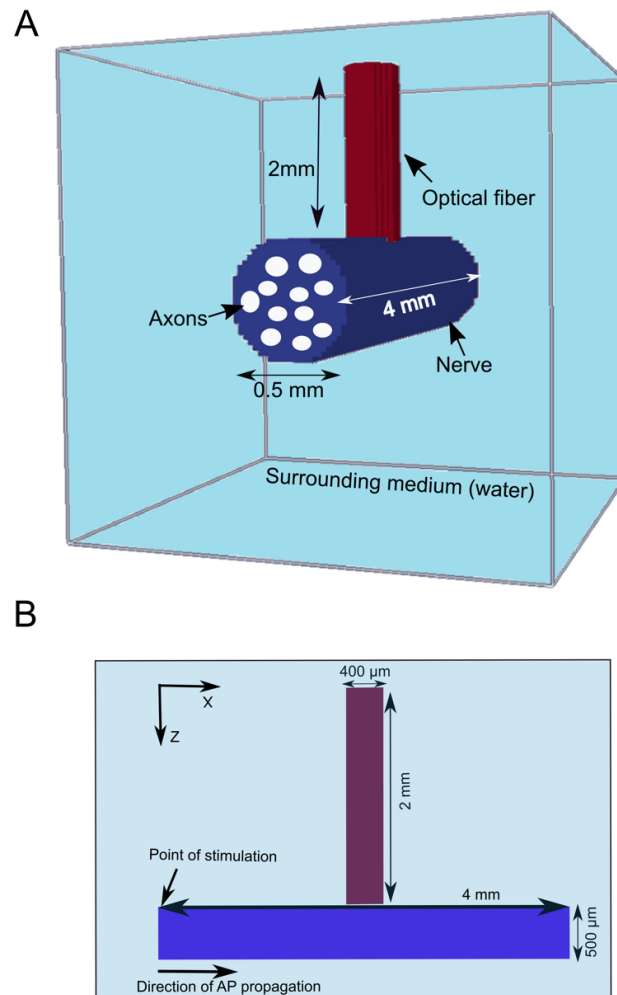
Figure 5-2: Model geometry used in the SESE model

(A): Model geometry used in the SESE model. It consists of a homogenous nerve fiber (blue cylinder, diameter = 0.5 mm) submerged in a water bath (light blue). An optical fiber (red cylinder, diameter = 400 µm) is shown to be touching the nerve surface in this geometry. The placement and the diameter of the optical fiber can be changed according to the desired setup and can be moved up or down on the Z axis. **(B):** Two-dimensional visualization of the SESE model geometry

in the X-Z plane. The time varying temperature distribution at the nerve surface (black double headed arrow) is extracted and fed into NEURON for further calculations. The point of stimulation and the direction of the action potential (AP) propagation is shown.

5.4.5.2   Multi-axon nerve model

In order to ascertain whether the model we developed agreed with the theoretically predicted and experimentally validated differential susceptibility to thermal blocks of fine vs large diameter nerve fibers (Lothet 2017), we built a multi-axon model in NEURON. We replicated a 7 mm-long section (diameter = 0.3 mm) of an *Aplysia fasciata* left-pleuro-abdominal-connective (LPAC) nerve in 3D space and used this model to predict the inhibitory effects of a steady-state 3D temperature distribution on the replicated LPAC nerve (Bedini 2000). We visualized the compound neural action potential (CNAP) resulting from the axons as the action potentials traveled through them. To start, all axons of the population were excited via current injection at one end and action potentials traveled along the length of the nerve were recorded. The action potentials traveling through a 3D steady-state temperature distribution placed along the length of the nerve. CNAP was calculated at a single point and each of the axons were checked for the presence of an action potential. Within the nerve, a population of unmyelinated axons of varying diameter was arranged in a strict cross-sectional grid layout of X and Y coordinate pairs. The axon count density within the cross-sectional nerve grid was 1 axon per 50.96 μm^2 (Bedini 2000), (for a total of 1379 axons). The distribution of axon diameters in the nerve is shown in Fig. 5-4C. We applied two types of temperature distribution on the nerve. In the first case, each axon in the nerve (regardless of the axon diameter or location) was subjected to a fixed region of elevated temperature (35 ℃ over a 300 μm length section of axon). In the second case, a 3D temperature distribution was a spatially-variant distribution resembling a temperature distribution from a nerve

irradiated by an IR fiber touching the surface of the nerve. The result of this heating is shown in Fig 5-4E.

5.4.6 Thermal damage model

There are various models to predict thermal damage in biological tissues due to temperature rise caused due to laser irradiation or any other means. These models represent various stages in the stages of tissue damage, which could be heat shock protein (HSP) expression – one of the earliest sign of thermal damage, disassociation of cell membrane, intracellular protein denaturation, extracellular protein denaturation, inflammatory response, and eventually cell death (Beckham 2004, Sapareto 1984, Thomsen 2005)- the point where the thermal damage is so large that cell death is observed. These models each represent a level (known as critical temperature) beyond which the tissue damage is highly likely. Each of these models are highly application specific and hence the critical temperature can vary highly between models and tissue types. We can safely ignore charring and ablation since the temperature rise predicted in the simulations aren't high enough to take those effects into account.

Our analysis for thermal damage throughout this study has only considered the heat shock protein 70 expression model parameters. Heat shock protein expression is one of the earliest markers of thermally induced changes (damage) in biological tissues which is characterized by the low activation energy and critical temperature. The quantitative parameters (frequency factor, activation energy, critical temperature) for this model are as listed in Table 5-4. The damage model used to calculate probability of tissue damage is based on the Arrhenius equations and mentioned in Eq. 5-14 (Moritz 1947).

The evaluation of Arrhenius damage parameters (Activation Energy E_a and Frequency factor A) is the not the objective of this chapter, and hence they have been used from existing literature (Beckham 2004). In the Arrhenius model of thermal damage, tissue injury is assumed ot be linearly proportional to time of exposure at a given constant temperature and models a protein denaturation kinetic model as its basis. On the basis of the Arrhenius model, the thermal damage caused to the tissue during exposure temperature is a function of both the temperature rise and the temporal dependence of the temperature, not just a temperature. Hence, a tissue exposed to a large temperature for very short time might experience a low probability of thermal damage than say a tissue exposed to slightly lower temperature for much longer.

$$\Omega(t) = \int_0^t A e^{\frac{-E_a}{RT}} dt \quad (5\text{-}14)$$

Model	Activation energy (E_a)	Frequency factor (A)	Critical temperature $(T_c = \frac{E_a}{R ln(A)})$
HSP expression	1740 kJ/mol	$6.9 * 10^{282}$(1/s)	48.2 °C

Table 5-4: HSP 70 Arrhenius damage model and parameters

Source: (Beckham 2004)

5.4.7 Validation of optical-thermal model

Thermocouple measurements were taken using a fine wire (12.7 μm diameter) type E thermocouple (FW05, Campbell Scientific, Logan UT) with a response time of ~10 ms (unpublished calculation done in lab by Jeremy Ford), connected to a data acquisition device with cold-junction compensation (Model DI-245, DATAQ Instruments, Akron OH) sampling at 200 Hz. A dual fiber probe (constructed for another study (Ford 2015)) was placed in a water bath,

and the thermocouple was positioned under the probe at the hottest point using the following

protocol. The laser was turned on and allowed to heat the water. Using a micromanipulator, the

thermocouple was translated along all three axes until a maximum temperature value was found.

Once the thermocouple was at this position of maximum temperature, the laser was turned off and

the temperature was allowed to relax back to baseline (room temperature). The laser(s) was then

triggered at 200 Hz with 200 µs pulses using a pulse generator (Model DG 535, Stanford Research

Systems, Inc., Sunnyvale CA). Temperatures were allowed to reach steady state, and the data were

analyzed once the temperature reached a dynamic equilibrium after 5 seconds of heating. A model

geometry identical to the experimental setup was developed in SESE. Two different experimental

cases were considered. The laser beam characteristics are summarized in Table 5-5. In each case,

the power irradiated from both fibers was varied. The laser powers in each of the cases are as

shown in Table 5-6.

Laser parameters	Symbol (Units)	Value
Frequency	f (Hz)	200
Pulse duration	τ_p(µs)	200
Beam radius	r (µm)	200
Wavelength	λ(nm)	1875

Time of Irradiation	t_{irr}	5 sec

Table 5-5: Infrared beam characteristics

Case No.	Laser Power (mW)
1	42.3
2	26.6

Table 5-6: Summary of cases and their laser powers for SESE validation

5.4.8 Code availability

All the codes for neural simulations and data processing (NEURON, Python, Matlab) have been uploaded on the GitHub repository (Link: https://github.com/mohitganguly/IRBlock_Vanderbilt). The SESE model was developed at the Air Force Research Laboratory (San Antonio, TX) and the results of the simulations were made available to us under an agreement between Vanderbilt University and Air Force Office of Sponsored Research (AFOSR).

5.4.9 Other tools

The SESE simulations were run on a high-performance computing cluster (72 cores, 384 GB) at the Air Force Research Laboratory at San Antonio, TX. The results of the simulations were visualized using ParaView (www.paraview.org). The NEURON simulations were run at the Biophotonics Center, Vanderbilt University on a Dell Precision Tower 7910 running (Intel Xeon®

E5-2637 3.5 GHz) Ubuntu 14.04 LTS. Further data processing and thermal damage analysis was done in Matlab.

5.5   Results

5.5.1   Integration of SESE and NEURON

To utilize our model to explore strategies to optimize temperature rise and thermal damage for neural inhibition process, a simple example of the integration of the results of SESE and NEURON model is shown in Fig. 5-3. This example will be used throughout the chapter to derive further insights on the optimal laser parameters. We define a parameter as optimal if the specific laser parameter causes thermal inhibition in the axon, without exceeding the thermal damage threshold. The colorful background (heat map) represents the time dependent temperature rise along the one-dimensional surface of the axon. This one-dimensional surface axis is highlighted in bold black horizontal arrow in Fig. 5-2B. The x-axis of the heat map in Fig. 5-3 represents the time dimension of the irradiation process. As we move from left to right on this axis, we progress further in time. The y-axis of the heat map represents the spatial dimension of the nerve surface. As we travel from top to down on the heat map, we traverse the length of the axon from the one end (x = 0) to the other (x = 4 mm). The heat map shows the transient temperature rise at various positions in the nerve axon. The region in the middle of the axon, which is closest to the laser fiber, is observed to be at the highest temperature. As time progresses, the region of the nerve experiencing higher temperatures increases, indicating diffusion of laser induced heat generated throughout the nerve axon.

Overlaid on top of the heatmap, is the propagation of action potentials along the axon. The axon is subjected to the temperature rise distribution represented in the heatmap in the background.

The axon is electrically stimulated at 2 Hz using NEURON's IClamp2 function. This function enables stimulation of an axon intracellularly at regular intervals. This function delivers a periodic supra-threshold pulse (2000 nA, lasting 1 ms) of depolarizing current into one end of the axon. The action potential generated at x = 0 end of the axon travels along the axon towards x = 4 mm. In the plot, this propagation can be observed traveling from the top of the plot to the bottom of the plot. A train of action potentials elicited using IClamp2 is shown from left to right (time axis) on the plot. In this case, the laser delivery fiber was placed 250 μm from the surface of the axon. The other laser parameters were identical to those mentioned in Table 5-5. A sample action potential (experiencing minimal temperature rise) elicited is shown in the inset Fig. 5-6A.

As the temperature in the axon rises, a drop in action potential amplitude is observed as the AP travels down the axon. In the region around elevated temperatures, a block of the action potential propagation is observed. In our analyses, we have defined a thermal block if the amplitude of the action potential at the end of the axon (x = 4 mm) drops below -50 mV (Seifter, Sloane, & Ratner, 2005). This is a conservative estimate, since the threshold of activation of action potential lies around -50 mV. A comparison of an unaffected versus blocked action potential is shown in the second inset Fig. 5-6B. In the following sections, this modeling pipeline will be used to derive insights about changing laser parameters and their effect on neural propagation along the axon.
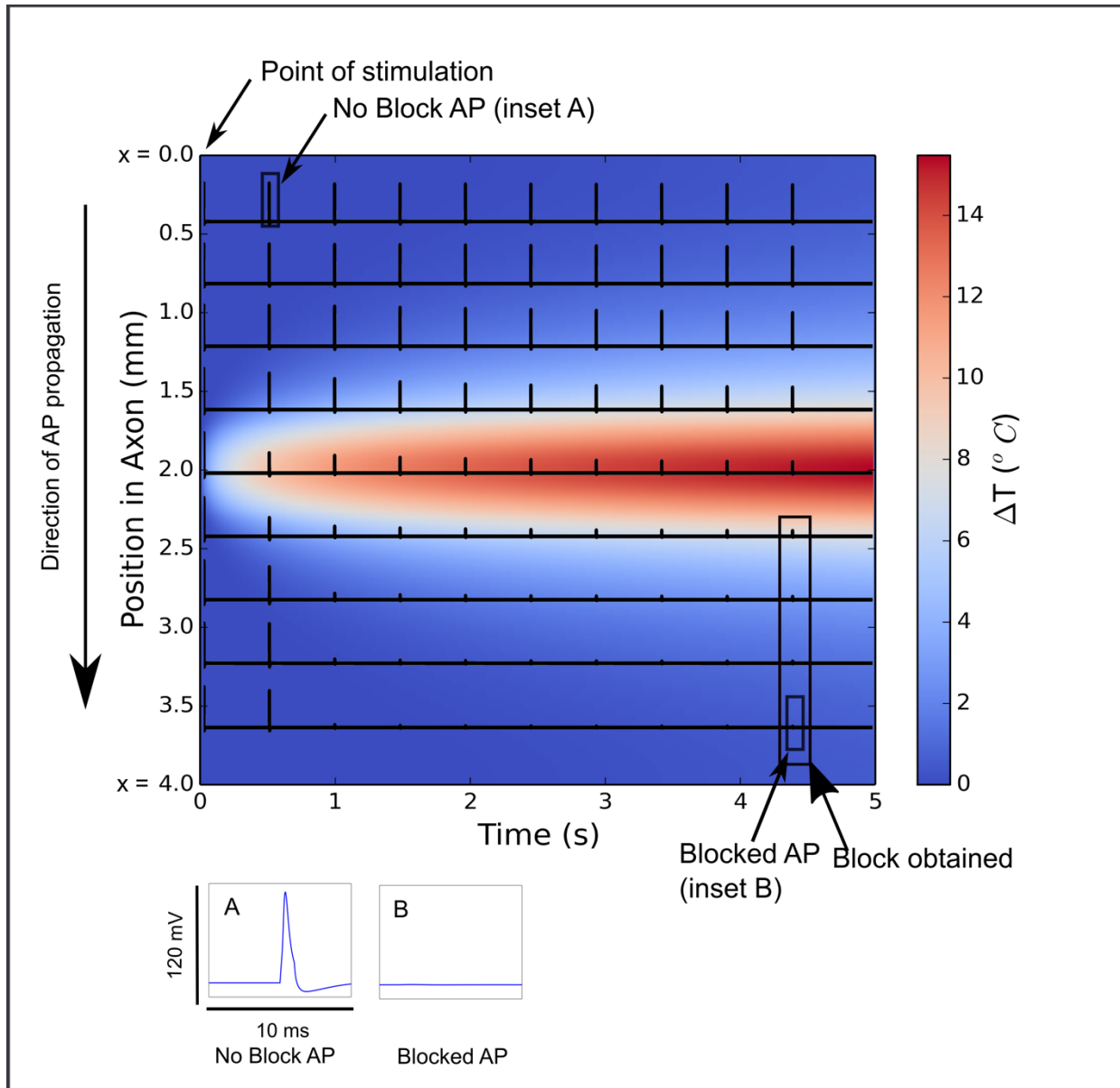
Figure 5-3: Effect of IR laser irradiation on a squid giant axon

Effect of IR laser irradiation on a squid giant axon of length 4 mm for a sample case of an irradiation by a 400 μm laser delivery fiber touching the nerve. (t_{irr} = 5sec, P_{avg} = 45 mW, f = 200 Hz, τ_p = 200 μs, optical fiber size = 400 μm, distance from nerve surface = 0 μm). The heat map in the background shows the one-dimensional temperature time distribution of the surface of an *Aplysia* axon as described in Fig 5-2(B). Inset shows a sample control action potential (A) and a sample blocked action potential (B).

5.5.2 Model validation

5.5.2.1 SESE

Before using the new multiphysics model to derive insights on optimization of the infrared neural inhibition process, the accuracy of the SESE model predictions was ascertained. The results of comparison of thermocouple measurements and SESE measurements are as shown in Fig. 5-4. The setup and the parameters for the cases used was as described in the Methods section. The SESE predictions of temperature rise were within 10 % of the thermocouple measurements. It should be noted that the thermocouple measurements are themselves subject to uncertainty (Nakos, 2004) and we believe a 10% error rate is acceptable. These sources of error in thermocouple measurements are discussed in detail in the Discussion section. SESE model has been used previously for determining temperature rises in infrared nerve stimulation studies (Beier 2014, Walsh 2016). However, in those cases, SESE's accuracy was not determined by comparing its temperature rise results through experimental measurements of temperature rise.

5.5.2.2 Validation for NEURON

NEURON has been used widely in numerous applications and exploring its accuracy was not considered for the purposes of this chapter. To evaluate the effect of axon diameter on the efficacy of thermal block in unmyelinated axons, the simulations were run for different axon diameters (5, 10, 25, 50 μm). For these analyses, temperature rise for 0 μm fiber-nerve separation was used (i.e. fiber in contact with the nerve surface). As the axon diameter increased, the threshold temperature required to produce a thermal block increased (Fig. 5-4B). This observation of selective inhibition of small diameter axons has been shown previously in *Aplysia* and in the musk shrew and also shown through analytical and computational modeling (Lothet 2017). This analysis shows that our model predictions are qualitatively consistent with the experimental

observations. We have highlighted earlier that the standard Hodgkin Huxley mechanism is not the ideal model for predicting neuronal responses at elevated temperatures and efforts to improve the predictions of Hodgkin Huxley model for elevated temperature have been the focus of recent papers (Ganguly 2016).

5.5.3 Variation of infrared inhibition with axon diameter

Simulation results shown in this chapter have employed a single axon model geometry. While that model is optimal for studying axon dynamics and membrane dynamics on a single axon level, it doesn't capture the physiological or anatomical reality of the nerve anatomy in mammals. In order to translate the technology to be used in humans in the future, steps should be taken to develop a model that more accurately represents the human neural anatomy where a nerve will consist of multiple axons of varying diameters. As a first step towards that goal, we developed a multi axon model to test if the model predictions agree with the experimental recordings in *Aplysia*. In the first case of heating, where all the axons were subjected to identical temperature distributions (applied to all axons), we observe that the larger axons are largely left uninhibited, whereas the smaller axons are inhibited. These results are shown in the cross axon of the nerve in Fig. 5-4D. The inhibited axons are shown in red dots, and the uninhibited ones are shown in blue dots. The dot in the figure are scaled to their sizes. These observations are consistent with what is observed in experiments in *Aplysia californica* (sea slug) and musk shrew (Lothet 2017). In the second heating case (where a three-dimensional heat distribution was used in the same nerve containing identical axon distribution), we see that (in Fig. 5-4F), larger axons are inhibited in regions of higher temperatures (mostly around center of the nerve). The color bar in Fig. 5-4F indicates the diameter at which inhibition stops occurring. For example, the center of the figure is the darkest, indicating that all axon diameters less than 24 μm are inhibited by the temperature distribution in

that location. The periphery is lighter, indicating that only small diameters of 6 μm and below are inhibited at that location due to the given temperature distribution.

Around the periphery of the nerve, where the temperatures are not as high, the smallest axons are the ones that are inhibited. This reinforces the point that the smaller axons are more sensitive to temperature rises than larger axons. This might also have important repercussions when translating this technology for clinical applications. Pain carrying C fibers are small diameter axons and mostly found near the surface of the nerve. An irradiation protocol that only targets smaller fibers near the surface would be beneficial for the development of this technology into a pain management clinical modality.
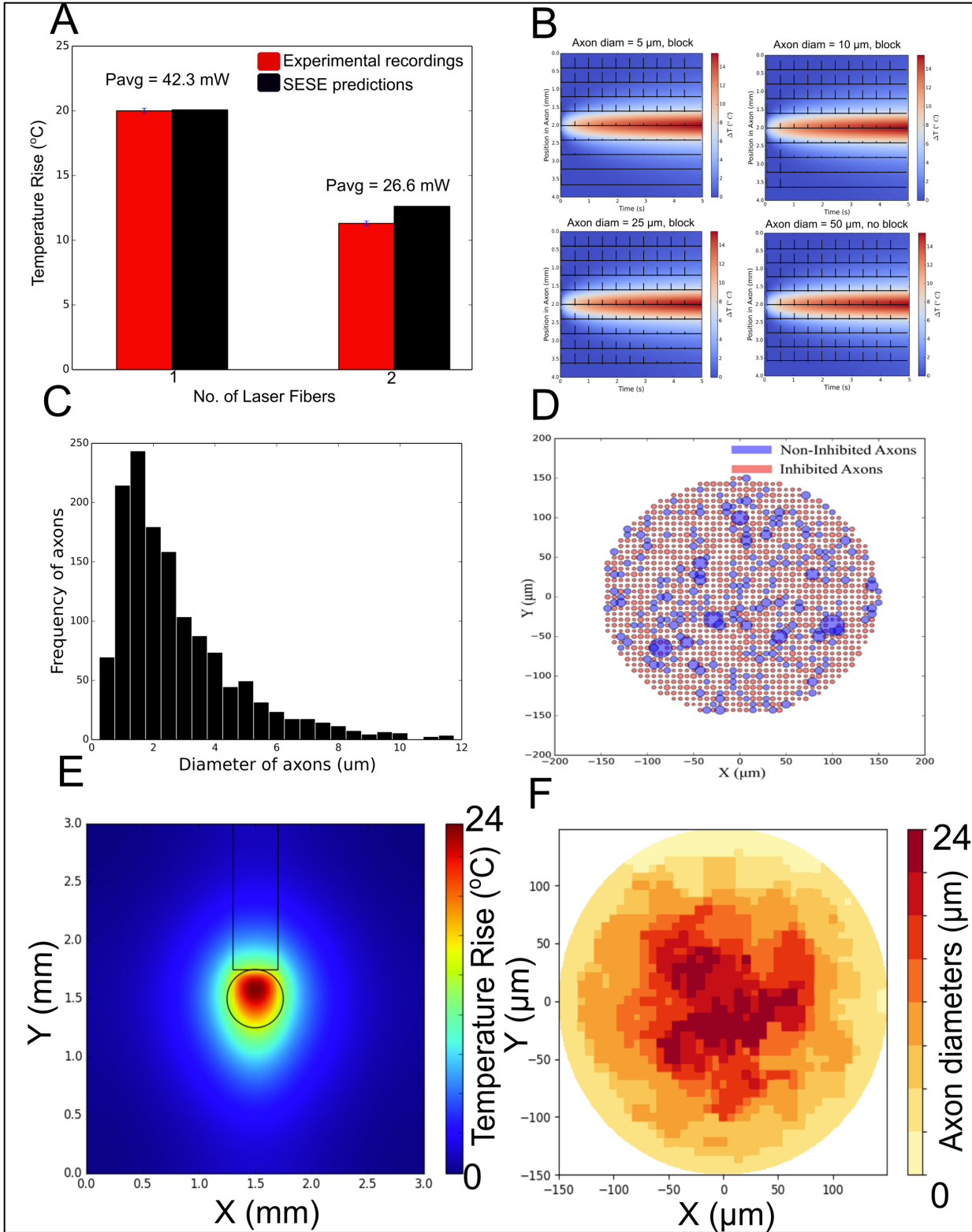
Figure 5-4: Demonstration of model accuracy

(A) Comparison of thermocouple measurements and corresponding SESE predictions of temperature rise for two different cases. Also shown are the average power readings from each fiber during irradiation. **(B)** Sensitivity of axon diameters to heat. Neural responses of axons of different diameters to IR irradiation. (t_{irr} = 5sec, P_{avg} = 45 mW, f = 200 Hz, τ_p = 200 μs, optical fiber size = 400 μm, distance from nerve surface = 0 μm). As the axon diameter increases, the threshold temperature required to produce a block in propagation of action potentials increases. As the axon diameters increases to a large value (50 μm), a block is not obtained. **(C)** axon diameter distribution for *Aplysia* multi axon model. **(D)** Cross section of nerve showing the blocked and unblocked axons, when all axons are subjected to identical temperature **(E)** Cross section of a nerve showing temperature distribution as a result of the IR irradiation **(F)** cross section of a nerve fiber (size 300 μm) on the nerve showing the variation of threshold axon diameter along any location in the nerve, when subjected to temperature distribution show in 5-4E. Axon diameter distribution was based on study actual measurements in *Aplysia* (Bedini 2000).

5.5.4 Fiber distance

In order to study the effect of fiber distance from the nerve surface, the model results were studied for multiple scenarios where the distance of the laser fiber from the nerve surface was varied. In Fig. 5-5A, the maximum temperature rise at the surface of the nerve is shown as a function of different laser delivery fiber distances. The maximum temperature on the nerve surface is observed when the laser delivery fiber is 150 ± 40 μm from the surface.

Fig. 5-5B shows various scenarios when a block was observed and when the action potential failed to be blocked. Using this block table, it is observed that, for the laser parameters used, a block is observed for axon diameters up to 25 μm irrespective of fiber distance. The only exception to this observation is the case of 1000 μm fiber distance and 25 μm axon diameter. Lower peak temperatures coupled with relatively large axonal diameter are factors that lead to a block failure in that case. No block was observed for axon diameter of 50 μm axon diameter for any fiber diameter. Furthermore, thermal damage analysis based on Arrhenius model of HSP expression (described in the Methods section) were performed for each of these cases. The interplay of thermal damage and inhibition are shown using colored boxes. Except for the case of

150 μm fiber distance from the nerve surface, no significant thermal damage was observed in any other cases. Since the thermal damage is solely dependent on the temperature-time relationship, and not on the axon diameter, it mirrors the variation of peak temperature as seen in Fig. 5-5A. Owing to thermal damage seen for 150 μm fiber distance, this case can be safely discarded for further analyses of inhibition simulations.
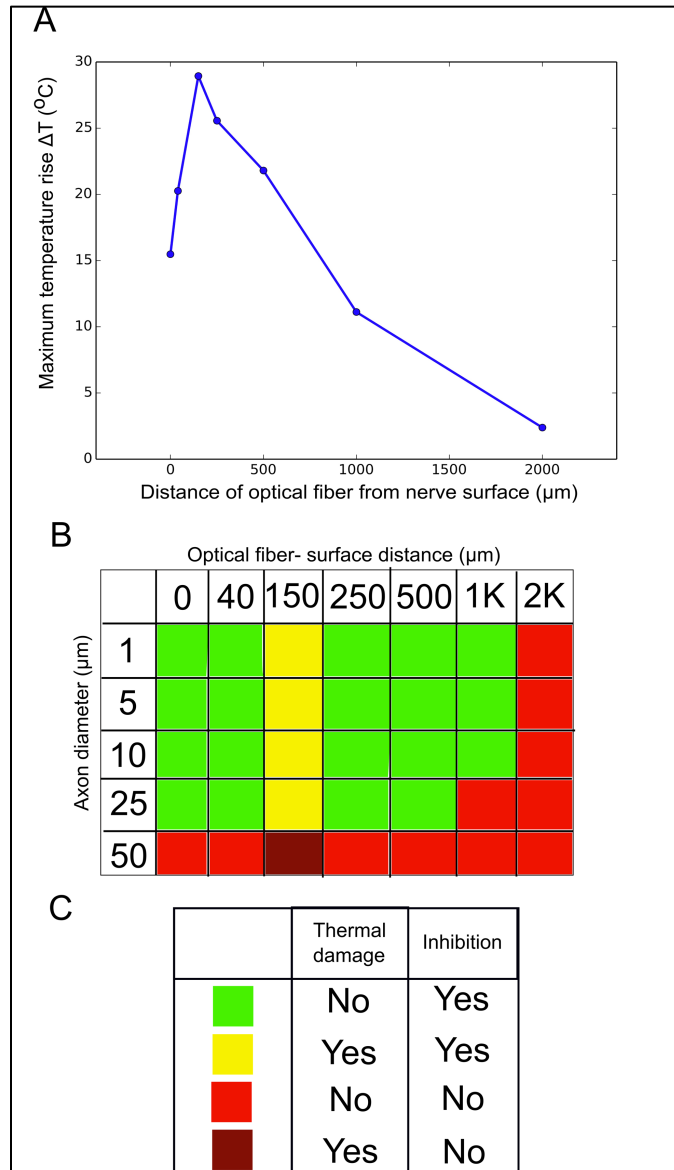
Figure 5-5: Effect of optical fiber distance from nerve surface

 (A) Maximum temperature rise calculated during IR irradiation as the distance between the laser delivery fiber and the nerve surface is varied. The maximum temperature rise is observed when

the laser fiber is 150 μm from the nerve surface. (t_{irr} = 5sec, P_{avg} = 45 mW, f = 200 Hz, τ_p = 200 μs, optical fiber size = 400 μm) **(B)** Combination of thermal damage probability calculated and whether inhibition was observed as the distance between IR fiber and the nerve surface increases. The neural response is observed for different axon diameters. **(C)** Color code representing the dependence of thermal damage probability and whether inhibition was observed.

5.5.5 Laser delivery fiber diameter

Keeping the laser delivery fiber distance from the nerve surface constant at 250 μm, we studied the effect of laser delivery fiber beam diameter on the inhibition process. Laser delivery fiber diameter directly correlates with the spatial distribution of the temperature over the axon surface. The modulation of spatial distribution of temperature can be used to decrease the laser irradiance and thus the temperature rise required to achieve inhibition. The temperature rise observed for different laser delivery fiber diameters was determined. Effects of four different laser delivery fiber diameters (100, 200, 300 and 400 μm) were studied. The spatial temperature rise distribution at the end of a 5 sec laser exposure for the multiple fiber diameters are as shown in Fig. 5-6A. Since laser power and exposure is constant across the different fiber diameters, the energy delivered per unit area (radiant exposure (J/cm^2)) decreases leading to lower temperature rise as laser delivery fiber diameter increases. Fig. 5-6B shows a block table of different cases of fiber diameters and axon diameters. Similar to the observations with the variation of fiber distance, inhibition was observed for all axon diameters of 25 μm and below. Thermal damage modeling shows thermal damage presence for the cases of 100 and 200 μm fiber diameters and hence won't be used for further analyses or experimentation. In further simulations and experiments, 400 μm fiber diameter will be used for neural inhibition.
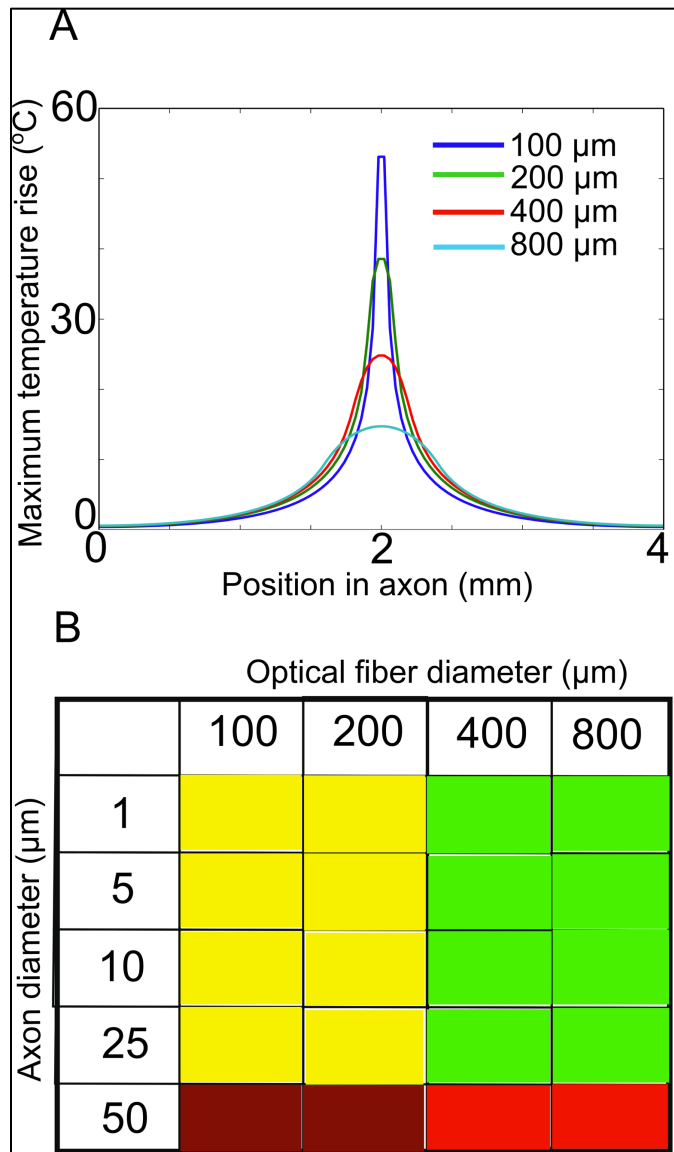
Figure 5-6: Effect of optical fiber diameter

 (A) Spatial temperature distribution on the nerve surface calculated during IR exposure as the diameter of the laser delivery fiber is varied (t_{irr} = 5sec, P_{avg} = 45 mW, f = 200 Hz, t_p = 200 µs). The maximum temperature rise is observed when the laser delivery fiber diameter is 100 µm. **(B)** Thermal damage calculated as the diameter of laser delivery fiber is varied (t_{irr} = 5sec, P_{avg} = 45 mW, f = 200 Hz, τ_p = 200 µs). The color scheme of the box is the same as in Fig. 5-5. Smaller laser delivery fiber diameters (100 µm, 200 µm), where temperature rises observed are higher, are more likely to cause thermal damage. The temperature rise observed for larger diameters (400 µm, 800 µm) do not cause thermal damage but block action potentials and hence serve as suitable candidates for inhibition studies.

Use of multiple laser delivery fibers

As shown by Ford et al. (Ford 2017), the occurrence of block is dependent on the block length (spatial extent of the nerve axon subjected to elevated temperatures) and the temperature attained along the axon. However, as the peak temperature increases, the probability of occurrence of thermal damage increases. We hypothesize that if the temperature is raised over a larger spatial extent over the axon, the peak temperature required to cause thermal block is decreased. This would lead to a reduction in the probability to cause thermal damage in the nerve. To test this hypothesis, a model setup of two adjacent fibers was developed in SESE. Various cases were simulated, and temperature rises were calculated. The time dependent temperature rises at the surface of the axon were used in NEURON to predict the neurophysiological responses of a surface axon for the various cases. We are interested in only surface axons since pain carrying C fibers are present near the surface of the nerve fiber. As a positive control, one fiber delivering a power of 45 mW was used on a 400 μm diameter axon and a successful block was observed. In a geometry consisting of two identical laser delivery fibers each emitting a reduced power (22.5 mW), a successful block was observed. Compared to the positive control case, the peak temperature rise in this case was only 44 % of the peak temperature observed single laser delivery fiber control. As a negative control, a single fiber delivering 22.5 mW (50 % of the positive control case) was modeled. Even though the peak temperature rise was almost equal to that observed with both laser delivery fibers (with 22.5 mW), no thermal block was observed. To extend this concept, we explored the effect of increasing the distance between the two laser delivery fibers. The rationale for doing these simulations was to examine if we can achieve further reduction in temperature while maintaining block efficacy. The temperature rise distribution for the two-fiber setup with varying distances between the laser delivery fibers is as shown in Fig. 5-7. There was an approximately 20 % further reduction (Fig. 5-7A) in peak temperature rise as the distance between

the fibers (side to side) was increased to 400 μm. In all the cases, neurophysiological responses (block/no block) and thermal damage (damaged/not damaged) were also calculated, and the results are shown in Fig. 5-7B as a block table. All the cases produced successful neural inhibition and were not likely to cause thermal damage during the inhibition process.

A

B

Distance between optical fibers (μm)				
	100	200	400	800
1				
5				
10				
25				
50				
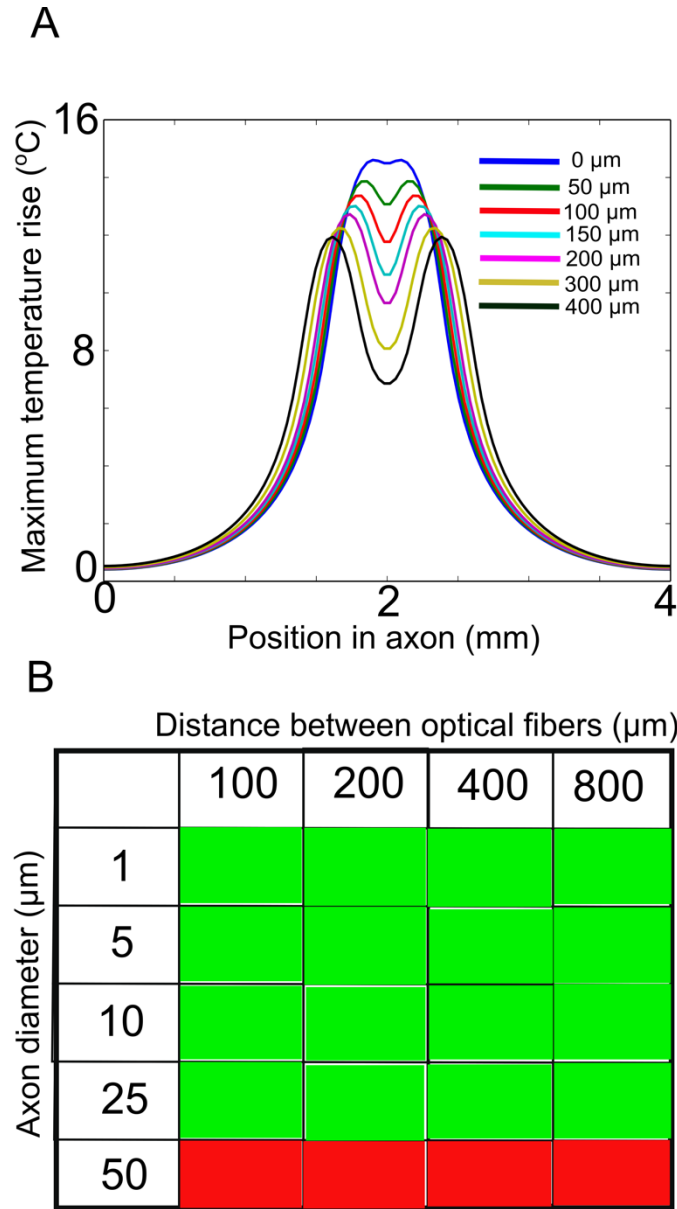
Figure 5-7: Effect of separation of optical fibers

(A) Variation of spatial temperature distribution for a two-fiber setup at the end of 5 sec irradiation for different inter-fiber distance. In the two-fiber setup, two optical fibers are used to irradiate the nerve surface and the distance between them is varied. As the distance between the laser delivery fibers increase, the maximum temperature rises at the nerve surface decrease. **(B)** Thermal damage observed as the distance between laser delivery fibers (t_{irr} = 5sec, P_{avg} = 45 mW, f = 200 Hz, τ_p = 200 µs, optical fiber size = 400 µm) is varied in a two-fiber setup. The color scheme of the box is the same as in Fig. 5-5. Thermal damage is not observed in any of the cases. However, we observe thermal block for all laser parameters. This suggests that using a two-fiber setup, we can cause a thermal block with a lower temperature rise and a reduced likelihood of causing thermal damage.

5.5.6   Other heat sources

The modularity of the model setup allows the model to use heat sources other than laser irradiation, which is useful when optimizing parameters for neural inhibition resulting from non-optical sources (Ackermann 2009, Juan 2014, Kilgore 2009, Min 2011). Since the observation of inhibition is assumed to be a temperature mediated process, this model has been setup to accept custom heat sources and ensuing temperature distributions. As an example, a case of resistive heating has been explored in this section, where heat is dissipated by a conductor as a current is passed through it.

A model consists of a helical steel coil placed around a nerve modeled as a cylinder of diameter 0.5 mm (Fig. 5-8A). The nerve geometry was identical to that as the IR inhibition simulation used in our analysis in the chapter. To simulate the heating characteristics of this coil, the coil was maintained at a temperature of 40 °C (313 K) throughout, for 5 secs. The simulations of this thermal source were performed in COMSOL Multiphysics (COMSOL Inc., Burlington, MA) using the heat transfer module.

In Fig. 5-8B, the resultant transient temperature rise at the surface of the nerve fiber is shown in the form of a heat map in the background. This representation is identical to the one

shown in Fig. 3 for IR laser induced block. As a result of this rise in temperature, the resultant neurophysiological response of 5 μm axon at the surface of the nerve is as shown in Fig 5-8B (overlay on thermal map). As observed in case of infrared heating, the action potentials undergo reduction in amplitude as the temperature on the surface of the axon increases. As the temperature increases, the peak value of the action potential gradually reduces to a value below -50 mV, resulting in a conduction block. In this example, we were able to successfully demonstrate that our model is able to integrate heat sources that are derived from process that do not include IR laser-induced heat generation. More implications for this model capability are discussed in the Discussion section (Section 5.6).
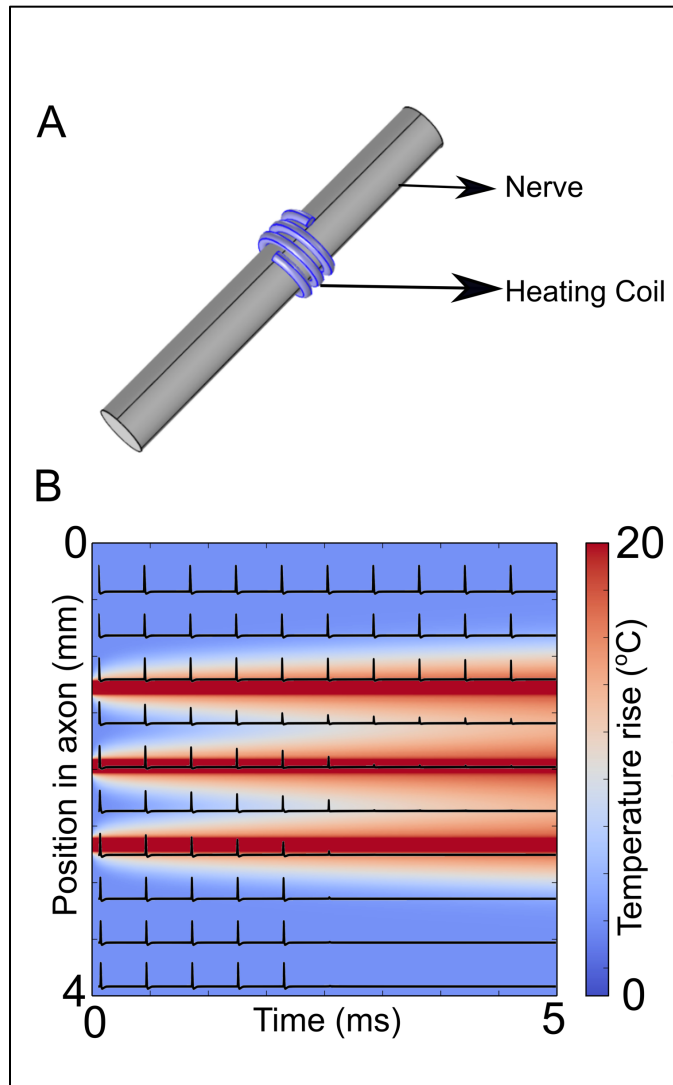
Figure 5-8: Effect of alternative heat source

 (A) Schematic of a model geometry used for a simple coil heating case. A helical coil made of steel (purple) is placed around the nerve (grey cylinder, diam = 0.5 mm). The coil is in touch with the nerve surface. The coil is maintained at 40 ºC and the temperature rise observed (time = 5 secs) at the nerve surface (bold line) is calculated and shown as a heat map in Fig. 5-5B. **(B)** Effect of coil heating on an *Aplysia* nerve of length 4 mm. The heat map in the background shows the one-dimensional temperature time distribution of the surface of an *Aplysia* nerve as described in Fig. 5-8(A). As time of simulation increases, temperature increases along the nerve. As a result, in an axon of diameter 5 μm, the action potentials arising at x = 0 experience elevated temperatures and are blocked.

5.6 Discussion

In this chapter, we describe the development of a model that combines an optical thermal model with a temperature dependent Hodgkin-Huxley model. The optical-thermal model is a combination of the light distribution model accomplished through Monte Carlo simulation, and a heat transfer model using the bioheat equation. We observed that the maximum temperature rise at the nerve surface occurs when the nerve is around 150 μm from the laser fiber. This is likely because the laser delivery fiber, made of silica, is a higher conducting material than the nerve tissue and the surrounding medium (refer to Table 5-2). When the laser delivery fiber is in contact with the nerve surface, the laser delivery fiber wicks away heat from the nerve surface and leads to less temperature rise than expected. When it is moved away from the nerve surface, this wicking effect is diminished since the medium between the laser delivery fiber and the nerve surface is covered with water, which has a lower conductivity than silica. Hence the temperature rise at the nerve surface is observed to increase until the laser delivery fiber is moved around 150 ± 40 μm away from the nerve surface. Beyond this point, the intensity of the laser light reaching the nerve surface begins to attenuate leading to decrease in temperature rise observed. Laser delivery fiber diameters below 400 μm are prone to cause to thermal damage during thermal inhibition in nerve. Small laser delivery fiber beam diameters generate larger radiant exposure (energy/unit area) leading to higher energy deposition in a smaller area. This accumulation of energy in a smaller area leads to greater temperature rise, and subsequently greater likelihood of observing thermal damage. Our observations predict that extending the block length, for example, by using two fibers, decreases the temperature rise threshold for thermal block in unmyelinated axon models. In order to show that the model can also predict neural responses when the nerve is heated using other source of heat, we also simulated the response of an unmyelinated nerve to a heated helical coil maintained

150

at a constant elevated temperature. This heat in the coil may be generated as a result of an electric current passing through the coil.

5.6.1 Limitations of the model and scope for future work

The model developed here is an initial attempt of developing an integrated platform to study how infrared laser irradiation affects neural behavior. However, there are a number of assumptions made during the development in the model which may contribute to the limitations of the model. In this subsection we highlight those limitations and future steps that can be undertaken to address those concerns.

In the optical thermal model, the optical and thermal properties of nerve tissue have been assumed to be equal to the skin tissues. We believe that this is a reasonable first order approximations since there is an absence of the exact parameters for nerve tissues, and its evaluation requires considerable experimental effort (Hale 1973) and was not the focus of this study.

The validation of the SESE model was done using temperature rise measurements performed using thermocouple measurements (Nakos 2004). Thermocouples allow for high precision temperature measurements with high temporal resolution, but contact with the sample is required, only a single point can be measured, and their presence alters the heating dynamics in the system. The fine-wire thermocouple (12.7 µm diameter) used here was chosen to minimize its interaction with the surrounding media, and its response time (~10 ms) is small enough to dissipate the effect of heat generation in the metal itself from direct irradiation within each time-step of the sampling frequency (200 Hz). This means any artifact due to direct irradiation would have

subsided for most of the sampling period. A temperature rise was measured in the thermocouple when irradiated in air (data not shown); however, no direct irradiation artifact could be discerned in the water bath experiment. The effects from the artifact are still present in the data; however, due to the small response time of the thermocouple, the dominant contribution to the signal should be from laser heating of the water.

In the neurophysiological model, the Hodgkin Huxley (HH) model equations have been used to simulate the response of nerve in response to elevated temperature. Several reports have described inherent limitations of the HH model since its publication in (Hodgkin 1952) and its inability to simulate the effect at elevated temperatures (Rattay 1993). Attempts at addressing these limitations have been made in the past (Clay 1998, Sangrey 2004) and continues to be an important aspect of our work with the model (Ford 2017, Ganguly 2016). Given the modular nature of the present model, an improved version of the HH model can be easily integrated into the pipeline in the future.

The SESE model uses a 3D geometry, although the NEURON geometry consists of a single one-dimensional axon. The temperature rise only at the surface of the SESE nerve model is used as a temperature distribution fed into the NEURON model. This approximation is reasonable based on the assumption that we are only interested in studying the response of the surface axons. We aim to use this technology to inhibit pain carrying fibers (C fibers) in humans, which are present near the surface of the nerve bundle. Further efforts with the model should focus on developing a 3D nerve geometry, consisting of multiple axons of different diameters. Instead of measuring single action potentials, future versions of the model can be designed to predict neural response in the form of a compound action potential instead of a single action potential. An example of

studying the feasibility of a simulation has been shown, but not explored in detail. Such a geometry and recording algorithm can also enable us to consider the effects of the surrounding anatomical and physiological environment on the neural response, for example, potassium ion accumulation due the membrane ion transfer during an action potential could be incorporated in the model (Fitzhugh 1964, Frankenhaeuser 1956, Van Egeraat 1993).

In this model, we have assumed that the infrared inhibition is only dependent on the photothermal interaction of laser in biological tissues which results in rise in temperature. We should also examine if other laser tissue interactions, in particular photomechanical effects play a role in the inhibition mechanism and incorporate them in the model (Wells 2007, Shapiro 2012), but these claims have been subject to intense debate (Plaksin 2018). Photothermal and photomechanical mechanisms have also been considered to be responsible in infrared nerve stimulations, another way pulsed infrared light affects nerves. This will allow us to make significant progress towards developing a unified model which considers all the effects of infrared irradiation on nerves. Such a model will help in evaluating the biophysical mechanisms behind these interactions and optimize the process to translate into clinical applications.

Finally, the temperature rises we observed required for efficient nerve block appear to be high. Using thermal damage analysis, we see that this level of temperature rise is not damaging in the short time durations. However, sustained exposure to these temperature levels are prone to cause thermal damage in the tissues. The parameters for the damage model analysis are derived from the HSP (heat shock protein) 70 expression in rat embryo cells (Beckham 2004). Several clinical procedures rely on the HSP 70 expression for the efficacy of their treatment, for example, in the treatment of small choroidal melanomas (Shields 1998) and age related macular

153

degeneration (Ip 1999; Reichel 1999). Parameters evaluated using murine studies may not be indicative of thermal damage in humans. The damage analysis shown here caused by the infrared laser irradiation, and it doesn't provide any indication for possibility of long-term damage. It is also not indicative of functional damage caused as a result of the irradiation. Long term effects that infrared laser induced blocks might have on a nerve needs to be evaluated using histological studies and monitoring of nerve functions. These studies are outside the scope of this dissertation. Currently, the Food and Drug Administration (FDA) has no specific guidelines on the limit of the temperature rise for a medical device, but our future experimental efforts will focus on limiting the temperature rise to 2°C. These efforts will be driven by the insights that we derive from our current and future versions of the model.

5.6.2   Impact of the model

The model developed in this chapter provides a comprehensive modular platform to simulate and study the effect of infrared irradiation on neural responses. This current model and its future improved versions will serve three main objectives.

1) Mechanisms of infrared nerve inhibition
a) The model provides a computational approach to quickly test multiple hypothesis for biophysical mechanisms that might be responsible for the phenomenon of the observation of infrared inhibition. This reduces the number of difficult time-consuming animal experiments that need to be performed and helps us home in on the mechanisms sooner and help us target the modality better. For example, we were able to quickly test whether the use of longer block length can lower the threshold temperature required to cause infrared inhibition. The results

were then validated in an experimental setting and showed agreement with the modeling results (Ford 2017).

b) Use of a computational model will allow us to study the biophysical changes occurring during the inhibition process. These changes can be microscopic and difficult to measure even using sophisticated experimental techniques. For example, we can investigate the change in the shape of a single action potential as temperature increases. The changes in certain features of the action potential (foot, peak, rate of rise, rate of fall, etc.) can point to specific biophysical changes and help us design an experimentally testable hypothesis around it. For example, we have noticed that the rate of rise (ROR) and rate of fall (ROF) of action potentials increase with the rise in temperature. However, the ROF increases at a much faster rate than the ROR (Rosenthal 2000). Since the ROF is governed by kinetics of potassium ion channels, it enables us to develop the hypothesis that potassium channels are affected to a larger extent than sodium channels when the nerves are heated (Ganguly 2016, Huxley 1959) . Similar analysis was done to optimize sodium and potassium ion channel conductance in squid giant axons in Chapter 3 (section 3.3.3).

2) Parametric analysis: The model developed here presents a convenient way to perform a parametric sweep of laser parameters and examine the sensitivity of the neural response to the change in those particular parameters. In this example, we have investigated the role of fiber distance from the nerve surface, laser delivery fiber diameter and the distance between dual fibers on the temperature rise on the nerve surface. For each case, we have also examined the sensitivity of the neural response to the axon diameter.

3) Potential medical device design

a) This model is the first step towards a platform that can aid in the development of a medical device that can potentially be used to treat pain (chronic or acute) in humans. We believe this is possible since the technique of infrared inhibition has been shown to work successfully in *Aplysia. Aplysia* consists of unmyelinated nerves, which are anatomically similar to the pain carrying C fibers in humans. Lothet et. al (Lothet 2017) were able to show the differential effect of infrared irradiation on axons of varying diameters. This suggested a technique of blocking conduction in smaller pain carrying C fibers with infrared irradiation leaving larger fibers intact. The results observed in this chapter provide useful insights on the optimal fiber distances and beam diameters to maximize heat absorption in the nerve, and prevent heat (energy) loss through the blood and surrounding tissues or through the laser delivery fiber. The idea of using multiple fibers is also proposed and future designs should further explore this idea by using more than two fiber or other approach to deliver the laser light over a larger area.

b) The combination of this model with thermal damage studies enables us to discard potentially harmful laser parameters. In our studies, we realized that fibers at certain distances (150 μm) from the nerve surface and of certain fiber diameter (<400 μm) are prone to cause thermal damage. This allows us to alter the design parameters such as fiber-tissue distance, laser fiber diameter etc., all through computational design. The results of the model must be validated in experimental setting for checking the accuracy of the model. Once the model is improved further, more complicated and realistic model geometries of neural interfaces and nerves can be tested for safety and efficacy over both short- and long-term use.

This variation on peak temperature shows that the optical fiber, made of fused silica, acts as a heat sink and 'wicks' away a considerable amount of heat from the nerve surface. This 'wicking effect' appears to diminish as the fiber distance from the nerve surface is increased. After a certain distance (~150 µm), the temperature rise decreases as the fiber distance increases since the absorption of laser energy in the water medium between the fiber tip and nerve surface is increased and less laser irradiation reaches the nerve surface. While this may be an advantage since it prevents thermal damage, this can increase power requirement for the light source, hindering design of a potential medical device in the future.

c) The model and its results highlight the feasibility of combining an optical-thermal model with a temperature dependent HH model. This combined multiphysics model can be used to optimize the laser parameters (irradiation time, radiant exposure, beam radius) that will help to achieve heat block 'efficiently'. In this way, we can design thermal block with a minimal rise in temperature so that in the future, it can be used in humans to block pain conducting C fibers.

5.7 Conclusions

This chapter shows that infrared laser irradiation on nerves and its effects can be modeled using a flexible and modular multiphysics computational model. We have developed such a model and shown its versatility and some of its capabilities. The model, when coupled with a thermal damage model can help us select parameters that are helpful or avoid that are harmful for infrared nerve inhibition. The modular nature of the model can also be put in use when the heat generated in the nerve tissue is not of infrared laser origin. Lastly, this model can be used to identify experimentally testable hypothesis for the mechanisms of infrared interaction with nerves, which is unclear, and remains to be resolved.

6   CONCLUSIONS AND FUTURE DIRECTIONS

6.1   Summary and conclusions

6.1.1   Summary

The overall objective of this dissertation was to uncover the mechanism of infrared neuromodulation of nerves. The dissertation was specifically focused on the inhibition effects caused in unmyelinated nerves as a result of infrared laser irradiation. The rationale behind the focus on the unmyelinated nerves was that their anatomy is similar to that of the pain conducting C fibers in mammals (Besson 1987, Dubin 2010). In the future, understanding the mechanism of infrared neuromodulation in unmyelinated nerves might be helpful in translating this technology from the laboratory to the clinic. The potential clinical applications of this technology could be in chronic pain management, epilepsy, or post-surgical pain. These applications will be discussed in detail in the following sections of this chapter.

Chapter 2 of this dissertation provides a historical background of the development of the technology of infrared neuromodulation. It mentions the efforts undertaken for the development of the technology since its invention. A brief explanation of the various scientific principles that aid in the understanding behind the phenomenon is also provided. This chapter also provides a detailed (but not necessarily exhaustive) review of the current efforts both in the understanding of the mechanisms as well as the clinical translation of the technology of infrared neuromodulation.

Chapter 3 discusses the efforts undertaken to develop a computational model to understand the mechanism of infrared inhibition in unmyelinated nerves. A computational model aids and expedites the generation of testable hypothesis. Development and use of computational models provide us the ability to test multiple iterations of the generated hypothesis, hence obviating the

need for numerous exploratory animal experiments. The computational model generated in this chapter led to the development of the hypothesis that <u>voltage-gated potassium channels are responsible for causing thermal block during infrared inhibition of unmyelinated axons.</u> The computational model developed in this chapter was based on the widely accepted Hodgkin Huxley (HH) model. However, multiple changes were made to the original HH model, since the HH model couldn't accurately predict the response of unmyelinated axons subjected to elevated temperatures, which results from infrared irradiation. Published experimental data from multiple studies done in squids were used to modify the HH model, in order to make the model compatible to use when predicting neurophysiological responses at elevated temperatures. Multiple assumptions that were originally built into the HH model were studied for validity. For example, the sodium and potassium maximum conductance were assumed to be a constant value (and independent of temperature) in the original HH model. These assumptions severely limited the scope of the HH model for its use at elevated temperatures. All the changes made to the HH model were backed up with rigorous fitting methodologies. Once the model was developed which satisfactorily explained neural responses at elevated temperatures, it was used to test under various modeling setups that resembled an experimental setup for an infrared inhibition experiment. Many important implications and relationships about threshold block length and axon diameters were also generated through the model. One of them was that <u>threshold block lengths scale directly with the square root of the axon diameter</u>. All the physiological predictions were benchmarked against the predictions of the HH model in similar setups. There was strong qualitative resemblance between the predictions of the HH model and the newly developed modified HH model (so called mHH model). The results obtained from this model provided an experimental setup that was used to validate the modeling conclusions. These efforts are discussed in Chapter 4 of the dissertation.

Chapter 4 of the dissertation discusses the experiments performed to test the hypothesis that was developed in Chapter 3 of the dissertation, which was that infrared inhibition was caused as a result of increased activity of voltage gated potassium channels. The observations in these experiments suggested that potassium channels are necessary to cause thermal block in unmyelinated nerves, as predicted by our modeling studies. In order to establish beyond doubt that potassium ion channels are necessary and sufficient to generate conduction block in unmyelinated nerves, studies were performed using sodium current and ion channel blockers. The results generated from the modeling and experimental studies can be extrapolated to other unmyelinated axons, possibly the pain conducting C fibers in humans.

Chapter 5 discusses the development of a multiphysics model that combines an optical-thermal computational model with a neurophysiological computational model. The optical-thermal model evaluates the temperature rise in the nerve tissue as a result of infrared laser irradiation. The results generated from the model indicated that the maximum temperature rise at the nerve surface occurs when the nerve is around 150 μm from the irradiating laser fiber. IR (infrared) fiber diameters below 400 μm are prone to cause to thermal damage during thermal inhibition in nerves. The observations from the modeling results also predicted that using two fibers decreases the temperature rise threshold for thermal block in unmyelinated axon models. Effect of using a heating coil is also shown as an example, to demonstrate the versatility of the model to be used with various types of heat sources.

6.2 Implications

6.2.1 Computational neuroscience and multiphysics modeling

A major part of this dissertation was dedicated to the development of a computational model that can predict the response of unmyelinated axons to infrared irradiation. There was a

need to first develop a model that can predict neural response to elevated temperatures, since infrared neuromodulation appears to work through a photothermal response (Huxley 1959, Mou 2012, Wells 2007). During the development of the computational model (mHH model), novel analyses were developed and used. Among these were the fits developed to match the maximum conductance of sodium and potassium ion channels at various temperatures, which helped to develop the relationship between temperature and maximum ionic conduction. This led to developing a mechanistic prediction would probably not have been possible using the standard HH model with all its in-built assumptions. Dynamic clamps (Sharp 1993) were implemented to keep the resting membrane potential of the nerve axons constant when the conductance of the ion channels were reduced to zero. Past techniques have involved changing leak conductance, or the Nernst potentials to adjust for the potential change(Carnevale 2005). All of these changes resulted in modifications that seemed to be beyond the possibilities of squid physiology. In the search of an existing model that can predict neural response to elevated temperatures, multiple existing models (Clay 1998, Sangrey 2004) were also reproduced and tested in NEURON. An example of this can be found here at this link:

https://senselab.med.yale.edu/modeldb/ShowModel.cshtml?model=189922.   In this work, a model (Clay 1998) discussing a modification to the HH model was reproduced in NEURON and posted for the entire community .

Along with the development of the NEURON model and making it easy to use, a multiphysics model was also developed that combined light transport and heat transport models with neural propagation model following the HH model. There have been efforts mimicking the development of a model that aims to deliver similar objectives (Mou 2012, You 2017), but to the best to my knowledge, the effort discussed in this dissertation was the first to combine a three-

dimensional, time dependent Monte Carlo light distribution and a heat transfer model with a temperature sensitive neurophysiological model in NEURON. Due to the modularity of the model, results from other heating simulations like RF heating (in COMSOL) can be also be used in NEURON. Applying the effects of time and space varying temperature distributions were enabled by the changes made to the mechanism files in NEURON. This provides the community with a tool to test the effect that their irradiation protocol might have on the nerve before performing a potentially time and cost intensive experiment. This effect is already in play with the development of a novel way of reducing threshold block temperatures using multiple laser fibers (Ford 2017).

Attention was also paid to make the model more accessible and the dissemination easier to future users of the model. Use of NEURON for a beginner can be challenging, since it involves the use of the installation of the software in the local user computer (https://neuron.yale.edu/neuron/download). Even though NEURON offers a GUI version of the software, which is helpful, customizations made in this dissertation required the use of using NEURON with Python, in the command line of MacOS, Windows terminal, or Ubuntu (Linux). It was understood that this might be a major challenge for the wide adaptation of the model developed, and hence considerable amount of time was spent to simplify the use of the model and reproduce its results. All the code used in the development of the model were posted on GitHub (the code sharing repository) with the link: (https://github.com/mohitganguly/IRBlock_Vanderbilt). Additionally, a Dockerfile (https://docs.docker.com/engine/reference/builder/) was written that helps produce the model results on a web browser, without the need for the user to download any software or dependencies. The user can see an interactive notebook generated by the mybinder (https://mybinder.org/) on the browser and make changes to suit their needs. For advanced users interested in making deeper

changes, they are requested to download the model on their local computer and follow the steps mentioned in the associated readme files.

6.2.2 Experimental neuroscience

Through the experimental work in this dissertation, it was identified that potassium channels are critically responsible for causing thermal blocks in unmyelinated nerves. It has long been hypothesized that thermal blocks in squid giant axons were caused when the potassium currents 'overwhelm' the effect of sodium currents (Ganguly 2016, Huxley 1959). Earlier experimental results described here suggests that the neural inhibition caused by infrared irradiation is a result of the photothermal interaction of infrared light. There appear no significant complementary optical interactions that might be contributing to the phenomenon (Duke 2013, Lothet 2017). Since the mechanism appears primarily dominated by photothermal effect, it might suggest that most thermal inhibition modalities might share an underlying mechanism of thermal inhibition (eg. ultrasound neuromodulation, RF heating, high frequency block)(Ackermann 2010, Colucci 2009, Juan 2014, Min 2011).

The 3-dimensional nerve chamber (described in Chapter 4, section 4.3.4) channel blocker experiments chamber provides a novel way of applying ion channel blockers to a specific region of the nerve. Past attempts for similar applications involved considerably more effort than the experiments discussed in this dissertation (Nussinovitch 2014, Petsche 1983). We have presented an effort that allows us to study the effect of ion-channel blockers on a specific region of the nerve while the nerve is undergoing infrared inhibition in real time, and this effect is reversible. Further design improvements to the chamber, which are currently underway, will allow us to study the effects of other channel blockers and agents (eg. glucose block) during infrared inhibition.

6.2.3 Development towards a clinical modality

The broader aim of the research discussed in this dissertation is the translation of the infrared neuromodulation modality into the clinic. Currently, the research is in relative infancy as many questions still remain to be answered, and this dissertation is a small step forward in that direction. The combined multiphysics model developed in this dissertation provides a robust modeling framework to develop and test potential medical device designs. The model enables us to perform a wide parametric sweep of laser parameters and examine the sensitivity of the neural response to the change in those parameters. For example, we have investigated the role of fiber distance from the nerve surface, fiber diameter, and the distance between dual fibers on the temperature rise on the nerve surface. Comparable studies using animals experiments could be time and resource intensive (Duke 2012). The computational model is a first step towards a potential pain management medical device in the future. We believe this is possible since the technique of infrared inhibition has been shown to work successfully in *Aplysia,* which have unmyelinated nerves consisting of unmyelinated axons, and the models discussed in Chapters 3 and 5 of this dissertation have been developed with unmyelinated axons in mind. These axons are anatomically similar to the pain carrying C fibers in humans. The results obtained through the analysis in this dissertation provide useful insights on the optimal fiber distances and beam diameters to maximize heat absorption in the nerve and prevent heat (energy) loss through the blood and surrounding tissues. As an example, the idea of using multiple (two) fibers was also proposed and validated as a result of the model's results, and future design modifications should further explore this idea by using more than two fibers (Jeremy Ford's work under review).

Inclusion of Arrhenius thermal damage analysis in the model will enable us to discard laser parameters from the consideration that appear unsafe. As an example, in our studies, we realized

that fibers at certain distances (>150 μm) from the nerve surface and of certain fiber diameter (<400 μm) can cause thermal damage when irradiating at inhibition parameters. This will allow us to alter the design parameters like laser fiber distance, beam diameter etc, all through computational design, without performing any animal experiments. Once the model is improved further, complicated and realistic model geometries of devices and the nerves can be tested for safety and efficacy over both short- and long-term use.

I personally envision the modeling based medical device design could follow the track of another pain management modality that is currently undergoing clinical trials, which is kilohertz high frequency AC conduction block (KHFAC). This modality uses electrical pulses of relatively high frequencies (2-20kHz) on a nerve to block a propagating nerve signal. Once the modality was invented (Kilgore 2004), multiple modeling studies (Ackermann 2009, Ackermann 2011, Ackermann 2010, Miles 2007) were performed to optimize and control the block of nerve signals and removal of side effect such as onset responses. The technology is currently in advanced clinical trials for the treatment of chronic post-amputation pain (Eisenstein 2013, Soin 2015).

6.3   Future directions

This dissertation has focused on the development and experimental validation of computational models that predict the response of infrared inhibition on unmyelinated axons. While this dissertation has provided insights into the critical role of voltage gated potassium channels, there are many unsolved problems and unanswered questions, which can all result in research projects in the future. They are discussed in the following paragraphs. The future directions are grouped into the challenges that remain in the 1) modeling efforts, 2) experimental

efforts, and the future directions that should be undertaken to 3) translate this technology into clinical use.

6.3.1 Modeling efforts

The modeling efforts discussed in this dissertation (Chapter 5) consists of three disparate modeling phenomena, each governed by a different set of equations. The light distribution model (Monte Carlo simulations) explains the distribution of photons inside the nerve and surrounding tissues when the infrared laser light is irradiated on the tissue. Once the light distribution is evaluated, the resultant temperature rise is calculated using the heat transfer equations. Finally, the neurological response as a result of the temperature rise is evaluated by a set of equations known as the Hodgkin Huxley equations. Each of these modeling equations have their own sets of assumptions and limitations (discussed in Chapter 5, section 5.6) which contribute to the weakness of the entire modeling pipeline. In this dissertation, those limitations have largely been managed by using suitable assumptions or have been ignored, owing to their relatively minor role (unpublished work done in our lab) in the final result. However, moving forward, those limitations need to be overcome, or at least an accurate set of parameters need to be determined experimentally and used for modeling. In this section, those steps have been discussed in detailed. The steps for improving the model has been grouped in terms of the improvements that need to be made in the optical model, the thermal model, and the neural model.

6.3.1.1 Optical model

The optical model (or the light distribution model) predicts the distribution of the infrared laser light in and around the biological nerve tissue (please refer the Background in Chapter 2 for more details on the theory and principle). The input parameters for these models include the

absorption coefficient, the scattering coefficient, and the tissue anisotropy. In our model, those parameters have been assumed or borrowed from the calculations from published sources. The parameters are evaluated for conditions that might be dissimilar to the experimental conditions in the inhibition experiments conducted for this dissertation. For example, since the optical (and thermal) properties of the nerve tissues are not known exactly, the corresponding properties from skin tissues are used instead. It is assumed that minor changes in properties will not lead to significant different outcomes of light distribution and temperature rise. Additionally, the efforts to evaluate exact optical and thermal properties for nerve tissues is not-trivial and was not the focus of this dissertation. One of the thrusts for future work should be the evaluation of optical properties that closely resemble, if not identical to, the experimental conditions used in the lab. There are some efforts underway in that directions by members of the lab. Efforts should be balanced by the degree of change that each parameter adds to the overall results. For example: unpublished simulations performed in our lab have shown that changes in scattering coefficients have relatively minor effect on the predicted temperature rise in nerve tissues.

6.3.1.2 Thermal model

The thermal model used here has been used and perfected for numerous applications over a long period of time (Pennes 1948). In this dissertation, the temperature rises observed in the nerve tissues were found to be within 10 % of the experimentally measured results in the lab when measured using a thermocouple (Chapter 4). Hence the accuracy of the thermal model in predicting temperature rise can be assumed to be reliable at this point. This dissertation has focused on the inhibition effects of infrared neuromodulation, and it has been assumed that a photo thermal effect is responsible for observing infrared inhibition. Other effects of the photothermal interactions like photomechanical and photochemical effects have been ignored. Along with the temperature rise,

the change in pressure resulting from the infrared irradiation must be accounted for in future iterations of model revisions. This might be specifically useful when attempting to model infrared stimulation in nerves since studies have shown pressure transients to have be playing a role in the observation of stimulation(Richter 2011, Tan 2015, Xia 2017).

The origins of this pressure can be a result of three different mechanisms. They may arise due to the tissue ablation or removal, generation of thermoelectric stresses (due to rapid thermal expansion of heated volume), and vaporization of tissue water (Oraevsky 1995, Vogel 2010). Studies by Wells et al. (Wells 2007) have shown that infrared stimulation might not be driven by photomechanical effects but modeling results provide contrasting indications (Plaksin 2018). Exploring the role of pressure in the origins of infrared neural stimulation should be examined in detail since they appear to play an important role in neural stimulation caused during ultrasound neuromodulation (Prieto 2018). The SESE model currently used in this dissertation can be used to model those mechanisms. The current version of SESE isn't capable of modeling pressure transients arising due to pulsed laser irradiation but could be incorporated at a later time. In case SESE doesn't serve that purpose, commercial finite element solvers like COMSOL Multiphysics (https://www.comsol.com/acoustics-module) can also model infrared irradiation pressure in tissues (Hatef 2015, Humphries 2013, Ko 2010, Wang 2012, Wen 2019).

6.3.1.3   NEURON model

In this dissertation, a NEURON model (based on the Hodgkin Huxley model) is developed that can a) reliably predict the neurological response of unmyelinated axons at elevated temperatures and b) integrate a time and space varying temperature distribution as input parameters for elevated temperature. While this is a solid introduction to the eventual aim of developing a

combined computational model for infrared neuromodulation, it leaves much to be desired and warrants further improvements.

At this point, the model geometry considers a one-dimensional unmyelinated axon. Apart from cases involving squid giant axons and similar animal models (lobsters and crayfish), that is rarely the case. Any neural model should incorporate multiple axons with varying axon diameters that closely mimics the anatomy present in majority of experimental animals (*Aplysia*, rats, frogs, dogs etc). Future efforts should include the scaling up of the present model to incorporate multiple axons with varying axon diameters. The model should be equipped to measure the extracellular compound action potentials at any three-dimensional point in space. This arrangement is similar to the suction electrode stimulation and recording protocols during infrared neuromodulation experiments. An effort in this direction has been undertaken by our lab and is currently in its preliminary stages. In this ongoing work, a NEURON model is being developed that aims to demonstrate the selective thermal inhibition of small-diameter unmyelinated axons on the left pleural-abdominal connective (LPAC) nerve of *Aplysia californica* through analysis of the compound action potential (CAP). The model aims to demonstrate the three-dimensional, time variant probabilistic inhibition of small-diameter axons of LPAC and the resulting effects of CAP as the LPAC is heated with an infrared laser over time. Initial preliminary results appear to show the relationship of block length and axon diameter with spatial and time variant temperature distributions. The relationships and apparent trends are consistent with the experimental findings in *Aplysia* (Lothet 2017). Future versions of the model will hinge on refining the model and incorporate improvements that makes the model results consistent with published experimental results. Eventually the model development should move towards building large networks that might help mimic networks similar to be found in mammalian models (Kovalsky 2009).

Adaptation to mammalian models will require modeling of additional phenomena, for example, effects of adding myelin sheath(McIntyre 2012, Rattay1989, Richardson 2000), incorporating effects of potassium ions etc (Frankenhaeuser 1956).

This dissertation has focused on modeling of inhibition effects of infrared neuromodulation. Future efforts should also be directed towards the development of stimulation effects of infrared neuromodulation. Experimental reports have shown that infrared laser pulses lead to change in membrane capacitance that results in membrane depolarization (Plaksin 2018, Shapiro 2012). Even if the phenomena has been believed to be largely driven by temporal and spatial gradients in temperature (Wells 2007), other effects (eg. membrane nanoporation) have been also been shown to result in infrared stimulation (Beier 2014, Moen 2016, Paris 2017, Walsh 2017) . Efforts should be undertaken to incorporate these mechanistic conclusions which are based on published experimental results. There are existing models which act as a good starting point for future developments (Eom 2018, Fribance 2016). Modeling efforts could also explore if the movement of ions across the cell membrane in response to elevated temperatures ('thermophoresis') would be responsible for infrared nerve stimulation (Jerabek-Willemsen 2011).

6.3.2   Experimental efforts

The current dissertation has provided preliminary experimental validation of the hypothesis that potassium channels are critical for infrared inhibition. This hypothesis was derived as a result of the computational modeling. While the experimental results shown in the dissertation are conclusive, much remains to be done to develop an exhaustive understanding of the mechanism of infrared inhibition. There are numerous types of potassium channel sub-types in mammals, and characterization and identification of dominantly responsible potassium channels could be an

obvious next step. This can be done by patch clamp studies, direct potassium channel measurements, potassium sensitive dyes, etc. (Rimmele 2014).

6.3.3 Clinical

To translate this technology into a clinical modality for pain management, various hurdles need to be cleared. To summarize, these hurdles can be grouped as technical hurdles and non-technical hurdles. All these hurdles call for the need for a mixture of strategic thinking and technical breakthroughs. The technical hurdles involve efforts to miniaturize the light delivery source (diode lasers), reducing power requirements, minimizing local temperature rise needed for therapy over long-term use, and negating potential side effects. The regulatory hurdles might include the lack of clear IP landscape, lack of clear guidelines for maximum permissible exposure parameters, FDA class III approval route, raising enough funds to conduct clinical trials, and working with partners to develop pricing and marketing strategies. The next couple of paragraphs will explain the hurdles in detail and list some potential solutions.

6.3.3.1 Technical hurdles

Several technical innovations need to be realized before this technology can be packaged as a viable medical device product that can be used in the clinic. A basic medical device design that could be envisioned to translate this technology will consist of two main components, an implantable light source, and a power source. The light source used in this dissertation is a portable, benchtop laser called Capella Infrared Nerve Stimulator developed by Lockheed Martin Aculight in partnership with Vanderbilt University. While this laser system has been immensely successful in multiple studies of infrared neuromodulation, a substantial redesign of the laser system is warranted for translation to a medical device. An example modification could be the "tripack"

used in the cochlear studies. The "tripack" was a wearable, 3-channel laser stimulator, with wireless software control. It consists of three side firing fibers (200 um, 1860 nm) covered in silicone (Moreno 2011). While this is an improvement, but a further reduction in size and power efficiency of the of implantable lasers is desired. VCSEL (vertical cavity surface emitting laser) could be one such option. VCSELs, a product of telecom industry, are semiconductor-based laser diodes that emit light beams vertically from its surface and can be arranged in the form of arrays. They appear to be ideal to fulfil the light delivery demands of infrared neuromodulation in terms of size and compactness, however they don't exist in the wavelength ranges required for our infrared neuromodulation applications. Longer wavelength VCSEL's suffer from low optical gain, and lack of semiconductor mirrors (Chang-Hasnain 2003, Keller 2013). Some recent advances have been made to develop power efficient lasers that might work in the desired range of 1550 nm(Hofmann 2008), but the VCSELs that could work in the range >1800nm remain rare (Ortsiefer 2000) and should be pursued as an area of future research. This suggests that, with the current state of technology, the use of 1460 nm IR wavelength VCSEL would be ideal for use in IR inhibition applications. Use of VCSELs for IR inhibition at higher wavelengths would require rethinking of current lasing technology and materials used (Chernov 2012) , and thinking beyond VCSELs, eg: microdisk lasers, photonic crystal lasers, and small metallic lasers (Hill 2014). Potential for side firing fibers (George 2009) and optrode (Dufour 2015, Wang 2010) should also be explored for the advantages they offer in terms of accessibility and ease of recording.

In my opinion, the innovation required for the delivery of infrared light to the tissue can be borrowed from the field of optogenetics. Multiple advances have been made in optogenetics that might be useful when adapting the technology of infrared neuromodulation into a clinical device. Development of LED (light emitting diode) based delivery solutions have been used and perfected

in optogenetics and are used an implantable light delivery source (Clements 2013). The design aspects used in the miniaturization of these LEDs could also be used in IR inhibition applications. However, LEDs might not be ideal for IR inhibition due to their large divergence which makes precise localization of the light difficult. These reviews provides an useful resource to study the various technological challenges that have been overcome for the translation of optogenetics into a clinical modality (Matveev 2015, Zhao 2017). Researchers in optogenetics also seem to have made advances in the field of wireless and power control of light delivery inside the animal using resonant interaction of RF (radio frequency) and intrinsic modes present in the animal (mice) (Ho 2015). This advance put optogenetics in firm footing for launch as an implantable medical device, which is evident from the launch of companies and ongoing clinical trials (Reardon 2016).

At present, the temperature rise required to achieve inhibition is prohibitively high (Ford 2017, Liljemalm 2014, Mou 2012, Thompson 2013) and almost certainly damaging (Liljemalm 2014). While FDA doesn't propose strict temperature rise threshold in its device specifications, the current temperature rises observed in experimental setups are not tenable. Efforts to reduce temperature rise during inhibition is a work in progress (Owen 2015) and is currently an active area of research in our lab (Ford 2017). Simulations developed in this dissertation have led to efforts that study ways to reduce temperature rises observed during infrared inhibition experiments. These efforts (unpublished) aim to build upon computational predictions that suggest that a longer irradiation length results in a lower temperature at inhibition threshold by using both multiple stationary spots and a single scanned spot along the nerve to reduce the heat deposition required at any given location, therefore reducing the probability of thermal damage, and allowing for longer irradiation times.

6.3.3.2   Non-technical hurdles

The non-technical hurdles in the translation of the technology include the challenges that are likely to encountered outside the lab, chief among them being a) lack of clarity in the intellectual property landscape around the technology and its use, and the eventual product design and packaging. At present, there already exist multiple patents (not all of them owned by Vanderbilt) which claim to invent various way to shine light on nerves. However, this shouldn't be the hurdle stifling innovation, since IP challenges by interested parties will be significant only if the envisioned product has major sales potential. Translating this technology to the market will require numerous innovations along the way which may spawn multiple patents to fend off any potential legal challenge in the future.

A significant obstruction to marketing the product would probably be the strict regulatory pathway. Depending on the application, the future device would probably be an implantable device, and would have to undergo class 3 (Pre-Market Approval) process of the Food and Drug Administration (FDA) (https://www.fda.gov/MedicalDevices/DeviceRegulationandGuidance/HowtoMarketYourDevice /PremarketSubmissions/PremarketApprovalPMA/default.htm). The device (being so novel) will face higher scrutiny from the FDA during the pre-clinical testing. For example, instead of the normal ISO 10993 testing, we might be required to do an active animal study where the device is implanted in animals and stimulated for 90-180 days to track local effects. Clinical feasibility studies would need to be done before conducting pivotal studies. Though a long and tedious process, the process can be simplified and expedited using the FDA HDE (Human Device Exemption) application

(https://www.fda.gov/medicaldevices/deviceregulationandguidance/howtomarketyourdevice/pre marketsubmissions/humanitariandeviceexemption/default.htm), testing and marketing the device for indications with less than 8000 incidences per year. In these cases, FDA might focus more on the efficacy, but the product would face relatively less scrutiny on the safety of the product. Another alternative could be launching and marketing the product in Europe instead of the USA, where the launch process is likely to be faster (Maak 2016).

Moving forward, strategic collaborations will need to be formed with opinion leaders and large medical firms for funding and networking opportunities. Successful collaborations would be highly contingent on the favorable results from the clinical feasibility studies. Finally, the largest non-technical hurdle would be financial in nature. Based on conversations with industry experts, it would require approximately $15-20 million for regulatory testing and an additional $15 million to hire and assemble a sales force to market the product. Considerable lobbying of the CMS (Centers for Medicaid and Medicare Services) and post market healthcare economic studies needs to be done to demonstrate the profitability to insurance companies to persuade them to cover the cost of the product and/or treatment.

Team

Mohit Ganguly, PhD Candidate, Biomedical Engineering, Vanderbilt University

Bryan Hartley, MD, Interventional Radiology, Vanderbilt University

Daniel Huang, MBA Candidate, Vanderbilt University

Walter Russ, MBA Candidate, Vanderbilt University

Siyi Shen, JD Candidate, Vanderbilt University

Advisors

E. Duco Jansen, PhD, Professor, Biomedical Engineering, Vanderbilt University

Marc Huntoon, MD, Director, Pain Medicine, Virginia Commonwealth University

Austin Duke, PhD, NexeonMed

Eric Fugett, JD, Waller Law

Date: 5/1/2017

Executive Summary / Need

This plan presents a path to commercialization for Allevien. Allevien is a novel technology that uses laser light of specific wavelength (infrared) to block the propagation of nerve signals. This technology can be used to prevent pain signals form traveling to the central nervous system (spinal cord), thereby used as a chronic pain management modality. Allevien has been shown to work on rats and other lower animals (*Aplysia* and shrew). Experiments on higher animals are curently in progress. The technology will be marketed as an implantable medical device powered by an implantable electrical generator. This document lays down the different aspects of the commercialization plan that will be used to bring this device to market. At this point, we are in research and development phase and not going forward to form a start-up venture or licensing the technology. However, all the different aspects of the commercialization have been considered and mentioned in this plan. After the required regularoty approvals from the U.S. Food and Drug Administration (FDA), we will begin marketing the product to veterans first. The medical device and the technology driving it is most suitable for managing chronic pain which originates from damaged nerves resulting from limb amputation (known as phantom pain). Veterans who have experienced amputation due to trauma in the battlefield are a strong market for early adoption for this device. The number of amputations equal around 175, 000 annually in the US with around 2 million total amputation patients in the US. The rationale behind the selection of the target demographic is through inputs from our technical and clinical advisors.

There are numerous issues associated with the plan which will be addressed in detail in the following sections. In addiditon to the numerous research challenges that need to be tackled before the device is deemed ready for clinical trials, the intellectual property landscape is muddy and patents required for commercializing our technology have not been granted. There are high barriers

of entry into the medical device industry owing to substaintial presence of established large market leaders. Apart from these, the device will have to go through Pre Market Approval (PMA) in the FDA which will be long and expensive. Reimbursement codes will also have to be identified to to make it possible for patients to get reimbursed for the procedures that they will need to use the implantable device.

Allevien technology

We are developing the use of infrared laser irradiation as a solution to the clinical problem mentioned in the paragraph above. We have shown that infrared laser irradiation is able to inhibit action potential propagation in small unmyelinated axons in the *Aplysia californica* (sea slug) animal model. We believe that since the anatomical organization of the nervous system in sea slug is similar to the pain conducting fibers in humans, it is possible that infrared laser irradiation can be used to inhibit pain signals in humans. Our method also compares well against the modern techniques of neuromodulation presently in research. Our method is free from the use of any genetic manipulation (optogenetics), has better spatial selectivity than focused ultrasound and is free of any sharp pain signals (onset response) as seen in HFAC (High Frequency Alternating Current) stimulation. We plan to introduce infrared laser inhibition as a cuff-like neural device implanted close to the source of the pain signals. We envision the cuff will be placed around the target nerve fiber (tibial nerve for above-knee amputations, peroneal nerve for below knee amputations) and will use diode lasers as a thermal source.

Our technology – Allevien™
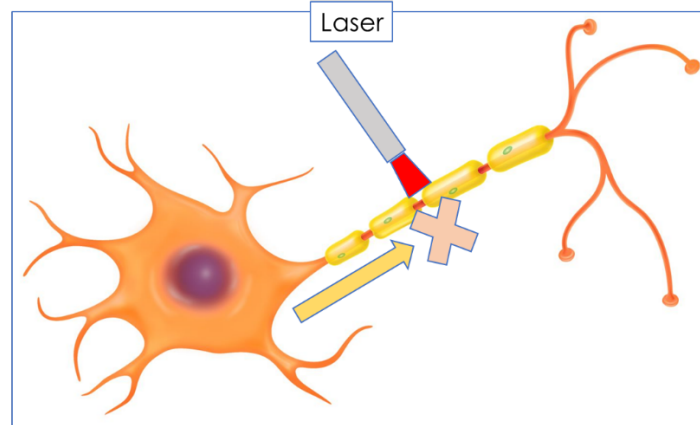
Figure A-1: Allevian inhibits peripheral nerve signaling with infrared light

The current pharmaceutical methods of chronic pain management include the use of opioids, analgesics, NSAIDs (Non-Steroidal Anti-Inflammatory Drugs) and anticonvulsants. The use of these drugs are accompanied by the side effects such as the development of tolerance, addiction, withdrawal symptoms and rebound pain. In severe cases, electrical methods to control chronic pain are used. These include the use of TENS (Trans-cutaneous Electrical Nerve Stimulation) which involves the use of electrode patches over an affected part of the body, and SCS (Spinal Cord Stimulators), implantable spinal cord stimulator that delivers small electrical signals through a lead implanted in the epidural space. The above electrical methods lack a clarity in the mechanism of action, suffer from high inter-patient variability, surgical complications, lead migration, paresthesia, electrode toxicity, and they interfere with MRI and pacemakers. We believe, that since our device does not involve delivering electrical signals in to nerve tissues, it will not suffer the drawbacks of electrical stimulation methods, especially paresthesia or the tingling like sensation felt by patients using spinal cord stimulators. However, these claims will have to be tested using thorough clinical trials.
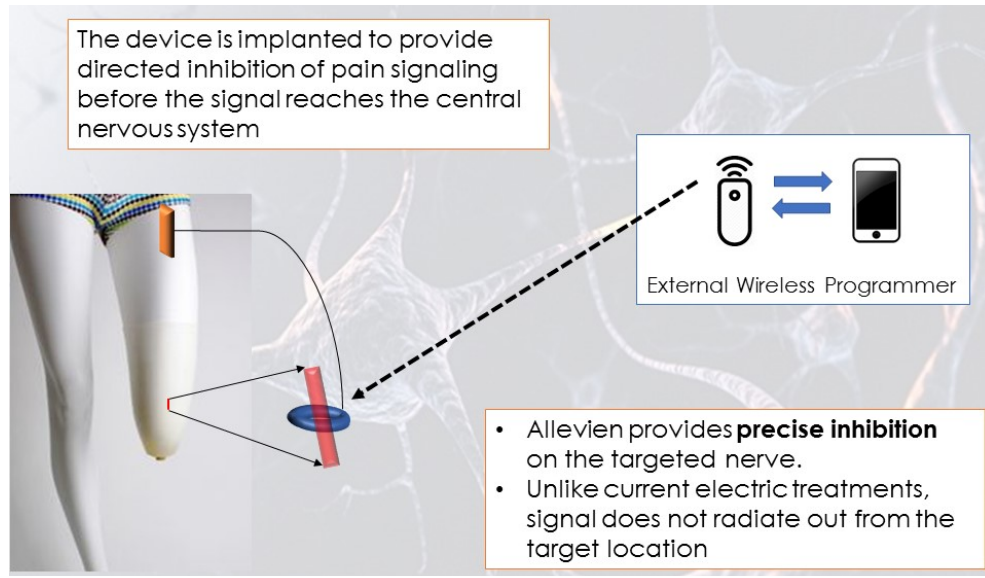
Figure A-2: Allevien cuffs around the peripheral nerve is powered by an implanted power source

Intellectual property

There is an existing patent for infrared irradiation on the central nervous system (US 9044596 B2: Method and apparatus of pulsed infrared light for central nervous system neurons, Granted June 2, 2015, Assignee: Vanderbilt University). This patent will enable us to use our technology for irradiating on the spinal cord.

However, for targeting the peripheral nerves, there is a rejected patent application (14/024544: Method and Apparatus for Selectively Controlling Neural Activities and Applications of Same).

According to USPTO's final rejection letter, the application was rejected as some claims being anticipated by an existing patent (Patent US 8721695 B2: "Device and Method for

Stimulating Neuronal Tissue by Means of Optical Stimuli".) More specifically, the USPTO explained its rejection reason as that existing patent was also "an apparatus for selectively controlling of neural activities . . . : at least one electrode . . . a light source . . . . and a probe . . . coupled to the at least one light source for selectively delivering the at least one light to the target of interest at selected locations to create a localized and selective inhibitory response therein." We cannot agree with the USPTO on the ground that Patent US 8721695 B2 had no claims about the inhibition or suppression of any neural activities. That patent targets the stimulation of certain neural activities, which is a totally different technology than our rejected application.

We are confident about the above argument, with the support from our technology mentor E. Duco Jansen and our legal mentor Eric Fugett. Nevertheless, because the application for Patent US 8721695 B2 has been closed, we are not able to present any further argument to the USPTO about Patent US 8721695 B2. Our plan is to apply for a new patent of our technology on the peripheral nerves, which requires some 'patentable improvements' based on our existing technology. Now we are on the stage of looking for a similar method (using infrared laser) that reaches the same outcome as the rejected patent application could do, so as to avoid patent rejection on the grounds of existing prior art. We plan to make 'patentable improvements' in the future as we progress in our phases of research and prototype development.

Industry analysis

We presented a thorough analysis (Porters analysis) of the medical device industry in the commercialization plan that we submitted in December 2016 and is summarized in the Fig. A-3. In this plan, we focus on the trends in the medical device industry and the neurostimulation industry in particular, and how these trends will affect the commercialization of our medical

device. These trends and insights are derived from our customer interviews, mentors, and medical device conferences. Over the next five years, industry is expected to grow at 2.9 %. The aging baby-boomer population and technological developments will continue to bolster industry growth, but the changing regulatory environment will likely hamper profitability.
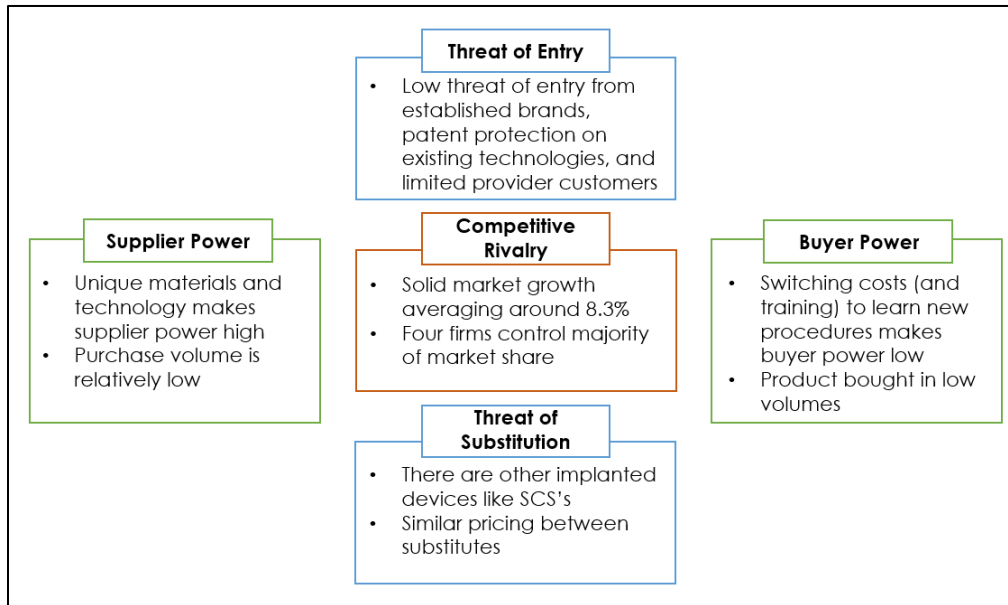
Figure A-3: Porter's five-forces analysis for our product Allevien™

The Affordable Care Act ('Obamacare') has created a degree of uncertainty for medical device companies. The 2.3% excise tax on medical device companies is expected to maintain its downward pressure on company profitability. The Physician Payment Sunshine Act is expected to increase industry costs and possibly reduce revenue because it requires covered manufacturers to annually report any transfers of value to physicians. Recent legislation overhaul, however, might benefit the industry, as US healthcare reform is aimed at expanding coverage to a broader range of patients. The act accomplishes this by significantly loosening the eligibility criteria for enrollment in Medicaid, as well as making private insurance more accessible to consumers. As a

result, more people will have access to healthcare, which will likely boost the average number of physician visits. This, in turn, will raise demand for some medical services and devices.

The prices that medical device manufacturers are able to charge will likely remain a concern in the future. Although access to insurance will increase, standards of reimbursement and regulatory approvals will become more stringent. Stricter reimbursement requirements could affect the revenue of customer groups, such as hospitals. Hospitals that receive small reimbursements per procedure will need to perform more procedures to justify new equipment purchases. In turn, manufacturers may be pressured to reduce per-unit costs to keep sales up.

With market saturation and growth stifling policies in the developed economies, medical device companies will likely aim to expand into emerging markets like China and India. Demand for medical devices and services is expected to grow in the future due to their improving economies, rapidly increasing and aging populations, and the prevalence of chronic diseases.

Competition analysis
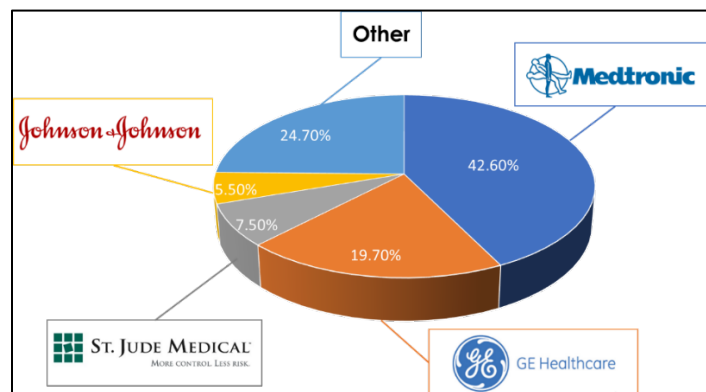
Figure A-4: The medical device industry has four main players

There are numerous technologies in the market that currently offer relief from chronic pain. In particular, because our technology takes the shape of an implantable device, we analyze the spinal cord stimulation market which offers a comparable industry. The various products and their specific advantages are mentioned in Fig. A-5.

Apart from these companies and products, we came across a few companies which are in similar stage of development as we do and offer technologies that can address the need in a manner similar to ours. The most promising of these companies is Neuros Medical Inc. Neuros uses high frequency conduction block technology to produces direct nerve block to mitigate phantom pain. Neuros is currently recruiting patients for their pivotal clinical trials. While this is a potential competition that we need to be careful about, past scientific reports have shown that this technology can suffer from side effects like onset responses that are potentially very uncomfortable to patients.

	Technology	Market Share (SCS for chronic pain)	Selective Advantage
Medtronic	RestoreSensor®	39%	Adapts to patient movement
Boston Scientific	Precision®	32%	More control over current delivery
St. Jude Medical	BurstDR™	25%	Paresthesia free
nevro	HF10	New Entrant	Paresthesia free

Figure A-5: There are currently a few neuromodulation devices in the market

Market analysis and financial projections

As mentioned above, phantom pain is an extremely underserved medical condition. Current treatments are ineffective and there is not a significant push in the market to create innovative functional solutions. Of the 1.9 million amputees in the United States, approximately 80% of them experience some degree of phantom pain. The majority of amputations in the United States (roughly 80%) occur because of vascular disease and vascular complications in diabetic patients. The remaining segment of the amputee population has lost limbs because of other reasons such as trauma.
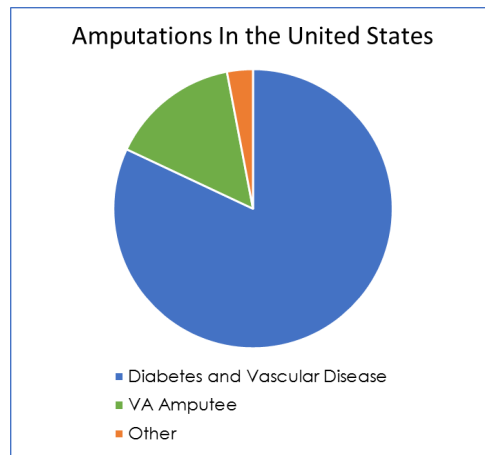
Figure A-6: Amputations in the United States

Over 80% of amputations in the US are performed because of Diabetes and vascular disease. Trauma amputations like those that occur in the military are a much smaller portion.

At Allevien, we have decided to focus on a specific subset of the population. Veterans constitute a large portion of the amputees not affected by diabetes or vascular disease. With trauma-based amputations, there will be fewer parallel or complication physiological amputations.

Also, though veterans make up a smaller portion of the trauma amputations than the whole trauma population, they are a very well documented market segment and their medical and support system is ideal for early adoption. First, according to the Department of Veterans Affairs a little less than 1% of America's 22 million veterans are amputees. This means about 175 thousand veterans are currently experiencing phantom pain. This is a significant population to first introduce to our new technology.

The VA medical system significantly simplifies our initial coming to market strategy as well. Instead of approaching multiple payor and provider groups, Allevien will start with a single entity with whom to transact. This greatly simplifies the marketing and sales efforts of our company. This strategy is complicated by the fact that we must now navigate the bureaucracy of government. However, Allevien will be able to mitigate many of the risks of this 'all in,' one customer approach by leveraging advocacy groups and the political capital politicians will gain by supporting our initiative. Many organizations, like Wounded Warrior, operate to aid injured soldiers and make their lives healthier and more comfortable. These groups would be some of the first advocates Allevien approaches. Also, not only does Allevien bring much needed comfort to these veterans, but it reduces the current costs spent by the VA to alleviate veteran's phantom pain. These cost savings will then be able to be in reduction of medication costs and also in freeing up scheduling to let more veterans be seen by the VA. As we have seen in recent news, the VA is currently overbooked and spread thin.
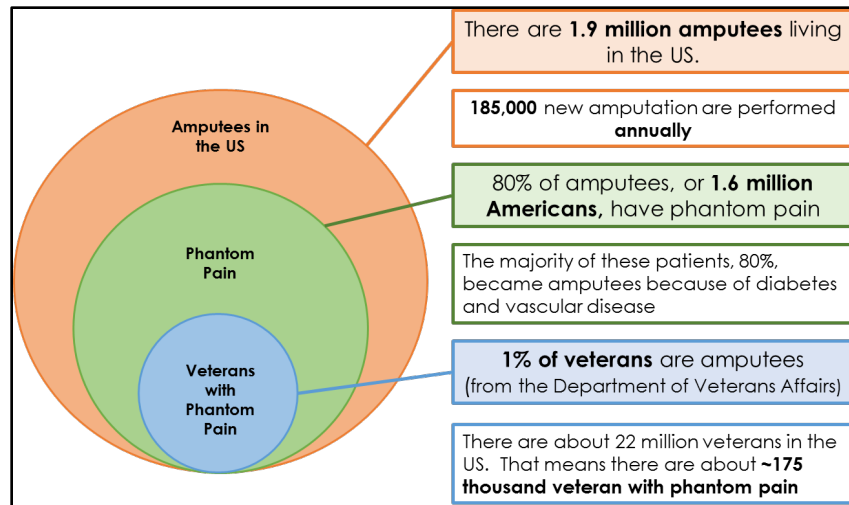
Figure A-7: The veteran market contains approximately 175 thousand potential patients

As a product, Allevien will have a significant margin, making entering the market a very attractive prospect. Spinal cord stimulators, which are currently being used to treat phantom pain, are sold for $20 thousand and the main components needed to create the Allevien device will cost around $10 thousand. This means that capturing 10% of the entry market there will be total profit margin of about $175 million. In total, the complete market of amputees in the United States is $16 billion for Allevien. Naturally, Allevien will not capture this entire market. Before Allevien can enter the market, there are a few development barriers that we must overcome.

Next Steps and Market Entry

The Allevien device is still in research infancy. Currently, research in laser inhibition is being performed using large laser devices on lower animal neural pathways. These lower animals (sea slugs) have nerves that are easy to manipulate in the laboratory and are similar to peripheral pain nerves. However, neither the current laser design nor the current biological samples are representative of the elements to a functioning Allevien medical device.

In order to reach a commercial product ready for the FDA Premarket Approval (PMA) application, Allevien must go through three more research phases: product development, pre-clinical trials, and clinical trials. For extended academic research at Vanderbilt University, the laser delivery needs to be optimized. Researchers need to find the ideal wavelength and laser intensity to efficiently inhibit the pain signal. The current Allevien device is also much larger than a medical device. A parallel research path will be needed to miniaturize the device. The academic product development stage will take approximately 5 years, the length of time of two parallel PhD projects. Funding for this phase will come from either the NIH, AFOSR, or DARPA. Since our early adopter target group is veteran amputees, DARPA (Defense Advanced Research Projects Agency) an AFOSR (Air Force Office of Scientific Research) are the ideal funding sources. AFOSR is the current funding of the Allevien project.

2017	2018	2019	2020	2021	2022	2023	2024	2025	2026	2027	2028

Product Development	Pre-Clinical	Clinical Research
Further academic research: • **Optimize** laser neuromodulation • **Miniaturize** the Allevien device	Pre-Clinical trials involve **testing in larger mammals** with nerves more similar to humans'	**Class III device human trials** for Allevien to verify safety and efficacy are the **last step before FDA approval**
Product development requires **5 more years** of research	Animal testing will take about **3 years**	Average clinical research schedule takes **4.5 years**
Funding will come from NIH, **AFOSR**, or **DARPA** grants	Funding will come from **SBIR grant** and angel funding	Funding will come from **venture capital** and **strategic partners**

Figure A-8: There are many research steps that Allevien will have to take before being market ready

After the device has been developed, research will go into preclinical trials. This FDA process involves testing Allevien in mammalian organisms with nervous systems more similar to humans. These tests will most likely be in dogs, in which the Allevien device can be successfully implanted. This phase of research usually takes three years. At this point, the project team will exit academia and become and incorporated company. Capital will be raised through SBIR grants and angel investment. SBIR grants are preferred and advantageous because they do not require equity to be distributed. The final stage of research will be clinical trials. Since Allevien is an implanted device, it will have to undergo the stringent Class III trial process. This process takes on average 54 months. Funding will come from our strategic partners and venture capital. After these twelve and a half years, Allevien will finally be ready to undergo the difficult PMA process.

Once Allevien is commercialized we will begin aiding amputees through Veterans Affairs. After establishing a significant footprint with our early adopter we will move into the larger market of diabetes and vascular disease phantom pain. Establishing ourselves with within these markets will be a much more complicated endeavor since we will have to establish relationships with providers, payors, and gain consumer confidence. In order to create a smooth transition from the VA to the general patient population, the Allevien team will begin establishing relationships with providers and payors during the clinical trials and throughout early adoption. As success of Allevien is proven with the veteran population, our team will approach other advocacy groups and organizations for diabetes. This will create champions within the system to push for adoption of our technology. If Allevien gets designated as a new medical device and needs a new billing code, and cannot be pooled in with devices like spinal cord stimulators, these groups will create pressure on the government to push through legislation creating an ICD-10 code. With expansion into these larger markets, Allevien will gain a high product valuation.
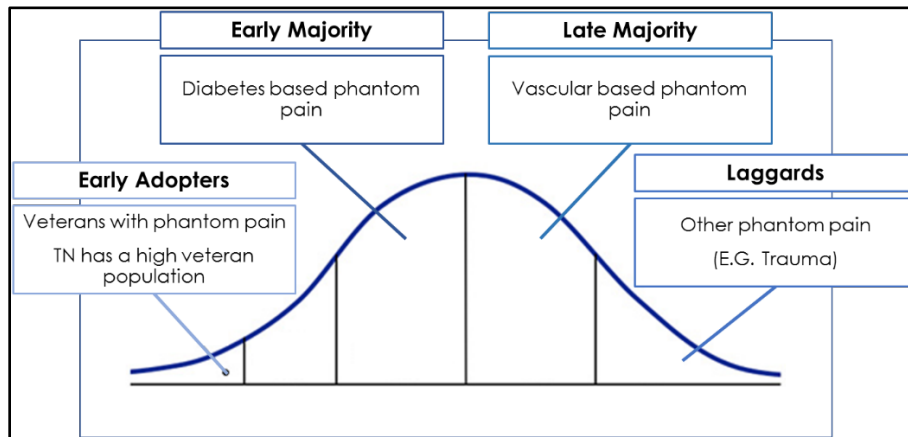
Figure A-9: Adoption cycle of Allevien

With Allevien, the underserved phantom pain patient population will finally be able to find relief. Though there is a long path ahead for Allevien, there is clear market need and financial demand for an innovative medical device to combat the condition. There are also organizations waiting to partner with a technology like Allevien from the military, to medical device businesses, to lobbyists and advocacy groups. Allevien will be able to change the lives for the better of many suffering patients, while creating a successful business.

Customer discovery highlights

(Based on our interviews with anesthesiologists)

1. Dr. Walters

2. Dr. Daniel Lanergan

3. Dr. Marc Huntoon

Major outcomes based of the conversations

- SCS procedures are performed about 3-4 times a month with a duration of 1-2 hours each.

- The process that delays the procedure is asking the patient for constant feedback to ascertain the coverage area of the implant

- Success rate: trials = 70-80 %, after 1 year post implant = ~50-70 %.

- Side effects include shock like tingling, lead movement with patient movement, development of tolerance

- Most common patient demographic is patients with back pain from prior decompression surgery with persistent back pain after surgery

- 10% of patients don't like the stimulation feeling after implanted and it has to be removed

- Alternative application could be targeting spastic patients to help release the muscles, because they traditionally required a baclofen pump placed by the neurosurgeons.

- Potential application be irradiation of dorsal root ganglion (DRG) in patients suffering from complex regional pain syndrome, phantom pain for amputees, carpel tunnel syndrome, and nerve trauma.

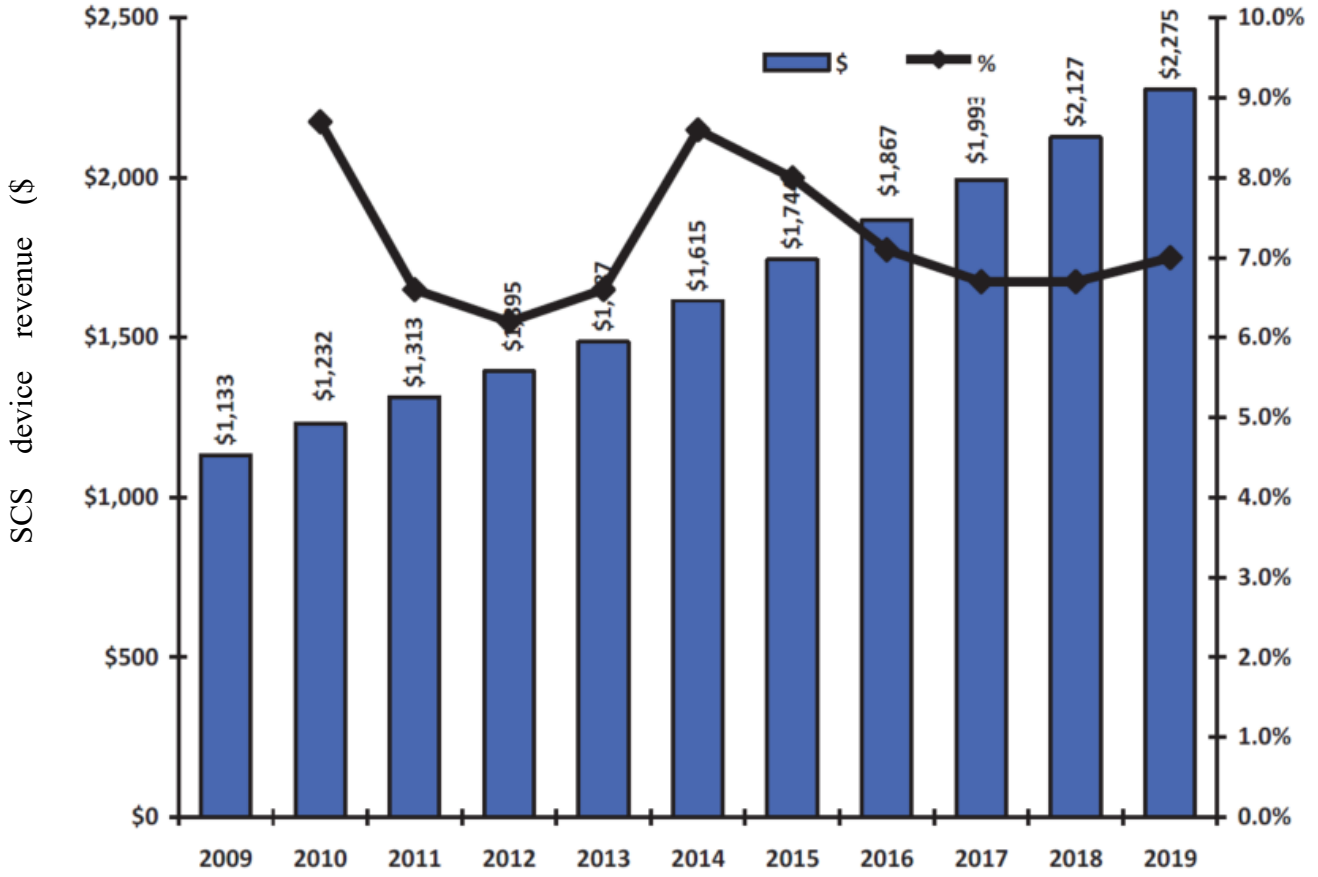**Global stimulation market and forecast**

Figure A-10: Global stimulation market and forecast

Source: Kalorama Information

Advice from business mentor to tackle some challenges in the long run:

1. FDA: Aim to make the pathway easier by engaging with FDA earlier through Early Feasibility Studies (EFS). Aim to find a condition that can qualify for Humanitarian Device Exemption (HDE).

   Try aiming for markets outside US (Europe) where we can launch faster.

2. Patent and IP try to aim for an IP as the research and development matures. Also discuss licensing opportunities with critical patent holders.

3. Reimbursement: Will need to do post market healthcare economic studies to demonstrate to insurance companies and Medicare that they should pay for the product. Finding out how to get paid is critical.

4. Collaborating with a partner: Study the strategic roadmaps of large companies to determine whether they will have any interest in what you are doing. Our best bet for collaboration will be after clinical feasibility study if we show good results. If we stick with proposing to work with one of those big companies, we have to make sure it's after you've got good clinical data.

Link to poster presented at SEMDA (South Eastern Medical Device Conference 2017), Atlanta GA (4/26/17): http://i.imgur.com/rLBCgQD.jpg

APPENDIX B: MODELING THE EFFECTS OF ELEVATED TEMPERATURES ON ACTION POTENTIAL PROPAGATION IN UNMYELINATED AXONS

Mohit Ganguly[a], Michael W. Jenkins[b, c], Hillel J. Chiel[c, d, e], E. Duco Jansen[a, f*]

[a]Department of Biomedical Engineering, PMB 351631, 2301 Vanderbilt Place, Nashville, TN 37235; [b]Department of Pediatrics, Case Western Reserve University, Cleveland, OH; [c]Department of Biomedical Engineering, 319 Wickenden Building, 10900 Euclid Avenue, Cleveland, OH 44106;[d]2080 Adelbert Road, Cleveland, OH 44106;[e]Department of Neurosciences, 10900 Euclid Avenue, SOM E653, Cleveland, OH 44106;[f]Department of Neurological Surgery, T-4224 Medical Center North, Nashville, TN 37232

ABSTRACT

Infrared lasers (λ=1.87 μm) are capable of inducing a thermally mediated nerve block in *Aplysia* and rat nerves. While this block is spatially precise and reversible in sensory and motor neurons, the mechanism of block is not clearly understood. Model predictions show that, at elevated temperatures, the rates of opening and closing of the voltage gated ion channels are disrupted and normal functioning of the gates is hindered. A model combining NEURON with Python is presented here that can simulate the behavior of unmyelinated nerve axons in the presence of spatially and temporally varying temperature distributions. Axon behavior and underlying mechanism leading to conduction block is investigated. The ability to understand the photothermal interaction of laser light and temperature dependence of membrane ion channels *in-silico* will help speed explorations of parameter space and guide future experiments testing the feasibility of selectively blocking pain conduction fibers (Photonic Analgesia of Nerves (PAIN)) in humans.

Keywords: Infrared Laser Heating, Neural Inhibition, Computational Modeling, Neurophotonics

INTRODUCTION

Electrical stimulation has been the gold standard for the control of nerve behavior. Some of the applications of electrical nerve stimulation include the treatment of foot drop (Kottink 2008), deep brain stimulation (DBS) for disorders such as Parkinson's disease (Kern 2007) cochlear implants (Shannon 2012), and vagus nerve stimulation for epilepsy and depression (Groves 2005). Apart from electrical stimulation, optical methods of neural inhibition have also been explored. Application of optical inhibition of nerves in the control of pain is an area of active research. One of the studies involving optical inhibition used pulsed infrared lasers to inhibit nerve signals in the

rat sciatic nerve and in *Aplysia californica* (Duke 2013, Lothet 2017). The successful use of infrared lasers in inhibition of unmyelinated nerves can lead to the development of implantable devices that can inhibit pain signals carried by unmyelinated C fibers. However, this requires proper characterization of the laser parameters required to observe conduction block in the specific nerve without exceeding the thermal damage threshold. A better understanding of the mechanism behind the observation of nerve conduction block is required so that we can optimize the parameter space in order to move towards clinical study. In the case of infrared nerve inhibition, the primary mechanism of heat generation is through the photothermal interaction of laser light by nerve and the surrounding tissues.

In this chapter, we have attempted to investigate the effect of elevated temperatures on nerve conduction in unmyelinated axons. As early as in 1959, Huxley commented that, at higher temperatures, sodium permeability is gradually overtaken by potassium permeability leading to a block of the onset or propagation of an action potential (heat block) (Huxley 1959). More recently, Mou et al. (Mou 2012) developed a model for studying the effect of heat on action potential propagation in myelinated axons. They showed the variation of conduction velocity versus temperature for different diameter fibers and electrical stimulus versus fiber diameter.

They simulated high temperatures at specific nodes in a frog (myelinated) sciatic nerve model at varying lengths along the axon. They showed that the threshold temperature (which is dependent on the stimulus current and fiber diameter) required to produce a propagation block is greater than the threshold temperature required to produce a generation block. While the results of Mou *et.al.* were significant and offered new insights, they were unable to provide a clear mechanism of the heat block (generation or propagation) observed in nerve due to axonal

temperature rise. The heat block simulated in the model was confined to limited spatial region in the axon. This spatial confinement of temperature is not practical in either electrophysiological experiments or in clinical settings. There was little quantitative or qualitative representation of the change in the gating variables or the ion channels due to increasing temperatures over time.

The computational model we have developed is designed to predict the effect of transient elevated temperatures on the membrane currents, and subsequently to the resulting action potentials. We present validation of our computer model against experimentally measured behavior of squid giant axons at elevated temperatures and also explore the mechanisms that lead to the arrest of a conducting action potential that leads to a thermal block.

MODELING METHODOLOLGY

2.1 Model Equations

The behavior of ion channels in unmyelinated axons is given by the Hodgkin Huxley equations (Hodgkin 1952). These equations are derived from the measurements performed inside the squid giant axon. The equations and their brief descriptions are shown below.

Hodgkin and Huxley predicted that the potassium current depends on the simultaneous activation of four gating elements, whose probability of moving into a conducting state is represented by the symbol n. Hodgkin and Huxley found the best fit for the potassium conductance data by assuming that there are four of these gates. Since they were assumed to act independently of one another, the overall probability of a potassium channel opening is the probability that all four of the gates have switched into a conducting state, or $n \times n \times n \times n = n^4$. Thus, if the maximum

possible conductance for the potassium channels is $\overline{g_{K+}}$, the overall conductance for the potassium channels is:

$$g_{K+} = \overline{(g_{K+})}n^4 \tag{B-1}$$

Similarly, the sodium current is dependent on the simultaneous activation of three gating elements, whose probability of moving into a conducting state is represented by m and another gating element, which was initially open at rest, but then closes with a probability h. The overall conductance of the sodium channel is represented by

$$g_{Na+} = \overline{(g_{Na+})}m^3h \tag{B-2}$$

Hodgkin and Huxley assumed that there would be some rate (α_n) at which a gate that is currently not conducting would become conducting and some rate (β_n) at which a gate that is currently conducting would move into a non-conducting configuration. The total rate of change in the probability of gates conducting would be the probability that some gates become conducting, minus the probability that some become non-conducting.

$$\frac{dn}{dt} = \alpha_n(1 - n) - \beta_n n \tag{B-3}$$

$$\frac{dm}{dt} = \alpha_m(1 - m) - \beta_m m \tag{B-4}$$

$$\frac{dh}{dt} = \alpha_h(1 - h) - \beta_n h \tag{B-5}$$

where α_i, β_i ($i = m, n, h$) are functions of the membrane voltage V_m.

This effect of elevated temperatures on ion channels is affected by the factor Q_{10}. The term Q_{10} describes the change in biological function for a 10°C rise in temperature. For unmyelinated axons, the gating variables (m,n,h) are affected due to the temperature rise by the thermic coefficient (κ_x) which is described as:

$$\kappa_{m,n,h} = Q_{10}^{\frac{(T-T_0)}{10}} \tag{B-6}$$

where T is the experimental temperature and T_o is the baseline temperature. (6.3 °C for giant squid axons). The temperature-dependent form of the gating variable x is now defined as:

$$\frac{dx}{dt} = \kappa_x[\alpha_x(1-x) - \beta_x x] \tag{B-7}$$

where x can be m, n, or h.

Modeling environment

To evaluate the behavior of unmyelinated axons when subjected to transient elevated temperatures, we used the NEURON programming environment (Carnevale 2005). NEURON is a widely used programming environment for modeling individual neurons and networks of neurons. It contains built-in functions that allow for the quick and efficient solving of the underlying differential equations in the Hodgkin Huxley mechanism. In this chapter, we have used Python as a scripting tool for NEURON that allowed us to combine Python data processing (Numpy) and plotting packages (matplotlib).

Model geometry

The model geometry in our studies consists of a 40 mm long and 0.5 mm wide one-dimensional unmyelinated axon divided into 999 computational segments with equal lengths of dx = 0.04 mm. The membrane voltage, gating variables and the ionic currents are calculated at these nodes. The time step used in the simulations is 0.01 msec. Fig. B-1 shows the model geometry. The stimulation current is inserted using NEURON's IClamp function. This spatially and temporally specified function (point process) delivers electrode current into the cell at the point of insertion, so positive current depolarizes the cell. All membrane currents were measured in the middle of a 40 mm axon stimulated with a current of 2000 nA.
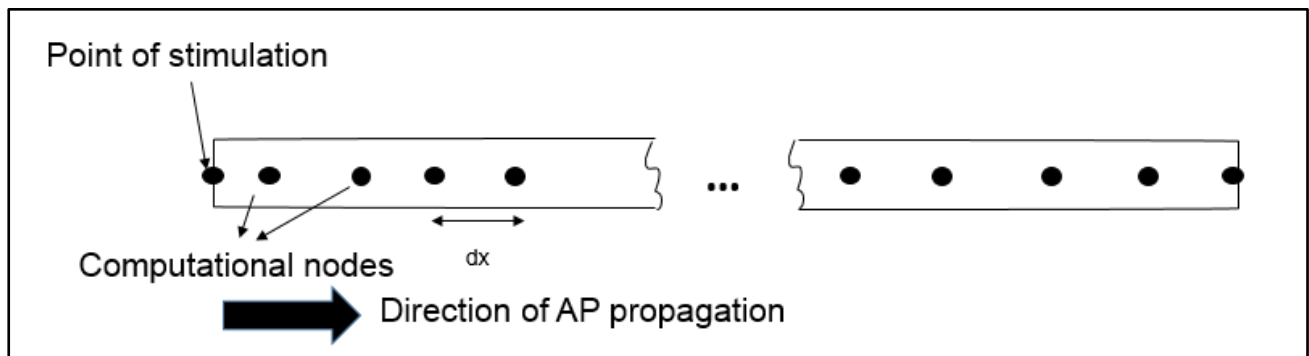
Figure B-1: Unmyelinated nerve axon geometry showing the nodes at which the membrane voltages and membrane currents are computed

RESULTS

3.1 Model Validation

To validate our modeling efforts, we compared our modeling results to the experimental results published by Rosenthal and Bezanilla (Rosenthal 2000). They studied seasonal acclimation of squid (*Loligo paelei*) giant axons caught in warm (August) and cold waters (May) and measured neurophysiological parameters at temperatures ranging from 0 to 25 °C. They observed that squid giant axons adapt seasonally to keep their conduction velocities constant with changing external temperatures. The parameters measured by Rosenthal and Bezanilla included the rates of fall and

rise of action potentials, conduction velocities, action potential widths and the normalized

conduction velocities (raw conduction velocities divided by the square root of axon diameter).We

used the program DataThief (www.datathief.org) to extract data points from the chapter. We

compared the rates of rise and fall of AP's at different temperatures with the published results using

the simple Hodgkin-Huxley model in which Q_{10} is equal to 3 (Fig. B-2). The authors, Rosenthal

and Bezanilla had observed that rates of AP's rise linearly with increase in temperature and rates

of fall rise exponentially with temperature. Using the standard HH model, we observed that the

differences between the modeling results and the published experimental results increase as the

temperature rises.
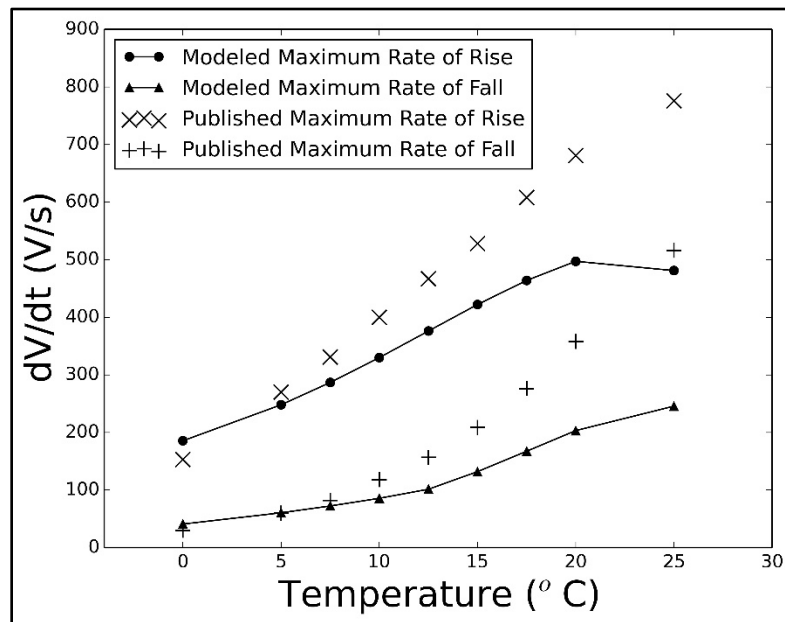
Figure B-2: Comparison of modeling and published experimental values of rates of rise and

fall using the standard Hodgkin Huxley model

Ionic membrane currents at elevated temperatures

We used our computational model to explore the specific contributions of the

neurophysiological parameters that result in thermal block in unmyelinated axons. As the

201

temperature increases, rates of fall of AP are greater than rates of rise of AP. Hence the rising phase of the AP is less accelerated and gets overtaken by the permeability changes (inactivation of sodium and activation of potassium) that lead to hyperpolarization (Hodgkin 1952). At higher temperatures, a decline in the inward sodium current is observed (Fig. B-3(a)) which explains the inability of the axon to generate an action potential. A corresponding plot shows the resulting action potentials at those temperatures (Fig. B-3b). A reduction in the peak voltage of the action potentials is observed with rise in temperature. These results are also consistent with the observations of Hodgkin and Katz (Hodgkin 1949). While this doesn't present a complete mechanism in itself, it does provide valuable insights for the mechanism behind the observation of thermal block.
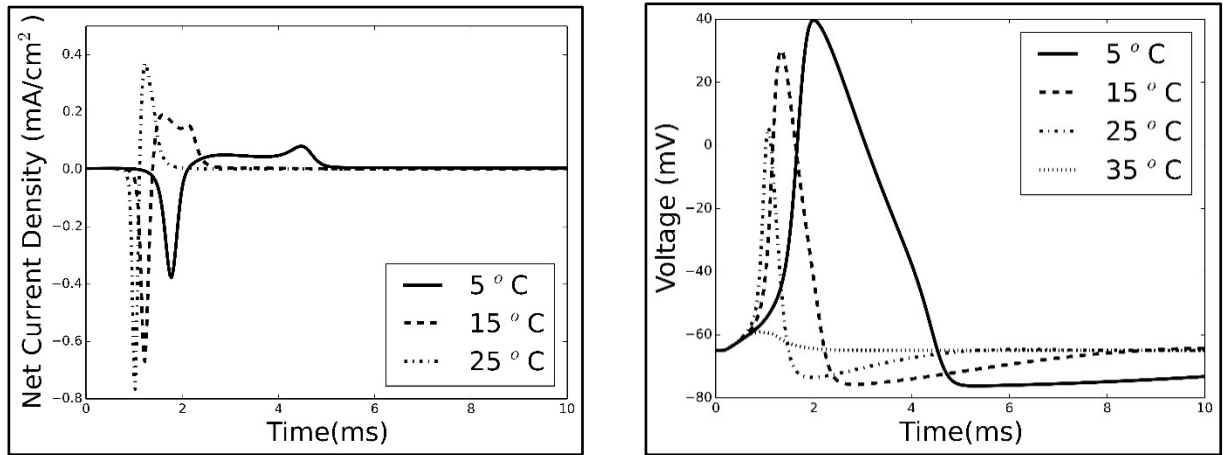
(a): Variation of net membrane current with increasing temperature. The sodium current becomes shorter with temperature and is gradually overtaken by the potassium currents at high temperatures. These changes lead to failure of AP generation. The net current density at 35°C is not shown since it is very close to the baseline (0 mA/cm²).

(b): Shape of action potentials generated at the various temperatures. The AP's get shorter and faster with increasing temperatures. At high temperature (35 °C), the AP's failed to initiate or were so weak that they didn't travel to the center of the axon where the AP's were recorded.

Figure B-3: Variation of AP with temperature

Reduction in axon excitability at elevated temperatures

We studied the effect of elevated temperatures on the propagation of a full-strength action potential. We define a full-strength action potential as an AP that has managed to propagate through the entire axon without any loss in peak voltage. In this modeling configuration, the first half of the axon (0-20 mm) was maintained at 6.3 °C while the temperature of the second half of the axon (20-40 mm) was varied. The axon was stimulated at 0 mm using the same stimulation parameters as described in the previous section. Four different temperatures (5, 15, 25, 35 °C) were applied to the right half of the axon. The temperatures were introduced in the axon as a step function. A plot showing the spatial distribution of the temperatures along the axon is shown in Fig. B-4(a). Once the temperature was applied to the axon, the peak potentials along the axon were calculated to analyze the behavior of the action potential propagation through a region of elevated

temperatures (Fig. B-4(b)). The effect of increasing temperature can be seen as the peak potentials decreasing progressively with increase in temperature in the second half of the axon. At 35°C, the peak potential decreases to a negligible value ($V_m \sim$ -65 mV) that denotes failed propagation of the action potential across the region of elevated temperature.
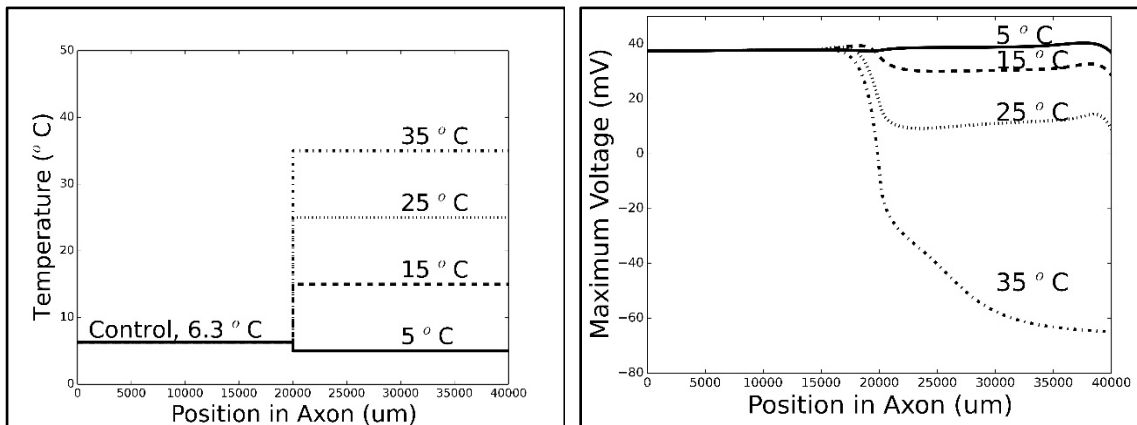
(a): Spatial distribution of temperature along the axon used for computing and comparing the peak potentials at different temperatures as shown in the figure on the left.

(b): Variation of peak membrane potential along the length of the unmyelinated axon as the right half of the axon is heated to different temperatures. This shows that higher temperatures attenuate action potentials and lead to failure of AP propagation. Computational artefacts are observed at the junctions (middle and far-right)

Figure B-4:Effect of elevated temperatures

DISCUSSION

In this study, we have presented a preliminary model that can be used to study the effect of transient elevated temperatures on unmyelinated axons for potential applications in achieving block of pain fibers. Huxley had noted that the standard model cannot account for behavior of unmyelinated axons at high temperatures. We have validated our modeling results using the

published results on the neurophysiological parameters of squid giant axons at various temperatures (Huxley 1959). The results from our computer model show that the differences between the published experimental results and the modeling results increase in the rise in temperature(Rosenthal 2000). Our model also predicts the effect of elevated temperatures on membrane currents. The observation that potassium kinetics 'overwhelm' sodium kinetics at elevated temperatures is consistent with the experimentally derived conclusions of Hodgkin and Katz (Hodgkin 1949), thus providing additional qualitative validation of our computational model. We are interested in knowing the mechanism by which a propagating action potential is blocked in a region of elevated temperatures. We observed that maximum voltage of action potentials decreases in regions of elevated temperatures. We have shown that elevated temperatures lead to reduction of axon excitability which affects the propagation of action potentials. One of the possible explanations might be increased potassium currents in the region of elevated temperature that might impede the propagation of action potentials. However, this hypothesis should be tested using the present computer model and experimental validation. Using our computational model, we can also evaluate the laser parameters that lead to the most thermal block with the least temperature rise. The parameters that need to be optimized include laser spot size, diameter of the targeted nerve, the laser repetition rate and the duration of irradiation required.

ACKNOWLEDGEMENTS

Ted Carnevale (Yale School of Medicine) for their assistance with NEURON programming environment.

APPENDIX C: COMPUTER MODEL TO STUDY THE EFFECT OF ELEVATED TEMPERATURES ON COMPOUND ACTION POTENTIALS

This appendix was submitted as an abstract for a poster presentation by Eric Yeats (EECS 2019) at the Biomedical Engineering Society (BMES) Annual Meeting in Atlanta on October 18, 2019.

Introduction: The selective inhibition of small-diameter unmyelinated axons in nerves has applications in treatment for chronic pain, nausea, and improper neural signaling to organs (Lothet 2017). Selective inhibition can be accomplished by heating neural tissue with an incident infrared laser, without causing tissue scarring, as observed when using conventional current- emitting electrodes. However, a thorough analysis and optimization of laser parameters is required before proceeding to use this technique for treatment. In this objective, a NEURON model has been developed that demonstrates the selective thermal inhibition of small-diameter unmyelinated axons in the left pleural-abdominal connective (LPAC) nerve of *Aplysia californica* through analysis of the compound action potential (CAP). The model aims to demonstrate the 3-dimensional, time-variant probabilistic inhibition of small-diameter axons of the LPAC and the resulting effects on the CAP as the LPAC is heated with an infrared laser over time.

Materials and Methods: Populations of axons corresponding to the LPAC of *Aplysia californica* are generated resembling data collected from a morphological study of *Aplysia fascinata* (Bedini 2000). 1379 Axons are represented in 3D space resembling the LPAC and ported to NEURON software (Carnevale 2005). Action potentials are initiated in all axons using current clamps at one end of the simulated nerve. Local field potentials (LFPs) are calculated at a point 10mm from the stimulus input along the length of the LPAC. An analog of Coulomb's law (Holt

1999) is used to determine extracellular voltage from the current emitted by the discretized axon sections. CAPs measured at certain points are determined by superimposing the LFP contribution of each axon in the population. As an example, multiple, independent LPAC axon populations (n=5) of axon diameters [0.8μm,25μm) and length 12 mm are generated and their CAPs are recorded at varying temperatures (5, 15, 25℃). The average of the 5 CAP waveforms is calculated for each temperature and the standard deviation is plotted above and below each average CAP.

Results and Discussion: The simulations constituting Fig. C-1 indicate that the CAP contributions of smaller axons in a typical LPAC population (diameter < 2 μm) are attenuated as nerve temperature exceeds 15℃. This becomes evident in the CAP waveform through the narrowing of the faster-conducting initial spikes and the diminishing of smaller-diameter axon 'noise' at the tail-end of the CAP signal. There is a decrease in CAP waveform amplitude from 15℃ to 25℃ as both small and intermediate diameter axons are inhibited, leaving a smaller, tighter CAP that appears to be mostly composed of larger-diameter axons (Lothet 2017).

Conclusions: Future steps will include the combination of this model with a Monte Carlo based light distribution and heat transfer model to make the model mimic realistic experimental setting. Thermally mediated optical inhibition of small-diameter axons has applications in chronic pain relief and nausea. Understanding the impact of temperature-dependent inhibition of small-diameter axon inhibition on the compound action potential can aid in quick assessment of optical inhibition efficacy.
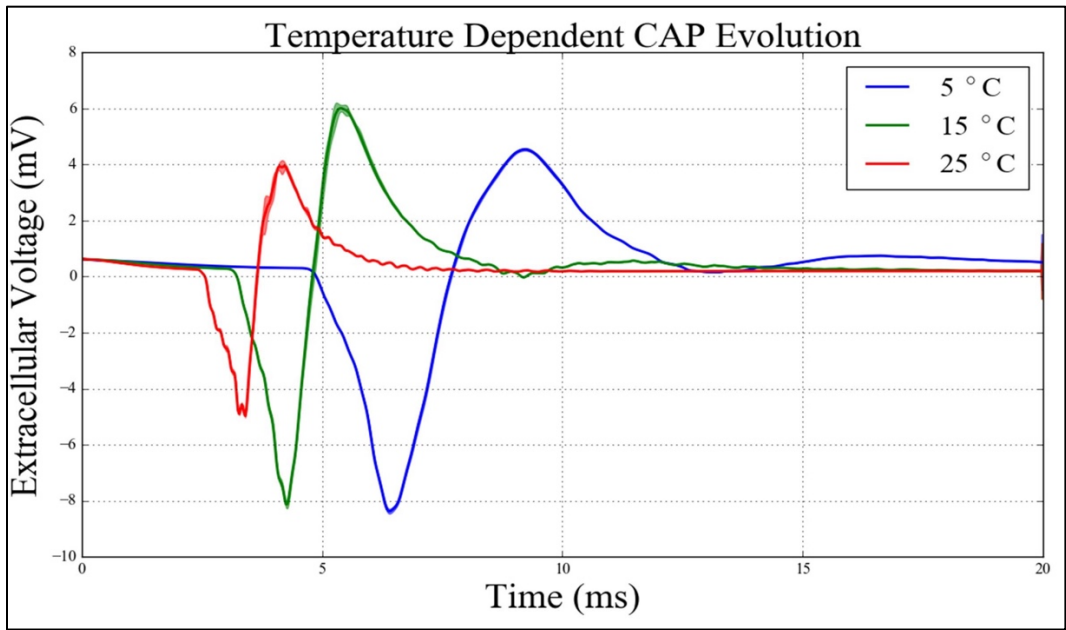
Figure C-1: Plots of average CAP waveforms and 95% confidence intervals for the 5 LPAC simulations

Note: Increases in temperature enhance the conduction velocity of non-inhibited axons

REFERENCES

Ackermann Jr., D. M., Ethier, C., Foldes, E. L., Oby, E. R., Tyler, D., Bauman, M., Kilgore, K. L. (2011). Electrical conduction block in large nerves: high-frequency current delivery in the nonhuman primate. *Muscle Nerve*, *43*(6), 897–899.

Ackermann Jr., D. M., Foldes, E. L., Bhadra, N., & Kilgore, K. L. (2010). Conduction block of peripheral nerve using high-frequency alternating currents delivered through an intrafascicular electrode. *Muscle Nerve*, *41*(1), 117–119.

Ackermann Jr., D. M., Foldes, E. L., Bhadra, N., & Kilgore, K. L. (2009). Electrode design for high frequency block: effect of bipolar separation on block thresholds and the onset response. *Conf Proc IEEE Eng Med Biol Soc*, *2009*, 654–657.

Ackermann Jr., D. M., Bhadra, N., Gerges, M., & Thomas, P. J. (2011). Dynamics and sensitivity analysis of high-frequency conduction block. *J Neural Eng*, *8*(6), 65007.

Ackermann Jr., D. M., Foldes, E. L., Bhadra, N., & Kilgore, K. L. (2010). Nerve conduction block using combined thermoelectric cooling and high frequency electrical stimulation. *J Neurosci Methods*, *193*(1), 72–76.

Ackermann Jr., D. M., Bhadra, N., Foldes, E. L., Wang, X.-F., Kilgore, K. L., & Kilgore, K. L. (2010). Effect of nerve cuff electrode geometry on onset response firing in high-frequency nerve conduction block. *IEEE Trans. Neural Syst. Rehabil. Eng.*, *18*(6), 658–665.

Albert, E. S., Bec, J. M., Desmadryl, G., Chekroud, K., Travo, C., Gaboyard, S., Chabbert, C. (2012). TRPV4 channels mediate the infrared laser-evoked response in sensory neurons. *J. Neurophysiol.*, *107*(12), 3227–3234.

Armstrong, C. M. (2004). Interaction of Tetraethylammonium Ion Derivatives with the Potassium Channels of Giant Axons. *J. Gen. Physiol.*, *58*(4), 413-37.

Baker, P. F., Blaustein, M. P., Hodgkin, A. L., Steinhardt, R. A. (1969). The influence of calcium on sodium efflux in squid axons. *J. Physiol.*, *200*(2), 431–458.

Beam, K. G., Donaldson, P. L. (1983). A quantitative study of potassium channel kinetics in rat skeletal muscle from 1 to 37 degrees C. *J. Gen. Physiol.*, *81*(4), 485–512.

Beckham, J. T., Mackanos, M. A., Crooke, C., Takahashi, T., O'Connell-Rodwell, C., Contag, C. H., & Jansen, E. D. (2004). Assessment of cellular response to thermal laser injury through bioluminescence imaging of heat shock protein 70. *Photochem. Photobiol.*, *79*(1), 76–85.

Bedini, C., Geppetti, L. (2000). A morphological study on the amount and origin of axons in the pleuroabdominal connectives of *Aplysia fasciata*. *Ital. J. Zool.*, *67*(1), 9–18.

Beier, H. T., Tolstykh, G. P., Musick, J. D., Thomas, R. J., Ibey, B. L. (2014). Plasma membrane nanoporation as a possible mechanism behind infrared excitation of cells. *J Neural Eng*, *11*(6), 66006.

Bendersky, D., Yampolsky, C. (2014). Is Spinal Cord Stimulation Safe? A Review of Its Complications. *World Neurosurg.*, *82*(6), 1359–1368.

Bernstein, J. (1902). Untersuchungen zur Thermodynamik der bioelektrischen Ströme. *Pflügers Arch. Eur. J. Physiol.*, *92*(10), 521–562.

Besson, J. M., Chaouch, A. (1987). Peripheral and spinal mechanisms of nociception. *Physiol. Rev.*, *67*(1), 67–186.

Bhadra, N., Bhadra, N., Kilgore, K., Gustafson, K. J. (2006). High frequency electrical conduction block of the pudendal nerve. *J. Neural Eng.*, *3*(2), 180.

Bixler, J. N., Hokr, B., Oian, C. A., Hoffman, A. F., Yakovlev, V. V, Thomas, R. J. (2015). Modeling tissue heating under tunable near IR radiation. *SPIE BiOS*, 93210D-93210D – 5. International Society for Optics and Photonics.

Boas, D. A., Culver, J. P., Stott, J. J., Dunn, A. K. (2002). Three dimensional Monte Carlo code for photon migration through complex heterogeneous media including the adult human head. *Opt. Express*, *10*(3), 159–170.

Bostock, H., Sears, T. A., Sherratt, R. M. (1981). The effects of 4-aminopyridine and tetraethylammonium ions on normal and demyelinated mammalian nerve fibres. *J. Physiol.*, *313*, 301–315.

Brown, A. G. (1976). Electric current flow in excitable cells. By J. J. B. Jack , D. Noble , R. W. Tsien . Clarendon Press, Oxford, 1975. Pp. xv+502. £18. *Q. J. Exp. Physiol. Cogn. Med. Sci.*, *61*(1), 75–75.

Cao, X.-J., Oertel, D. (2005). Temperature Affects Voltage-Sensitive Conductances Differentially in Octopus Cells of the Mammalian Cochlear Nucleus. *J. Neurophysiol.*, *94*(1), 821–832.

Carnevale, N. T., Hines, M. L. (2005). *The NEURON book*. Cambridge: Cambridge University Press.

Carpenter, D. O., Alving, B. O. (1968). A Contribution of an Electrogenic Na+ Pump to Membrane Potential in Aplysia Neurons. *J. Gen. Physiol.*, *52*(1), 1–21.

Cayce, J M, Kao, C., Malphrus, J. D., Konrad, P., Jansen, D., Mahadevan-Jansen, A. (2008). Optical Stimulation of the Central Nervous System in vitro. *Biomedical Optics*,. Optical Society of America.

Cayce, J. M., Friedman, R. M., Chen, G., Jansen, E. D., Mahadevan-Jansen, A., Roe, A. W. (2014). Infrared neural stimulation of primary visual cortex in non-human primates. *Neuroimage*, *84*, 181–190.

Chang-Hasnain, C. J. (2003). Progress and prospects of long-wavelength VCSELs. *IEEE Commun. Mag.*, *41*(2), 64–68.

Chapman, R. A. (1967). Dependence on temperature of the conduction velocity of the action potential of the squid giant axon. *Nature*, *213*, 1143–1144.

Chernov, M. M., Duke, A. R., Cayce, J. M., Crowder, S. W., Sung, H.-J., Jansen, E. D. (2012). Material considerations for optical interfacing to the nervous system. *MRS Bull.*, *37*(06), 599–605.

Chiu, S. Y., Mrose, H. E., Ritchie, J. M. (1979). *Anomalous temperature dependence of the sodium conductance in rabbit nerve compared with frog nerve*.

Clay, J. R. (1998). Excitability of the squid giant axon revisited. *J. Neurophysiol.*, *80*(2), 903–913.

Clements, I. P., Gnade, A. G., Rush, A. D., Patten, C. D., Twomey, M. C., Kravitz, A. V. (2013, March 8). *Miniaturized LED sources for in vivo optogenetic experimentation* (S. K. Mohanty & N. V. Thakor, Eds.). International Society for Optics and Photonics.

Colucci, V., Strichartz, G., Jolesz, F., Vykhodtseva, N., Hynynen, K. (2009). Focused ultrasound effects on nerve action potential in vitro. *Ultrasound Med. Biol.*, *35*(10), 1737–1747.

Cortright, D. N., Krause, J. E., & Broom, D. C. (2007). TRP channels and pain. *Biochim. Biophys. Acta - Mol. Basis Dis.*, *1772*(8), 978–988.

Dale Purves, et. al. (2001). *Neuroscience*. Sunderland: Sinauer Associates.

Debanne, D., Campanac, E., Bialowas, A., Carlier, E., Alcaraz, G. (2011). Axon Physiology. *Physiol. Rev.*, *91*(2), 555–602.

Diller, K. R. (2010). Laser Generated Heat Transfer. In *Optical-Thermal Response of Laser-Irradiated Tissue* (pp. 353–397). Dordrecht: Springer Netherlands.

Dittami, G. M., Rajguru, S. M., Lasher, R. A., Hitchcock, R. W., Rabbitt, R. D. (2011). Intracellular calcium transients evoked by pulsed infrared radiation in neonatal cardiomyocytes. *J Physiol*, *589*(Pt 6), 1295–1306.

Dubin, A. E., Patapoutian, A. (2010). Nociceptors: the sensors of the pain pathway. *J. Clin. Invest.*, *120*(11), 3760–3772.

Duchesne, M., Magy, L., Richard, L., Ingrand, P., Neau, J.-P., Mathis, S., Vallat, J.-M. (2016). Simultaneous Quantification of Unmyelinated Nerve Fibers in Sural Nerve and in Skin. *J. Neuropathol. Exp. Neurol.*, *75*(1), 53–60.

Dufour, S., De Koninck, Y. (2015). Optrodes for combined optogenetics and electrophysiology in live animals. *Neurophotonics*, *2*(3), 031205.

Duke A. R., Cayce J.M., Malphrus J.D., Konrad P.E., Mahadevan Jansen A., Jansen E.D., A. R. (2009). Combined optical and electrical stimulation of neural tissue in vivo. *Soc. Neurosci.* Washington, DC.

Duke, A. R., Lu, H., Jenkins, M. W., Jansen, E. D., Chiel, H. J. (2012). Identifying and controlling sources of variability in hybrid opto-electrical neural stimulation. *BIOS Biomed. Opt. Photons Neurons IV, SPIE Photonics West*. San Francisco, CA: SPIE.

Duke, A. R., Jenkins, M. W., Lu, H., McManus, J. M., Chiel, H. J., Jansen, E. D. (2013). Transient and selective suppression of neural activity with infrared light. *Sci. Rep.*, *3*(1), 2600.

Eisenstein, M. (2013). Neurodevice startups target peripheral nervous system. *Nat. Biotechnol.*, *31*(10), 865–866.

Eliasson, S. G., Monafo, W. W. (1989). 4-aminopyridine restores conduction in heat-blocked sciatic branches. *J. Burn Care Rehabil.*, *10*(6), 499–503.

Eliasson, S. G., Monafo, W. W. (1991). Effects of 4-aminopyridine on protein phosphorylation in heat-blocked peripheral nerve. *J. Neurol. Sci.*, *105*(2), 175–182.

Eliasson, S. G., Monafo, W. W., Meyr, D. (1986). Potassium ion channel blockade restores conduction in heat-injured nerve and spinal nerve roots. *Exp. Neurol.*, *93*(1), 128–137.

Eom, K., Byun, K. M., Jun, S. B., Kim, S. J., Lee, J. (2018). Theoretical Study on Gold-Nanorod-Enhanced Near-Infrared Neural Stimulation. *Biophys. J.*, *115*(8), 1481–1497.

Fang, Q. (2010). Mesh-based Monte Carlo method using fast ray-tracing in Plücker coordinates. *Biomed. Opt. Express*, *1*(1), 165–175.

Fanjul-Vélez, F., Arce-Diego, J. L. (2008). Modeling thermotherapy in vocal cords novel laser endoscopic treatment. *Lasers Med. Sci.*, *23*(2), 169–177.

Feng, Y., Fuentes, D. (2011). Model-based planning and real-time predictive control for laser-induced thermal therapy. *Int. J. Hyperthermia*, *27*(8), 751–761.

Fitzhugh, R., Cole, K. S. (1964). Theoretical potassium loss from squid axons as a function of temperature. *Biophys. J.*, *4*(4), 257.

Fleischmann, B. K., Washabau, R. J., Kotlikoff, M. I. (1993). Control of resting membrane

potential by delayed rectifier potassium currents in ferret airway smooth muscle cells. *J. Physiol.*, *469*, 625–638.

Ford, J. B., Jenkins, M. W., Chiel, H. J., Jansen, E. D. (2017). *Reducing peak temperatures during infrared inhibition of neural potentials* . *10052*, 100520B-100520B – 7.

Ford, S. M., Watanabe, M., Jenkins, M. W. (2018). A review of optical pacing with infrared light. *J. Neural Eng.*, *15*(1), 011001.

Frankenhaeuser, B., Hodgkin, A. L. (1956). The after-effects of impulses in the giant nerve fibres of Loligo. *J. Physiol.*, *131*(2), 341.

Frankenhaeuser, B., Moore, L. E. (1963). The effect of temperature on the sodium and potassium permeability changes in myelinated nerve fibres of Xenopus laevis. *J. Physiol.*, *169*(2), 431–437.

Fribance, S., Wang, J., Roppolo, J. R., de Groat, W. C., Tai, C. (2016). Axonal model for temperature stimulation. *J. Comput. Neurosci.*, *41*(2), 185–192.

Futamachi, K., & Smith, T. G. (1982). Action of tetrodotoxin on pacemaker conductances in Aplysia neurons. *Brain Res.*, *233*(2), 424–430.

Galarza-Muñoz, G., Soto-Morales, S. I., Holmgren, M., & Rosenthal, J. J. C. (2011). Physiological adaptation of an Antarctic Na+/K+-ATPase to the cold. *J. Exp. Biol.*, *214*(Pt 13), 2164–2174.

Ganguly, M., Jenkins, M. W., Chiel, H. J., & Jansen, E. D. (2016, March 9). *Modeling the effects of elevated temperatures on action potential propagation in unmyelinated axons* (S. J. Madsen, V. X. D. Yang, E. D. Jansen, Q. Luo, S. K. Mohanty, & N. V. Thakor, Eds.). International Society for Optics and Photonics.

Gardner, E. P., & Johnson, K. O. (2013). The somatosensory system: Receptors and central pathways. *Princ. Neural Sci.*, *5*, 475–495.

Garrett, S., & Rosenthal, J. J. C. (2012). RNA Editing Underlies Temperature Adaptation in K+ Channels from Polar Octopuses. *Science (80-.).*, *335*(6070), 848–851.

Geduldig, D., & Gruener, R. (1970). Voltage clamp of the Aplysia giant neurone: early sodium and calcium currents. *J. Physiol.*, *211*(1), 217–244.

George, R., & Walsh, L. J. (2009). Performance assessment of novel side firing flexible optical fibers for dental applications. *Lasers Surg. Med.*, *41*(3), 214–221.

Gorman, A. L. F., & Marmor, M. F. (1970). Temperature dependence of a sodium—potassium permeability ratio of a molluscan neurone. *J. Physiol.*, *210*(4), 919.

Gould, T., Wang, Q., & Pfefer, T. J. (2014). Optical-thermal light-tissue interactions during photoacoustic breast imaging. *Biomed. Opt. Express*, *5*(3), 832–847.

Graham, H. T., & Gasser, H. S. (1931). Modification of nerve response by veratrine, protoveratrine and aconitine. *J. Pharmacol. Exp. Ther.*, *43*(1), 163–185.

Groves, D. A., & Brown, V. J. (2005). Vagal nerve stimulation: a review of its applications and potential mechanisms that mediate its clinical effects. *Neurosci Biobehav Rev*, *29*(3), 493–500.

Hale, G M, & Querry, M. R. (1973). Optical Constants of Water in the 200-nm to 200-microm Wavelength Region. *Appl. Opt.*, *12*(3), 555–563.

Hale, George M., & Querry, M. R. (1973). Optical Constants of Water in the 200-nm to 200-μm Wavelength Region. *Appl. Opt.*, *12*(3), 555.

Hasgall, P. A., Neufeld, E., Gosselin, M. C., Klingenböck, A., & Kuster, N. (2015). IT'IS Database for thermal and electromagnetic parameters of biological tissues. *Version 2.6*.

Hatef, A., Darvish, B., Dagallier, A., Davletshin, Y. R., Johnston, W., Kumaradas, J. C., Meunier, M. (2015). Analysis of Photoacoustic Response from Gold–Silver Alloy Nanoparticles Irradiated by Short Pulsed Laser in Water. *J. Phys. Chem. C*, *119*(42), 24075–24080.

Henyey, L. G., Greenstein, J. L. (1941). Diffuse radiation in the galaxy. *Astrophys. J.*, *93*, 70–83.

Hermann, A., Gorman, A. L. (1981). Effects of tetraethylammonium on potassium currents in a molluscan neurons. *J. Gen. Physiol.*, *78*(1), 87–110.

Hermann, A., Gorman, A. L. F. (1979). External and internal effects of tetraethylammonium on voltage-dependent and ca-dependent k ÷ currents components in molluscan pacemaker neurons. In *Neuroscience Letters* (Vol. 12).

Hill, M. T., Gather, M. C. (2014). Advances in small lasers. *Nat. Photonics*, *8*(12), 908–918.

Hille, B. (1967). The selective inhibition of delayed potassium currents in nerve by tetraethylammonium ion. *J. Gen. Physiol.*, *50*(5), 1287–1302.

Hines, M. L., Carnevale, N. T. (1997). The NEURON Simulation Environment. *Neural Comput.*, *9*(6), 1179–1209.

Hines, Michael L, Davison, A. P., Muller, E. (2009). NEURON and Python. *Front. Neuroinform.*, *3*.

Ho, J. S., Tanabe, Y., Iyer, S. M., Christensen, A. J., Grosenick, L., Deisseroth, K., Poon, A. S. Y. (2015). Self-Tracking Energy Transfer for Neural Stimulation in Untethered Mice. *Phys. Rev. Appl.*, *4*(2), 024001.

Hodgkin, A. L. (1954). A note on conduction velocity. *J. Physiol.*, *125*(1), 221–224.

Hodgkin, A. L., Huxley, A. F. (1952). A Quantitative Description of Membrane Current and its Application to Conduction and Excitation in Nerves. *J. Physiol.*, *117*(4), 500–544.

Hodgkin, A. L., Huxley, A. F., Katz, B. (1952). Measurement of current-voltage relations in the membrane of the giant axon of *Loligo*. *J. Physiol.*, *116*(4), 424–448.

Hodgkin, A. L., Katz, B. (1949). The effect of temperature on the electrical activity of the giant axon of the squid. *J Physiol*, *109*(1–2), 240–249.

Hofmann, W., Görblich, M., Ortsiefer, M., Böhm, G., & Amann, M.-C. (2008, February 7). *Monolithic 2D high-power arrays of long-wavelength VCSELs* (C. Lei & J. K. Guenter, Eds.). International Society for Optics and Photonics.

Holt, G. R., Koch, C. (1999). Electrical interactions via the extracellular potential near cell bodies. *J. Comput. Neurosci.*, *6*(2), 169–184.

Howells, J., Czesnik, D., Trevillion, L., Burke, D. (2013). Excitability and the safety margin in human axons during hyperthermia. *J. Physiol.*, *591*(12), 3063–3080.

Humphries, A., Lister, T. S., Wright, P. A., Hughes, M. P. (2013). Finite element analysis of thermal and acoustic processes during laser tattoo removal. *Lasers Surg. Med.*, *45*(2), 108–115.

Huxley, A. F. (1959a). Ion movements during nerve activity. *Ann. N. Y. Acad. Sci.*, *81*, 221–246.

Huxley, A. F. (1959b). Local activation of muscle. *Ann N Y Acad Sci*, *81*, 446–452.

Huxley, H. E., Hanson, J. (1959). The structural basis of the contraction mechanism in striated muscle. *Ann N Y Acad Sci*, *81*, 403–408.

Ip, M., Kroll, A., Reichel, E. (1999). Transpupillary thermotherapy. *Semin. Ophthalmol.*, *14*(1), 11–18.

Izzo, A., Richter, C., Jansen, E. D., Walsh, J. (2006). Laser stimulation of the auditory nerve. *Lasers Surg. Med.*, *38*(8), 745–753.

Jacques, S. L. (2010). Monte Carlo Modeling of Light Transport in Tissue (Steady State and Time of Flight). In *Optical-Thermal Response of Laser-Irradiated Tissue* (pp. 109–144). Dordrecht: Springer Netherlands.

Janssen, R. (1992). Thermal Influences on Nervous System Function. In *Neuroscience andBiobehavioral Reviews* (Vol. 16).

Jaunich, M., Raje, S., Kim, K., Mitra, K., Guo, Z. (2008). Bio-heat transfer analysis during short pulse laser irradiation of tissues. *Int. J. Heat Mass Transf.*, *51*(23–24), 5511–5521.

Jenkins, M W, Duke, A. R., Gu, S., Chiel, H. J., Fujioka, H., Watanabe, M., Rollins, A. M. (2010). Optical pacing of the embryonic heart. *Nat. Photonics*, *4*, 623–626.

Jenkins, Michael W, Wang, Y. T., Doughman, Y. Q., Watanabe, M., Cheng, Y., Rollins, A. M. (2013). Optical pacing of the adult rabbit heart. *Biomed. Opt. Express*, *4*(9), 1626–1635.

Jerabek-Willemsen, M., Wienken, C. J., Braun, D., Baaske, P. Duhr, S. (2011). Molecular Interaction Studies Using Microscale Thermophoresis. *Assay Drug Dev. Technol.*, *9*(4), 342–353.

Jeremy Ford Micheal Jenkins, Hillel Chiel, E. Duco Jansen (2015). Neural Inhibition Using
Pulsed Infrared Light from Multiple Optical Fibers. *Society for Neuroscience* . Chicago, IL.

Juan, E. J., González, R., Albors, G., Ward, M. P., Irazoqui, P. (2014). Vagus nerve modulation
using focused pulsed ultrasound: potential applications and preliminary observations in a
rat. *Int. J. Imaging Syst. Technol.*, *24*(1), 67–71.

Karch, G. K., Sadlo, F., Meister, C., Rauschenberger, P., Eisenschmidt, K., Weigand, B., Ertl, T.
(2013). Visualization of piecewise linear interface calculation. *Visualization Symposium
(PacificVis), 2013 IEEE Pacific*, 121–128. IEEE.

Keller, M. D., Stafford, J. W., Stafford, R. C., Norton, B. J., Wells, J. D., Bendett, M. C., Hibbs-
Brenner, M. (2013). Laser source development for infrared neural stimulation. *2013 Saudi
International Electronics, Communications and Photonics Conference*, 1–4. IEEE.

Kern, D. S., Kumar, R. (2007). Deep brain stimulation. *Neurologist*, *13*(5), 237–252.

Kilgore, K L, Foldes, E. A., Ackermann, D. M., Bhadra, N. (2009). Combined direct current and
high frequency nerve block for elimination of the onset response. *Conf Proc IEEE Eng Med
Biol Soc*, *2009*, 197–199.

Kilgore, Kevin L., Bhadra, N. (2004). *Nerve conduction block utilising high-frequency
alternating current*. *42*(3), 394–406.

Ko, S. H., Lee, D., Pan, H., Ryu, S.-G., Grigoropoulos, C. P., Kladias, N., Domoto, G. A. (2010).
Laser-induced acoustic wave generation/propagation/interaction in water in various internal
channels. *Appl. Phys. A*, *100*(2), 391–400.

Kole, M. H. P., Ilschner, S. U., Kampa, B. M., Williams, S. R., Ruben, P. C., Stuart, G. J. (2008). Action potential generation requires a high sodium channel density in the axon initial segment. *Nat. Neurosci.*, *11*(2), 178–186.

Kottink, A. I., Hermens, H. J., Nene, A. V, Tenniglo, M. J., Groothuis-Oudshoorn, C. G., & MJ, Ij. (2008). Therapeutic effect of an implantable peroneal nerve stimulator in subjects with chronic stroke and footdrop: a randomized controlled trial. *Phys Ther*, *88*(4), 437–448.

Kottink, A. I., Hermens, H. J., Nene, A. V, Tenniglo, M. J., van der Aa, H. E., Buschman, H. P., Ijzerman, M. J. (2007). A randomized controlled trial of an implantable 2-channel peroneal nerve stimulator on walking speed and activity in poststroke hemiplegia. *Arch Phys Med Rehabil*, *88*(8), 971–978.

Kovalsky, Y., Amir, R., Devor, M. (2009). Simulation in sensory neurons reveals a key role for delayed Na+ current in subthreshold oscillations and ectopic discharge: implications for neuropathic pain. *J. Neurophysiol.*, *102*(3), 1430–1442.

Kreiner, T., Kirk, M. D., Scheller, R. H. (1987). Cellular and synaptic morphology of a feeding motor circuit in Aplysia californica. *J. Comp. Neurol.*, *264*(3), 311–325.

Krouchev, N. I., Rattay, F., Sawan, M., Vinet, A. (2015). From Squid to Mammals with the HH Model through the Nav Channels' Half-Activation-Voltage Parameter. *PLoS One*, *10*(12), e0143570.

Lee, S. C., Deutsch, C. (1990). Temperature dependence of K(+)-channel properties in human T lymphocytes. *Biophys. J.*, *57*(1), 49–62.

Liljemalm, R., Nyberg, T. (2014). Quantification of a thermal damage threshold for astrocytes using infrared laser generated heat gradients. *Ann. Biomed. Eng.*, *42*(4), 822–832.

Liu, B., Hui, K., Qin, F. (2003). Thermodynamics of heat activation of single capsaicin ion channels VR1. *Biophys. J.*, *85*(5), 2988–3006.

Lothet, E. H., Kilgore, K. L., Bhadra, N., Bhadra, N., Vrabec, T., Wang, Y. T., Chiel, H. J. (2014). Alternating current and infrared produce an onset-free reversible nerve block. *Neurophotonics*, *1*(1), 011010.

Lothet, E. H., Shaw, K. M., Lu, H., Zhuo, J., Wang, Y. T., Gu, S., Jenkins, M. W. (2017). Selective inhibition of small-diameter axons using infrared light. *Sci. Rep.*, *7*(1), 3275.

Lucas, K. (1908). The temperature-coefficient of the rate of conduction in nerve. *J. Physiol.*, *37*(2), 112–121.

Maak, T. G., Wylie, J. D. (2016). Medical Device Regulation. *J. Am. Acad. Orthop. Surg.*, *24*(8), 537–543.

Margallo-Balbás, E., French, P. J. (2007). Shape based Monte Carlo code for light transport in complex heterogeneous tissues. *Opt. Express*, *15*(21), 14086–14098.

Matic, A. I., Walsh Jr., J. T., Richter, C. P. (2011). Spatial extent of cochlear infrared neural stimulation determined by tone-on-light masking. *J Biomed Opt*, *16*(11), 118002.

Matveev, M. V., Erofeev, A. I., Terekhin, S. G., Plotnikova, P. V., Vorobyov, K. V., Vlasova, O. L. (2015). Implantable devices for optogenetic studies and stimulation of excitable tissue. *St. Petersbg. Polytech. Univ. J. Phys. Math.*, *1*(3), 264–271.

McIntyre, C. C., Richardson, A. G.,Grill, W. M. (2002). Modeling the Excitability of Mammalian Nerve Fibers: Influence of Afterpotentials on the Recovery Cycle. *J. Neurophysiol.*, *87*(2), 995–1006.

Mekhail, N. A., Cheng, J., Narouze, S., Kapural, L., Mekhail, M. N., Deer, T. (2010). Clinical

Applications of Neurostimulation: Forty Years Later. *Pain Pract.*, *10*(2), 103–112.

Miles, J. D., Kilgore, K. L., Bhadra, N., Lahowetz, E. A. (2007). Effects of ramped amplitude

waveforms on the onset response of high-frequency mammalian nerve block. *J Neural Eng*,

4(4), 390–398.

Miller, N., Saada, R., Fishman, S., Hurwitz, I., Susswein, A. J. (2011). Neurons controlling

Aplysia feeding inhibit themselves by continuous NO production. *PLoS One*, *6*(3), e17779.

Min, B.-K., Bystritsky, A., Jung, K.-I., Fischer, K., Zhang, Y., Maeng, L.-S., Yoo, S.-S. (2011).

Focused ultrasound-mediated suppression of chemically-induced acute epileptic EEG

activity. *BMC Neurosci.*, *12*(1), 23.

Moen, E. K., Beier, H. T., Ibey, B. L., Armani, A. M. (2016, May 13). *The role of membrane

dynamics in electrical and infrared neural stimulation* (A. Wax & V. Backman, Eds.).

International Society for Optics and Photonics.

Moreno, L. E., Rajguru, S. M., Matic, A. I., Yerram, N., Robinson, A. M., Hwang, M., Richter,

C. P. (2011). Infrared neural stimulation: beam path in the guinea pig cochlea. *Hear Res*,

282(1–2), 289–302.

Moritz, A. H. F. (1947). Studies of thermal injury II. The relative importance of time and surface

temperature in the causation of cutaneous burns. *Am. J. Patho.*, (23).

Moroz, L. L. (2011). Aplysia. *Curr. Biol.*, *21*(2), R60-1.

Mou, Z, Triantis, I. F., Woods, V. M., Toumazou, C., Nikolic, K. (2012). A simulation study of

the combined thermoelectric extracellular stimulation of the sciatic nerve of the Xenopus

laevis: the localized transient heat block. *IEEE Trans Biomed Eng*, *59*(6), 1758–1769.

Mou, Zongxia, Triantis, I. F., Woods, V. M., Toumazou, C., Nikolic, K. (2012). A simulation study of the combined thermoelectric extracellular stimulation of the sciatic nerve of the Xenopus laevis: the localized transient heat block. *IEEE Trans Biomed Eng*, *59*(6), 1758–1769.

Musio, C., Bedini, C. (1990). Fine structure and axonal organization in the buccal ganglia nerves ofAplysia (Mollusca, Gastropoda). *Zoomorphology*, *110*(1), 17–26.

Nakos, J. T. (2004). *Uncertainty Analysis of Thermocouple Measurements Used in Normal and Abnormal Thermal Environment Experiments at Sandia's Radiant Heat Facility and Lurance Canyon Burn Site*.

Neishabouri, A., Faisal, A. A. (2014). Saltatory conduction in unmyelinated axons: clustering of Na+ channels on lipid rafts enables micro-saltatory conduction in C-fibers. *Front. Neuroanat.*, *8*, 109.

Norton, B. J., Bowler, M. A., Wells, J. D., Keller, M. D. (2013). Analytical approaches for determining heat distributions and thermal criteria for infrared neural stimulation. *J Biomed Opt*, *18*(9), 98001.

Nussinovitch, U., Shinnawi, R., Gepstein, L. (2014). Modulation of cardiac tissue electrophysiological properties with light-sensitive proteins. *Cardiovasc. Res.*, *102*(1), 176–187.

Oliver, D. L., Beckius, G. E. (1992). Fine structure of GABA-labeled axonal endings in the inferior colliculus of the cat: immunocytochemistry on deplasticized ultrathin sections. *Neuroscience*, *46*(2), 455–463.

Oraevsky, A. A. (1995). *Laser-Induced Acoustic and Shock Waves in Ocular Tissues.*

Ortsiefer, M., Shau, R., Bohm, G., Zigldrum, M., Rosskopf, J., & Amann, M.-C. (2000). 90/spl deg/C continuous-wave operation of 1.83-μm vertical-cavity surface-emitting lasers. *IEEE Photonics Technol. Lett.*, *12*(11), 1435–1437.

Overgaard, J., & Overgaard, M. Hyperthermia as an adjuvant to radiotherapy in the treatment of malignant melanoma. *Int. J. Hyperthermia*, *3*(6), 483–501.

Owen, J. M., Keller, M. D., Yuan, S. (2015). *Apparatus and method for managing chronic pain with infrared light sources and heat*. Google Patents.

Pahapill, P. A., Schlichter, L. C. (1990). Modulation of potassium channels in human T lymphocytes: effects of temperature. *J. Physiol.*, *422*, 103–126.

Paintal, A. S. (1965). Effects of temperature on conduction in single vagal and saphenous myelinated nerve fibres of the cat. *J. Physiol.*, *180*(1), 20–49.

Paris, L., Marc, I., Charlot, B., Dumas, M., Valmier, J., Bardin, F. (2017). Millisecond infrared laser pulses depolarize and elicit action potentials on in-vitro dorsal root ganglion neurons. *Biomed. Opt. Express*, *8*(10), 4568.

Patapoutian, A., Peier, A. M., Story, G. M., Viswanath, V. (2003). Sensory systems: ThermoTRP channels and beyond: mechanisms of temperature sensation. *Nat. Rev. Neurosci.*, *4*(7), 529–539.

Patwardhan, S. V, Dhawan, A. P., Relue, P. A. (2005). Monte Carlo simulation of light-tissue interaction: three-dimensional simulation for trans-illumination-based imaging of skin lesions. *IEEE Trans. Biomed. Eng.*, *52*(7), 1227–1236.

Pearce, J. (2011). Mathematical models of laser-induced tissue thermal damage. *Int. J. Hyperthermia*, *27*(8), 741–750.

Pekala, D., Szkudlarek, H., Raastad, M. (2016). Typical gray matter axons in mammalian brain fail to conduct action potentials faithfully at fever-like temperatures. *Physiol. Rep.*, *4*(19), e12981.

Peng, Y. B., Ringkamp, M., Meyer, R. A., Campbell, J. N. (2003). Fatigue and paradoxical enhancement of heat response in C-fiber nociceptors from cross-modal excitation. *J. Neurosci.*, *23*(11), 4766–4774.

Pennes, H. H. (1948). Analysis of tissue and arterial blood temperatures in the resting human forearm. *J. Appl. Physiol.*, *1*(2), 93–122.

Petsche, U., Fleischer, E., Lembeck, F., Handwerker, H. O. (1983). The effect of capsaicin application to a peripheral nerve on impulse conduction in functionally identified afferent nerve fibres. *Brain Res.*, *265*(2), 233–240.

Pfefer, T. J., Kehlet Barton, J., Chan, E. K., Ducros, M. G., Sorg, B. S., Milner, T. E., Welch, A. J. (1996). A three-dimensional modular adaptable grid numerical model for light propagation during laser irradiation of skin tissue. *Sel. Top. Quantum Electron. IEEE J.*, *2*(4), 934–942.

Plaksin, M., Shapira, E., Kimmel, E., Shoham, S. (2018). Thermal Transients Excite Neurons through Universal Intramembrane Mechanoelectrical Effects. *Phys. Rev. X*, *8*(1), 11043.

Prahl, S. A., Keijzer, M., Jacques, S. L., Welch, A. J. (1989). A Monte Carlo model of light propagation in tissue. *Dosim. Laser Radiat. Med. Biol.*, *5*, 102–111.

Prieto, M. L.., Madison, D. V., Khuri-Yakub, B. T., Maduke, M. (2018). Focused Ultrasound
Activates Task Potassium Channels, Increases Membrane Capacitance, and Modulates
Action Potential Waveform and Firing Properties in Hippocampal Brain Slices. *Biophys. J.*,
114(3), 669a.

Prieto, M. L., Firouzi, K., Khuri-Yakub, B. T., & Maduke, M. (2018). Activation of Piezo1 but
Not NaV1.2 Channels by Ultrasound at 43 MHz. *Ultrasound Med. Biol.*, *44*(6), 1217–1232.

Prinz, A. A., Abbott, L., Marder, E. (2004). The dynamic clamp comes of age. *Trends Neurosci.*,
27(4), 218–224.

Prosser, C. L.,Nelson, D. O. (1981). The Role of Nervous Systems in Temperature Adaptation of
Poikilotherms. *Annu. Rev. Physiol.*, *43*(1), 281–300.

Pusch, M., Ludewig, U., Jentsch, T. J. (1997). Temperature dependence of fast and slow gating
relaxations of ClC-0 chloride channels. *J. Gen. Physiol.*, *109*(1), 105–116.

Rakowski, R. F., Gadsby, D. C., De Weer, P. (1989). Stoichiometry and voltage dependence of
the sodium pump in voltage-clamped, internally dialyzed squid giant axon. *J. Gen. Physiol.*,
93(5), 903–941.

Rasminsky, M. (1973). The effects of temperature on conduction in demyelinated single nerve
fibers. *Arch. Neurol.*, *28*(5), 287–292.

Rattay, F. (1986). Analysis of models for external stimulation of axons. *IEEE Trans Biomed
Eng*, *33*(10), 974–977.

Rattay, F. (1989). Analysis of models for extracellular fiber stimulation. *IEEE Trans Biomed
Eng*, *36*(7), 676–682.

Rattay, F., Aberham, M. (1993). Modeling axon membranes for functional electrical stimulation. *IEEE Trans. Biomed. Eng.*, *40*(12), 1201–1209.

Reardon, S. (2016). Light-controlled genes and neurons poised for clinical trials. *Nature*.

Reichel, E., Berrocal, A. M., Ip, M., Kroll, A. J., Desai, V., Duker, J. S., Puliafito, C. A. (1999). Transpupillary thermotherapy of occult subfoveal choroidal neovascularization in patients with age-related macular degeneration. *Ophthalmology*, *106*(10), 1908–1914.

Ren, N., Liang, J., Qu, X., Li, J., Lu, B., Tian, J. (2010). GPU-based Monte Carlo simulation for light propagation in complex heterogeneous tissues. *Opt. Express*, *18*(7), 6811–6823.

Richardson, A. G., McIntyre, C. C., Grill, W. M. (2000). Modelling the effects of electric fields on nerve fibres: influence of the myelin sheath. *Med. Biol. Eng. Comput.*, *38*(4), 438–446.

Richter, C. P., Rajguru, S. M., Matic, A. I., Moreno, E. L., Fishman, A. J., Robinson, A. M., Walsh, J. T. (2011). Spread of cochlear excitation during stimulation with pulsed infrared radiation: inferior colliculus measurements. *J Neural Eng*, *8*(5), 56006.

Rimmele, T. S., Chatton, J.Y. (2014). A novel optical intracellular imaging approach for potassium dynamics in astrocytes. *PLoS One*, *9*(10), e109243.

Robertson, R. M., Money, T. G. (2012). Temperature and neuronal circuit function: compensation, tuning and tolerance. *Curr. Opin. Neurobiol.*, *22*(4), 724–734.

Rosenthal, J. J., Bezanilla, F. (2000). Seasonal variation in conduction velocity of action potentials in squid giant axons. *Biol. Bull.*, *199*(2), 135–143.

Rosenthal, J. J. C., Bezanilla, F. (2002). A comparison of propagated action potentials from tropical and temperate squid axons: different durations and conduction velocities correlate with ionic conductance levels. *J. Exp. Biol.*, *205*(12), 1819–1830.

Rosenthal, J. J. C., Seeburg, P. H. (2012). A-to-I RNA Editing: Effects on Proteins Key to Neural Excitability. *Neuron*, *74*(3), 432–439.

Rutkove, S. B., Kothari, M. J., Shefner, J. M. (1997). Nerve, muscle, and neuromuscular junction electrophysiology at high temperature. *Muscle Nerve*, *20*(4), 431–436.

Sangrey, T. D., Friesen, W. O., Levy, W. B. (2004). Analysis of the optimal channel density of the squid giant axon using a reparameterized Hodgkin–Huxley model. *J. Neurophysiol.*, *91*(6), 2541–2550.

Sapareto, S. A., Dewey, W. C. (1984). Thermal dose determination in cancer therapy. *Int. J. Radiat. Oncol.*, *10*(6), 787–800.

Schauf, C. L. (1987). Amantadine restores impulse conduction across demyelinated nerve segments. *Clin Exp Pharmacol Physiol*, *14*(4), 273–281.

Schauf, C. L., Davis, F. A. (1974). Impulse conduction in multiple sclerosis: a theoretical basis for modification by temperature and pharmacological agents. *J Neurol Neurosurg Psychiatry*, *37*(2), 152–161.

Seifter, J., Sloane, D., Ratner, A. (2005). *Concepts in medical physiology*. Lippincott Williams & Wilkins.

Seteikin, A. Y., Krasnikov, I. V., Drakaki, E., Makropoulou, M. (2013). Dynamic model of thermal reaction of biological tissues to laser-induced fluorescence and photodynamic therapy. *J. Biomed. Opt.*, *18*(7), 075002.

Shannon, R. V. (2012). Advances in auditory prostheses. *Curr Opin Neurol*, *25*(1), 61–66.

Shapiro, M. G., Homma, K., Villarreal, S., Richter, C.-P., Bezanilla, F. (2012). Infrared light excites cells by changing their electrical capacitance. *Nat. Commun.*, *3*(1), 736.

Sharp, A. A., O'Neil, M. B., Abbott, L. F., Marder, E. (1993). Dynamic clamp: computer-generated conductances in real neurons. *J. Neurophysiol.*, *69*(3), 992–995.

Shen, H., Wang, G. (2010). A tetrahedron-based inhomogeneous Monte Carlo optical simulator. *Phys. Med. Biol.*, *55*(4), 947.

Shields, C. L., Shields, J. A., Cater, J., Lois, N., Edelstein, C., Gündüz, K., Mercado, G. (1998). Transpupillary thermotherapy for choroidal melanoma. *Ophthalmology*, *105*(4), 581–590.

Shim, J. H. (2015). Limitations of spinal cord stimulation for pain management. *Korean J. Anesthesiol.*, *68*(4), 321–322.

Soin, A., Syed Shah, N., Fang, Z.-P. (2015). High-Frequency Electrical Nerve Block for Postamputation Pain: A Pilot Study. *Neuromodulation Technol. Neural Interface*, *18*(3), 197–206.

Sun, H., Hosszufalusi, N., Mikula, E. R., Juhasz, T. (2011). Simulation of the temperature increase in human cadaver retina during direct illumination by 150-kHz femtosecond laser pulses. *J. Biomed. Opt.*, *16*(10), 108001.

Tan, X., Rajguru, S., Young, H., Xia, N., Stock, S. R., Xiao, X., Richter, C.-P. (2015). Radiant energy required for infrared neural stimulation. *Sci. Rep.*, *5*(1), 13273.

Tasaki, I., & Fujita, M. (1948). Action currents of single nerve fibers as modified by temperature changes. *J. Neurophysiol*, *11*(3).

Thompson, A. C., Stoddart, P. R., & Jansen, E. D. (2014). Optical Stimulation of Neurons. *Curr. Mol. Imaging*, *3*(2), 162–177.

Thompson, A. C., Wade, S. A., Cadusch, P. J., Brown, W. G. A., Stoddart, P. R. (2013). Modeling of the temporal effects of heating during infrared neural stimulation. *J. Biomed. Opt.*, *18*(3), 035004.

Thompson, A. C., Wade, S. a, Brown, W. G. A., Stoddart, P. R. (2012). Modeling of light absorption in tissue during infrared neural stimulation. *J. Biomed. Opt.*, *17*(7), 075002.

Thomsen, S. (2005, April 14). *Nonthermal effects in thermal treatment applications of nonionizing irradiation* (T. P. Ryan, Ed.). International Society for Optics and Photonics.

Tolstykh, G. P., Olsovsky, C. A., Ibey, B. L., Beier, H. T. (2017). Ryanodine and IP $_3$ receptor-mediated calcium signaling play a pivotal role in neurological infrared laser modulation. *Neurophotonics*, *4*(2), 025001.

Tozburun, S., Lagoda, G. A., Burnett, A. L., Fried, N. M. (2012). Subsurface near-infrared laser stimulation of the periprostatic cavernous nerves. *J. Biophotonics*, *5*(10), 793–800.

Van Egeraat, J. M., Wikswo Jr, J. P. (1993). A model for axonal propagation incorporating both radial and axial ionic transport. *Biophys. J.*, *64*(4), 1287.

Verrills, P., Sinclair, C., Barnard, A. (2016). A review of spinal cord stimulation systems for chronic pain. *J. Pain Res.*, *9*, 481–492.

Verzar, F. (1912). The gaseous metabolism of striated muscle in warm-blooded animals. *J. Physiol.*, *44*(4), 243–258.

Voets, T. (2014). *TRP Channels and Thermosensation*.

Vogel, A., & Venugopalan, V. (2010). Pulsed Laser Ablation of Soft Biological Tissues. In *Optical-Thermal Response of Laser-Irradiated Tissue* (pp. 551–615). Dordrecht: Springer Netherlands.

von Maltzahn, G., Park, J.-H., Agrawal, A., Bandaru, N. K., Das, S. K., Sailor, M. J., & Bhatia, S. N. (2009). Computationally Guided Photothermal Tumor Therapy Using Long-Circulating Gold Nanorod Antennas. *Cancer Res.*, *69*(9), 3892–3900.

Walsh, A. J., Cantu, J. C., Ibey, B. L., Beier, H. T. (2017, February 15). *Short infrared laser pulses increase cell membrane fluidity* (E. D. Jansen & H. T. Beier, Eds.). International Society for Optics and Photonics.

Walsh, A. J., Tolstykh, G. P., Martens, S., Ibey, B. L., Beier, H. T. (2016). Action potential block in neurons by infrared light. *Neurophotonics*, *3*(4), 40501.

Wang, J., Borton, D. A., Zhang, J., Burwell, R. D., Nurmikko, A. V. (2010). A neurophotonic device for stimulation and recording of neural microcircuits. *Conf Proc IEEE Eng Med Biol Soc*, *2010*, 2935–2938.

Wang, L., Jacques, S. L., Zheng, L. (1995). MCML—Monte Carlo modeling of light transport in multi-layered tissues. *Comput. Methods Programs Biomed.*, *47*(2), 131–146.

Wang, Y. T., Rollins, A. M., Jenkins, M. W. (2016). Infrared inhibition of embryonic hearts. *J. Biomed. Opt.*, *21*(6), 60505.

Wang, Z., Ha, S., Kim, K. (2012, February 23). *Evaluation of finite element based simulation model of photoacoustics in biological tissues* (J. G. Bosch & M. M. Doyley, Eds.). International Society for Optics and Photonics.

Welch, A. J., Gemert, M. J. C. van. (2010). *Optical-thermal response of laser-irradiated tissue*. Springer.

Welch, A. J., van Gemert, M. J. C. (Eds.). (2011). *Optical-Thermal Response of Laser-Irradiated Tissue*. Dordrecht: Springer Netherlands.

Wells, J., Kao, C., Jansen, E. D., Konrad, P., Mahadevan-Jansen, A. (2005). Application of infrared light for in vivo neural stimulation. *J. Biomed. Opt.*, *10*(6), 064003.

Wells, J., Kao, C., Konrad, P., Milner, T., Kim, J., Mahadevan-Jansen, A., Jansen, E. D. (2007). Biophysical Mechanisms of Transient Optical Stimulation of Peripheral Nerve. *Biophys. J.*, *93*(7), 2567–2580.

Wells, J., Kao, C., Mariappan, K., Albea, J., Jansen, E. D., Konrad, P., Mahadevan-Jansen, A. (2005). Optical stimulation of neural tissue in vivo. *Opt. Lett.*, *30*(5), 504–506.

Wen, S.-B., Ly, K. (2019). Direct numerical simulation of laser induced breakdown and the associated micro-cavitation in a bio-tissue. *Int. J. Heat Mass Transf.*, *131*, 873–889.

Wilson, B. C., Adam, G. (1983). A Monte Carlo model for the absorption and flux distributions of light in tissue. *Med. Phys.*, *10*(6), 824–830.

Wu, B. S., Walker, V. K., Robertson, R. M. (2001). Heat shock-induced thermoprotection of action potentials in the locust flight system. *J. Neurobiol.*, *49*(3), 188–199.

Wu, J., Wikswo, J. P. (1997). Effects of bath resistance on action potentials in the squid giant axon: myocardial implications. *Biophys. J.*, *73*(5), 2347–2358.

Xia, N., Tan, X., Xu, Y., Richter, C.-P. (2017, February 15). *Pressure generation during neural stimulation with infrared radiation* (E. D. Jansen & H. T. Beier, Eds.). International Society for Optics and Photonics.

You, M., Mou, Z. (2017). Model study of combined electrical and near-infrared neural stimulation on the bullfrog sciatic nerve. *Lasers Med. Sci.*, *32*(5), 1163–1172.

Zhao, H. (2017). Recent Progress of Development of Optogenetic Implantable Neural Probes. *Int. J. Mol. Sci.*, *18*(8).

Zhao, K., Tan, X., Young, H., Richter, C.-P. (2016). Stimulation of Neurons with Infrared Radiation. In *Biomedical Optics in Otorhinolaryngology* (pp. 253–284). New York, NY: Springer New York.

Zhu, C., Liu, Q. (2013). Review of Monte Carlo modeling of light transport in tissues. *J. Biomed. Opt.*, *18*(5), 50902.